

## **INFORMATION TO USERS**

**This manuscript has been reproduced from the microfilm master. UMI films the text directly from the original or copy submitted. Thus, some thesis and dissertation copies are in typewriter face, while others may be from any type of computer printer.**

**The quality of this reproduction is dependent upon the quality of the copy submitted. Broken or indistinct print, colored or poor quality illustrations and photographs, print bleedthrough, substandard margins, and improper alignment can adversely affect reproduction.**

**In the unlikely event that the author did not send UMI a complete manuscript and there are missing pages, these will be noted. Also, if unauthorized copyright material had to be removed, a note will indicate the deletion.**

**Oversize materials (e.g., maps, drawings, charts) are reproduced by sectioning the original, beginning at the upper left-hand corner and continuing from left to right in equal sections with small overlaps.**

**Photographs included in the original manuscript have been reproduced xerographically in this copy. Higher quality 6" x 9" black and white photographic prints are available for any photographs or illustrations appearing in this copy for an additional charge. Contact UMI directly to order.**

**ProQuest Information and Learning  
300 North Zeeb Road, Ann Arbor, MI 48106-1346 USA  
800-521-0600**

**UMI<sup>®</sup>**





## ABSTRACT

**Title of Dissertation:** TRANSPORT PHENOMENA OF ANOMALOUS  
COSMIC RAYS DURING THE RECOVERY  
PHASE OF SOLAR CYCLE 22

**Matthew Eric Hill, Doctor of Philosophy, 2001**

**Dissertation directed by:** Professor Douglas C. Hamilton  
Department of Physics

We study anomalous cosmic ray (ACR) transport phenomena in the heliosphere during the 1991 to 2000 recovery phase, a period of positive heliomagnetic polarity. Using measurements from the Low Energy Charged Particle (LECP) instruments aboard the outer heliospheric Voyager 1 and 2 spacecraft and the Low-energy Ion Composition Analyzer (LICA) on the low-Earth orbit SAMPEX satellite, we calculate ACR  $H^+$ ,  $He^+$ , and  $O^+$  time-intensity profiles and energy spectra. The 0.6- to 39-MeV/nucleon energy range reaches the lowest ACR energies studied, Voyager 1 provides the most distant *in situ* observations made ( $\sim 80$  AU), and the spacecraft cover the entire recovery phase, making this the most complete study of low-energy ACRs to date.

We present a technique, the quasi-local gradient method, to simultaneously determine radial and latitudinal intensity gradients using data from fewer than three

spacecraft, something not possible with the non-local gradient method. Both gradient techniques are valid under different sets of conditions, but agree when conditions are mutually satisfied. We study ACR transport with two additional methods, including a time-dependent numerical solution to the spherically symmetric Fokker-Planck equation, and these methods corroborate the results of the quasi-local procedure. During ~1994 to 1999, for 1.3-, 6-, and 21-MeV/nucleon  $O^+$  the radial gradients from ~50 to 70 AU are  $+11.2 \pm 1.1$ ,  $+6.8 \pm 0.8$ , and  $-0.2 \pm 0.5$  %/AU, respectively, and the latitudinal gradients from ~10 to 30 degrees of absolute latitude are  $-5.5 \pm 1.2$ ,  $-2.6 \pm 0.8$ , and  $+2.9 \pm 0.3$  %/degree, respectively.

In 1998 and 1999 a statistically significant periodicity of  $150 \pm 10$  days is observed in the intensities of the three ACR species at Voyager 1, all three in phase. This may be related to similar periodicities observed in solar and near-Earth measurements, but never before reported in outer heliospheric or ACR data.

We show that the dominant ACR transport processes are convection and diffusion and that a quasi-steady state is reached after 1994. A spherically symmetric transport model with a constant ACR source at the termination shock is consistent with the data, and gradient and curvature drift effects, away from the heliospheric current sheet, are significant only for ACRs with rigidities above ~2 GV.



**TRANSPORT PHENOMENA OF ANOMALOUS COSMIC RAYS  
DURING THE RECOVERY PHASE OF SOLAR CYCLE 22**

**by**

**Matthew Eric Hill**

**Dissertation submitted to the Faculty of the Graduate School of the  
University of Maryland, College Park in partial fulfillment  
of the requirements for the degree of  
Doctor of Philosophy  
2001**

**Advisory Committee:**

**Professor Douglas C. Hamilton, Chair  
Professor Michael A. Coplan  
Professor James F. Drake  
Professor George Gloeckler  
Dr. Frank B. McDonald**

**UMI Number: 3035788**

**Copyright 2001 by  
Hill, Matthew Eric**

**All rights reserved.**

**UMI<sup>®</sup>**

---

**UMI Microform 3035788**

**Copyright 2002 by ProQuest Information and Learning Company.  
All rights reserved. This microform edition is protected against  
unauthorized copying under Title 17, United States Code.**

---

**ProQuest Information and Learning Company  
300 North Zeeb Road  
P.O. Box 1346  
Ann Arbor, MI 48106-1346**



**©Copyright by**

**Matthew Eric Hill**

**2001**



# DEDICATION

To

**Frank L. Innacelli, Benjamin I. Hill, and Julius W. Drenzek**

## ACKNOWLEDGEMENTS

I thank my dissertation advisor, Professor Douglas C. Hamilton, for his thoughtful guidance, insight, and efforts on my behalf throughout the five and a half years I have been a graduate student. He has generously shared his time with me and consistently provided careful and instructive suggestions, for which I am greatly appreciative. I am indebted to all of the members of the dissertation advisory committee for their time, effort, and patience. In Particular, I would thank Professor Michael Coplan for representing the dean, Professor James Drake for his mathematical methods and electrodynamics courses, Professor George Gloeckler for his role in developing the LECP instruments, and Dr. Frank McDonald for useful discussions and kind provision of galactic cosmic ray observations. Additionally, I thank Professor Glenn Mason who, but for a scheduling conflict, would have been a member of my examining committee.

I would like to thank the entire Space Physics Group for their professionalism, assistance, and good humor. In particular, I benefited from the abilities of Nathan Cramer, who assisted me in the analysis and processing of LECP data during 1999 and 2000. Scott Lasley, Laurence Bleau, and Jeanette Williams have provided invaluable assistance with computer difficulties, and I thank them. I extend my gratitude to Jody Reed, JoAnn Simms, and Pat Ipavich for ably dispatching the financial and administrative matters associated with my studies. I thank Dr. Mihir Desai for lending me his books, and for helpful conversations. I would also like to thank Robert

**Lundgren and Drs. George Ho and Michael Collier for assistance they provided to me when I first joined the Space Physics group.**

**To our colleagues at the Applied Physics Laboratory at Johns Hopkins University, Drs. Tom Krimigis and Robert Decker, I am thankful for assistance and collaborations involving the LECP instruments, and I thank Dr. Ed Keath for helping with problems related to the LECP electronics. I thank Dr. Joseph Mazur of the Aerospace Corporation for his collaboration involving the sharing of ACR oxygen data from the LICA sensor on the SAMPEX spacecraft, and Dr. J.T. Hoeksema for Wilcox Solar Observatory data of heliospheric current sheet tilt angles.**

**Personally, my family and friends have been very supportive of my studies and I very much appreciate this. My brother and his family have been steadfast in their encouragement. My wife's parents and grandparents have provided outstanding support. To my mother, Lucia Limbach, I owe everything. Tracy, my wife, has been patient throughout this time and deserves my heartfelt thanks, which I gladly give. It is her hard work that has enabled me to pursue this goal. Most recently, I thank her for her considerable labors in assisting me with my final revision of this document.**

**Finally, the opportunity to be involved with the Voyager mission, which I followed enthusiastically as a child, has been a particular thrill and I thank everyone involved in its success. This work has been supported by NASA via the Johns Hopkins University Applied Physics Laboratory subcontract 735138 to the University of Maryland.**

# TABLE OF CONTENTS

<b>Acknowledgements</b> .....	iii
<b>List of Figures</b> .....	vii
<b>List of Tables</b> .....	viii
<b>Chapter 1 – Introduction</b> .....	1
<b>1.1 – Anomalous Cosmic Ray (ACR) Phenomena</b> .....	1
1.1.1 – The Heliosphere .....	1
1.1.2 – Cosmic Rays .....	3
1.1.3 – The Discovery of Anomalous Cosmic Rays.....	6
1.1.4 – The Classical Model of ACR Geneses and Transport.....	8
1.1.5 – Progress in ACR and Outer Heliospheric Science.....	12
<b>1.2 – Thesis and Overview</b> .....	17
1.2.1 – Thesis.....	17
1.2.2 – Overview .....	18
<b>Chapter 2 – Instrumentation and Analysis</b> .....	23
<b>2.1 – The Voyager 1 and 2 Spacecraft</b> .....	23
<b>2.2 – The Low Energy Charged Particle (LECP) Experiment</b> .....	30
2.2.1 – Instrument Layout .....	30
<b>2.3 – Particle Data Properties</b> .....	34
<b>Chapter 3 – Anomalous Cosmic Ray (ACR) Transport</b> .....	36
<b>3.1 – Introduction</b> .....	36
<b>3.2 – ACR Observations from 1991 to 2000</b> .....	38
3.2.1 – Outer Heliospheric Time Profiles .....	38
3.2.2 – Outer Heliospheric Energy Spectra.....	46
3.2.3 – Inner and Outer Heliospheric Observations .....	52
<b>3.3 – Phenomenology of ACR Recovery</b> .....	63
3.3.1 – Parameterization of the Data.....	63
3.3.2 – A Phenomenological Recovery Model.....	74
3.3.3 – Format of Phenomenological Analysis .....	81
3.3.4 – Model Fits to Observations.....	86
<b>3.4 – Radial and Latitudinal Intensity Gradients</b> .....	97
3.4.1 – Non-Local Intensity Gradients.....	97
3.4.2 – Quasi-Local Intensity Gradients .....	103
3.4.3 – Analysis and Format of Gradient Results.....	108
3.4.4 – Observed Intensity Gradients.....	113
<b>3.5 – Numerical Solutions to the Transport Equation</b> .....	135
3.5.1 – The Cosmic Ray Transport Equation .....	135
3.5.2 – The Numerical Solution .....	136
3.5.3 – Format of Model Comparisons with Observations .....	143
3.5.4 – Model Comparisons with Observations .....	149

<b>Chapter 4 – Periodic ACR Phenomena</b> .....	158
4.1 – Introduction .....	158
4.2 – Data Analysis .....	161
4.2.1 – Residual Intensity Variations .....	161
4.2.2 – Periodogram Analysis .....	163
4.2.3 – Galactic and Interplanetary-Accelerated Particles .....	167
4.3 – Observations.....	170
4.3.1 – Voyager 1 ACR Periodicities .....	170
4.3.2 – Voyager 2 ACR Periodicities .....	171
4.4 – Discussion .....	172
4.4.1 – The ACR Periodicity and Interplanetary Variations .....	172
4.4.2 – The Lack of 151-day Periodicities at Voyager 2 .....	174
4.4.3 – Implications for the Sun and Heliosphere .....	176
4.5 – Summary .....	177
<b>Chapter 5 – Discussion</b> .....	179
5.1 – Summary of Data Analysis .....	179
5.1.1 – Analysis of ACR Transport .....	179
5.1.2 – Periodicity Analysis .....	184
5.2 – Theory and Observation.....	186
5.2.1 – The Scale of Transport Parameters .....	186
5.2.2 – Drifts and Intensity Gradients.....	188
5.2.3 – Neutral Current Sheet Conditions in the Outer Heliosphere .....	192
5.2.4 – Comparison of Intensity Gradient Observations.....	201
5.3 – Interpretation and Implications .....	208
5.3.1 – Anomalous Cosmic Ray Transport Phenomena .....	208
5.3.2 – Global Heliospheric Implications .....	217
5.4 – Conclusions .....	219
<b>Appendices</b> .....	222
<b>A – Flux Calculations with the LECP Instruments</b> .....	222
A.1 – Particle Identification .....	222
A.2 – Flux Calculation .....	228
<b>B—Notation</b> .....	231
<b>C – A Heuristic Approach to Cosmic Ray Transport</b> .....	234
<b>References</b> .....	240

## LIST OF FIGURES

Figure 2.1.1 Voyager 1 & 2 Ephemeris — Heliographic Coordinates.....	27
Figure 2.1.2 Voyager 1 & 2 Trajectories — HG Equatorial Projection .....	28
Figure 2.1.3 Voyager 1 & 2 Trajectories — HG Meridional Projection .....	29
Figure 2.2.1 Voyager Low Energy Charged Particle Instrument Diagram.....	31
Figure 3.2.1 Voyager 1 & 2 H, He & O Spectrograms 1987-2000 .....	40
Figure 3.2.2 Voyager 1 & 2 Hydrogen Time-Intensity Profiles 1991-2000 .....	42
Figure 3.2.3 Voyager 1 & 2 Helium Time-Intensity Profiles 1991-2000.....	44
Figure 3.2.4 Voyager 1 & 2 Oxygen Time-Intensity Profiles 1991-2000 .....	45
Figure 3.2.5 Voyager 1 & 2 Hydrogen Spectral Evolutions 1991-2000 .....	47
Figure 3.2.6 Voyager 1 & 2 Helium Spectral Evolutions 1991-2000 .....	49
Figure 3.2.7 Voyager 1 & 2 Oxygen Spectral Evolutions 1991-2000.....	50
Figure 3.2.8 SAMPEX, Voyager 1 & Voyager 2 Oxygen Spectra .....	61
Figure 3.2.9 SAMPEX, WIND, ACE & Voyager Oxygen Time-Intensity Profiles .....	62
Figure 3.3.1 Voyager 1 & 2 ACR H, He & O Recovery Fits .....	64
Figure 3.3.2 Inner and Outer Heliospheric ACR O Recovery Fits.....	67
Figure 3.3.3 Recovery Time Parameters vs. ACR Properties.....	70
Figure 3.3.4 Phenomenological Model Summary—Best Fit Without Source Model .....	94
Figure 3.3.5 Phenomenological Model Summary—Best Fit with $g\lambda > 0$ .....	95
Figure 3.3.6 Phenomenological Model Summary—Best Fit with Source Model .....	96
Figure 3.4.1 Quasi-Local Intensity Gradient Fits for 0.6- to 3-MeV/nucleon $O^+$ .....	123
Figure 3.4.2 Quasi-Local Intensity Gradient Fits for 1- to 5-MeV/nucleon $O^+$ .....	124
Figure 3.4.3 Quasi-Local Intensity Gradient Fits for 3- to 14-MeV/nucleon $O^+$ .....	125
Figure 3.4.4 Quasi-Local Intensity Gradient Fits for 7- to 28-MeV/nucleon $O^+$ .....	126
Figure 3.4.5 Quasi-Local Intensity Gradient Fits for 12- to 39-MeV/nucleon $O^+$ .....	127
Figure 3.4.6 Quasi-Local Intensity Gradient Fits for 3- to 12-MeV/nucleon $He^+$ .....	128
Figure 3.4.7 Quasi-Local Intensity Gradient Fits for 21- to 30-MeV/nucleon $He^+$ .....	129
Figure 3.4.8 Quasi-Local Intensity Gradient Fits for 5- to 11-MeV $H^+$ .....	130
Figure 3.4.9 Quasi-Local Intensity Gradient Fits for 24- to 30-MeV $H^+$ .....	131
Figure 3.4.10 Quasi-Local Intensity Gradient—Large Time Variations.....	132
Figure 3.4.11 Non-Local Intensity Gradients of ACR Oxygen .....	133
Figure 3.4.12 Quasi-Local Intensity Gradients with Latitudinal Symmetry Off .....	134
Figure 3.5.1 Numerical Solution Compared with Force Field Approximation.....	142
Figure 3.5.2 Demonstration Solution to the Cosmic Ray Transport Equation .....	148
Figure 3.5.3 Numerical Solution with Optimized Late-Recovery Agreement .....	157
Figure 4.1 Periodicity in the Voyager 1 Oxygen Time-Intensity Profile .....	162
Figure 4.2 Residual Intensity Variations of H, He, and O in 1998-1999 .....	164
Figure 4.3 Periodogram Analysis of Outer Heliospheric ACRs .....	168
Figure 5.2.1 Heliospheric Current Sheet in the Meridional Plane.....	199
Figure 5.2.2 Tilt Angle of the HCS and Voyager 1 & 2 Latitudes.....	200
Figure 5.3.1 The Radial and Energetic Dependence of the ACR Recovery Profile.....	216
Figure A.1 LECP Energy Thresholds in D1 vs. D2 PHA Matrix .....	223
Figure A.2 Flow Chart of the LECP Particle Identification Algorithm.....	227
Figure A.3 Sample PHA Matrix with Flux Boxes.....	230



## LIST OF TABLES

<b>Table 2.1.1</b>	<b>Voyager 1 &amp; 2 statistics during 1987-2001 .....</b>	<b>24</b>
<b>Table 2.3.1</b>	<b>Properties of Particle Data.....</b>	<b>35</b>
<b>Table 3.3.1</b>	<b>Parametrization of ACR Recovery Profiles .....</b>	<b>68</b>
<b>Table 3.3.2</b>	<b>Radial and Latitudinal Gradients from the Phenomenological Model .....</b>	<b>90</b>
<b>Table 3.4.1</b>	<b>Spatial Intensity Gradients of Outer Heliospheric ACRs .....</b>	<b>120</b>
<b>Table 3.4.2</b>	<b>Non-Local Gradient Ranges for ACR O<sup>+</sup> in 1993 to 1996 .....</b>	<b>120</b>
<b>Table 3.4.3</b>	<b>Quasi-Local Gradient with 10° S Latitude of Symmetry.....</b>	<b>122</b>
<b>Table 3.5.1</b>	<b>ACR O<sup>+</sup> Radial Gradients (%/AU) Calculated by Three Methods .....</b>	<b>152</b>
<b>Table 4.1</b>	<b>Period (in Days) of Selected Periodogram Peaks From Figure 4.3 .....</b>	<b>178</b>
<b>Table 5.2.1</b>	<b>Drift and Solar Wind Velocities for ACR Species .....</b>	<b>191</b>
<b>Table 5.2.2</b>	<b>Minimum Rigidities for Possible Neutral Region Effects .....</b>	<b>199</b>
<b>Table 5.2.3</b>	<b>Compilation of ACR Intensity Gradient Values .....</b>	<b>207</b>

# **Chapter 1 – Introduction**

## **1.1 – Anomalous Cosmic Ray (ACR) Phenomena**

### **1.1.1 – The Heliosphere**

The solar wind is the expanding upper atmosphere of the Sun, consisting primarily of a hot tenuous gas of disassociated protons and electrons in the plasma state. This nearly radially-emitted plasma flow pushes against the local interstellar medium (LISM) resulting in a cavity in that medium called the heliosphere, where the influence of the sun is dominant, and within which all of the Sun's known planets presently orbit. As predicted by Parker (1958) the magnetic field of the rotating Sun is "frozen into" the expanding, highly conductive solar wind and carried outward, forming the familiar Archimedian spiral shape of the magnetic field lines, as viewed from above the solar poles. This idealized field configuration is often referred to as the Parker spiral. In the meridional plane, it is useful to consider that the solar field is a strongly modified dipole. Near the solar surface the magnetic field is roughly dipolar, however, farther out along the equatorial plane, the dipolar loop structure is distorted and stretched by the solar wind to form a neutral heliospheric current sheet (HCS). For the distances from the sun considered here (1 to 80 AU) the dipole features are unimportant and the Parker field is appropriate with field lines lying along cones of constant latitude, outwardly directed north of the HCS and inwardly directed south of the HCS, for positive solar polarity (the polarity reverses every 11 years).

Sunward of the heliopause (HP) region where the pressure of the LISM balances that of the supersonic solar wind flow, there is expected to be a termination

shock (TS), which is thought to surround the Sun at a distance of ~100 astronomical units (AU), where the solar wind becomes subsonic. The Sun and heliosphere move with respect to the neutral and charged particles of the LISM at roughly 25 km/s (Bertin *et al.*, 1993). Beyond the solar wind termination shock the subsonic solar wind flow is expected to be modified by the influence of the relative motion of the LISM. The charged LISM material should be diverted to flow around the heliosphere causing the subsonic solar wind to change directions (e.g., near the apex of the heliosphere) and flow back around the heliosphere, perhaps forming an extended heliotail in the direction opposite the relative motion of the Sun. The neutral LISM material can flow into the heliosphere, as its interaction with heliospheric matter and fields is much weaker. The surface that separates the diverted LISM material from the redirected solar wind flow is the heliopause and is perhaps ~150 AU from the sun. The region between the TS and the HP is the heliosheath (or inner heliosheath if the LISM flow is supersonic and a heliospheric bow shock exists, in which case the region between the HP and the bow shock is called the outer heliosheath). The termination shock and the heliopause form natural boundaries that serve to define the extent of the heliosphere.

The heliosphere is not static, as is not the sun. The Sun's well-known 11 year solar cycle was first observed in the sunspot measurements of Heinrich Schwabe in 1851, although telescopic observations of sunspots date to the seventeenth-century (Russell, 1995). This periodicity drives the entire heliosphere—solar flares, solar particle events, interplanetary magnetic field, and perhaps heliospheric boundaries—in oscillations between relatively quiescent states and states of turbulent activity. Since the Sun's spin axis and axis of magnetic symmetry are not aligned, there exists an

angle between the HCS and the heliographic equatorial plane (defined with respect to the Sun's spin axis), called the tilt angle. This angle is also correlated with the solar cycle, with larger tilt angles being associated with solar maximum and smaller tilt angles occurring near solar minimum. Moreover, in some sense the HCS may be thought of as "flipping" at solar maximum, corresponding to the bulk reversal of the heliomagnetic polarity as the tilt angle reaches and continues past 90 degrees, although this picture greatly simplifies the complicated and not very well understood process. This interplanetary magnetic field reversal occurred for example in 1990; the inward pointing northern heliomagnetic field reversed while the tilt angle was large during the prevailing solar maximum-like conditions and became an outward pointing field with a large tilt angle, followed by a decrease in the tilt angle as conditions approached minimum later in the decade. The periods of the inwardly and outwardly directed magnetic field in the northern heliosphere are known as periods with negative and positive heliomagnetic polarity, respectively, often denoted  $A < 0$  and  $A > 0$ .

### **1.1.2 – Cosmic Rays**

From the perspective of Earth-bound observers cosmic rays can be neatly divided into two classes: Primary and secondary cosmic rays. Primary cosmic rays are energetic particles, mostly protons, that impinge upon the Earth's upper atmosphere from above, originating in some remote region of space (see below). Secondary cosmic rays are those energetic particles that result from the collision of primary cosmic rays with atmospheric particles; cosmic ray muons are a well-known example. Primary cosmic rays do not preferentially seek out the Earth and in fact are believed to

permeate the galaxy. Although primary cosmic rays measured beyond the Earth's atmosphere are the subject of this work, a few comments about the Earthly discovery of cosmic radiation are deserved.

Cosmic rays, as a concept of scientific interest, came into existence in 1912. In August of that year a balloon lifted Victor F. Hess and two other men three miles into the air on a 125 mile, morning trip from Aussig, Austria to Pieskow, Germany. Along with these men were three electroscopes, with which Hess made measurements to try to understand why charged objects were observed to spontaneously discharge over time. The surprising result of this balloon observation, was Hess's conclusion that "radiation of very great power enters our atmosphere from above." Thus began the study of cosmic rays, although the term was not used until Robert A. Millikan coined it in the 1920s. A very readable account by Rossi (1964) and more technical publications edited by Heisenberg (1946) and Flügge (1961) summarize the state of cosmic ray research at the start of the space age and tell the interesting early story of cosmic rays and the scientists who investigated them. (Hereafter "cosmic rays" should be understood to denote primary cosmic rays only, and unless otherwise noted, cosmic ray ions.)

Before the 1970's, combined ground-based, balloon, aircraft, rocket, and spacecraft measurements of cosmic radiation seemed to indicate that there were two categories of "cosmic rays": solar energetic particles and galactic cosmic rays (hereafter the convention will be never again to refer to solar energetic or interplanetary-accelerated particles as cosmic rays, although the term "solar cosmic ray" does appear in the literature). As the names suggest, solar energetic particles

(SEPs) are those ions originating at the Sun or accelerated by interplanetary phenomena closely related to solar activity (such as shock waves). The second category, the galactic cosmic rays (GCRs), are so named because they are thought to originate in the region of the galaxy outside our heliosphere, perhaps in supernova explosions or interstellar shocks associated with these or other violent events.

The SEPs and GCRs are distinguished from one another in many ways, for example, SEPs are dominant at kinetic energies below, say, some tens of MeV/nucleon and characteristically take the approximate form—in their differential energy spectra—of a decreasing power law  $j = T^{-\gamma}$ , where  $j$  is the differential particle intensity (or flux),  $T$  is the total kinetic energy of the particle, and  $\gamma$  is the spectral index. On the other hand GCRs are well-observed at higher energies, and peaks in the energy spectra are often seen at several hundred MeV/nucleon. Cosmic rays, unlike SEPs, were observed to exhibit an increasing, approximately linear relationship  $j = aT$ , where  $a$  is a constant, between the flux and total kinetic energy over a broad energy band below the energy of peak cosmic ray intensity at several hundred MeV [Rygg and Earl, 1971]. Another major distinction is that solar energetic particles are observed most often, and at higher intensities, during the maximum phase of the 11-year solar activity cycle, while cosmic rays are just the opposite, there being an anticorrelation between cosmic ray intensity and solar cycle activity (Forbush, 1954). (The cosmic ray intensities are said to be *modulated* by the solar activity.) Other differentiating factors include the fact that solar energetic particles exhibit a negative

heliocentric intensity gradient, indicating that the SEP source is near the Sun. Cosmic rays lack these characteristic negative gradients.

There were investigations into other possible particle populations besides SEPs and GCRs, such as the continually accelerated proton and helium nuclei studied by Fan, Gloeckler and Simpson (1965). The authors considered solar, galactic and interplanetary acceleration to attempt to explain their observations. Today, interplanetary-accelerated particles comprise an accepted category of energetic particles, those particles accelerated in the interplanetary (IP) medium, although not near the Sun, such as particles accelerated at so called corotating interaction regions (Barnes and Simpson, 1976). There is some overlap between the SEP and IP accelerated concept as the division between acceleration related or unrelated to the Sun is indistinct. Nevertheless, despite developing progress toward an understanding of IP-accelerated particles, the SEP-GCR picture was an established, if temporary, perspective on the rapidly evolving understanding of solar and interplanetary phenomena that existed in the early years of the space age.

### **1.1.3 – The Discovery of Anomalous Cosmic Rays**

Then IMP-5 satellite measurements were reported by Garcia-Munoz, Mason, and Simpson (1973) revealing a previously unobserved feature of the differential energy spectrum of helium, which was observed during a three-month solar quiet time period in 1972. Unlike the previous spectral observations of cosmic rays showing the approximately linear relationship  $j = aT$  below the energy of peak cosmic ray intensity, the IMP-5 data showed a distinctly flattened He spectrum below 80

MeV/nucleon that was essentially independent of kinetic energy. Garcia-Munoz, Mason, and Simpson (1973) tried to simultaneously fit their observed cosmic ray proton spectrum with a model which did not show an unusual enhancement, and the helium spectrum, utilizing previously adequate combinations of parameters from contemporary modulation theory (Jokipii, 1971) and were unable to do so. Consistent with their simplifying assumptions the authors concluded that modulation theory, under the assumption that the enhanced He particles were GCRs, could not explain the anomaly. Hovestadt *et al.* (1973), utilizing low-energy quiet time observations made with the IMP-7 satellite, extended the unusual cosmic ray observations to a new species. They found a flattening of the O spectrum between 2 and 8.5 MeV/nucleon and suggested a possible relation to the similarly unusual He spectrum.

Additional and complimentary measurements of similarly anomalous enhancements of nitrogen and oxygen relative to other nuclei, along with the first interpretation of the strange phenomena soon followed (McDonald *et al.* 1974). The Pioneer 10 spacecraft data were analyzed, showing that the difference between solar or galactic elemental abundance ratios and those associated with the anomalous component was as high as a factor of 20. It was argued by the authors that this unusual, nonsolar particle composition, combined with the preliminary determination that 8- to 30-MeV/nucleon He and O possessed a positive radial intensity gradient, supported the conclusion that the anomalous low-energy cosmic rays were of extrasolar origin. McDonald *et al.* (1974) went on to suggest that the low-energy phenomena could be “produced by a unique nearby source” or a galactic process. This was the first experiment to demonstrate that carbon was not enhanced; i.e., there was



an anomalous composition, knowledge of which was instrumental to the Fisk, Kozlovsky, and Ramaty (1974) interpretation discussed in the next section.

#### **1.1.4 – The Classical Model of ACR Geneses and Transport**

An elegantly simple interpretation (now widely accepted) of the anomalous ion enhancements was proposed by Fisk, Kozlovsky, and Ramaty (1974) within months of the published experimental results. The model centers on the role of interstellar neutral atoms, as follows. Ambient neutrals in the local interstellar medium, unlike interstellar ions, are supposed to enter the heliosphere owing to relative motion of the heliosphere with respect to the LISM. These atoms can become ionized through interaction with solar ultraviolet photons, or charge-exchange with the constituent particles of the solar wind. Upon ionization, these ions, today known as pick-up ions (PUIs) immediately interact with and become “picked up” by the magnetized solar wind, becoming accelerated in the process. The pick-up ions were predicted to have energies up to roughly 1-keV/nucleon (appropriate to ~450 km/s solar wind velocity) in the solar wind frame and to be singly ionized, thus distinguishing them from other solar wind ions, and providing unambiguous means by which to experimentally test the prediction. Fisk, Kozlovsky, and Ramaty (1974) point out that H, He, N, O, and Ne each have a higher first ionization potential (FIP) than do other possible interstellar constituents, such as C, Mg, Si, and Fe, therefore increasing the likelihood that a significant fraction of the former set of particles remain neutral in the LISM, while members of the latter set should be mainly ionized before they encounter the heliosphere. Therefore H, He, N, O, and Ne to varying degrees will have substantially greater opportunity to be swept into the heliospheric cavity than do the low-FIP

species, partially explaining why the anomalies were seen in O, N and He. The remainder of the explanation involves the singly-charged, and accelerated nature of pick-up ions in the solar wind, whose relatively large gyroradii compared to solar wind particles could potentially allow “an acceleration mechanism operating somewhere in the solar cavity” (Fisk, Kozlovsky, and Ramaty, 1974) to preferentially accelerate the high-FIP pick-up ions. The authors noted that the lack of observational evidence, at the time, for a low-energy proton enhancement was related to the fact that there is only one possible H charge state. This results in the relative exclusion of H PUIs accelerated at the “mechanism” from the inner heliosphere in a way indistinguishable from GCRs of comparable energies. At the same time as the interpretive work of Fisk, Kozlovsky, and Ramaty (1974), additional results were published (Chan and Price, 1974), experimentally confirming the anomalous cosmic ray (ACR) oxygen enhancements.

An unsatisfactorily resolved aspect of the new paradigm, at the time, involved the mechanism to accelerate  $\sim$ keV/nucleon PUIs to  $\sim$ 10 MeV/nucleon ACR energies. This was addressed by Pesses, Jokipii, and Eichler (1981) when they presented their model of pick-up ion acceleration at the solar wind termination shock (by the shock-drift or “ $V \times B$ ” and the compressive Fermi acceleration mechanisms) “near the heliospheric poles, with subsequent drift-related transport to the heliospheric equatorial regions.” This acceleration and drift mechanism favors the acceleration of singly ionized PUIs over particles with higher charge states, such as solar wind ions, since the potential difference between the heliospheric pole and the equator is estimated to be  $\Delta V = 240$  MV. Thus pole-to-equator drifting particles undergo a

kinetic energy/nucleon loss of  $E_d = ze\Delta V/A$ , where  $z$  and  $A$  are the ion charge and atomic mass numbers, respectively, so a source energy/nucleon  $E_s$ , and an observed equatorial energy/nucleon  $E_o$  are approximately related by  $E_o = E_s - E_d$ . The required acceleration energy/nucleon is  $E_s = E_o + ze\Delta V/A$ , making it clear that acceleration to a given observed energy/nucleon is easier for heavy, low charge ions. It was also suggested that expected strong turbulence near the shock could inhibit drift and allow acceleration. As pointed out by Jokipii (1990) the above model agreed with data until 1985, failing afterwards when the predicted factor of 3 to 5 between particle intensities at the respective spectral peak energies during the 1985  $A < 0$  period and the  $A > 0$  period of the previous solar cycle failed to materialize, (the observed factor being significantly smaller). A later modification to the original model relies on the use of a non Parker field over the solar poles (Jokipii and Kota, 1989) resulting in the poles being no longer considered preferential injection sites for pick-up ions (Jokipii, 1990).

At this point the crux of the “classical” drift-diffusion model of anomalous cosmic ray acceleration and transport has been presented. In summary, the model consists of ambient interstellar neutral atoms with high first ionization potentials (He, N, O, and Ne) preferentially enter the heliosphere, where they become ionized due to solar wind or UV interactions, at which time the newly generated, singly ionized, pick-up ions are carried away with the solar wind (Fisk, Kozlovsky, and Ramaty, 1974). The PUIs are convected to the termination shock where they are accelerated due to some combination of shock-drift and first-order Fermi acceleration (Pesses, Jokipii, and Eichler, 1981; Jokipii, 1990). Once accelerated some of these particles, now called anomalous cosmic rays, drift and diffuse back toward the inner

heliosphere, where they were first observed in energy spectra as anomalous low-energy enhancements in helium (Garcia-Munoz, Mason, and Simpson, 1973), oxygen (Hovestadt *et al.*, 1973; McDonald *et al.*, 1974) and nitrogen (McDonald *et al.*, 1974).

Three important predictions of the preceding model are the existence of pick-up ions (Fisk, Kozlovsky, and Ramaty, 1974), the dependence of the sign of the heliolatitudinal ACR intensity gradient on the 22-year heliomagnetic cycle (Jokipii and Kopriva, 1979), and the singly charged nature of PUIs and anomalous cosmic rays (Fisk, Kozlovsky, and Ramaty, 1974). Experimental confirmation of the existence of PUIs was presented by Möbius *et al.* (1985) in the first direct observations of pick-up  $\text{He}^+$ , (the measurements were made at the AMPTE/IRM spacecraft upstream of the Earth's bow shock). This was followed by the discovery of H pick-up ions by Gloeckler *et al.* (1993) utilizing Ulysses spacecraft data. Both groups of investigators took advantage of the sharp drop in the phase space density of PUIs at ion velocities twice that of the local solar wind to distinguish the PUIs from suprathermal solar wind ions; this sharp drop is a consequence of the PUIs essentially zero initial speed in the inertial heliospheric frame. The predicted reversal of the sign of the latitudinal ACR intensity gradient coincident with the heliomagnetic polarity reversal gained observational support through three consecutive solar minima. McKibben (1989) determined a positive latitudinal gradient for ACR He during the 1975-1976 ( $A > 0$ ) period using Pioneer 11 data; Cummings, Stone, and Webber (1987) measured a negative latitudinal gradient for ACR oxygen using Pioneer 10 and Voyager data from 1985 ( $A < 0$ ); and Cummings *et al.* (1995a) reported small positive latitudinal gradients for O based on analysis of data from a fleet of spacecraft in 1993 ( $A > 0$ ).

Thirdly, the singly charged nature of ACRs was considered by McKibben (1977) who argued that observed anomalous cosmic rays behaved in a manner similar to particles with a high rigidity comparable to the rigidity of singly charged ACRs and inconsistent with the rigidity of multiply charged ACRs. Cummings, Stone and Webber (1984) made assumptions about the form of the ACR source spectra and used mass per charge scaling of the modulated spectra to arrive at the conclusion that ACRs are indeed singly ionized. Singh *et al.* (1991) and Adams *et al.* (1991) used the magnetosphere of the Earth as a geomagnetic rigidity filter to determine the charge state of ACRs. First Singh *et al.* (1991) determined upper limits of ACR N, O, and Ne charge states from 10 particle events observed during the Space Shuttle Spacelab-3 orbit, and found eight singly charged particles and two particles with low charge states, consistent with predominantly singly charged ACRs. Adams *et al.* (1991) made simultaneous charge state measurements of ACRs using the Cosmos, IMP-8 and ISEE-3 (ICE) satellites, and confirmed the singly ionized charge state of anomalous cosmic rays. Later, high-quality charge state measurements were made with data from the SAMPEX spacecraft (Klecker *et al.*, 1995) providing convincing evidence for singly charged ACRs. For higher-energy ACRs, such as oxygen above 20 MeV/nucleon, it was suggested (Mewaldt *et al.*, 1996) that multiple charged states are more important than was previously thought.

#### **1.1.5 – Progress in ACR and Outer Heliospheric Science**

Although this introduction is intended to present the generally accepted observational evidence and “baseline” model of ACR phenomena, with which to later contrast more recent science, and not to be a survey of state-of-the-art theoretical and

experimental results, it is still of use to extend the classical picture somewhat before proceeding with the original analysis that occupies the succeeding chapters. Findings regarding developments in modulation theory and phenomenology and the discovery of ACR protons will be discussed in turn, as these topics will help to frame the subsequent exposition. Other important results, such as those resulting from the various Ulysses investigations, will be discussed at the appropriate point in the text.

Initial work on the relationship between cosmic ray intensities and the magnetic and other properties of transient interplanetary disturbances predated the ACR discovery (Burlaga *et al.*, 1985, and references therein). A common view now is that drift effects dominate ACR transport during solar minima and that modulation due to transient disturbances (i.e., diffusive barriers) prevails during solar maxima. This is due simply to the comparative lack of such disturbances during solar minimum periods, at which time, moreover, the less-turbulent interplanetary magnetic field (IMF) is well-ordered with a roughly equatorial current sheet, conditions suitable for drifts. A useful concept in regard to diffusive modulation is the so called CR- $B$  relation, where CR stands for cosmic ray intensity and  $B$  is the IMF strength, given by  $dj/dt \propto -(B/B_p - 1)$ , for  $B/B_p > 1$ , and  $dj/dt \propto 1$ , for  $B/B_p < 1$  (Burlaga *et al.*, 1985), where the time derivative of CR flux is related to the ratio  $B/B_p$  of the local IMF strength to that predicted by the Parker field. The CR- $B$  relation predicts that  $j$  will decrease when  $B$  is elevated and increase when  $B$  is depressed. This relation was supported theoretically by Chih and Lee (1986) when they considered Forbush decreases and CR solar cycle variations by linearizing the standard cosmic ray transport equation (CRTE) first enunciated by Parker (1965), wherein they found a

close relationship between the IMF ratio and a perturbation  $\delta\kappa$  in the local diffusion coefficient  $\kappa$ . There is apparent general agreement that small scale variations of interplanetary parameters such as  $B/B_p$  or  $\delta\kappa$  explain short term CR modulation. What is less well-established is the relationship long-term solar-IP variations have on modulation. For example, while the classical ACR model (as well as standard CR modulation theory in general) predicts an association between CR intensities and the HCS tilt angle, particularly during  $A < 0$  periods, when cosmic rays are supposed to gain access to the heliosphere near the HCS, it has also been suggested that most of these intensity variations could be due to variations in the bulk solar field strength (e.g., Cane, 1999). Since both the IMF strength and the tilt angle are correlated to solar activity, it is nontrivial to distinguish between the two interpretations.

The classical model has been widely supported by observations, such as the results referred to in the previous section, and received confirmation by independent numerical modeling (Potgieter and Moraal, 1985). However, as was mentioned in the preceding section, data after 1985 were not consistent with the model, and results from the Ulysses mission to high heliolatitudes confirmed the need for changes (e.g., Jokipii *et al.*, 1995; Potgieter, 2000). The most dramatic potential conceptual change from the original theory (Pesses, Jokipii, and Eichler, 1981) concerned the preferred acceleration above the solar poles and subsequent drift to the heliographic equator. The existence of large-scale fluctuations in the solar polar magnetic field (Jokipii *et al.*, 1995, and references therein) and the evidence of *small* latitudinal gradients at high latitudes (Simpson, Zhang and Bame, 1996; Trattner, Marsden and Sanderson, 1997) point to a view at variance with the classical model. As summarized by Van

Allen (2000) the increased polar turbulence appears to inhibit access of cosmic rays to the poles, during both heliomagnetic polarities, and may in fact lead to preferential ACR transport in the heliographic equatorial region, rather than above the poles.

Hydrogen, helium and oxygen ions will be the primary three species studied in this dissertation. Therefore, the existence of ACR He and O having been addressed above in the review of the classical model and initial discovery of ACRs, the status of anomalous hydrogen merits discussion. Fisk (1986) suggested that an, at the time, undetected anomalous hydrogen component may exist, yet be difficult to detect since the spectrum might be very similar to and overlap significantly with the GCR H spectrum. Analysis of data from the Voyager 1 and 2 Cosmic Ray Subsystem (CRS) instruments was performed for periods in 1985 and 1987 (Christian, Cummings and Stone, 1988). The authors compared the changes in the spectra of the readily identifiable ACR He to that of low-energy H over the two near-solar-minimum periods in the outer heliosphere ( $> 18$  AU), and also considered GCR carbon. They concluded that the most likely explanation for the observed enhancements at 60 MeV was the presence of ACR H, bolstered by the fact that no similar enhancement was observed for carbon. The spectral differences were subtle, requiring a modified ordinate for the energy spectrum to bring out the variations.

Reinecke and Moraal (1992) suggested that the enhanced low energy cosmic rays (not limited to H) might simply be a natural manifestation of the modulation process. They solved the two-dimensional (i.e., longitudinally symmetric), drift-free cosmic ray transport equation numerically and found, with a broad range of parameters, that “bulges” appeared in their calculated spectra at energies below the



GCR peaks. These bulges represent a transition below the peak energy to the classical convection-diffusion limit (i.e., where adiabatic deceleration is negligible), *not* a transition to the convective-adiabatic limit (where diffusion is negligible) as is commonly seen at 1AU resulting in the familiar  $j \propto \mathcal{T}$  form (Rygg and Earl, 1971). The convection-diffusion bulges appear in the model calculations (Reinecke and Moraal, 1992) of outer heliospheric cosmic rays (as opposed to cosmic rays near the Sun) because, in the outer heliosphere the term in the cosmic ray transport equation (Eq. C.2) containing the divergence of the solar wind ( $2V/r$  for constant radial flow with solar wind speed  $V$  and helioradius  $r$ ) is small. These calculations suggest that the assumption that the  $j \propto \mathcal{T}$  spectral form is universal for low-energy GCRs can be mistaken, also making consideration of the 1985 and 1987 ACR H observations (Christian, Cummings and Stone, 1988) difficult to evaluate.

It wasn't until the approach to solar minimum, in ~1993, with more distant heliospheric spacecraft and during the opposite solar polarity that McDonald, Lukasiak, and Webber (1995) and Christian, Cummings, and Stone (1995) detected anomalous cosmic ray protons unambiguously, each using data from among the Pioneer 10, Voyager 1 and Voyager 2 spacecraft. Christian, Cummings, and Stone (1995) used a method similar to their previous detection of ACR H (1988), however this time the larger separation in kinetic energy between ACR and GCR H revealed a more distinct ACR enhancement in the  $j \propto \mathcal{T}$  portion of the GCR spectrum, particularly at Voyager 1. McDonald, Lukasiak, and Webber (1995) presented Pioneer 10 and Voyager 1 measurements from 1994 that exhibit H spectra significantly modified by the

anomalous component with respect to the expected form of the galactic spectrum. Furthermore they compared the H and He spectra from the 1994 period as well as the two previous solar minima, and note the similar total kinetic energy species scaling in all three cases, as expected for these singly ionized particles (e.g., Steenberg, Moraal, and McDonald, 1997). The temporal evolutions of the H and He spectra remain similar throughout the 1990's (e.g., Stone, Cummings, and Webber, 1997; see also Chapter 3), with the ACRs exhibiting the characteristic rapid recovery as compared with GRC ions, and ACR H forming a peak distinct from the galactic component.

## **1.2 – Thesis and Overview**

### **1.2.1 – Thesis**

The long-term transport of anomalous cosmic rays during the recovery period beginning in late 1991 is dominated by convective and diffusive processes which evolve the particle distributions to a quasi-steady state throughout the observed heliosphere by mid-1994. Consequently, the large increases of low-energy anomalous cosmic ray  $H^+$ ,  $He^+$ , and  $O^+$  intensities detected at the Voyager probes from 1994 to 1999 are primarily due to the motion of these spacecraft through sizeable spatial intensity gradients. To a significant degree the observations can be explained by a spherically symmetric transport model with a constant source of anomalous cosmic rays at the putative termination shock of the solar wind. Phenomena of secondary importance, such as effects due to curvature and gradient drifts, appear to be rigidity dependent, with anomalous cosmic rays having rigidities above approximately 2 GV noticeably affected by drift processes while lower-rigidity anomalous cosmic rays are

largely unaffected by drifts. A portion of the support for these interpretations comes from the application of a method, which we present, that determines *quasi-local* intensity gradients. Superposed on the long-term recovery trend are coherent short-term periodicities with a period of approximately 150 days in 1998 and 1999 in the anomalous cosmic ray intensities observed at Voyager 1. These variations may be due to regions of compressed solar wind, with elevated interplanetary magnetic field strength, periodically propagating from the inner to the outer heliosphere, inhibiting the transport of anomalous cosmic rays as the regions pass the spacecraft.

### **1.2.2 – Overview**

In Chapter 1 a general introduction to the subject of anomalous cosmic rays in the heliosphere (§1.1) and the central thesis (§1.2.1) of this dissertation are presented, followed by the present overview of the entire work. Subsequently the Voyager 1 and 2 spacecraft and their position in the heliosphere (§2.1) are discussed in the second chapter along with an introduction to the Low Energy Charged Particle instruments (§2.2) with which energetic particle measurements are made, and upon which the bulk of this thesis is based. The general properties and naming conventions associated with the ions having particular energy ranges discussed herein (§2.3) are described at the end of Chapter 2.

In Chapter 3 the long term transport of ACRs referred to in section 1.2.1 is analyzed in depth. The primary goal of the analysis is to distinguish those effects on the ACR intensity measurements that are due to inherently temporal (solar cycle) effects from those effects resulting from the motion of the spacecraft through the

heliosphere. Since there are only two spacecraft in the outer heliosphere returning low-energy ACR data, there are some limitations on what can be unambiguously determined, but a consistent picture does emerge from the analysis. Together with the initial presentation of the basic observations, a discussion is put forth that attempts to put these observations in the context of the broader solar cycle while highlighting the features of the data most important to the subsequent analysis (§3.2). The time-intensity profiles (§3.2.1) and energy spectra (§3.2.2) are introduced in turn along with a discussion of the 1-AU data obtained with SAMPEX and other near-Earth spacecraft (§3.2.3). The time intensity profiles of the recovering ACRs are all fit with a four-parameter function, and their general form and dependence on particle properties are discussed (§3.3.1) before the core analysis begins (§3.3.2-3.5.4).

Three techniques are employed to separate the *spatial* phenomena from the *temporal* phenomena. First this is done phenomenologically (§3.3) in such a way that some physical insight into the detailed dependence of specific features of the recovery is garnered, such as the timescale of the initial recovery. In this section all of the ACR time-intensity profiles are fit simultaneously (§3.3.2-3.3.4) to extract the common features of the time-intensity profiles and their dependence on particle rigidity. In the next section (§3.4) a method of calculating intensity gradients is developed (§3.4.1-3.4.2) and applied (§3.4.3-3.4.4) to the Voyager LECP observations. This *quasi-local* gradient method is distinct from the standard non-local gradient method (§3.4.1) because fewer than three spacecraft are adequate to determine two (or more) intensity gradients, in particular the radial and latitudinal gradients. This is accomplished by making temporal assumptions analogous to the spatial assumptions implicit in the

non-local gradient method. It has been pointed out that Paizis et al. (1995) have independently used a very similar method to analyze data from the Ulysses spacecraft. A third method of analysis is presented in chapter 3. The Fokker-Planck equation appropriate to the problem of cosmic ray transport in the heliosphere (§3.5.1-3.5.2, and Appendix C) is solved numerically and compared with ACR oxygen data from the inner and outer heliosphere (§3.5.2-3.5.4). For the time, energy, and spatially dependent solution we present, spherical symmetry is assumed; two and three dimensional solutions are beyond the scope of this work.

In terms of the thesis statement in section 1.2.1, the convective-diffusive dominance is primarily addressed in sections 3.2.3 and 3.5.4. The completion of initial recovery and subsequent quasi-steady state of ACRs in the heliosphere are discussed throughout the chapter but primarily so in sections 3.3.4 and 3.5.4. The predominant role of the effects of spacecraft motion on the low-energy ACR intensity increases is seen most clearly in section 3.5.4, although also, importantly, in section 3.4.4, and throughout the chapter. The success of the spherically symmetric model with a constant outer source is a central aspect of section 3.5. The novel gradient method is the previously mentioned topic of section 3.4.

In Chapter 4 the topic shifts from the long-term behavior of ACRs to the short term behavior. In particular the 150-day periodicity observed in the Voyager 1 data from 1998 and 1999 is considered in detail. A possible connection between this periodicity and similar periodicities in the inner heliosphere and solar measurements that have been reported by many scientists since 1984 is discussed (§4.4.1); however, before this, the history of these potentially related periodicities is given in the

introduction (§4.1). The analysis of the data with the goals of quantitatively describing the periodicity and determining its statistical significance is described in sections 4.2.1 and 4.2.2. The harmonic analysis performed (§4.2.2) is the periodogram analysis method of Scargle (1982), which is applied to 5-day averaged V1 and V2 H, He, and O residual intensity variation with respect to the exponential trend (4.2.1). The resulting periodograms of normalized power vs. frequency are examined in section 4.3. The potential exists that the clearly observed V1 ACR periodicities are due to periodically propagating regions of elevated magnetic field intensity that reach the outer heliosphere and impede ACR transport as the regions pass the spacecraft. This is discussed in section 4.4, along with the interesting lack of this periodicity at Voyager 2 (§4.4.2). Finally a summary of the topic of ACR periodicities is given (§4.5). In terms of the thesis statement (§1.2.1) the existence and coherent nature of the 150-day periodicity at Voyager 1 in 1998 and 1999, in phase across several species, is made clear in sections 4.2 and 4.3. The possible interpretation in terms of propagating regions of compressed solar wind that may be due to the previously reported inner heliospheric and solar periodicities is discussed in section 4.1 and 4.4.

The summary, discussion, and interpretation of the data analysis of Chapters 3 and 4 is primarily presented in Chapter 5, although some interpretation is necessarily made as the data analysis of Chapters 3 and 4 unfolds. First, the considerable amount of analysis to be presented is summarized as relates to long-term ACR transport (§5.1.1) and the ACR periodicities (§5.1.2). The observations from Chapter 3 are considered in light of transport theory (§5.2). Specifically, the scaling of transport parameters such as the ACR source radius, diffusion coefficient and “species scaling”

of ACRs is dealt with in section 5.2.1. The important topic of gradient and curvature drifts is taken up in sections 5.2.2 and 5.3.2. In the former section (§5.2.2) drift velocities are compared to the solar wind speed and consideration of latitudinal gradients is given. In the latter section (§5.3.2) the implications of the observations and analysis herein are considered broadly in terms of global heliospheric processes, including particle drifts. A potentially important effect regarding the heliospheric current sheet under outer-heliospheric conditions is taken up in section 5.2.3. In relation to the statement from section 1.2.1 the relative importance of the curvature and gradient drifts is considered most directly in section 5.2.2. The rigidity dependence of these drifts is considered in this section as well. In section 5.2.4, published outer heliospheric ACR intensity gradients are compared with our results, and the assumptions required of the non-local and quasi-local gradient methods are discussed.

In section 5.3.1 the core thesis (§1.2.1) is summarized and defended in light of the overall analysis of ACRs from 1991-2000, and broader implications are considered in section 5.3.2. Finally the main body is completed with a summary of the results and conclusions of this work in section 5.4. A more detailed discussion of the flux calculations made using the Voyager LECP instrument is given in Appendix A. Definitions of symbols and conventions used throughout this dissertation are provided in Appendix B for easy reference. In Appendix C topics relating cosmic ray transport theory and energetic particle measurements are treated in an elementary way to highlight the essential physics and to conceptually unite the observations with the theory.

## **Chapter 2 – Instrumentation and Analysis**

### **2.1 – The Voyager 1 and 2 Spacecraft**

In 1977 the two Voyager spacecraft were launched from Cape Canaveral, Florida toward the outer planets, taking advantage of a fortuitous alignment of Jupiter, Saturn, Uranus and Neptune. Following a high latitude Saturn encounter in late 1980, after traversing 9.5 AU (1.4 billion km) Voyager 1 (V1) left the vicinity of the ecliptic plane, subsequently climbing to high northern heliolatitudes, while continuing to recede from the Sun. Voyager 2 (V2) remained near the ecliptic until the Neptune encounter in 1989, at which time a northern polar pass of the planet sent the spacecraft south of the ecliptic plane. The present work concentrates on Low Energy Charged Particle (LECP) instrument data returned from the Voyager spacecraft during the nine year period from 1992 to 2000. The LECP instruments make composition and differential flux measurements of energetic particles with energies typically between 0.3 and 30 MeV/nucleon (depending on the ion species). Over the course of this work, data from 1987 to 1991 have also been newly analyzed. Although there is reference to these data, the later period has been selected for study as the 1992-2000 period corresponds to the ACR recovery period. (Note that data from the V2 Neptune encounter in 1989 are omitted from the data set, since interplanetary measurements alone are desired.) Table 2.1.1 lists some kinematic statistics for the two spacecraft during the 1987 to 2001 period.



ACR oxygen data from the Low-Energy Ion Composition Analyzer (LICA) experiment on the SAMPEX Earth-satellite, provided by J. E. Mazur (private communication, 2000; Mazur *et al.*, 2000; see also, Hill *et al.*, 2001) are also analyzed in this work. These low-energy data, along with published higher-energy near-Earth ACR O data, provide an important 1-AU baseline, with nearly the LECP energy range, with which to compare the outer heliospheric Voyager data. Those seeking instrumental or spacecraft details of SAMPEX/LICA are referred to the above captioned references, to section 3.2.3, and to the respective LICA and SAMPEX overview papers (Mason *et al.*, 1993; Baker *et al.*, 1993).

**Table 2.1.1 Voyager 1 & 2 Statistics During 1987-2001**

Year	$r_1^{a,c}$ (AU)	$\lambda_1^{a,c}$ (°)	$V_1^{b,c}$ (AU/yr)	$\omega_1^{b,c}$ (°/yr)	$r_2^{a,c}$ (AU)	$\lambda_2^{a,c}$ (°)	$V_2^{b,c}$ (AU/yr)	$\omega_2^{b,c}$ (°/yr)
1987	29.2	28.3	3.4	1.0	21.8	1.8	2.9	1.0
1988	32.6	29.3	3.5	0.8	24.7	2.8	3.2	0.8
1989	36.1	30.1	4.0	0.7	27.9	3.6	3.3	-1.3
1990	40.1	30.8	3.5	0.5	31.2	2.3	2.4	-4.0
1991	43.6	31.3	3.5	0.4	33.6	-1.7	2.6	-3.4
1992	47.1	31.7	3.7	0.4	36.2	-5.1	2.8	-3.1
1993	50.8	32.1	3.7	0.3	39.0	-8.2	2.9	-2.6
1994	54.5	32.4	3.5	0.2	41.9	-10.8	2.8	-2.2
1995	58.0	32.6	3.7	0.3	44.7	-13.0	3.0	-2.1
1996	61.7	32.9	3.7	0.2	47.7	-15.1	3.1	-1.8
1997	65.4	33.1	3.5	0.2	50.8	-16.9	2.9	-1.5
1998	68.9	33.3	3.7	0.1	53.7	-18.4	3.1	-1.4
1999	72.6	33.4	3.7	0.2	56.8	-19.8	3.1	-1.3
2000	76.3	33.6	3.5	0.1	59.9	-21.1	3.0	-1.0
2001	79.8	33.7	3.4	0.1	62.9	-22.1	2.9	-1.0

<sup>a</sup> Helioradius ( $r$ ) or heliolatitude ( $\lambda$ ) of spacecraft on the first day of the year.

<sup>b</sup> Average radial ( $V$ ) or angular ( $\omega$ ) speed of spacecraft throughout the year.

<sup>c</sup> Numerical subscripts indicate either Voyager 1 or Voyager 2.

The three-dimensional position of each Voyager spacecraft as a function of time is represented in Figure 2.1.1, using Heliographic (HG) Inertial coordinates, which are used throughout this work. The most notable differences between V1 and V2, seen in Figure 2.1.1 as well as Table 2.1.1, are that V1 is about 15 AU farther from the Sun (and increasing this separation at the rate of 0.6 AU/yr) than is V2 and that V1 is at northern heliolatitudes while V2 is at southern heliolatitudes during the period of interest. The longitudinal and rectilinear differences between the two spacecraft are clearly seen in Figures 2.1.2 and 2.1.3. Longitudinal differences are mostly ignored, as the radial and latitudinal coordinates are thought to be more important for the ACR transport phenomena of interest and since 26-day (or longer) averages are used throughout (except in some portions of Chapter 4) as the standard short-term time scale. This sampling period averages over the solar rotation period, thus minimizing longitudinal effects and the 26-day period is long enough to provide reasonable statistics for most purposes. Only rarely are shorter averages valuable for the present use of the LECP measurements.

Figure 2.1.2 displays an HG equatorial plane projection with the two Voyager trajectories indicated. The SAMPEX spacecraft at Earth, of course, is located at 1 AU, and the yearly longitude variations are not shown for the reasons discussed above. The region of interest for the Voyager portion of this investigation lies beyond the average radial distance from the Sun to Pluto (40 AU), as indicated by the large dotted circle in Figure 2.1.2. The more relevant latitudinal and north/south separations of V1 and V2 are shown in Figure 2.1.3, displaying the spacecraft trajectories in a meridional projection, which ignores the longitudinal coordinate. Of interest is the

**fact that V1 lies nearly at a constant latitude during the 1990's while V2, by comparison, is changing latitude rapidly, as can also be seen in Table 2.1.1. This situation provides the possibility of separating the latitudinal from the radial effects on ACR transport during the recovery phase of solar cycle 22.**

# Voyager 1 & 2 Ephemeris

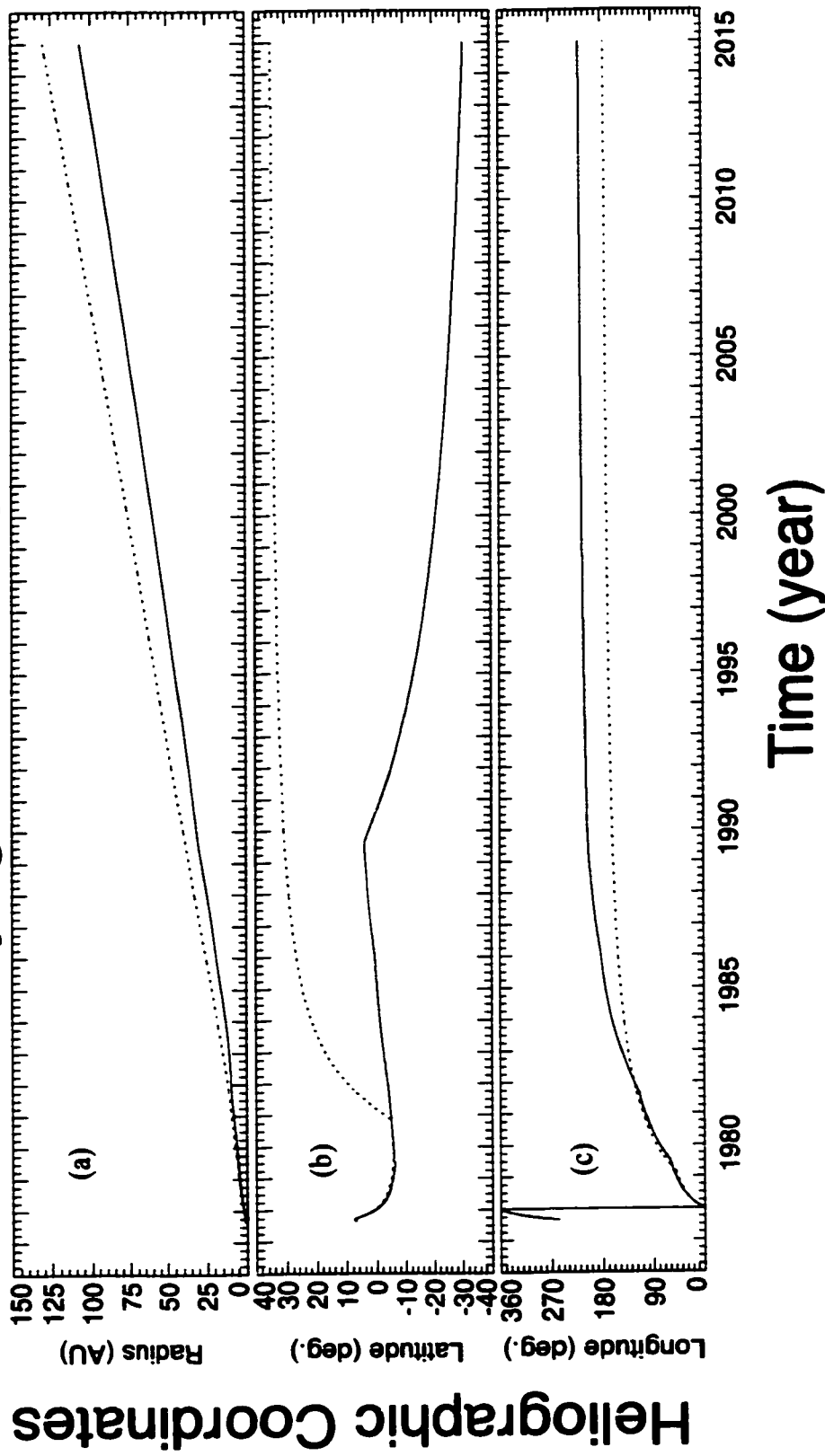


*Figure 2.1.1 Voyager 1 & 2 Ephemeris --- Heliographic Coordinates  
 The Voyager 1 (dotted line) and Voyager 2 (solid line) ephemeris are displayed graphically from 1977 (launch) through 2015. Heliographic coordinates are used in displaying (a) the radial location and (b) the degrees of latitude of each spacecraft. Heliographic Inertial coordinates are used (c) for the spacecraft longitudes.*

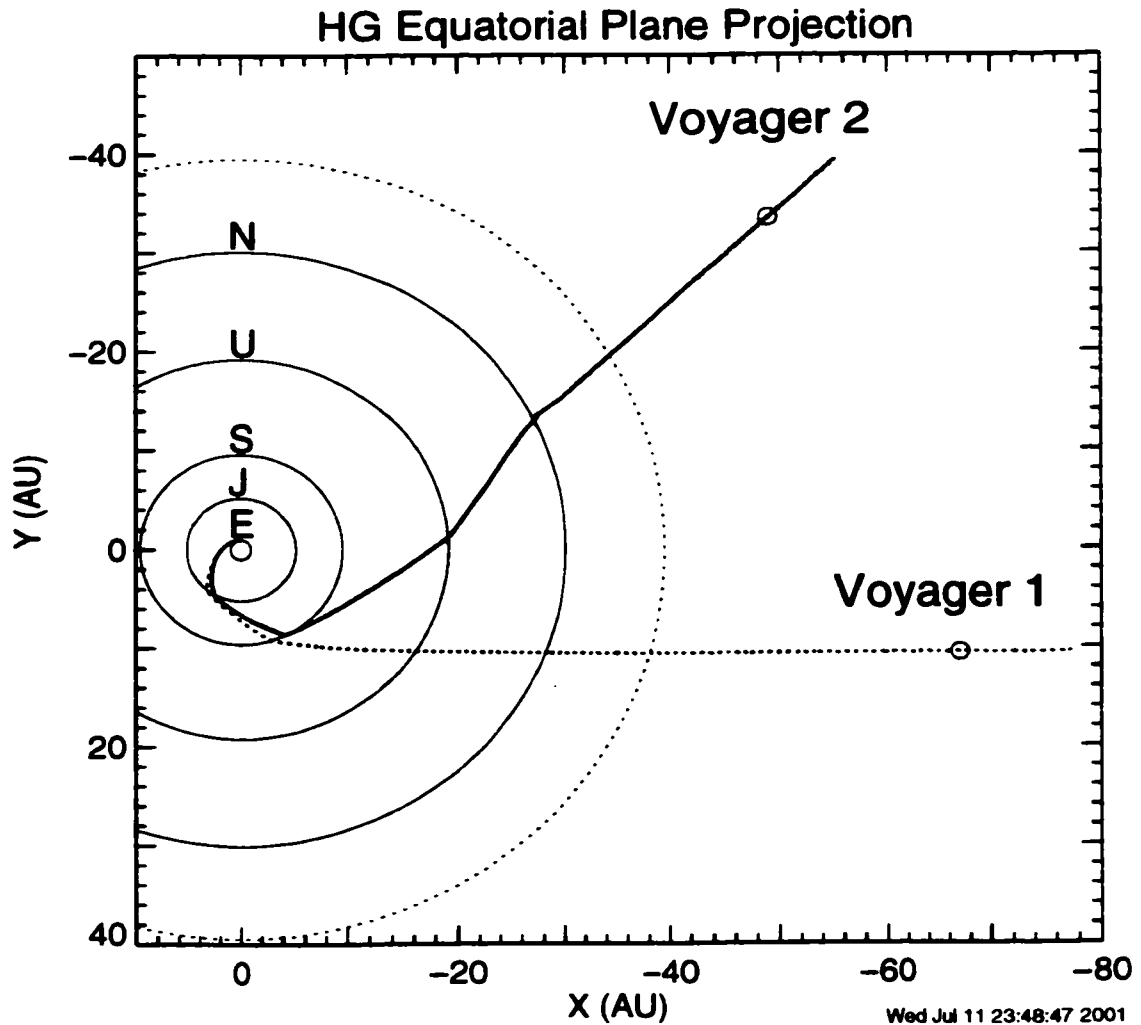


**Figure 2.1.2 Voyager 1 & 2 Trajectories — HG Equatorial Projection**  
*The trajectories of the Voyager 1 (dotted line) and Voyager 2 (solid line) spacecraft are represented in an equatorial plane projection (from above the north solar pole), using Heliographic Inertial coordinates, from the launch dates in 1977 through the end of 2004. The locations of the spacecraft in mid-2001 are indicated by the small solid circles near the spacecraft labels. The approximate counter-clockwise orbits of Earth, Jupiter, Saturn, Uranus, and Neptune are indicated by the labeled solid circles. The large dotted circle has a radius equal to the average radial distance to Pluto (40 AU), but does not represent the planet's orbit due to its large eccentricity.*

## Voyager 1 & 2 Trajectories

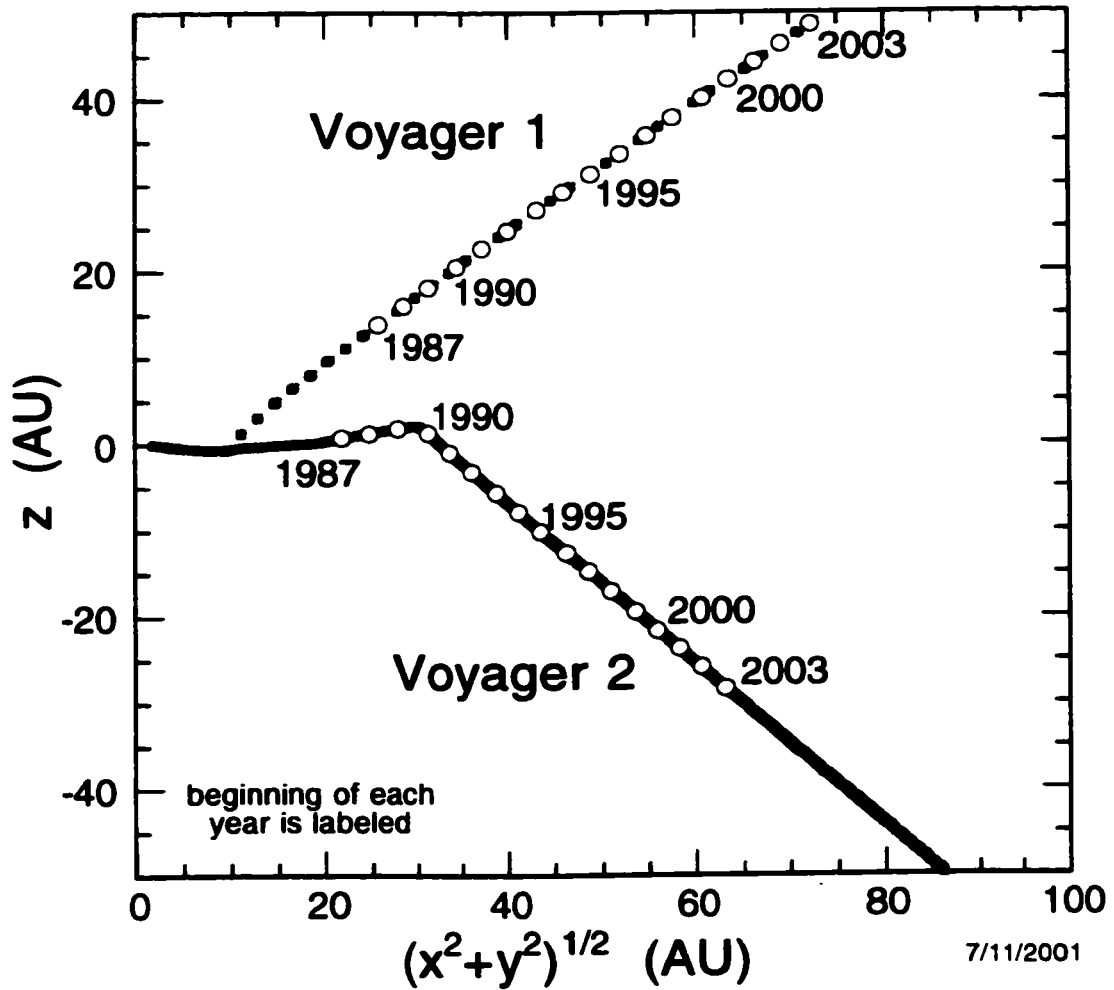


*Figure 2.1.3 Voyager 1 & 2 Trajectories — HG Meridional Projection*  
 The trajectories of the Voyager 1 (dotted line) and Voyager 2 (solid line) spacecraft are represented in a meridional plane projection using Heliographic Inertial coordinates. The ordinate represents distances above and below the equatorial plane, parallel to the solar spin axis Z, while the abscissa represents the orthogonal distance from that axis. The starts of each year from 1987 to 2003 are indicated by small solid circles, some of which are labeled.

## **2.2 – The Low Energy Charged Particle (LECP) Experiment**

A full description of the Low Energy Charged Particle (LECP) instruments can be found in the literature (Krimigis *et al.*, 1977; Peletier *et al.*, 1977); however, a brief discussion with emphasis and additional comments on those aspects of the instruments that are most relevant to this work is given below. A version of most of this section, along with much more detail, is presented by Hill (1998). University of Maryland online resources for Voyager/LECP are as follows: Instrumental notes, <http://space.umd.edu/voyager/inst.html>; LECP science and general information, <http://space.umd.edu/voyager>.

### **2.2.1 – Instrument Layout**

The Low Energy Charged Particle instrument consists of two subsystems, the Low Energy Particle Telescope (LEPT) and the Low Energy Magnetospheric Particle Analyzer (LEMPA). Data from the former will be discussed almost exclusively in this paper; therefore, no description of the latter will be given. (As a practical matter, the acronym LECP should be understood hereafter to exclude LEMPA unless explicitly mentioned.) In the instrument papers cited in section 2.2, LEPT refers to the entire dual-aperture telescope (Figure 2.2.1), however in this thesis an alternate convention is used: Charged Particle Telescope (CPT) refers to the dual aperture telescope, LEPT refers to the low energy aperture of the CPT, while HEPT (High Energy Particle Telescope) refers to the high energy CPT aperture.

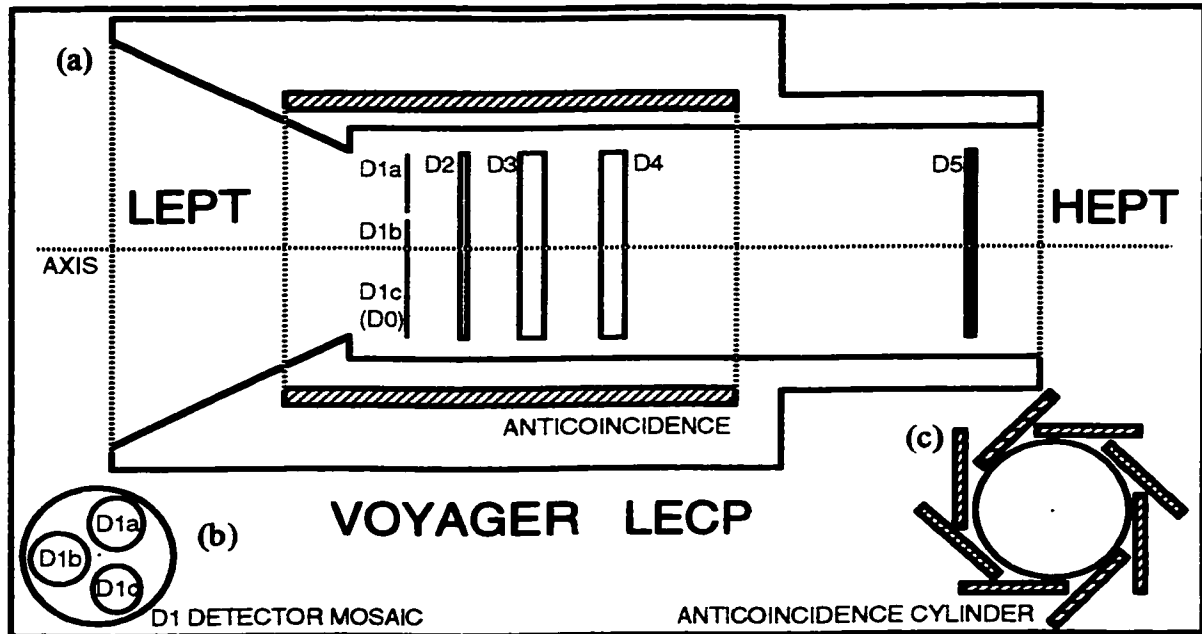


**Figure 2.2.1 Voyager Low Energy Charged Particle Instrument Diagram**  
 (a) A simplified depiction of the CPT subsystem of the Low Energy Charged Particle Instrument (not drawn to scale), featuring the Low- and High-Energy Particle Telescope (LEPT and HEPT) apertures. The five detector planes, and the anticoincidence "cylinder" are labeled. (b) A view of the LEPT aperture showing the three constituent detectors (D1a, D1b, and D1c) forming the D1 detector mosaic, as viewed along the axis. (c) An axial view of the eight detectors composing the anticoincidence "cylinder" that surrounds detectors D1 through D4.

There are five detector planes in the LECP instrument, labeled D1 to D5. The D1 "detector" consists of three separate silicon solid state detectors, D1a, D1b, and D1c (D1c is also called D0). The lower left diagram (Figure 2.2.1c) illustrates the arrangement of the D1 detector-mosaic schematically, viewed along the symmetry axis (normal to the detector planes). D1a and D1b have nominally the same thickness of roughly 5  $\mu\text{m}$ . (This is strictly true only for Voyager 2, while Voyager 1 has two mismatched detectors.) D0 is the thinnest detector, measuring roughly 2  $\mu\text{m}$ . (The D0 detector is used only on V1 since the V2 D0 detector was damaged during the Saturn



encounter in the summer of 1981.) D2 and D5 are thicker detectors (~150 and ~90  $\mu\text{m}$ , respectively). The thickest detectors are D3 and D4, both nominally 2450  $\mu\text{m}$  thick. D1 through D5 are oriented concentrically about the axis as shown in Figure 2.2.1a. Surrounding these detectors is a system of eight rectangular detectors composing the anticoincidence shell (Figure 2.2.1c) describing a cylinder centered on the axis. The LECP instrument has two apertures: particles entering the telescope via the LEPT aperture would tend to impact on the D1 and D2 detectors first, while particles that happen to pass through the HEPT aperture would (after passing through a thin nickel foil, not shown) reach the D5 detector plane first.

Primarily two types of data returned by the LECP instruments are used for the determination of ion composition and differential flux. These are counting-rate data and pulse height analyzer (PHA) data. (See section A.1. for a more complete discussion of these two data types and the LECP particle identification.) To illustrate, consider a 1-MeV proton incident upon the LEPT aperture. Suppose the proton passes first through the D1a detector and subsequently stops in the D2 detector. Each of these detectors will then produce a signal correlated with the energy deposited in that detector. The signal is the result of electrons and holes liberated from the silicon in the detector as the passing ion's electromagnetic field interacts with the atoms of the detector. These electrons and holes are swept out of the active region by a voltage bias across the detector. The detector signals are then interpreted by pulse height discriminator and coincidence circuitry that rejects the event or places it in one of 36 rate-channels. (An event may be rejected, for example, if the anticoincidence shell is triggered, ideally indicating that the ion has exited the instrument.) The 36 rate-

channels correspond to a relatively coarse compositional determination (See Appendix A). For example, the 1-MeV proton should be identified as belonging to channel one (CH01). When this identification is made, a count rate accumulator (rate scaler) is incremented; thus, (by concurrently recording the time coverage over a specified period), the counting rate is determined for this rate-channel.

For a subset of the identified ions, detailed PHA data are retained in addition to the rate data. If it is determined (by means of a priority scheme, discussed below) that the pulse height (PH) analysis should be completed, then the analog-to-digital converter that is part of the PHA circuitry determines channel values corresponding to pulse height, a measure of the energy deposited in four of the detectors. These PHA channel values and an identification byte (essentially indicating the rate-channel determined for this ion)—together referred to as a PHA data point—are subsequently telemetered to Earth by the spacecraft. A collection of such PHA data points, together with rate data, can be analyzed to determine the composition and differential flux of various ion species over some period of time (see section A.2 for a discussion of the flux calculation). The priority scheme referred to above is intended to make effective use of limited transmission rates available on the spacecraft for PHA data. The scheme uses three priority levels with the goal that rare species should not be "crowded out" by more common species.

The instrument rotates through eight 45-degree azimuthal sectors driven by a stepper motor upon which LECP (LEMPA and CPT) is mounted. The telescope remains stationary during the active period of each total accumulation interval (see "TAP" in section A.1) during which time the data are collected. Then, during the

inactive period, the telescope quickly rotates into the next sector. A record identifying the sector is made for each active period; thus, this information can be used to study particle flux anisotropy. The sector nominally directed toward the sun (sector 8) is protected by a sun shield, which also contains an  $\alpha$ -particle source for in-flight calibration. Details of the particle identification algorithm and the intensity calculations made with the LECP instruments are presented in Appendix A.

### 2.3 – Particle Data Properties

In this section some kinematic and plasma properties of the particles discussed in this dissertation are presented, primarily in Table 2.3.1, along with the definition of standard nomenclature used to identify particles. The terms “low”, “low<sub>2</sub>”, “med”, “high<sub>2</sub>”, and “high” will be often used to indicate the energy of particles discussed in this work, as defined in the table.

In the non-relativistic limit, which is used throughout this work, there are some relations that are of use. To determine the rigidity of a particle with energy  $E$  in units of MeV/nucleon, mass number  $A$ , and charge  $q = ze$ , the relation  $R = 43.3 \text{ MV } AE^{1/2}/z$  may be used. The velocity with respect to the speed of light  $c$  is determined by the relation  $\beta = 0.0462 E^{1/2}$ . With the conversion  $1 \text{ AU yr}^{-1} = 4.74 \text{ km s}^{-1}$ , the speed of light is given by  $c = 63,241 \text{ AU yr}^{-1}$ . For a magnetic field strength  $B$  in units of nT, a particle with rigidity  $R$  in units of MV has the approximate gyroradius  $\rho = 1/3 \cdot 10^7 R/B \text{ m}$ , or in terms of astronomical units,  $\rho = 2/9 \cdot 10^{-4} R/B \text{ AU}$ .

**Table 2.3.1 Properties of Particle Data**

Particle Identification			Kinetic Energy per Nucleon (MeV/nucleon)			Total K.E. (MeV)	Rigidity (MV)	Rel. Speed (c)	Gyroradius w/ 0.02 nT (AU)
Ion	Range	S/C	$E_{\min}$	$E_{\max}$	$E^a$	$\mathcal{T}$	$R$	$\beta$	$\rho$
${}^1_1\text{H}^+$	Low	V1	0.631	1.391	0.937	0.937	41.9	0.05	0.045
${}^1_1\text{H}^+$	Low	V2	0.600	1.130	0.823	0.823	39.3	0.04	0.043
${}^1_1\text{H}^+$	Med	V1	4.993	11.34	7.52	7.52	119	0.13	0.131
${}^1_1\text{H}^+$	Med	V2	4.800	9.800	6.90	6.90	114	0.12	0.125
${}^1_1\text{H}^+$	High	V1	23.91	29.50	26.6	26.6	225	0.23	0.245
${}^1_1\text{H}^+$	High	V2	24.40	28.60	26.4	26.4	224	0.23	0.244
${}^4_2\text{He}^+$	Low	V1	0.608	1.267	0.878	3.51	162	0.04	0.178
${}^4_2\text{He}^+$	Low	V2	0.600	1.150	0.831	3.32	158	0.04	0.174
${}^4_2\text{He}^+$	Med	V1	2.986	11.48	5.85	23.4	420	0.11	0.461
${}^4_2\text{He}^+$	Med	V2	3.710	12.30	6.76	27.0	451	0.12	0.495
${}^4_2\text{He}^+$	High	V1	20.65	29.74	24.8	99.2	868	0.23	0.950
${}^4_2\text{He}^+$	High	V2	20.80	29.00	24.6	98.4	865	0.22	0.945
${}^{16}_8\text{O}^+$	Low	V1	0.646	2.643	1.31	21.0	793	0.05	0.873
${}^{16}_8\text{O}^+$	Low	V2	0.600	3.170	1.38	22.1	814	0.05	0.895
${}^{16}_8\text{O}^+$	Med	V1	2.644	13.57	5.99	95.8	1699	0.11	1.870
${}^{16}_8\text{O}^+$	Med	V2	3.170	12.10	6.19	99.0	1727	0.11	1.890
${}^{16}_8\text{O}^+$	High	V1	13.57	38.56	22.9	366	3336	0.22	3.640
${}^{16}_8\text{O}^+$	High	V2	12.10	38.30	21.5	344	3232	0.20	3.280
${}^{16}_8\text{O}^+$	Low <sub>2</sub>	V1	1.00	4.05	2.01	32.2	983	0.07	1.080
${}^{16}_8\text{O}^+$	Low <sub>2</sub>	V2	0.95	4.78	2.13	34.1	1012	0.07	1.110
${}^{16}_8\text{O}^+$	Low <sub>2</sub>	1AU	1	5	2.2	35	1028	0.07	1.120
${}^{16}_8\text{O}^+$	High <sub>2</sub>	V1	6.89	27.6	13.8	221	2584	0.17	2.830
${}^{16}_8\text{O}^+$	High <sub>2</sub>	V2	8.00	27.4	14.8	237	2677	0.18	2.940
${}^{16}_8\text{O}^+$	High <sub>2</sub>	1AU	7	29	14.3	229	2631	0.17	2.880

<sup>a</sup> The geometric mean  $E = (E_{\min}E_{\max})^{1/2}$  has been used.

## **Chapter 3 – Anomalous Cosmic Ray (ACR) Transport**

### **3.1 – Introduction**

We studied Voyager 1, Voyager 2, and SAMPEX spacecraft data (along with additional published data from the ACE and WIND spacecraft) to discover the properties of primarily outer heliospheric anomalous cosmic ray (ACR) transport during the solar cycle 22 recovery phase from 1991 to 2000 (1991 to 1997 in the inner heliosphere). The type of data employed for this investigation is comprised of predominantly two kinds; 26-day averaged ion intensity time series (time-intensity profiles), and annually averaged energy spectra, mostly from the Voyager LECP instruments. Protons, helium, and oxygen are the only species considered here, and inner and outer heliospheric comparison involves only oxygen, since 1-AU ACR oxygen spectra are available in the literature (Mazur *et al.*, 2000; Hill *et al.*, 2001) as well as time-intensity profiles for both high<sub>2</sub>-energy (Selesnick *et al.*, 2000) and low<sub>2</sub>-energy (Hill *et al.*, 2001) ACR O<sup>+</sup>.

The understanding of the recovery of the anomalous component of cosmic rays will be advanced if the purely temporal behavior can be separated from phenomena associated with the motion of the two Voyager probes through the interplanetary medium. North-south and longitudinal symmetries are assumed throughout this chapter; therefore, the dimensions considered are heliographic radius and absolute heliographic latitude. In this way the degrees of freedom that are central to this analysis become time  $t$ , radius  $r$ , absolute latitude  $\lambda$ , and energy  $E$  (and/or rigidity  $R$ ). Upon completion of a general overview and analysis of the observations (§3.2), the

variations of ACR intensities are parameterized (§3.3.1). Then the ACR recovery profiles are modeled phenomenologically (§3.3), based on known physical considerations, in an attempt to gain insight into the possible dependence of the intensity  $j$  on  $r$ ,  $\lambda$ ,  $t$ , and  $R$ .

Direct measurements are needed, in addition to modeling, to understand the radial and latitudinal dependencies of ACR ions. Previously used techniques (§3.4.1) are not completely appropriate for this work due to complications involved in transport at these low energies and the sizeable intensity variations in space and time compared to other cosmic rays. A method is developed (§3.4.2) that is appropriate to the case at hand and derived values of radial and latitudinal intensity gradients are presented (§3.4.4). These values are compared with the work of other investigators where this comparison is appropriate, and with the estimates provided by other techniques used herein (§3.3.4, §3.4.4, §3.5.4). A connection with cosmic ray transport theory is made directly by solving the Fokker-Planck equation appropriate to cosmic ray transport (§3.5, see also Appendix C). The numerical solutions obtained (§3.5.4) retain both time and energy dependence, while assuming spherically symmetry.

## **3.2 – ACR Observations from 1991 to 2000**

### **3.2.1 – Outer Heliospheric Time Profiles**

Solar activity waned in 1990, a year after the solar maximum of solar cycle 22. In March and June, 1991 the largest solar event occurrences of the cycle took place. The cosmic rays, which were already beginning to recover, were sharply modulated, with for example  $> 70$  MeV galactic cosmic rays in the outer heliosphere at Voyager 1, Voyager 2 and Pioneer 10 dropping to their lowest levels of the cycle in the latter half of 1991 (McDonald *et al.*, 1994). The noted universality of large Forbush decreases associated with this renewed solar activity at widely separated spacecraft throughout the heliosphere, despite the localized nature of the initial active regions on the Sun, is indicative of a global merged interaction region (GMIR), a phenomenon in which the coalescence of adjacent propagating interaction regions forms a large-scale disturbance that may encompass a large range of heliolatitudes and heliolongitudes at great distances from the Sun (Burlaga *et al.*, 1985). These conditions diminished the anomalous cosmic ray populations throughout the heliosphere and established a heliosphere, largely empty of ACRs, into which anomalous ions began to propagate as the disturbance moved beyond the termination shock, the likely ACR source.

An overview will be given of some of the phenomena associated with the transport of the ACRs beginning near the end of 1991, after the passage of the GMIR, and continuing until 2000, when solar modulation of nearly all of the ACRs discussed here has begun to increase again. This recovery period, specifically excluding the truncated recovery before the GMIR, allows a particularly neat comparison of the transport of ACRs of various species and at various heliospheric locations since the

onset time of recovery is well known, corresponding to the timing of the observed propagation of the disturbance region from the inner to the outer heliosphere at roughly the solar wind bulk speed.

Figure 3.2.1 contains spectrograms of outer heliospheric ions detected by the LECP instruments at Voyager 1 & 2 from 1987 to 2000. Intensity is plotted as a function of both energy and time, providing a concise summary of particle phenomena during the 1992-1999 recovery phase and the solar maximum period immediately preceding. In the top two panels of this figure evidence of solar activity is clearly seen in the behavior of  $\sim 1$  MeV interplanetary-accelerated protons from about 1988 to 1992 at V1 and for a more extended period at V2 (since V2, as shown for this period in Figure 2.1.3, is near the ecliptic where shocks and locally accelerated particles associated with the heightened solar activity are preferentially observed). An intensity increase in late 1991, associated with the March/June 1991 solar events can be seen for all three species and at both spacecraft, but is most obvious for low-energy protons. The characteristic power-law energy spectra associated with this intensity increase can be seen in 1991 for H, He, and O in Figures 3.2.5, 3.2.6, and 3.2.7. Immediately following the enhancement at the end of 1991 a Forbush decrease in 10 MeV/nucleon ACR oxygen can be seen in the bottom left panel of Figure 3.2.1, or in the oxygen time-intensity profiles of Figure 3.2.4c – f.



# Outer Heliospheric Ions

H, He & O Spectrograms (1987-2000)

Voyager 1 / LECP

Voyager 2 / LECP

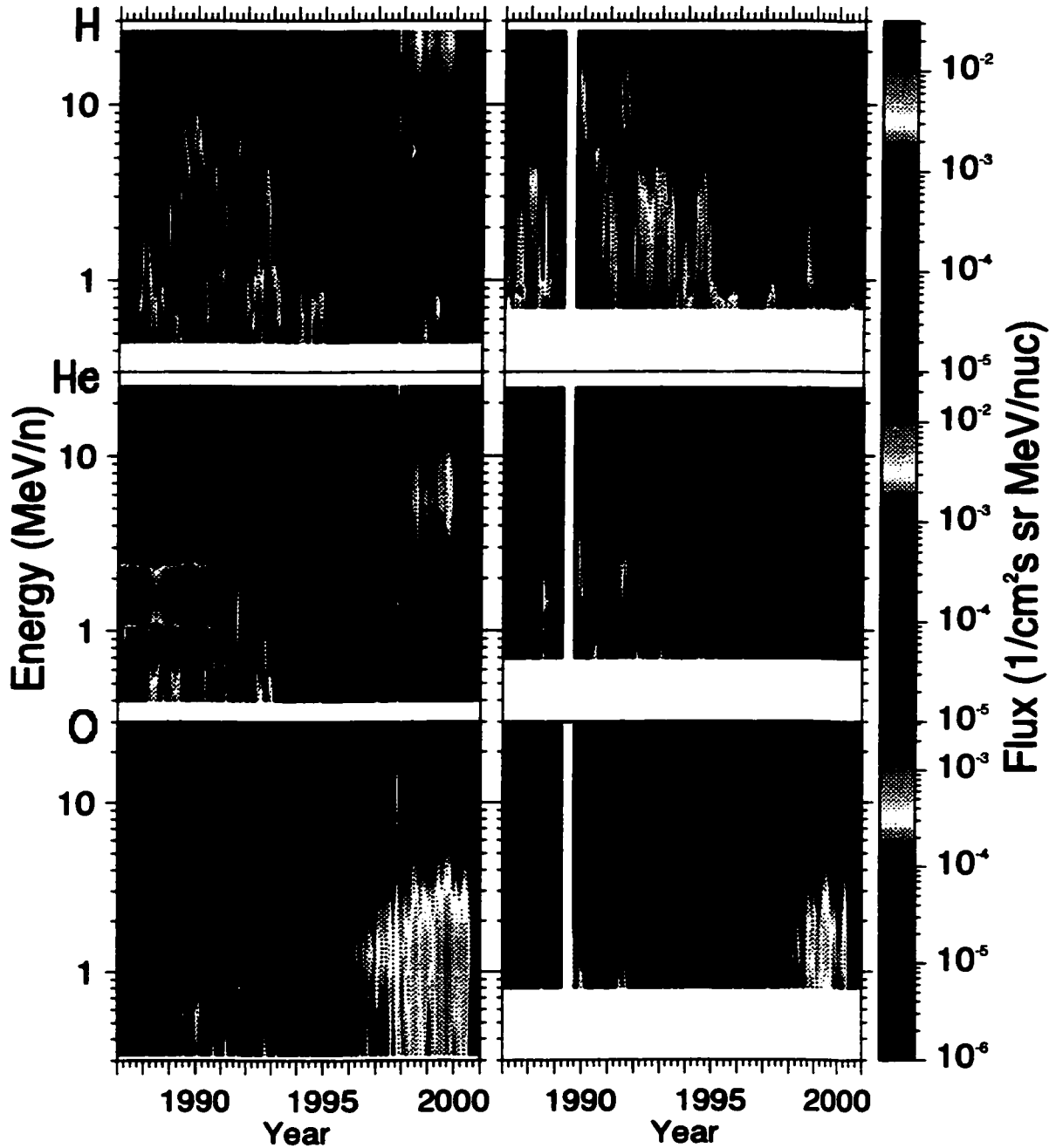
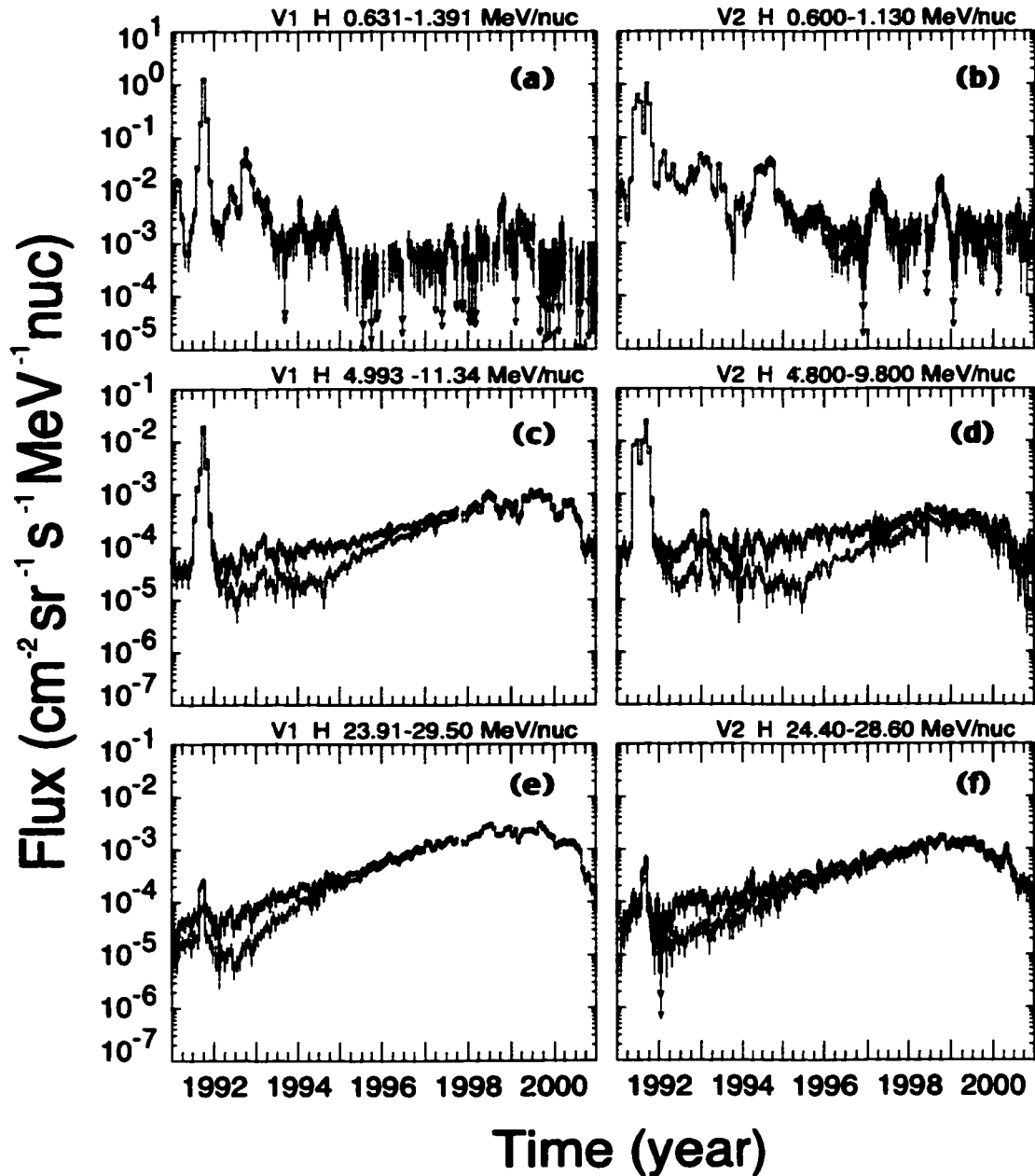


*Figure 3.2.1 Voyager 1 & 2 H, He & O Spectrograms 1987-2000*  
V1 and V2 data are on the left and right, respectively, with H shown in the top row, He in the middle row, and O in the bottom row. Intensity, represented by the color-scale at right, is plotted against the time abscissa and energy/nucleon ordinate.

After these early events of solar cycle 22, the ACR recovery ensues. In Figure 3.2.1 the roughly 25-MeV, 7-MeV/nucleon, and 1-MeV/nucleon peaks in the proton, helium, and oxygen spectrograms, respectively, are observed to steadily increase in intensity until the end of 1999 at both spacecraft, at which time these anomalous cosmic rays are dominating the LECP response. In Figure 3.2.2 the 26-day-averaged H data show both the decline of solar activity evidenced by decreasing levels of interplanetary accelerated protons in panels (a) and (b) as well as the anti-correlated increase in anomalous cosmic ray protons in the remaining four panels. Note most significantly for protons the distinction between the uncorrected and background subtracted time profiles. Hundreds of separate background corrections, for each of the flux boxes from each *detector pair* (see section A.2), for each species, from each spacecraft, and during each year from 1987 to 2000 were carefully performed, using detailed pulse height analysis data to ensure the accuracy of these measurements. These corrections were either not necessary or not significant for most of the He and O data, as can be seen in Figures 3.2.3 and 3.2.4. The large peaks in late 1991 of panels (a) – (d) are due to shock accelerated particles associated with the solar events of that year. In panels (e) and (f), the ~26 MeV protons show a more complicated temporal profile in 1991 consisting of a slow increase to mid-year probably due to recovering ACR protons, followed by a sharp increase indicating the high energy component of the solar and interplanetary-accelerated ions and then a decrease as the underlying cosmic rays are modulated by the disturbance. These features are more clear at V1 than at V2.

# Voyager 1 & 2 / LECP Protons



Corrected  
Uncorrected

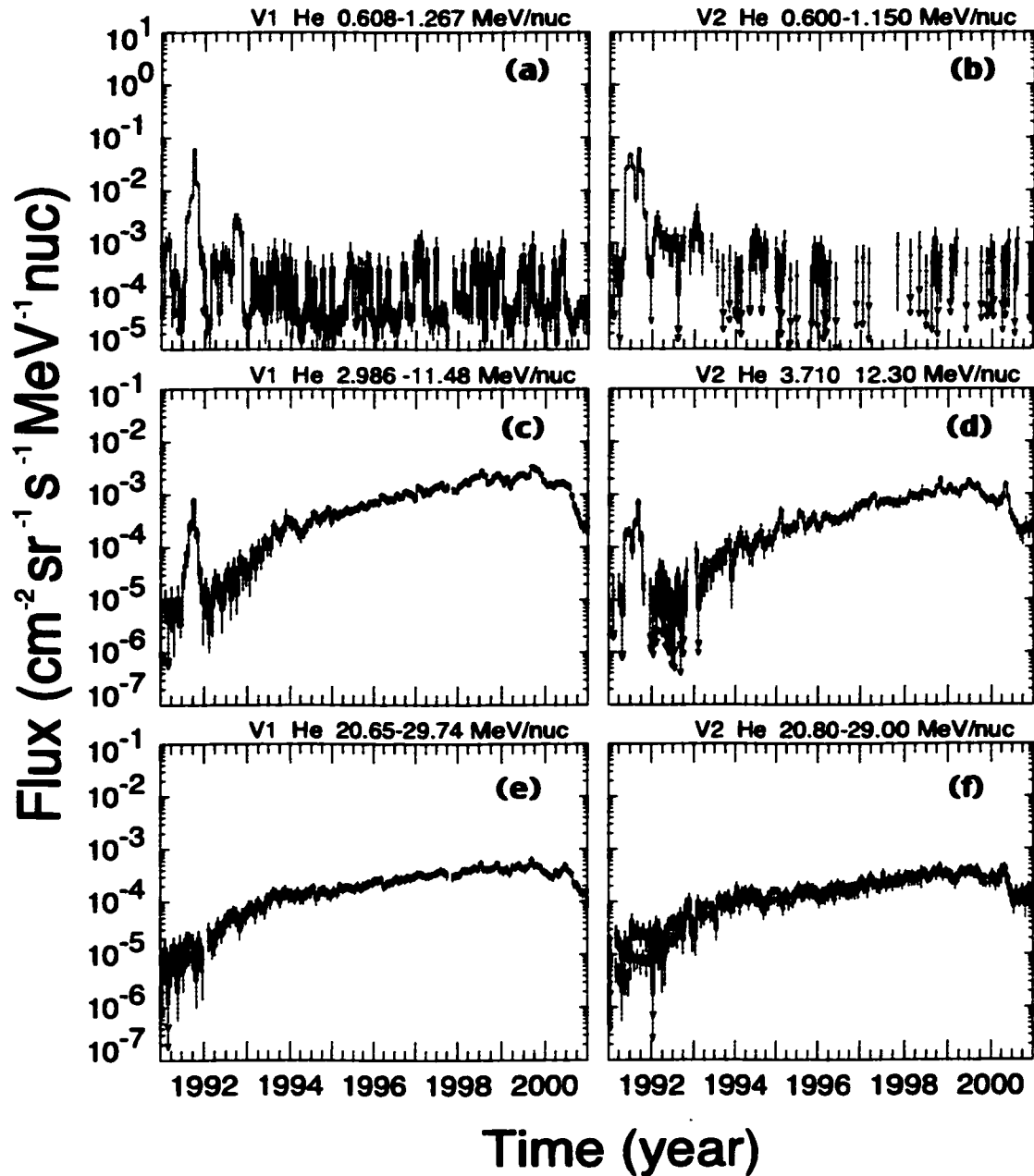
Thu Oct 18 21:53:10 2001

*Figure 3.2.2 Voyager 1 & 2 Hydrogen Time-Intensity Profiles 1991-2000*  
*Low-, medium- and high-energy V1 & V2, 26-day-averaged H data are plotted in the top, middle, and bottom row, respectively, with V1 on the left. Uncorrected (black) and background-corrected (red) intensities are plotted against time in each panel.*

Panels (c) – (f) of Figure 3.2.3 also show the ACR recovery, in this case He ions. Note that the rate of increase of the medium energy ions, (c) and (d), is noticeably larger than the higher energy ions, (e) and (f), and, after the initial recovery ending in 1994, that the profiles are quite exponential in nature for over five years until about mid-1999 for  $\sim 7$  and  $\sim 25$ -MeV/nucleon ions at both spacecraft, (c) – (f). The low energy panels, (a) and (b), indicate the 1991 solar activity of IP-accelerated He, but reveal statistically limited quiet conditions for most of the subsequent period for  $\sim 1$ -MeV/nucleon He. As with protons, signs of the 1991 event can be seen below 12 MeV/nucleon, (a) – (d), but are not identifiable at the highest energies, (e) and (f).

After 1991, all six panels in Figure 3.2.4 are dominated by anomalous oxygen. At around 1 MeV/nucleon the signature of the 1991 activity is seen at both V1 (a) and V2 (b), just as in the interplanetary H and He ions. At the higher energies, except possibly for the small sharp increase in panel (d) at about 1991.7, there appears to be no direct detection of accelerated particles; however, the Forbush decreases seen in all four time series (c) – (f) at the end of 1991 for 3 – 38 MeV/nucleon V1 and V2 ACR oxygen clearly indicate the passage of the globally merged interaction region, and establish the starting point from which the bulk of the present analysis will begin. Just as with He, the oxygen recovery is distinctly exponential in character after the initial recovery and the lower-energy particles, (a) and (b), increase at a significantly faster rate than do the higher-energy particles. In fact the  $\sim 1$ -MeV/nucleon ACR oxygen intensities increase by almost two orders of magnitude from 1993 to 1999, while the 13- to 38-MeV/nucleon oxygen intensities, (e) and (f), are nearly constant.

# Voyager 1 & 2 / LECP Helium

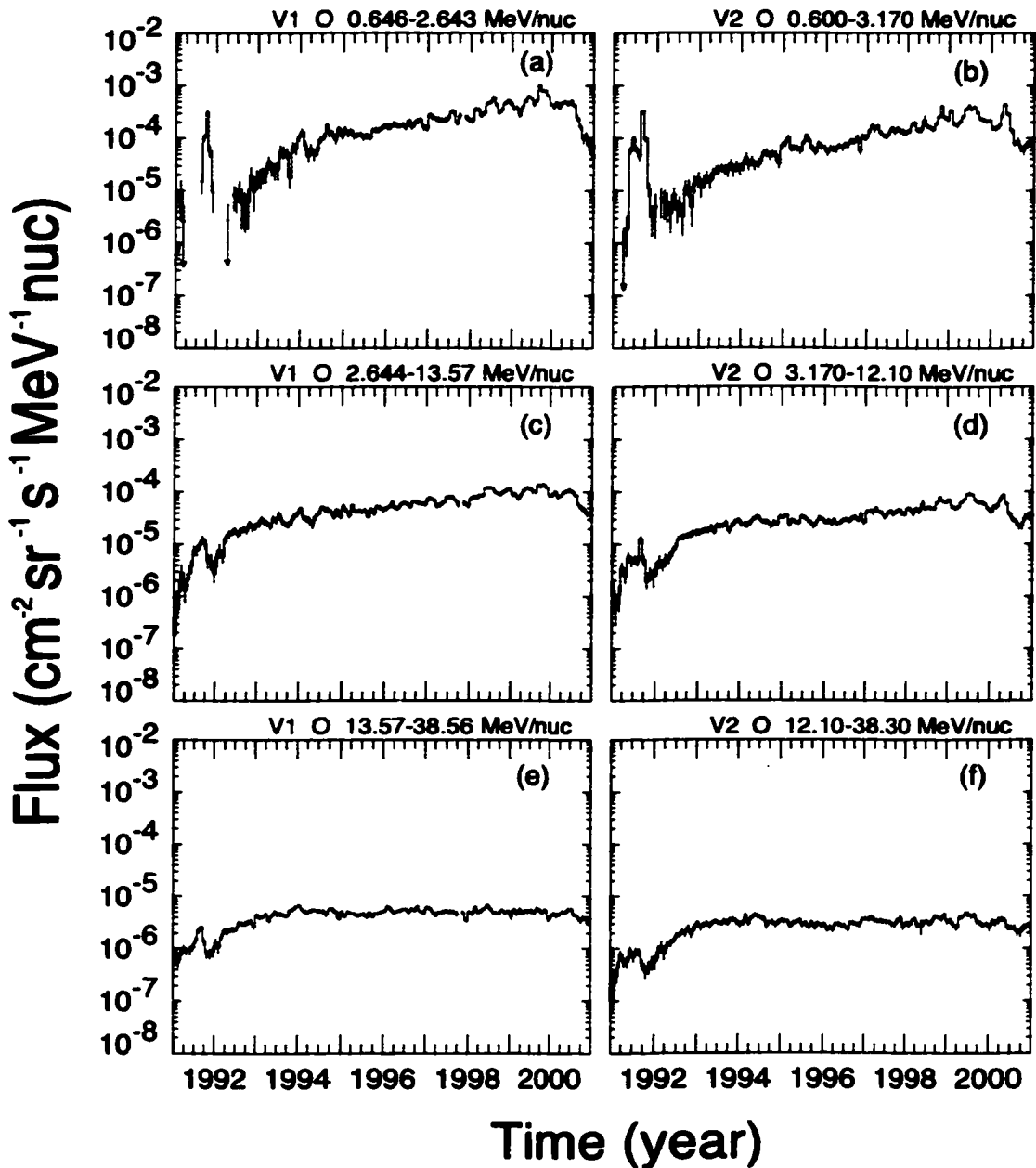


Corrected  
Uncorrected

Thu Oct 18 21:53:10 2001

*Figure 3.2.3 Voyager 1 & 2 Helium Time-Intensity Profiles 1991-2000*  
 Low-, medium- and high-energy V1 & V2, 26-day-averaged He data are plotted in the top, middle, and bottom row, respectively, with V1 on the left. Uncorrected (black) and background-corrected (blue) intensities are plotted against time in each panel.

# Voyager 1 & 2 / LECP Oxygen



Corrected  
Uncorrected

Thu Oct 18 21:53:11 2001

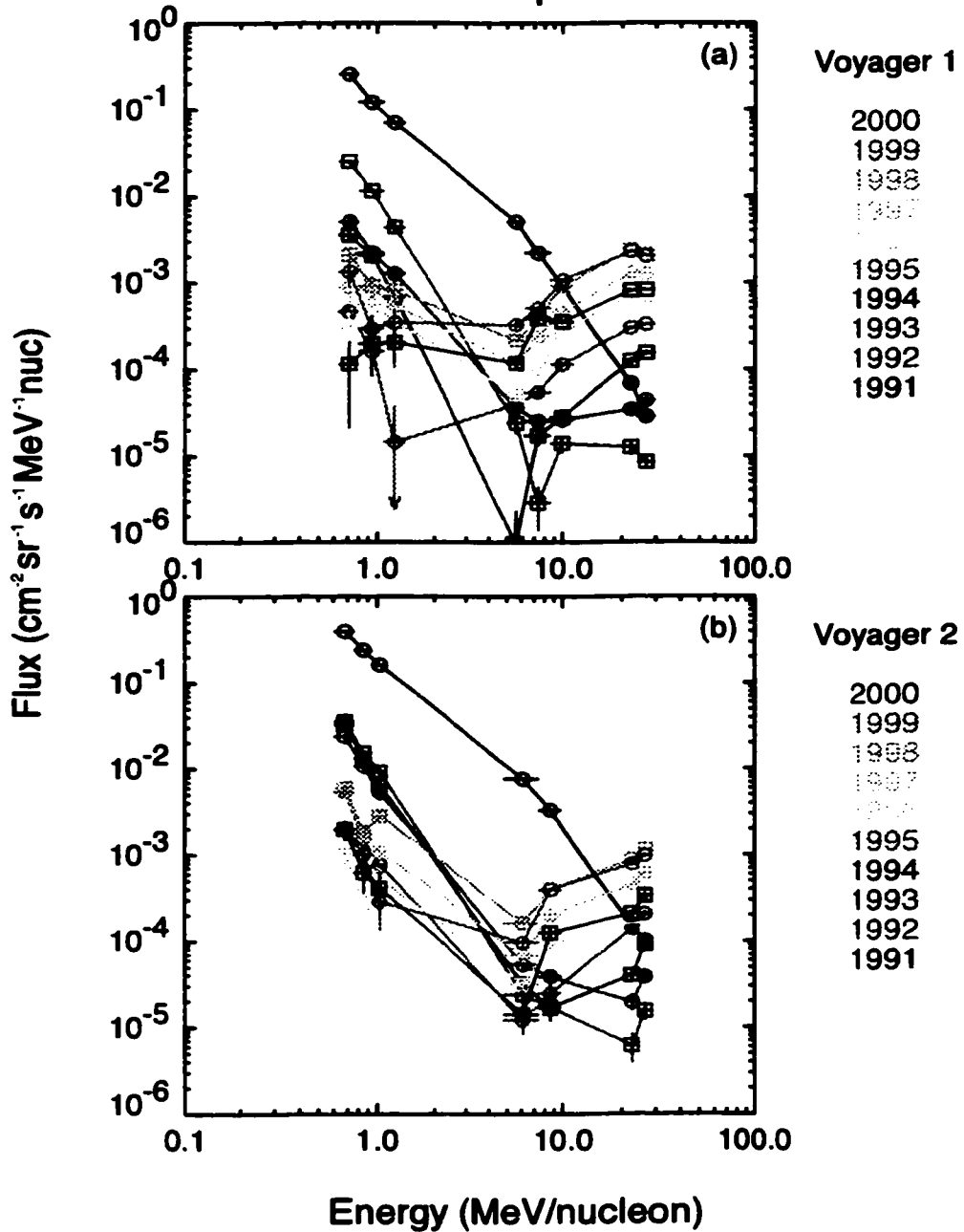
*Figure 3.2.4 Voyager 1 & 2 Oxygen Time-Intensity Profiles 1991-2000*  
 Low-, medium- and high-energy V1 & V2, 26-day-averaged O fluxes are shown vs. time in the top, middle, and bottom row, respectively, with V1 on the left. Uncorrected (black) and background-corrected (green) intensities are nearly indistinguishable.

### **3.2.2 – Outer Heliospheric Energy Spectra**

The Voyager time-intensity profiles (Figures 3.2.2-4), which are essentially horizontal cross-sections of the spectrograms in Figure 3.2.1, are contrasted with the energy spectra (Figures 3.2.5-7), which are essentially vertical cross-sections of the spectrograms. In Figures 3.2.5-7, ten annually-averaged spectra from 1991 to 2000 are plotted on the same set of axes to save space and to facilitate intercomparisons between different years. The energy range of the abscissa and the number of decades along the ordinate are the same for these figures to aid comparisons. Proton spectra (Figure 3.2.5) are shown for V1 (a) and V2 (b), indicating the differential intensity  $j$  of H as a function of energy/nucleon  $E$ . As pointed out above, the roughly power-law form of the 1991 spectra are characteristic of shock accelerated particles associated with the interplanetary disturbances of that year. Notice that V2 protons (b) maintain a shock-accelerated component around 1 MeV throughout the period, while the similarly accelerated protons at V1 (a) are persistent only until around 1994, after which the low energy spectra flatten. This is another indication of the distinction between the V1 and V2 environments, V2 being nearer the heliographic equator than V1, and thus experiencing the enhanced level of IP disturbances associated with the active regions of the solar streamer belt which is increasingly restricted to lower latitudes as the Sun's state evolves from maximum to minimum activity levels.

Coincident with the weakening shock-accelerated spectra, is the development of the ACR peak up to ~30 MeV. Association of this spectral peak with anomalous

# V1 & V2 H Spectral Evolutions



Hard Drive:Desktop Folder:V1V2 H SpectEvol.PS

Fri Oct 19 04:46:28 2001

*Figure 3.2.5 Voyager 1 & 2 Hydrogen Spectral Evolutions 1991-2000*  
*Annual proton spectra are plotted from 1991 to 2000 with the color indicated on the right. Circular (square) symbols are used in odd (even) years for added clarity.*

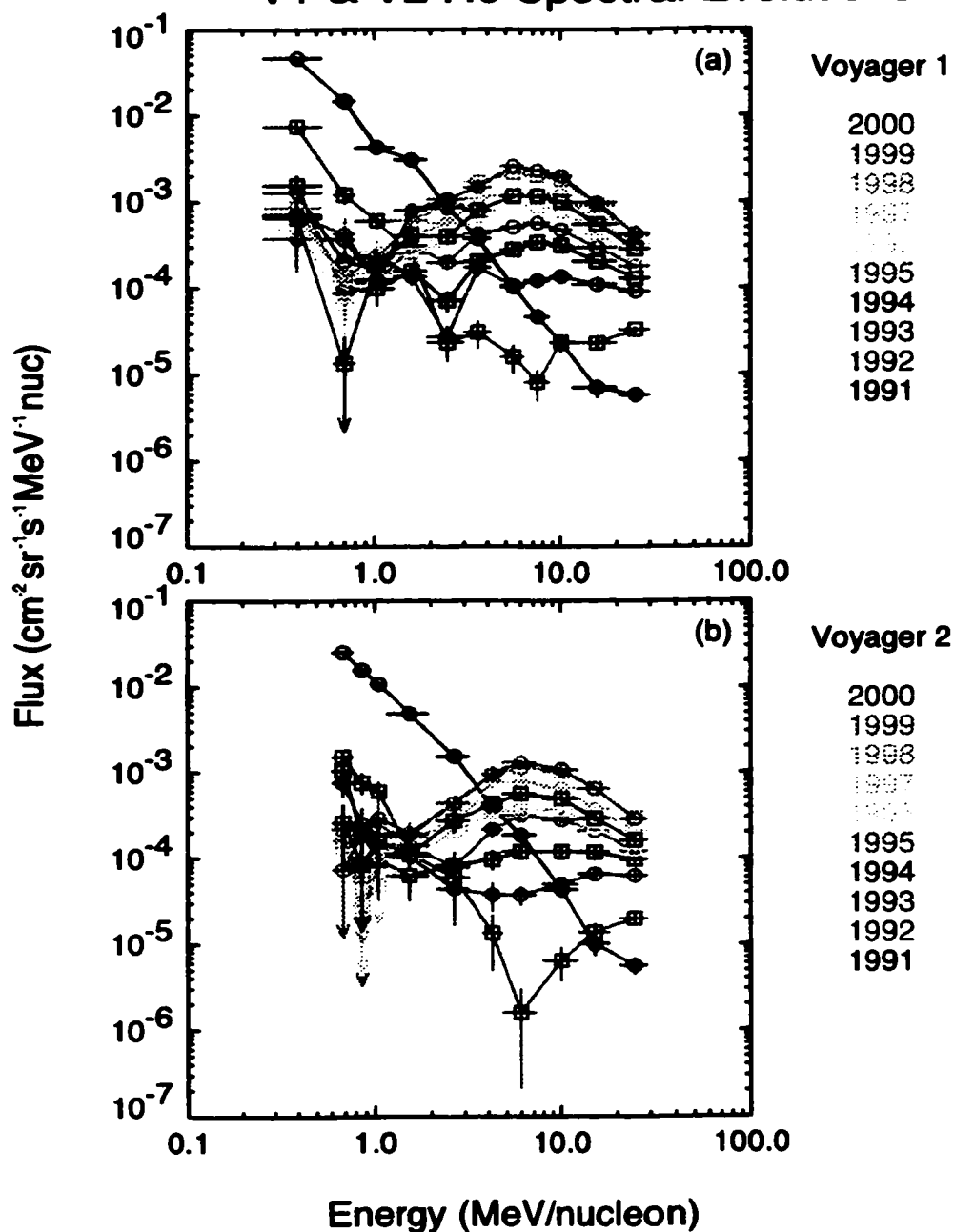


rather than galactic cosmic ray particles is discussed in section 1.1.5, and is clear when higher energies are examined. The highest energy proton points in Figure 3.2.5 are a few MeV below the peak in the ACR proton spectrum at V1 and V2, as indicated by high energy measurements by the CRS instruments (Stone et al., 1999). Notice that the spectra with the highest ACR intensity are from 1998 and 1999 and that the 2000 spectra are significantly reduced from this peak intensity at both V1 and V2.

The situation for outer heliospheric helium ions (Figure 3.2.6) is similar to protons except that the peak ACR energy at the end of the recovery is shifted down in energy compared to anomalous protons. The fully developed ACR helium peak is at about 6 MeV/nucleon, although it is closer to 30 MeV/nucleon at the onset of recovery in 1992. This shifting of the peak energy with time, as well as the offset in energy between species (species scaling) is discussed in section 5.2.1. As with protons the recovery of the anomalous component is accompanied by a decrease in IP-accelerated ions, an expression of the well-known anti-correlation between cosmic rays and solar activity (see section 1.1.2). The shock-accelerated He spectra are apparent at both spacecraft in 1991, but for He, unlike protons, there is an indication of a flattening of the spectra at the highest energies, probably due to the barely-detectable presence of ACR helium. Also unlike protons, the portion of the helium spectrum below the peak is relatively flat at both V1 and V2 after about 1994, indicating a low level of interplanetary acceleration of helium ions at both locations.

The spectral evolutions of oxygen shown in Figure 3.2.7 are dominated by the anomalous component throughout the period of interest. Even in 1991 when the large solar events dominated H and He, anomalous oxygen is clearly evident as a fully

## V1 & V2 He Spectral Evolutions

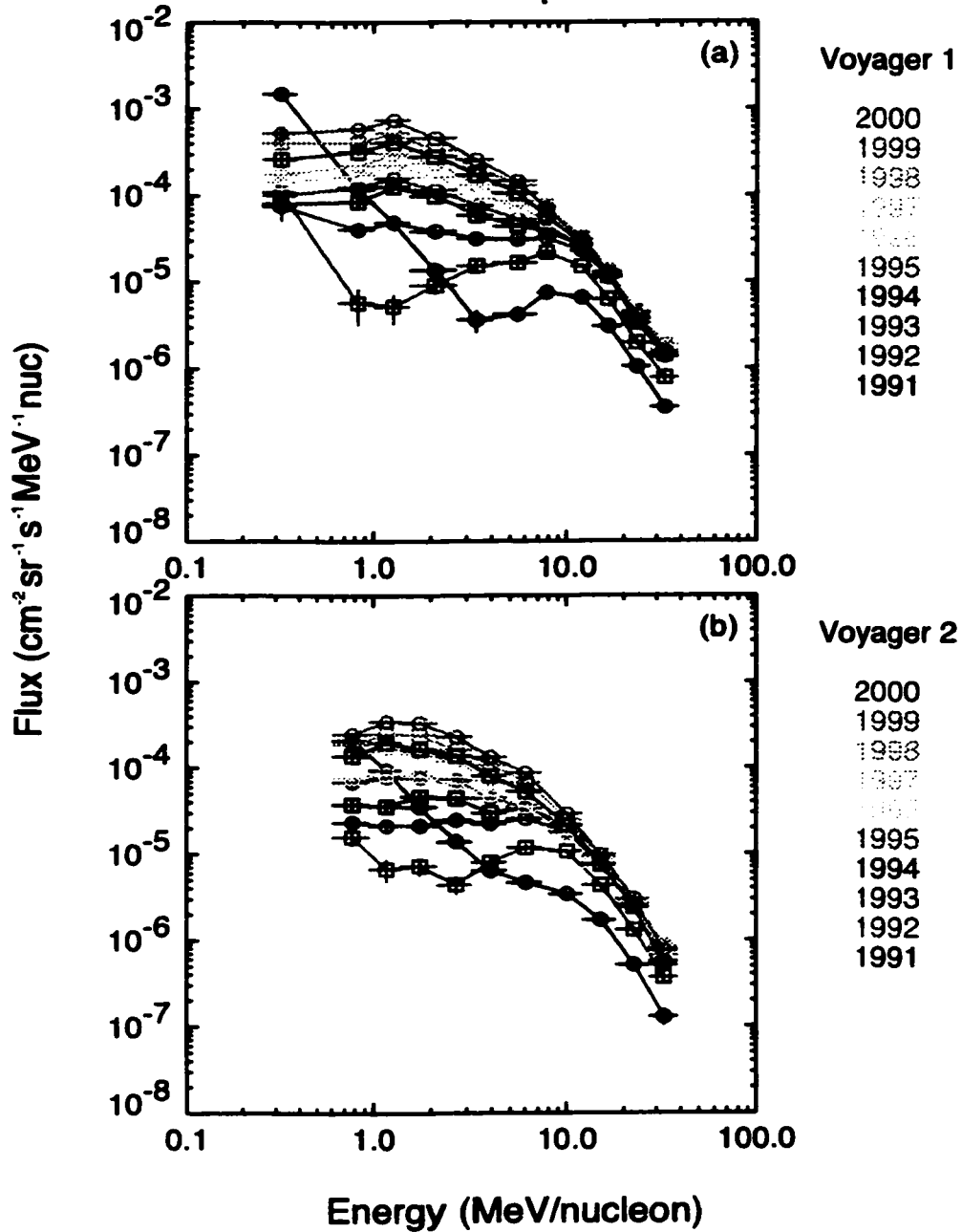


Hard Drive:Desktop Folder:V1V2 He SpectEvol.PS

Fri Oct 19 04:46:32 2001

*Figure 3.2.6 Voyager 1 & 2 Helium Spectral Evolutions 1991-2000*  
*Annual helium spectra are plotted from 1991 to 2000 with the color indicated on the right. Circular (square) symbols are used in odd (even) years for added clarity.*

## V1 & V2 O Spectral Evolutions



Hard Drive:Desktop Folder:V1V2 O SpectEvol.PS

Fri Oct 19 04:46:37 2001

*Figure 3.2.7 Voyager 1 & 2 Oxygen Spectral Evolutions 1991-2000*  
*Annual oxygen spectra are plotted from 1991 to 2000 with the color indicated on the right. Circular (square) symbols are used in odd (even) years for added clarity.*

formed peak at 10 MeV/nucleon at V1 (a) and as a distinct shoulder near the same energy at V2 (b). The lower energies are consistent with local accelerations in 1991 and 1992. The only other potentially non-ACR points are the lowest-energy V1 points at about 0.3 MeV/nucleon. Although these points are found to be substantially free of background, and therefore are believed to be responsive to real heliospheric oxygen ions, the spectral shape potentially suggests a source other than anomalous cosmic rays. Whereas the other species present clear peaks, with a significant drop-off in intensity (both above and below the peak) that becomes more pronounced as the recovery unfolds, the V1 ACR O spectrum is quite flat over a wide energy range and remains so or even becomes flatter with time. In section 3.5 it is also seen that this point is the most difficult to reconcile with transport theory. It is noted that Steenberg (1998), using a significantly more sophisticated model than has been used here, also was unable to explain this point with his numerical solutions. The anti-correlation with the solar cycle would seem to rule out a substantial solar energetic or interplanetary accelerated component. The possibility exists that this elevated low-energy oxygen point could be related to an observation of pick-up ion oxygen inferred from Voyager LECP data (Krimigis *et al.*, 2000), perhaps as an indication of a high-energy tail of the pick-up ion distribution. Further investigation into this question on the basis of LECP data is still possible, but is placed beyond the scope of this work.

There is an offset in the peak energy between O and the other two species, ACR O peaking in 1999 at about 1.3 MeV/nucleon. As can also be seen in Figure 3.2.4, ACR oxygen reaches its highest intensity somewhat later than H and He, and for the 13- to 38-MeV/nucleon range no decrease at all is seen through the end of 2000.

Above about 10 MeV/nucleon it is notable that the V1 and V2 spectra essentially reach their ultimate level of intensity and spectral shape as early as 1993, and maintain this form with little change through the end of 2000, a unique situation among the H, He, and O ions accessible to the LECF instruments. This nearly constant intensity has been noted in data from the CRS experiment for 7- to 17-MeV/nucleon ACR O and 30- to 56-MeV/nucleon ACR He (Stone *et al.*, 1999; McDonald *et al.*, 2000). Also of interest, as was alluded to above, the ACR oxygen spectral peak energy, as with helium, changes with time, evolving from about 10 MeV/nucleon to a little over 1 MeV/nucleon from 1991 to 1994 and then maintains the same peak energy thereafter. The striking observation of the substantially unchanged spectral peak energy for ACR O, He and H after the initial recovery period (see Stone *et al.*, 1999, for the complete H peak) is significant to the task of separating temporal recovery features from spectral changes associated with spacecraft motion, as well as providing information concerning the extent of the heliosphere, as is discussed in section (§5.2.1).

### **3.2.3 – Inner and Outer Heliospheric Observations**

The anomalous oxygen measurements presented in this section were made in three heliospheric regions: 1 AU – ecliptic measurements, outer heliospheric – northern heliolatitudes, and outer heliospheric – southern heliolatitudes. Many of the results from this subsection were published in an earlier paper (Hill *et al.*, 2001). The 1-AU data are from LICA, a time-of-flight mass spectrometer aboard the SAMPEX Earth-satellite, supplemented by published data from various instruments aboard the SAMPEX, ACE and WIND near-Earth spacecraft. The outer heliospheric data are from the LECF experiments on Voyager 1 and Voyager 2. From 1992 to the end of

2000 V1 varies in heliographic radius from 47 to 80 AU, and in heliographic latitude from 32° N to 34° N. During this period the V2 coordinates range from 36 to 63 AU and 5° S to 22° S. In 1996, the time of the annual Voyager spectra shown in Figure 3.2.8, the V1 and V2 coordinates are approximately 64 AU, 33° N and 49 AU, 16° S, respectively. (See section 2.1.)

Energy spectra for anomalous cosmic ray oxygen are shown in Figure 3.2.8 at three heliospheric positions. The 1-AU data below 10 MeV/nucleon are from the Earth-orbiting SAMPEX/LICA sensor while the SAMPEX satellite was at high geomagnetic latitudes, where interplanetary (IP) ions are well observed. The spectrum is averaged over the six-year period from 1993 to 1998, and subject to the quiet-time constraint that the LICA measurement of daily-averaged 0.6-0.85 MeV/nucleon  $^4\text{He}$  flux is less than 0.02 particles/cm<sup>2</sup>-sec-sr-MeV/nucleon. The diamond symbols in Figure 3.2.8 represent the IP oxygen spectrum, including the low-energy component composed of solar energetic particles (SEPs) and ions accelerated in corotating interaction regions (CIRs). To obtain a time history of low-energy ACR oxygen (Figure 3.2.9a), yearly averaged SAMPEX spectra were analyzed and the SEP/CIR components (below ~2 MeV/nucleon) were fitted with power-laws and subtracted from each annual spectrum. The average of the six annual power-law fits is indicated by the solid line in Figure 3.2.8. The difference between the combined six-year spectrum and the SEP/CIR component is shown in Figure 3.2.8 (upward triangular symbols) and represent the ACR oxygen component. This ACR O spectrum agrees well with that given by Mazur *et al.* (2000) and the slight discrepancies between the two spectra are easily understood as statistical in nature, arising from the different

techniques employed (i.e., in Mazur *et al.*, 2000, the SEP/CIR component of the spectrum is determined from the total six-year averaged spectrum, not individually from each of the six annual spectra). At and above 10 MeV/nucleon (downward triangular symbols), published, late-1995 ACR oxygen fluxes from the SAMPEX/HILT and SAMPEX/MAST sensors are shown (Mazur *et al.*, 2000). In Figure 3.2.8, as well as in Figure 3.2.9a, where the published uncertainties were too small to detect, the estimated numerical precision in determining the value from the published figure is indicated by an error bar.

In Figure 3.2.8 the annually averaged V1 (circular symbols) and V2 (square symbols) O spectra are from 1996 (this year was chosen since it is roughly in the middle of the 1993-1998 SAMPEX period, and is at a time when both inner and outer heliospheric ACRs are still in the recovery phase). These spectra are totally determined by ACR oxygen except possibly for the lowest energy V1 point at 0.3 MeV/nucleon.

The time-intensity profiles of inner and outer heliospheric low-energy ACR oxygen are shown in Figure 3.2.9a. The 1-AU data (triangular symbols) are a combination of SAMPEX/LICA observations and published ACE and WIND spacecraft data. The four published data points are 3-4 MeV/nucleon IP ACR oxygen data from the LEMT instrument on the WIND spacecraft with times centered on 1995.55 (Reames *et al.*, 1997), 1995.61, and 1996.14 (Cummings *et al.*, 1997) and ACE/ULEIS measurements of 2-4 MeV/nucleon IP ACR oxygen centered on 1997.95 (Christian *et al.*, 1999). Note that the 1995.55 and 1995.61 data points are so similar as to practically appear as one symbol in Figure 3.2.9a. We calculated the five

remaining data points in Figure 3.2.9a from the same SAMPEX/LICA data used to construct the 1-AU spectrum in Figure 3.2.8. The 1.75- to 5.00-MeV/nucleon ACR oxygen fluxes were determined from the 1993 to 1998 SEP/CIR-subtracted annual ACR oxygen spectra discussed above. A SAMPEX/LICA data-point from 1995 has been suppressed due to poor statistics.

The Voyager data shown in Figure 3.2.9a are 26-day averaged ACR O measurements from the LECP instruments with V1 and V2 energy ranges of 1.00 to 4.05 MeV/nucleon and 0.94 to 4.78 MeV/nucleon, respectively. In Figure 3.2.9b the time-intensity profiles for high-energy ACR oxygen are shown. For the 1-AU region, published SAMPEX/HILT, SAMPEX/MAST, and ACE/SIS measurements show 7- to 29-MeV/nucleon intensities versus time from the years 1992 to 2000 (Selesnick *et al.*, 2000). For the outer heliosphere, again Voyager/LECP observations are presented, utilizing 26-day averages and energy ranges of 6.89 to 27.6 MeV/nucleon and 8.00 to 27.4 MeV/nucleon for V1 and V2, respectively.

The energy spectra in Figure 3.2.8 show the energy at the peak in the ACR oxygen spectra to be about 1.3 MeV/nucleon in the outer heliosphere as compared with a peak energy value of 3-4 MeV/nucleon at 1-AU. The V2-to-SAMPEX intensity ratio is  $\sim 8$  at 3 MeV/nucleon and  $\sim 2$  at 20 MeV/nucleon. These observations are in qualitative agreement with the large-scale diffusion of ACRs from the outer to the inner heliosphere, with the lower-rigidity particles being more efficiently shielded from the inner heliosphere, (as we also show with the model spectra in section 3.5).

One of the striking features of the ACR O time histories at both low and high energies (Figure 3.2.9a and b) is the large delay between the onset of renewed



modulation at 1 AU and that in the outer heliosphere. For high-energy oxygen (Figure 3.2.9b) there is no sign of significant large scale modulation at V1 or V2 until the second half of 2000, despite a rapid drop at 1-AU beginning in the second half of 1997. ACR O with an energy range of 13 to 38 MeV/nucleon at V1 and V2 (Figure 3.2.4e and f) shows no sign of renewed modulation through the end of 2000, as was mentioned in section 3.2.2. In the low-energy data (Figure 3.2.9a), as in the high-energy data, the flux at 1-AU drops noticeably in 1997 and continues to do so in 1998, while the outer heliospheric low-energy anomalous oxygen does not decrease significantly until late 1999 or early 2000.

These facts indicate a large-scale modulation lag time of 2 to 3 years between the inner and outer heliosphere, showing that modulation is much less effective in the outer heliosphere, although this region does appear to respond to some shorter term (~150 day) solar variations, a topic covered in Chapter 4. The large, factor of ~10 increase in the V1 and V2 low-energy flux from 1994 to 2000 (Figure 3.2.9a) might therefore be explainable by a significant spatial effect resulting from the spacecraft moving through a relatively stable spatial structure with a significant radial gradient. This view appears to require substantial disturbances in the IP medium, perhaps resulting from the heliomagnetic polarity reversal, before the outer heliospheric spatial structure, and perhaps the termination shock source itself, is disrupted and eventually rapidly brought out of equilibrium, resulting in a comparatively sudden decrease such as is observed in the last half of 2000 (Figure 3.2.9a). The continued modest modulation of high energy oxygen flux (Figure 3.2.9b) and lack of modulation above 13 MeV/nucleon (Figure 3.2.4e and f) could indicate that the ACR source flux at

higher energies is still relatively stable even as solar maximum approaches, and that the solar disturbances are still too weak as of 2000 to significantly impede the high-rigidity particles from gaining access to the outer heliosphere.

A comparison of inner and outer heliospheric low-energy ACR O intensities versus time (Figure 3.2.9a), in light of both simple and sophisticated transport models also suggests that a large portion of the low-energy ACR increase at V1 and V2 is due to spatial rather than temporal effects (see sections 3.5 and 5.3.1, and Figure 5.3.1). The simple observation that the rates of increase at V1 and V2 (both with rates of  $15 \pm 6$  %/year) are larger than the rate of increase at 1 AU ( $10 \pm 9$  %/year) has potentially quite interesting implications since, if one assumes a weak influence of the spacecraft motion on the observations, it would be expected that the recovery in the inner heliospheric would be slower than in the outer heliosphere. (The rates of increase were determined from exponential fits to the data during the period after the initial, rapid recovery, and before the onset of modulation.)

Figure 5.3.1a shows this expected behavior from the numerical solutions of the transport equation discussed in section 3.5. This behavior is also born out in a more sophisticated acceleration/modulation model of ACR H in the heliosphere from Steenberg and Moraal (1996). Their numerical solutions to the transport equation model ACR H time-dependently, with momentum as a variable along with two spatial dimensions, radius and latitude. The acceleration of pick-up ions at the termination shock is explicitly handled in their calculations. This model (Steenberg and Moraal, 1996) does not include drift effects but a later model does (Steenberg, 1998). If we assume that the spatial dependence of the low-energy ACR O intensities at V1 and V2

is weak, then our model and the model of Steenberg and Moraal (1996) disagree with the observations, since the rates of increase in the outer heliosphere are somewhat *larger* than in the inner heliosphere, and the models predict the opposite (although the statistical limitations of the  $10 \pm 9$  %/year rate in the inner heliosphere are significant). This suggests either that (1) ACR O is evolving in a manner inconsistent with large scale diffusion from the outer to the inner heliosphere, or that (2) there is a significant non-temporal component in the increasing low-energy oxygen observed at the two Voyager spacecraft from 1994 to 2000 (Figure 3.2.9a). The spectral evidence (Figure 3.2.8) is in strong disagreement with possibility (1), and the most probable weak-diffusion model is a drift dominated heliosphere. However, the smaller than expected latitudinal gradients observed at Ulysses (e.g., McKibben, 1998) have already placed limits on the relative importance of drifts during the  $A > 0$  period, at least at high latitudes, and easy access of ACRs over the solar poles is also not expected (Jokipii *et al.*, 1995). This leaves possibility (2) as the more likely explanation. In particular, this supports the interpretation that the large low-energy increases seen at V1 and V2 after 1994 (Figure 3.2.9a) are substantially governed by spatial effects. The explicit comparison of the ACR oxygen observations to our model supports this case even more directly (§3.5).

For high-energy oxygen (Figure 3.2.9b) the situation is reversed, with the 1-AU data from 1994 to 1997 evidencing a slightly larger rate of increase ( $3 \pm 1$  %/year) than observed in the outer heliosphere ( $2.4 \pm 0.4$  and  $2.4 \pm 0.5$  %/year for V1 and V2, respectively). This is what would be expected from both the simple (Figure 5.3.1) and sophisticated (Steenberg and Moraal, 1996) transport models, since at these energies,

there is no sign of a sizeable spatial gradient in the outer heliosphere (see e.g., Figure 3.2.9b and Cummings *et al.*, 1997) to prevent a primarily temporal interpretation of the high-energy time histories.

When the high- and low-energy ACRs (Figure 3.2.9a and b) are compared to one another, however, the acceleration and transport model (Steenberg and Moraal, 1996) is not supported by the observations. This model predicts, at a given location, that the lower energy particles will approach the asymptotic values significantly earlier than do the higher-energy particles. This is physically reasonable in terms of the model, as the acceleration time for the higher-energy particles is longer than the acceleration time for the relatively easily accelerated low-energy particles. The data show that the rate of increase of the high-energy 1-AU ACRs is smaller than the rate of increase of the low-energy 1-AU ACRs. In the outer heliosphere, unless all of the post-1994 variation of low-energy ACR oxygen is due to a positive radial gradient (see section 3.4.4), then the temporal variation of the low-energy ACRs at a fixed position is probably increasing at a rate faster than the high-energy ACRs. If spatial effects do dominate the low-energy increase then, in the extreme, the low-energy temporal increase at a fixed location might be the same as the high-energy ACR oxygen rate of increase, while ongoing acceleration at the TS would be expected to result the lower-energy particles reaching a constant asymptote before the higher-energy particles. Thus the Voyager and 1-AU observations are not in agreement with significant time-dependent acceleration at the termination shock after ~1994. In fact, all of these observations are explainable if one assumes that the TS source is nearly constant (i.e., steady state acceleration) during most of the recovery period and that

**diffusive effects dominate the particle transport. These issues are taken up in section 5.3.1 and the rest of Chapter 3, where more detailed support for this interpretation is given.**

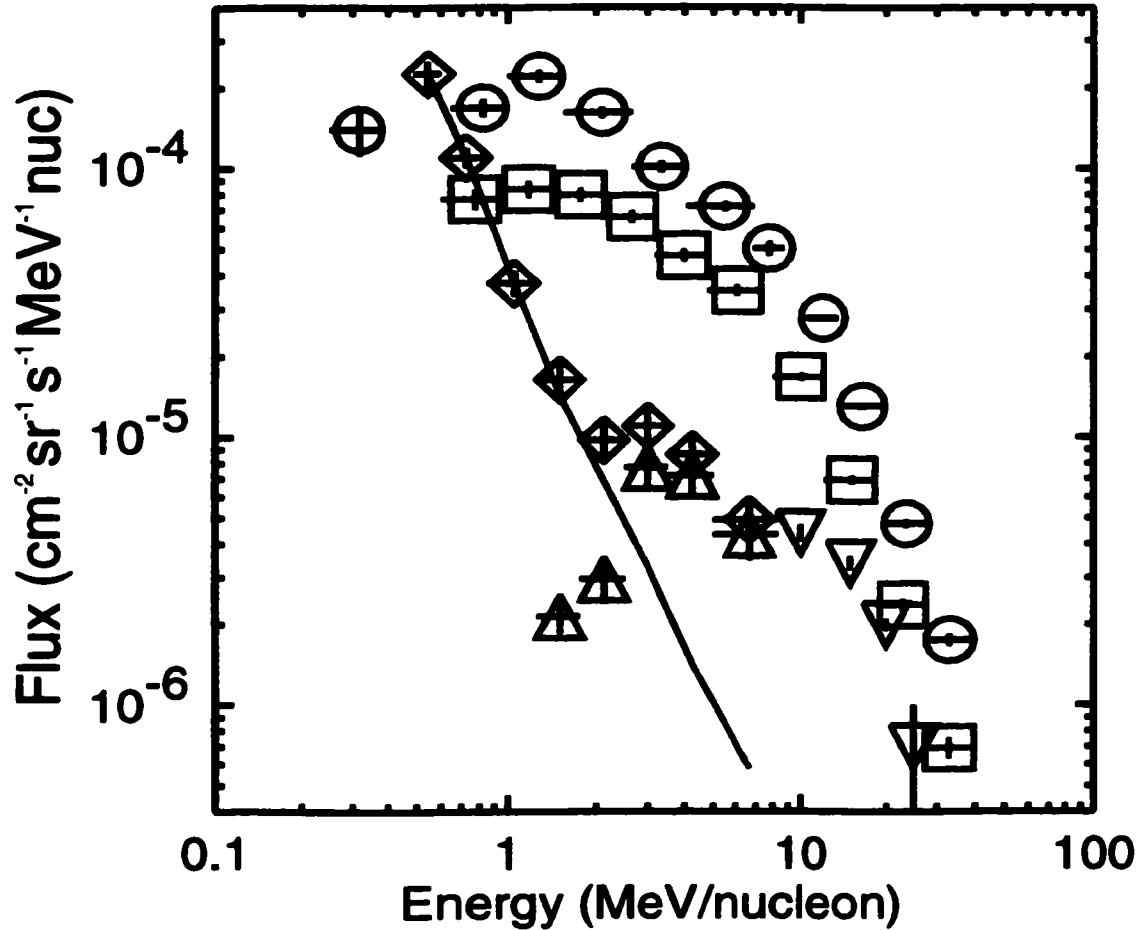


*Figure 3.2.8 SAMPEX, Voyager 1 & Voyager 2 Oxygen Spectra*  
 Interplanetary oxygen spectra from SAMPEX LICA (black diamonds) are shown along with the average of six annual power-law fits to residual SEP/CIR components (solid red line; see text), and the ACR oxygen spectrum (green upward triangles) resulting from the difference of these spectra (all from 1993-1998). The 1-AU ACR oxygen at and above 10 MeV/nucleon (green, downward triangles) are from late-1995 SAMPEX HILT & MAST data (Mazur et al. 2000). Annual Voyager 1 (blue circles) and Voyager 2 (red squares) oxygen spectra from 1996 are composed entirely of ACR ions, except possibly for the lowest energy V1 point at 0.3 MeV/nucleon.

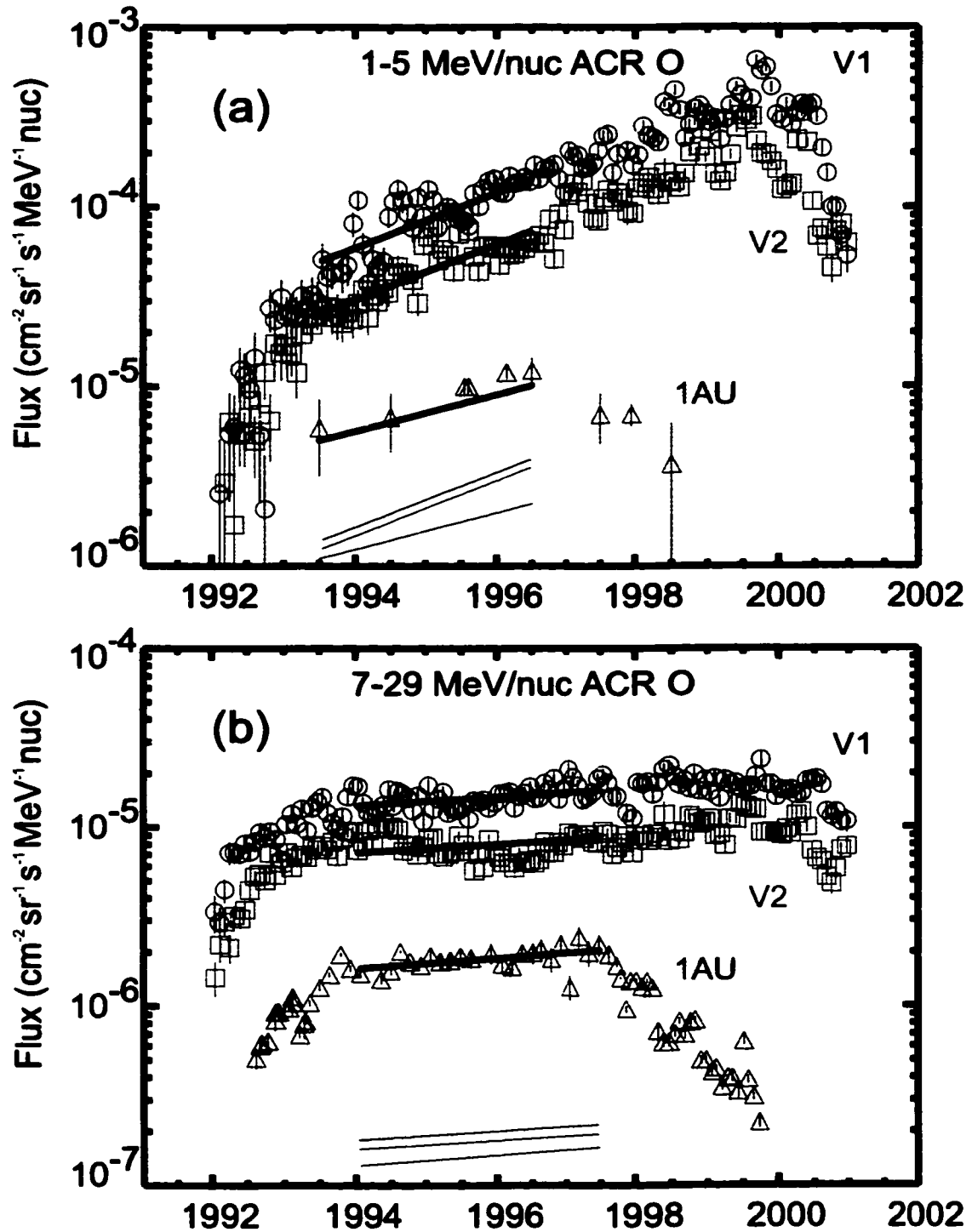


Figure 3.2.9 SAMPEX, WIND, ACE & Voyager Oxygen Time-Intensity Profiles  
 Plots of 1-AU (green triangles), V1 (blue circles), and V2 (red squares) ACR oxygen intensity vs. time are shown for the low-2 (a) and high-2 (b) energy ranges. Segments of exponential fits (see text) are shown to highlight relative rates of flux increase.

### 3.3 – Phenomenology of ACR Recovery

#### 3.3.1 – Parameterization of the Data

The parameterization of the ACR recovery profiles is necessary for section 3.3 as a comparison with the phenomenological model fits and for section 3.4 as a prerequisite to applying the “quasi-local” gradient method. The species listed in Table 2.3.1 that are dominated by anomalous cosmic rays are all fit with a function of time  $t$ , and four parameters  $j_a$ ,  $t_i$ ,  $\tau$ , and  $T$ , as follows,

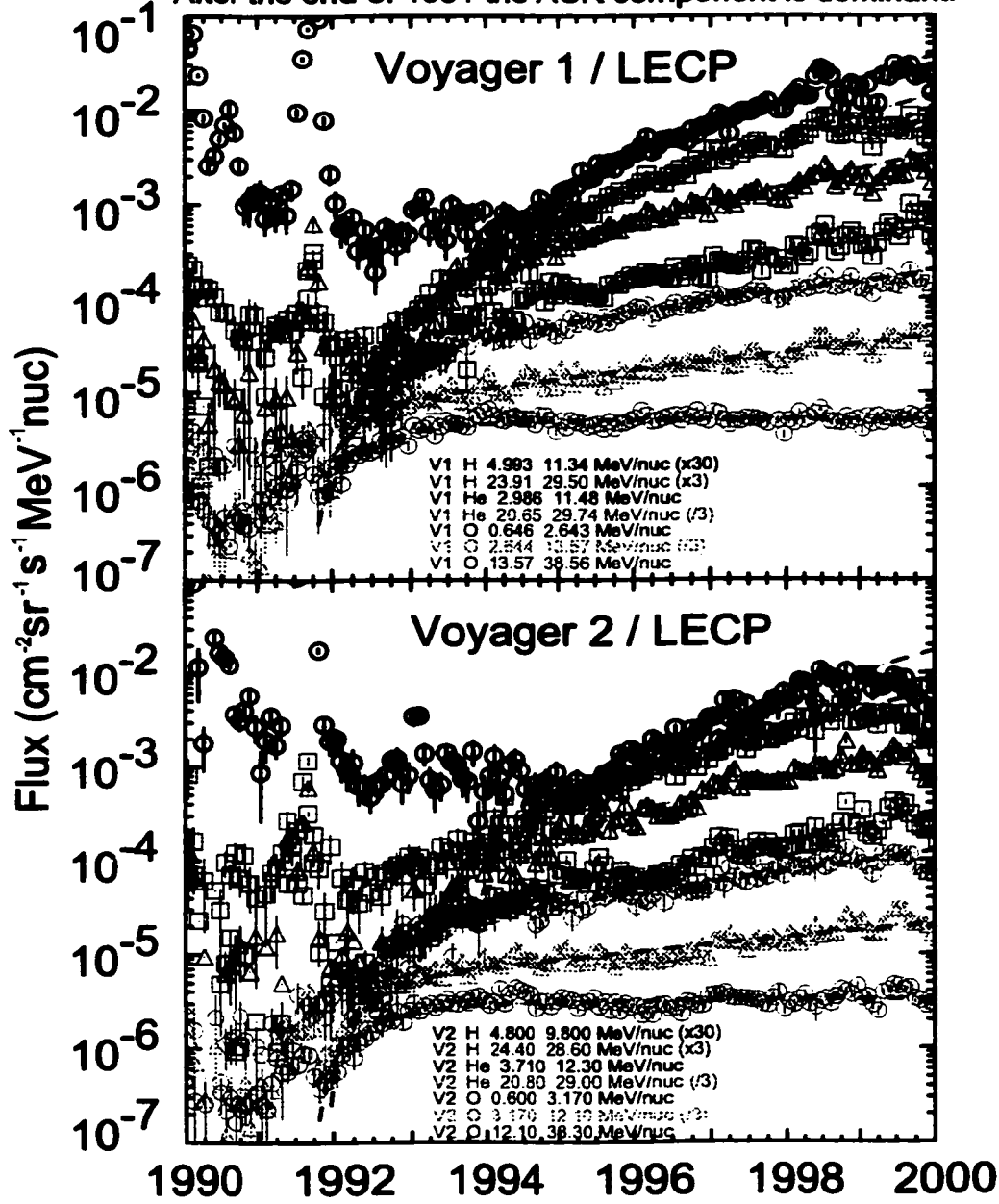
$$j(t) = j_a(1 - e^{-(t-t_i)/\tau})e^{(t-t_i)/T}, \quad (3.3.1)$$

where  $j_a$  is the time-asymptotic value of the initial recovery factor  $j_a(1 - \exp(-(t-t_i)/\tau))$ ,  $t_i$  is the initial time defined by  $j(t_i) = 0$ ,  $\tau$  is the  $e$ -folding recovery time, and  $T$  is the  $e$ -folding time of the exponential growth factor  $\exp((t-t_i)/T)$ . The fit parameters for all the anomalous cosmic rays studied herein can be found in Table 3.3.1. These fits are displayed graphically in Figure 3.3.1 for Voyager 1 and 2 H, He, and O ions. Taken as a whole the recovery profiles are slightly better ordered by rigidity  $R$  than by total kinetic energy  $\mathcal{T}$  for both V1 and V2, although from Figure 3.3.3, e.g., panels (n) and (o), it is seen that both total energy and rigidity order many of the parameters similarly. (See below for a complete discussion of Figure 3.3.3.) Figure 3.3.1 shows that in general, the higher rigidity particles begin their recoveries earlier than other particles, but that they have lower rates of increase after the initial recovery has ended. This can also be seen in Figure 3.3.3 where  $t_i$  is earlier for ACRs with higher total kinetic energies (b) or rigidities (c), and the exponential growth times  $T$  are larger,



# ACR H, He and O

In 1990 & 1991 there is a mixture of ACR and SEP/IP accelerated ions.  
 After the end of 1991 the ACR component is dominant.



V1V2\_199099ACRHHHeO\_jvt3Enrg.PS

Mon Oct 22 05:36:20 2001

*Figure 3.3.1 Voyager 1 & 2 ACR H, He & O Recovery Fits*  
 Recovery fits to Voyager 1 (top) and 2 (bottom) ACR H, He, and O time-intensity profiles using the parameters from table 3.3.1.

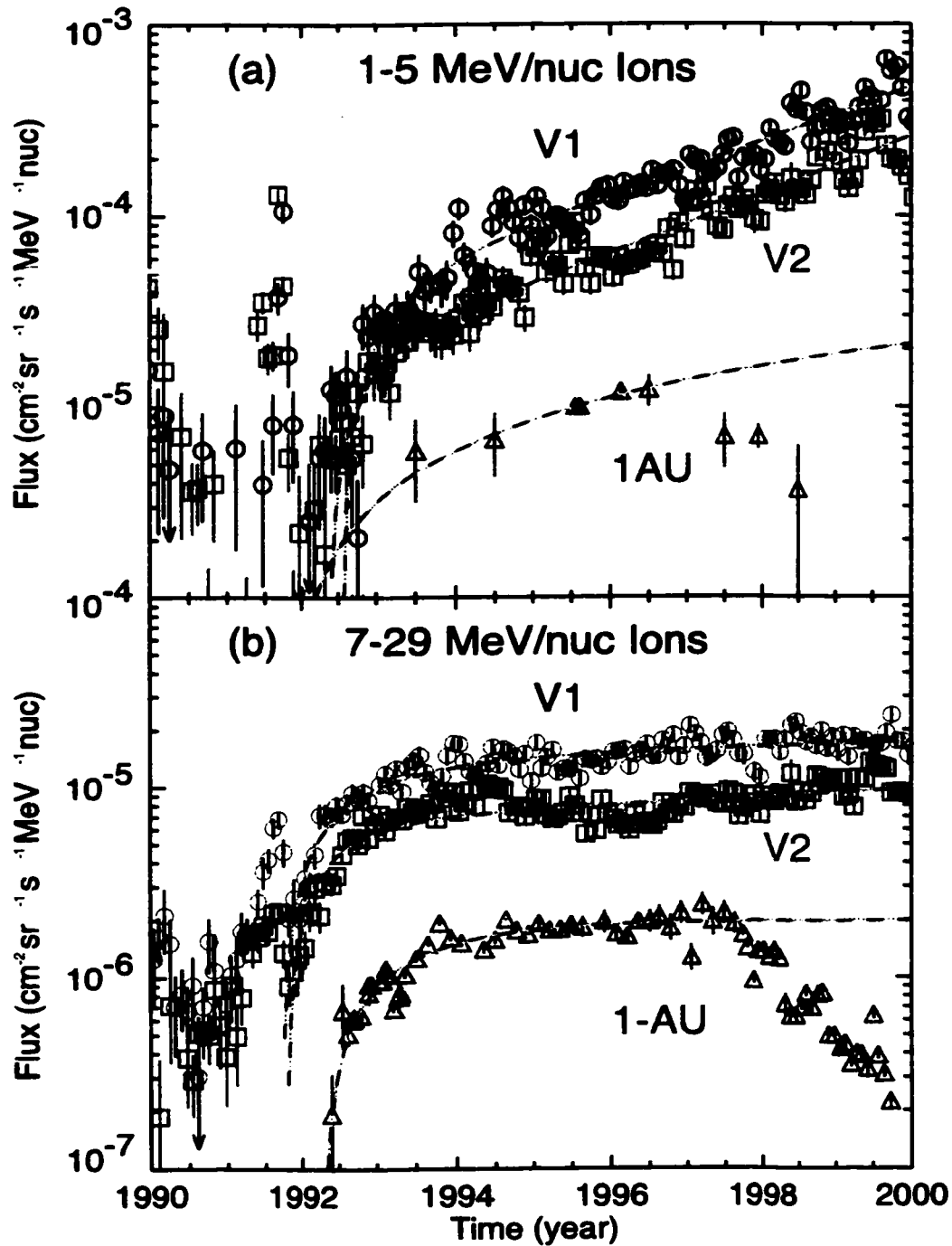
Another significant feature of the recovery curves in Figure 3.3.1 is the striking exponential nature many of them exhibit over a large fraction of the recovery period. For the last four to six years of the period shown, the oxygen and helium data are well-represented by linear fits to the logarithm of intensity, i.e., exponential growth. Why these cosmic rays take on distinct and sustained forms of exponential growth rather than the  $1 - \exp(-t)$  recovery form predominantly observed for galactic cosmic rays and high-energy ACRs during cycle 22 is an important topic in this work (see section 3.4.2), and as was mentioned section 3.2.3 is related to the relative importance of effects of spacecraft motion. The range of behaviors of these particle is itself quite remarkable, with  $\sim 6$  MeV/nucleon helium increasing more than two orders of magnitude, for example, while the highest energy oxygen ions remain nearly constant throughout the post-initial-recovery period.

In Figures 3.3.1 and 3.3.2 the fits were made to data within the recovery period only, therefore periods of increasing modulation, significant background, or enhanced interplanetary acceleration were avoided. For instance the Voyager 2 4.8- to 9.8-MeV proton data in bottom panel of Figure 3.3.1 clearly show evidence of increasing modulation by 1998.5, and before about 1995 the interplanetary background prevents detection of the anomalous component (the fit periods are listed in table 3.3.1). Regardless of the limited fitting periods, the curves are extrapolated both forward and backward in time to better display the features of the recovery and to facilitate comparison.

Some of the features of Figure 3.3.2 were discussed in the text surrounding the similar plot, Figure 3.2.9. The Voyager data parameterized in panel (a) have energy ranges that overlap with the data discussed above. The fit to the 1-AU data (see section 3.2.3 for references) is merely suggestive and has been done for completeness; clearly a varied family of curves could fit these data nearly as well. In panel (b) the Voyager data again overlap measurements previously discussed and the 1-AU oxygen data are SAMPEX and ACE spacecraft observations from Selesnick *et al.* (2000), supplemented by the two earliest data points which are from the IMP-8 spacecraft (Mewaldt *et al.*, 1993). It is interesting that the inner and outer heliospheric time profiles have similar *e*-folding constants of around 1 year, but are offset by 6 months, with the outer heliospheric ACRs recovering earlier. There is an order of magnitude difference between the inner and outer heliospheric anomalous oxygen intensity in 1996, before the renewed solar activity steadily modulated the near-Earth oxygen.

Table 3.3.1 contains the fit parameters for all of the studied ACR ions. The  $\chi^2$  minimization procedure was performed on 26-day-averaged data that were smoothed with 1-year running averages, since it is only the long-term features that are of interest here (shorter-term variations are discussed in Chapter 4). In a few cases edge-effects from the smoothing routine resulted in poor fits and the unsmoothed data were fit instead. As addressed in section 3.4, an eventual application of these recovery fits is the separation of the time profiles into temporally and spatially dependent forms. It will be shown phenomenologically (§3.3), observationally (§3.4) and theoretically (§3.5) that associating the recovery factor with the temporal dependence and the

# Oxygen in the Inner and Outer Heliosphere



Mon Oct 22 07:00:57 2001

*Figure 3.3.2 Inner and Outer Heliospheric ACR O Recovery Fits*  
Fits to (a) low<sub>2</sub> and (b) high<sub>2</sub> energy ACR O time-intensity profiles at V1 (blue circle) V2 (red squares) and 1-AU (green triangles) using the table 3.3.1 parameters.

**Table 3.3.1 Parameterization of ACR Recovery Profiles**

Anomalous Cosmic Ray Recovery <sup>a</sup>	Energy $E$ (MeV/nuc)	Intensity <sup>b</sup> $j_a$ (flux <sup>c</sup> )	Initial Time $t_i$ (year)	Recovery Time $\tau$ (year)	Growth Time $T$ (year)	Fitting Period (years)
S/C - Ion - Range						
V1 $^1_1\text{H}^+$ - Med	4.993 - 11.34	$1.9 \pm 0.9 \cdot 10^{-4}$	$1993.50 \pm 0.83$	$10.4 \pm 5.6$	$2.44 \pm 0.24$	'94.0-98.0
V2 $^1_1\text{H}^+$ - Med	4.800 - 9.800	$1.6 \pm 1.0 \cdot 10^{-4}$	$1994.19 \pm 0.98$	$13.4 \pm 8.9$	$2.51 \pm 0.55$	'95.0-98.5
V1 $^1_1\text{H}^+$ - High	23.91 - 29.50	$4.8 \pm 1.4 \cdot 10^{-4}$	$1992.67 \pm 0.54$	$11.2 \pm 3.6$	$2.40 \pm 0.11$	'93.0-98.0
V2 $^1_1\text{H}^+$ - High	24.40 - 28.60	$3.4 \pm 1.6 \cdot 10^{-4}$	$1992.24 \pm 0.99$	$17.1 \pm 8.4$	$2.72 \pm 0.18$	'93.0-99.0
V1 $^4_2\text{He}^+$ - Med	2.986 - 11.48	$1.9 \pm 0.2 \cdot 10^{-4}$	$1992.74 \pm 0.18$	$1.23 \pm 0.21$	$2.49 \pm 0.10$	'92.8-98.5
V2 $^4_2\text{He}^+$ - Med	3.710 - 12.30	$9.5 \pm 9.2 \cdot 10^{-5}$	$1993.01 \pm 2.50$	$1.11 \pm 0.52$	$2.31 \pm 0.28$	'93.1-98.5
V1 $^4_2\text{He}^+$ - High	20.65 - 29.74	$8.2 \pm 1.5 \cdot 10^{-5}$	$1991.95 \pm 0.63$	$1.24 \pm 0.31$	$4.13 \pm 0.34$	'92.0-99.0
V2 $^4_2\text{He}^+$ - High	20.80 - 29.00	$5.0 \pm 0.4 \cdot 10^{-5}$	$1992.18 \pm 0.19$	$0.69 \pm 0.17$	$3.90 \pm 0.22$	'92.2-99.5
V1 $^{16}_8\text{O}^+$ - Low	0.646 - 2.643	$5.2 \pm 0.9 \cdot 10^{-5}$	$1992.54 \pm 0.53$	$0.97 \pm 0.20$	$3.06 \pm 0.16$	'92.5-99.0
V2 $^{16}_8\text{O}^+$ - Low	0.600 - 3.170	$2.0 \pm 0.1 \cdot 10^{-5}$	$1992.44 \pm 0.17$	$0.68 \pm 0.15$	$2.72 \pm 0.08$	'92.5-99.0
V1 $^{16}_8\text{O}^+$ - Med	2.644 - 13.57	$2.1 \pm 0.1 \cdot 10^{-5}$	$1991.91 \pm 0.08$	$0.52 \pm 0.07$	$4.63 \pm 0.11$	'91.9-00.0
V2 $^{16}_8\text{O}^+$ - Med	3.170 - 12.10	$1.5 \pm 0.1 \cdot 10^{-5}$	$1991.94 \pm 0.08$	$0.61 \pm 0.08$	$5.70 \pm 0.24$	'91.9-99.0
V1 $^{16}_8\text{O}^+$ - High	13.57 - 38.56	$5.1 \pm 0.0 \cdot 10^{-6}$	$1991.74 \pm 0.27$	$1.00 \pm 0.06$	$\infty^d$	'91.8-00.5
V2 $^{16}_8\text{O}^+$ - High	12.10 - 38.30	$3.0 \pm 0.1 \cdot 10^{-6}$	$1991.77 \pm 0.08$	$0.84 \pm 0.08$	$81.5 \pm 42.3$	'91.8-00.5
V1 $^{16}_8\text{O}^+$ - Low <sub>2</sub>	1.00 - 4.05	$4.2 \pm 0.3 \cdot 10^{-5}$	$1992.55 \pm 0.14$	$0.80 \pm 0.13$	$3.10 \pm 0.10$	'92.5-99.0
V2 $^{16}_8\text{O}^+$ - Low <sub>2</sub>	0.95 - 4.78	$1.8 \pm 0.1 \cdot 10^{-5}$	$1992.37 \pm 0.16$	$0.57 \pm 0.13$	$2.84 \pm 0.07$	'92.5-99.0
1AU $^{16}_8\text{O}^+$ - Low <sub>2</sub>	1 - 5	$2.4 \pm 2.8 \cdot 10^{-4}$	$1991.83 \pm 4.55$	$90 \pm 110$	$\infty^d$	'92.0-97.0
V1 $^{16}_8\text{O}^+$ - High <sub>2</sub>	6.89 - 27.6	$1.3 \pm 0.0 \cdot 10^{-5}$	$1991.72 \pm 0.03$	$1.03 \pm 0.06$	$29.5 \pm 2.5$	'91.8-00.5
V2 $^{16}_8\text{O}^+$ - High <sub>2</sub>	8.00 - 27.4	$6.5 \pm 0.2 \cdot 10^{-6}$	$1991.78 \pm 0.17$	$0.67 \pm 0.05$	$19.8 \pm 1.8$	'91.8-00.5
1AU $^{16}_8\text{O}^+$ - High <sub>2</sub>	7 - 29	$2.0 \pm 0.0 \cdot 10^{-6}$	$1992.28 \pm 0.54$	$1.21 \pm 0.09$	$\infty^d$	'92.0-97.5

<sup>a</sup> The recovery fit function is  $j(t) = j_a(1 - \exp(-(t-t_i)/\tau))\exp((t-t_i)/T)$ .

<sup>b</sup> Time asymptotic intensity of the recovery factor  $j_a(1 - \exp(-(t-t_i)/\tau))$ .

<sup>c</sup> Flux units are  $\text{cm}^{-2}\text{sr}^{-1}\text{s}^{-1}(\text{MeV/nucleon})^{-1}$ .

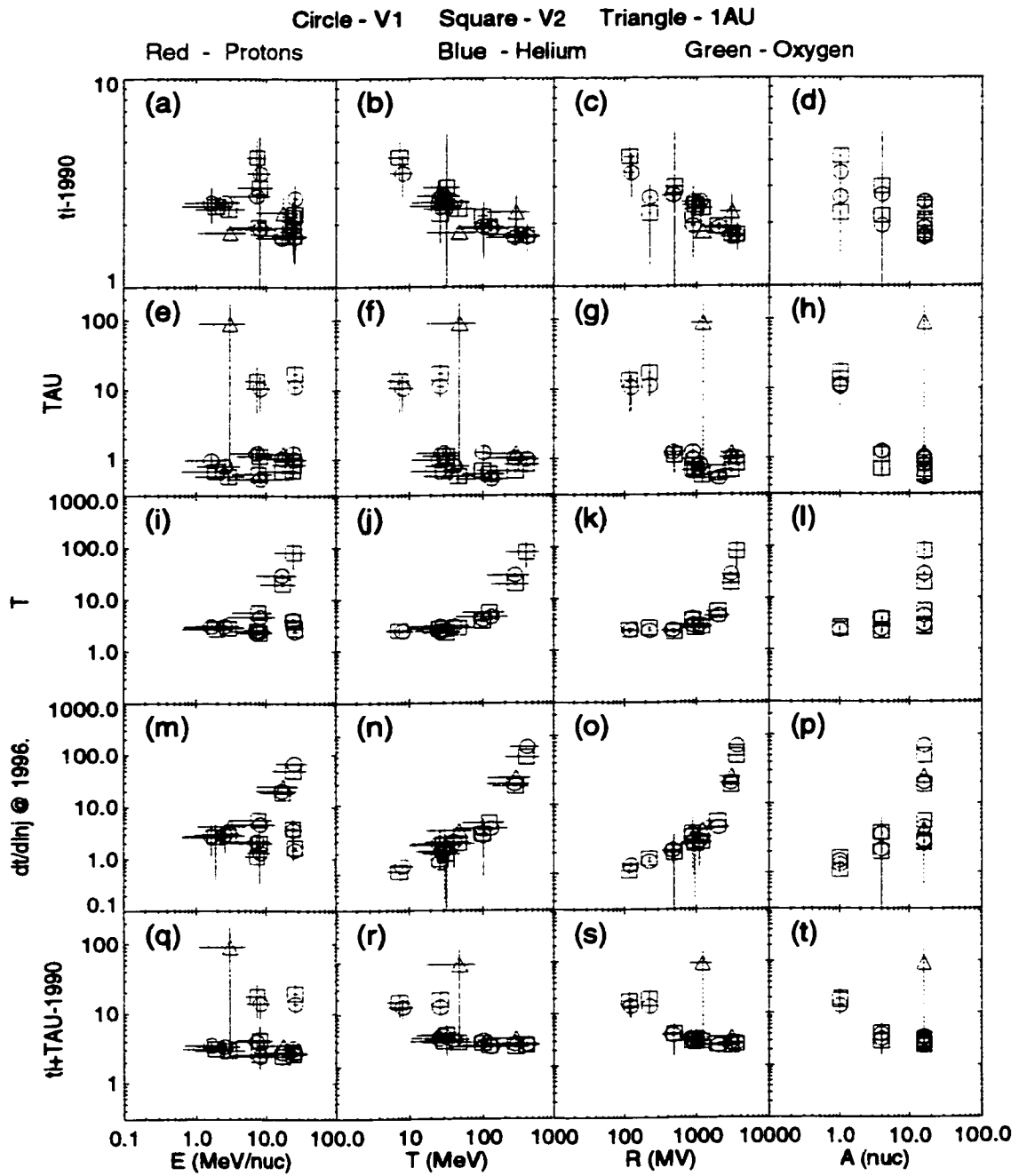
<sup>d</sup> The growth factor  $\exp((t-t_i)/T)$  was found not to be necessary for these fits.

exponential growth factor with the spatial dependence (i.e., due to spacecraft motion) is reasonable, and indeed the most appropriate division. All of the oxygen data and to a lesser degree the helium data are unambiguously representable by the Eq. 3.3.1 form. That is, the resulting fit parameters ( particularly  $\tau$  and  $T$ ) are relatively insensitive to reasonable choices of starting parameters owing to the quite distinct initial recovery

(usually before 1994) and exponential growth phases evident in the data. The proton recoveries were more difficult to fit because the final fit parameters, especially  $\tau$ , were relatively sensitive to varied reasonable choices of initial parameter estimates. Relevant for the application in section 3.4, the exponential growth factor  $T$  was less sensitive to these variations than the recovery time, but none of the proton fit parameters were as stable as were the analogous O and He parameters. The reason for this is simply that the proton “initial” recovery period is longer, and the exponential growth phase is less well defined than for the other species, making it difficult to distinguish the two periods. Moreover, low-energy anomalous protons are undetectable (due to the locally-accelerated proton background) before about 1995, further complicating the fitting, since most of the initial recovery period is unobserved. For these reasons the other species, and mostly oxygen, are given more weight in the analysis. (Oxygen also has the great advantage of having near-Earth observations available, and the ACR O peak is uniquely resolved by the LECP instruments during solar cycle 22.) Note that the 9- to 27-MeV/nucleon ACR O<sup>+</sup> values for  $\tau$  are almost identical to those determined by McDonald *et al.* (2000b).

The dependence of the fit parameters upon the ACR particle properties is a topic of interest as it can shed light on the underlying physics. This is addressed by Figure 3.3.3, in which individual and combinations of the time parameters are plotted against four ion properties. The time quantities  $t_i$ ,  $\tau$ ,  $T$ ,  $(\partial \ln j / \partial t)^{-1}$ , and  $\tau + t_i$  are plotted in the rows begun by panel (a), (e), (i), (m), and (q), respectively, against the ion properties. The data in the columns headed by panels (a), (b), (c), and (d) are

# Time Parameters (years) vs. Ion Properties



Hard Drive:Desktop Folder:tPARAMvsIONprop111101.PS

Sun Nov 11 18:53:12 2001

**Figure 3.3.3 Recovery Time Parameters vs. ACR Properties**  
 Combinations of time parameters (years) from Table 3.3.1 are plotted for V1 (circle), V2 (square), and 1-AU (triangle) H, He, and O (red, blue, and green respectively) ACRs vs. nucleon energy, total energy, rigidity, and atomic mass number.

plotted against  $E$ ,  $\mathcal{T}$ ,  $R$ , and  $A$  (mass number), respectively. While the significance of the four abscissae is evident, the five time-related ordinates deserve discussion. First note that in each panel of the figure, the colors red, blue, and green are used for symbols representing H, He, and O data, respectively, and circular, square, and triangular symbols are used to indicate the V1, V2, near-Earth observation platforms. These conventions provide two additional dimensions with which to probe the ACR behavior.

In the top row (Figures 3.3.3a-d) the difference between the initial time  $t_i$  and an arbitrary reference year 1990 is plotted, indicating the extrapolated time at which the ACR recovery begins at zero flux. Although the low-intensity measurements near  $t_i$  are difficult, this parameter allows a meaningful comparison of the start of recovery for different ions. If one were to alternatively base the start of recovery upon the first indication of elevated ACR flux alone, for example, the times could be skewed by factors not directly related to cosmic ray physics, such as instrumental background levels and coincident IP particle events; therefore,  $t_i$  is used. Energy per nucleon (a) and atomic mass (d) clearly do not organize this parameter at all, but total kinetic energy (b) and rigidity (c) do, and about equally as well.

The recovery time  $\tau$  is plotted in Figures 3.3.3e-h, indicating the characteristic time-scale of the initial recovery factor  $j_0(1-\exp(-(t-t_i)/\tau))$ , which (it is argued in section 3.4.2 and subsequent sections) is related to the recovery time of the particles one would expect if the spacecraft position were held constant. None of the independent variables organize this parameter particularly well, but perhaps  $A$  does the



best, followed by  $R$ . Except for protons and the 1-AU low<sub>2</sub>-energy oxygen, all of the ACR recovery times cluster around 1 year. The parameter  $t_i + \tau$  is perhaps a better quantity to measure the timing of the initial recovery, and is discussed below.

The middle row (Figures 3.3.3i-l) contains plots of the exponential growth  $e$ -folding time  $T$  vs. each abscissa. The time  $T$  is associated with the spatial intensity gradient of the particles (we argued in this chapter), but ignoring this,  $T$  is simply related to the time-asymptotic rate of increase of the anomalous component before the end of the recovery phase. Both  $T$  and  $R$  organize this constant well with a dependence that, from right to left in panels (j) and (k), rapidly approaches a minimum  $T$  of 2.3 years, corresponding to a doubling time of around 19 months. The data become flat for the mid and low energy (or rigidity) particles indicating that  $T$  becomes proportional to  $T^0$  and  $R^0$  for the less energetic particles. This may be somewhat influenced by the difficulties discussed above associated with determining the proton parameters, but is supported by the fact that the high-quality oxygen parameters do independently display this tendency, and with this both H and He are consistent.

As the appearance of the recoveries in Figure 3.3.1 seems to reveal a better organization with rigidity than the parameters so far indicate, particularly at low rigidities, a parameter directly related to the rate of increase of intensity in the late recovery period has been calculated. This instantaneous  $e$ -folding time is defined by the relation  $T_e = (\partial \ln j / \partial t)^{-1}$  and has a different value for each time  $t$ . It was chosen such that  $T_e$  approaches  $T$  for  $t - t_i \gg \tau$ . In Figure 3.3.3m-p  $T_e$  is plotted at  $t = 1996.0$ ,

before the solar minimum conditions in the inner heliosphere begin to yield to approaching solar activity. What is seen in panels (n) and (o) is that  $\mathcal{T}$  and  $R$  clearly organize this parameter over the full range of each independent variables. Close inspection of these panels indicates the  $R$  is slightly preferable as a organizing particle characteristic, because the dependence of  $T_2$  at a given spacecraft is noticeably smoother in panel (o) than in panel (n), there being discontinuities at about 30 MeV in panel (n).

The bottom row (Figure 3.3.3q-t) involves the quantity  $t_{\text{rec}} = t_i + \tau$  (minus the arbitrary reference time, 1990), which, better than either constituent parameter alone, provides information about when the recovery phase has ended for a given species. The value of  $t_{\text{rec}}$  is the time when the recovery factor  $1 - \exp(-(t-t_i)/\tau)$  of the fit function equals 0.63; this is a useful measure of the transition time from the initial recovery phase to the eventual exponential growth period. The atomic mass number does a fair job at organizing this parameter, with the exception of the low<sub>2</sub>-energy 1-AU oxygen point. The value of this is difficult to gauge because there is not a large overlap in rigidities between species, although the total energy overlap between species is more substantial. As with all of the other parameters,  $E$  provides no correlation, but some semblance of this can be seen in panels (r) and (s), for  $\mathcal{T}$  and  $R$ , with  $R$  again slightly preferable. However, this correlation is rather weak if one excludes H from consideration (for reasons discussed above). It should be noted that although the 1-5 MeV/nuc 1-AU O value for  $t_{\text{rec}}$  has poor statistics, it would not be surprising if the value was not among the cluster of other values, as it is expected that both lower

rigidity and smaller helioradius should separately be associated with later recovery times in the case of drift-free transport from a constant outer source with a rigidity dependent scattering mean free path (see sections 3.2.3 and 3.5, and Figure 5.3.1).

Overall, these time parameters tend to be about equally as well organized by rigidity as by total kinetic energy, with  $R$  perhaps slightly preferable to  $T$  in some instances. This similarity is not surprising if a power-law-dependent scattering mean free path  $\Lambda \propto R^\eta$  has an index  $\eta$  near unity (see section 3.5). One significant feature of these parametric results is merely to demonstrate that the recovery profiles of these particles, with mass numbers ranging from 1 to 16, at heliospheric positions between 1 and 80 AU from the Sun, and with rigidities spanning from  $\sim 100$  to over 4000 MV, are quite closely related. This suggests, from a physically-based phenomenological standpoint, that it is possible to model the transport of the anomalous cosmic ray recovery systematically so as to understand the dependence that detailed features of these phenomena have on known physical quantities. This is the work of the remainder of section 3.3.

### **3.3.2 – A Phenomenological Recovery Model**

In this section we develop a model based on the form of spatial intensity gradients (see section 3.4.1), to study the phenomenology of the anomalous cosmic ray recovery from 1991 to 2000. This physically-based model reveals the dependence several ACR recovery features have on various heliospheric and particle properties and provides an essentially independent result with which to compare the measurement (§3.4) and numerical modeling (§3.5) efforts to follow.

The goal of the recovery model is to construct analytical representations for the radial and latitudinal gradients and to then use these gradients to arrive at a functional form for the intensity  $j = j(r, \lambda, t; a_0, \dots, a_N; b_0, \dots, b_N)$ , where the  $a_i$  represent parameters such as intensity normalization and time constants and the  $b_i$  represent givens such as rigidity and solar wind speed. Armed with this expression for  $j$ , fourteen outer heliospheric ACR time-intensity series are simultaneously to be fitted by the  $j$  model using a combination of Marquardt gradient-expansion and *brute force* grid-search least squares fitting algorithms. The fourteen time series (shown in Figure 3.3.1) span V1 and V2 H, He, and O ACR ions with energies from 1 to 40 MeV/nucleon. By simultaneously fitting all of these data (in contrast to the separate fits of section 3.3.1) with as few parameters as possible some insight is gained into global aspects of the heliosphere such as the radius and spectral properties of the source (likely to be the termination shock), and cosmic ray properties such as the radial and rigidity dependence of the radial gradient forms used in the model. Application of the gradient model also allows us to probe the resulting model anomalous cosmic ray distribution in space and time to, for example, estimate the values of radial and latitudinal gradients for particular species. The resulting phenomenological model might also be of use to theoreticians and others who model cosmic ray transport since a manageable, analytical expression for the ACR intensity at arbitrary radius, latitude, time and, rigidity provides random access to quantitative information that is closely related to the observations, but is considerably more user friendly.

Before the details of the model are presented, the form of the spatial intensity gradients needs to be determined. The definitions of these gradients are discussed in

more detail in sections 3.4.1 and 3.4.2. The standard equation used to measure radial and latitudinal intensity gradients of cosmic rays is given by Eq. 3.4.3. This form is not strictly consistent for cases in which the radial gradient  $g_r$  depends on independent variables other than the helioradius  $r$  (and likewise for the latitudinal gradient  $g_\lambda$  with respect to the heliolatitude  $\lambda$ ). For example with a constant latitudinal gradient, if the radial gradient depends on  $r$  and  $t$  separably as  $g_r(r,t) = q(r)h(t)$  we will have  $dj/j = q(r)h(t)dr + g_\lambda d\lambda$ , which must be integrated in order to apply this form to the modeling of  $j$ , yielding:

$$\ln(j / j_s) = \int_{r_s}^r q(r')h(t)dr' + g_\lambda \lambda.$$

(The  $s$  subscript indicates the source value, the *source latitude* is taken to be zero without loss of generality.) If we wish to retain the applicability of this equation to any spacecraft trajectory  $r(t)$  we will not know how  $t$  and  $r$  are related, so we cannot bring  $h(t)$  outside of the integral before integrating without introducing some error. (The inconsistency is clear if one integrates after bringing  $h(t)$  outside of the integral and then calculates  $dj/j$  again; the result differs in form from the initial differential equation.) It turns out for the gradient forms actually used in this study, with the typical resulting parameters, the error is not large for times  $t$  after the initial recovery period has ended, and is therefore directly applicable to most of the ACR recovery period in question.

It is not necessary to rely on the error being small since we are using the expression for  $dj/j$  merely as a guide to suggest an appropriate form for the model of the intensity; another way to obtain a usable functional form of  $j$  is to begin with an

alternate expression that does not result in the integration problem above. We can formally add a *temporal gradient* to the model. Firstly, we could reasonably pick the form of such a temporal gradient to depend on the time derivative of the time-factor,  $\partial h/\partial t$ . However, the temporal gradient should also vary with radius in such a way that is consistent with the observation that outer heliospheric ACRs recover earlier than those in the inner heliosphere (see sections 3.3.2 and 3.3.1, and Figure 5.3.1a). That is, after an initial recovery, the outer heliospheric time-intensity profile approaches a constant asymptote, so a temporal gradient at this time should be very small, while the inner heliospheric particles continue to increase at a non-vanishing rate. Choosing the temporal gradient to be  $\partial h/\partial t(\int q dr)$ , with the integration from  $r_s$  to  $r$ , as above, accomplishes these goals. This leads to,

$$dj/j = q(r)h(t)dr + g_\lambda d\lambda + \partial h/\partial t(\int q dr)dt,$$

which upon integrating by parts becomes,

$$\ln(j/j_s) = h(t) \int_{r_s}^r q(r')dr' + g_\lambda \lambda, \quad (3.3.2)$$

which is integrable for a general trajectory  $r(t)$ , and is thus in a usable form.

Motivated by this gradient form, the notion was to pick a simple time dependence that decreased the radial gradient with time as experience with numerical and analytical solutions to the cosmic ray transport equation (see section 3.5) suggests will happen as an empty (or nearly empty) heliosphere becomes filled with inward propagating cosmic rays at the onset of the recovery period. The gradient will be very steep at first since the ions at the source, the outer boundary of the model, cannot make their way into the inner heliosphere (due to, for example, propagating diffusive

barriers associated with interplanetary disturbances and/or global changes in the transport properties just after solar maximum). Then as the transport becomes easier for the particles the gradient should approach a steady state value. The most natural function of the type described has the form  $1 + e^{-L\tau}$  (note the plus sign) as is seen below in Eq. 3.3.3. The lessons of section 3.3.1 support the step of making the time-asymptotic (~steady-state) radial gradient described above dependent on rigidity with high-rigidity particles exhibiting shallower gradients than low-rigidity particle since they are less-inhibited from entry into the heliosphere. Thus an  $e^{-R}$  form appears in Eq. 3.3.3 for the radial gradient (a power-law form was found to result in generally poor fits). There is also an observational and theoretical expectation of an energy or rigidity dependence for the rate of the initial recovery, with lower-rigidity particle recovering more gradually (see sections 3.2.3 and 3.3.1, and Figure 5.3.1b), thus an  $e$ -folding time constant in  $1 + e^{-L\tau}$  with a rigidity dependence such as  $\tau = \tau_0 (R/R_H)^{-\gamma_2}$  is called for. A radially dependence of the form  $r^{-a_1}$  has been found to well-represent ACR gradients during cycle 22 and 21 (Cummings *et al.*, 1995a; Fujii and McDonald, 1997; and references therein) so this too is included in the radial gradient model of Eq. 3.3.3. The latitudinal gradient form (Eq. 3.3.4) was arrived at by requiring that the sign of the gradient be able to reverse in a rigidity dependent way, as this was thought to be a possibility.

The physical and phenomenological basis having been described, further details of the model are hereupon addressed. A distinction between the variables, givens, and parameters needs to be made. The variables and parameters will be followed by the name used in the program output (Figure 3.3.4-6) when it is not

obvious. The variables are  $r$ ,  $\lambda$ , and  $t$  (hr, hl, and t) for this model. The given quantities are the solar wind speed  $V$  and the particle rigidity  $R$ . Although the Compton-Getting factor  $C$  appears in the models in section 3.3.4 it has been set to unity in all cases. This means that the spectral slopes do not enter this model, as would be the case for convection and diffusion without adiabatic deceleration. This is reasonable for the outer heliosphere, as was discussed in section 1.1.5 in relation to the work of Reinecke and Moraal (1992). There are two models discussed, a *no-source* model in which the H, He, and O source spectra are not modeled and an *ACR-source* model which does parameterize the source spectrum. The no-source model is treated first, and then the differences in the ACR-source model are discussed.

The fourteen time-series are modeled by eighteen parameters as follows. The source or termination shock radius  $r_s$  (hrTS), as well as the seven source intensities  $J_{s1}, \dots, J_{s7}$  are listed in the first line of panel (o) of Figure 3.3.4. The ion source intensities  $J_{s1}, \dots, J_{s7}$  are the same at V1 and V2 and are associated with H-med, H-high, He-med, He-high, O-low, O-med, and O-high, respectively, (where the energy-shorthand of table 2.3.1 has been used). In the next row of parameter names in Figure 3.3.4o are the steady state radial gradient coefficient  $g_r^\infty$  (grinf), the latitudinal gradient coefficient  $g_\lambda^0$  (glo), the recovery coefficient  $\Delta$ , the reference time  $t_0$ , and the recovery time coefficient  $\tau_0$ . In the third parameter-row four parameters related to rigidity dependence are listed  $\gamma_1, \gamma_2, \gamma_4, \gamma_5$  (gamma3 is not used). (It is unfortunate that *gamma*'s are used in this section to indicate rigidity dependence as the symbol  $\gamma$  is retained for the energy dependence, and  $\eta$  for the rigidity dependence of the diffusion coefficient in section 3.5 and elsewhere.) In the final row of parameters (Figure



3.3.4o) only the first parameter  $a_1$  is used, and is the index of the radial power-law dependence of the radial gradient,  $g_r \propto r^{-a_1}$ . In panel (p) are the two reference rigidities which are merely a convenience,  $R_L$  (Rreflo) and  $R_H$  (Rrefhi). The unused parameters,  $\gamma_3$ ,  $a_2$ ,  $a_3$ ,  $b_1$ ,  $b_2$ , and  $b_3$  reflect the facility of the modeling routine to accept various model forms with more parameters than are presently used.

With these definitions the motivating gradient models can be given:

$$g_r = \frac{g_r^0 V}{\exp(\gamma_1 R / R_L)} \left[ 1 + \Delta \exp\left(-\frac{(t-t_0)}{\tau_0 (R/R_H)^{-\gamma_2}}\right) \right] r^{-a_1} \quad (3.3.3)$$

and

$$g_\lambda = g_\lambda^0 V \left(1 - \gamma_4 (R/R_L)^{-\gamma_5}\right). \quad (3.3.4)$$

We can define  $q(r) = r^{-a_1}$  and the remainder of Eq. 3.3.3 as  $h(t,R)$ , and using the notation and motivation leading up to Eq. 3.3.2 arrive at the model for the intensity,

$$j_i(r, \lambda, t, R) = j_{si} \exp\left[-h(t, R) \frac{r_s^{1-a_1} - r^{1-a_1}}{1-a_1} + g_\lambda(R) \lambda\right], \quad (3.3.5)$$

where the  $i$  indexes the seven particles species. It should be emphasized that in this form of the model only the normalization factors  $j_{si}$  are specific to a given type of ion, and that these factors are the same at Voyager 1 and 2. The remaining parameters apply to all of the ACR varieties, all of which are fit simultaneously.

This is the no-source version of our phenomenological gradient model. The ACR-source version is obtained simply by formally replacing  $j_{si}$  in Eq. 3.3.5 with  $j_s$ , where  $j_s$  links the normalization factors, using six (rather than seven) parameters. They are the proton, helium, and oxygen source intensities,  $j_H$ ,  $j_{He}$ , and  $j_O$ , the power

law index in total kinetic energy  $\gamma$  (nn), the exponential cutoff energy  $T_c$  ( $= AE_c$ , see section 3.5.2), and the rigidity index  $\eta$  (gamma (sic), see above). The source spectrum  $j_s$ , with the index  $i$  labeling the three source intensities ( $j_H$ ,  $j_{He}$ , and  $j_O$ ), is defined as,

$$j_s = j_{si} (T / T_c)^{\gamma} \exp(-b(T / T_c)^a), \quad (3.3.6)$$

where the  $\eta$ -dependent parameters  $a$  and  $b$  are described in section 3.5.2 and come from the termination shock source spectrum, parameterized by Steenberg and Moraal (1999). The six parameters described above are found in Figure 3.3.6 in the top row of panel (o), with the last parameter  $J_{s7}$  unused. The gradient model with the ACR-source thus requires one fewer parameters, i.e., seventeen, to simultaneously model the fourteen time-intensity ACR recovery profiles of interest.

### 3.3.3 – Format of Phenomenological Analysis

The conveyance of the results of the present analysis is nontrivial due to the density of information and the relative complexity of the model. This section attempts to address this by systematically describing the layout of Figures 3.3.4 to 3.3.6, in which a great deal of information is condensed, with not all of which the reader need concern himself. All of the comments in this subsection relate to all three of the figures in section 3.3.4, (the section where their physical significance is discussed), except where otherwise noted.

Panels (a) and (b) present 26-day averaged flux (in units of  $\text{cm}^{-2} \text{sr}^{-1} \text{s}^{-1} \text{MeV}^{-1} \text{nuc}$ ) as a function of time, from 1990-1999. The format is very similar to that of Figure 3.3.1, and the intensities are adjusted by the factors indicated next to the particle labels to clarify the presentation. Seven time-intensity profiles are displayed

in each panel, with the particle species labeled below the data by color (not order). The order of the particle data shown in these panels from the top down is H-med, H-high, He-med, O-low, He-high, O-med, and O-high, where Table 2.3.1 defines the given energy labels pertaining to energies ranging from 1 to 40 MeV/nucleon. The (red and black dashed) lines overlaid on the data, unlike in Figure 3.3.1, represent the simultaneous fit of the model to all of the data shown. Also unlike Figure 3.3.1, there is no extrapolation of the curves in these two panels, so the fitting periods are obtainable from the extent of the lines, and were selected to limit the analysis to ACR particles during the recovery period, similarly to section 3.3.1.

Panels (c) through (g) are all in the same concatenated format with the left-to-right labeling of each discontinuous segment in the following order: V1-H-med, V1-H-high, V1-He-med, V1-He-high, V1-O-low, V1-O-med, V1-O-high, V2-H-med, V2-H-high, V2-He-med, V2-He-high, V2-O-low, V2-O-med, and V2-O-high (see Table 2.3.1). Each segment represents data, variables and given values in time-order from left to right. Panel (c) shows intensities (black) overlaid with the model fit (red). Panel (d) is a plot (from top to bottom) of ion rigidity (MV, black), solar wind velocity (AU/year, red), nucleon energy (MeV/nucleon, blue), and particle velocity relative to the speed of light (green), all plotted on the same logarithmic axis. The solar wind velocity is set to 84.3 AU/year (400 km/s) throughout. The top (black) trace in panel (e) displays the  $J_{Si}$  index, which is  $i = 1, \dots, 7$  for the no-source version (Figures 3.3.4 and 3.3.5) and  $i = 1, 2, 3$  for the ACR-source version (Figure 3.3.6), as described in section 3.3.2. Also in panel (e) is the potential Compton-Getting factor  $C$ , (red) although this is set to unity throughout. Panel (f) has spatial information associated

with each of the fourteen time series with helioradius (AU) displayed on top (black), and heliolatitude (degrees) plotted below (red). The relative constancy of the V1 latitude compared with the 'rapid' change experienced by V2 is clearly seen. In the last of this set of five concatenated data panels, panel (g), the time in year associated with the data lying directly above is plotted (black). The abscissa value of panel (g), and thus the entire set of panels, is a label for each 26-day data point running from 1 to almost 1300.

Panels (h) and (i) are a set with intensity in the usual units plotted versus time from 1990 to 1999 in both cases. Panel (h) provides time-intensity profiles of 900 MV model particles at (from top to bottom) 80 AU (red), 50 AU (orange), 20 AU (green), 10 AU (blue) and 1 AU (black, if on the scale), all at the heliographic equator. Panel (i) has time-intensity profiles of particles at 50 AU and 33 degrees (in the model heliosphere) with rigidities, from top to bottom, of 3300 MV (red), 2000 MV (orange), 900 MV (green), 300 MV (blue), and 120 MV (black). Panel (j) indicates intensity vs. helioradius (AU) for 900 MV particles at 30 degrees. The spatial profiles are given, from right to left (and black to red), in the model years 1992 through 1998.

In panels (k) through (m) model heliospheres are shown, with distance above the heliographic equator (from 1 to 100 AU) plotted along the ordinates, and distance along the heliographic equator (from 1 to 100 AU) as the abscissa. (The orientation is similar to that in Figures 2.1.3. and 5.2.1) The color scale indicates particle intensity with white (and then back) the lowest flux level up through the spectrum to red, the highest flux (in arbitrary logarithmically scaled units covering about ten orders of magnitude). The multiplicative value by which the intensities are scaled to prevent

saturation or under exposure is indicated below the model heliosphere dimensions in the upper left corner of each panel. Each panel shows the intensity distribution of particles at a different rigidity, 200, 800, and 3300 MV for panels (k), (l), and (m), respectively. To the extent it makes a difference (potentially for Figure 3.3.6 alone), oxygen is the species shown. These model heliospheres will be discussed in section 3.3.4, but for orientation note in panel (m) of Figure 3.3.4, that the high intensity (red) above the solar pole and the low intensity (blue) along the equator is representative of a positive latitudinal gradient. The positive radial gradient is indicated as well by the lowest intensity region at the origin, compared with the high flux at the source radius.

The description of the phenomenological gradient model is given in panel (n) and is directly related to Eqs. 3.3.3 to 3.3.6, except for some different notation. See section 3.3.2 for more information. The parameter name lines (every third row) in panel (o) were described thoroughly in section 3.3.2, however the two rows of numbers below each parameter name and the significance of the red parameter names was not. A red parameter means that that parameter has been fixed during that run of the model and is therefore not a free parameter in this case. The numerals directly below the parameter names are the starting parameters supplied by the user (or default), from which the least squares fitting routine begins the minimization. The row of numbers below this row gives the final parameter values determined by the fitting procedure. These parameters control the shape of the fit curves in panels (a) through (c).

A few useful reference values and combinations of parameters are given in panel (p). From the top, the first value,  $R_{\text{reflo}}$ , is the low-rigidity reference value  $R_L$

(MV), and the second,  $R_{refhi}$ , is the high-rigidity reference value  $R_H$ . They are strictly for convenience and have no physical interpretation besides representing the rigidity range of the data. The third value is a combination of parameters,  $\gamma/R_L$  ( $MV^{-1}$ ), related to the rigidity dependence of the time-asymptotic radial gradient and is listed to aid certain by-hand calculations. Likewise the fourth value  $\tau_o R_H^{\gamma_2}$  ( $MV^{\gamma_2}$ ) is of little general use. The last value, however, is a physically meaningful combination  $R_c \equiv R_L \gamma_4^{1/\gamma_3}$ , and is the “critical rigidity” (MV) at which the sign of the latitudinal gradient reverses.

The final panel (q) of Figures 3.3.4 to 3.3.6 contains fitting statistics and calculated radial and latitudinal gradients. The top line lists the reduced  $\chi^2$  statistic and the number of iteration through which the fitting procedure cycled in arriving at the final results. The next three lines are related to intensity gradients. The topmost of these lines lists the non-local radial gradients (%/AU) between 50 and 70 AU at the heliographic equator in 1999 for the seven rigidities listed in the bottom row. The middle of the three bottom lines lists the non-local latitudinal gradients (%/degree) from 0 to 35 degrees of latitude at 60 AU in 1999 for the same set of seven rigidities as above. The final row lists the seven rigidities (MV) referred to above. These rigidity values were selected to coincide with the following particles, from left to right (and employing the Table 2.3.1 labeling conventions), H-med, H-high, He-med, O-low, He-high, O-med, and O-high, and can be interpreted directly as such since the gradient model depends on no particle property besides rigidity (see Eqs. 3.3.3 and

3.3.4). The (red) label in the lower right of this panel is a date/time stamp, indicating the run-time of the model procedure.

### **3.3.4 – Model Fits to Observations**

The model of Eqs. 3.3.3 – 3.3.6 has been applied to the data as discussed in sections 3.3.2 and 3.3.3. As indicated in section 3.3.2 multiple fitting methods were used to attempt to minimize the  $\chi^2$  statistic. In addition, significant effort was made to vary the initial parameters to avoid local minima, and occasionally certain parameters were fixed when it was found to improve the speed or quality of the fit. Since, in the initial stages, the model itself was varied there are an inexhaustible number of variations one could pursue. Given this, the goal set here was not to focus on aggressively scanning *model space* and parameter space, but rather to obtain as simple a model as appeared to represent the essential features of the observations well and, within this model, to arrive at parameters that bring the model into reasonable agreement with the data. For example no attempt was made to filter the high frequency variation from the data even though they are explicitly excluded from the modeling goal, since it was assumed that these variations should agree with the long term model on the average, and no advantage (besides a smaller  $\chi^2$  value) was seen in further complicating the analysis. Finally, as was discussed in section 3.3.2, during the development of the model, the first form of a particular dependence that brought the fitted curves into reasonable agreement was typically used.

First the best fit obtained is discussed, which is the no-source model with seven particle species normalizations. In Figure 3.3.4 the results of this modeling effort are summarized in a condensed format detailed in section 3.3.3. A comparison

of panels (a) and (b) of Figure 3.3.4 with both panels in Figure 3.3.1 reveals that the simultaneous model fit, with 18 parameters, agrees with the data nearly as well as the independent fits, with a total of 56 parameters. The expected feature of a delayed recovery in the inner heliosphere relative to that in the outer heliosphere for diffusively dominated transport from the outer source to the Sun (§3.2.3, §3.5, Figure 5.3.1) is retained in this model as shown in panel (h). Similarly, the expected short recovery time for high-rigidity and longer recovery time for low-rigidity particles is evident in panel (i), although perhaps somewhat exaggerated due to the possible difficulties in modeling the initial recovery, and in modeling the recovery at a fixed position, with the gradient form in use (see the discussion preceding Eq. 3.3.2). Of course since the possible dependencies are built into the model their appearance is not surprising, but the point is that the final parameters give the magnitude and sign of these features, and these are as described above.

As the model heliospheres (Figures 3.3.4k-m) make clear, the latitudinal gradient  $g_\lambda$  does not have the same sign for all rigidities. In particular at 3300 MV (22 MeV/nucleon oxygen), the highest intensity in panel (k) is above the poles, indicating a positive latitudinal gradient, while this is reversed at the two lower-rigidities (k) and (l). This determination of negative latitudinal gradients at lower rigidities is independently arrived at in section 3.4 and 3.5 as well and is a key result of this work, due to the implications for the gradient and curvature drift theory of cosmic ray transport (see section 5.2.2). (The possibility of explaining the observations with a purely positive latitudinal gradient is addressed below.) The rigidity at which  $g_\lambda$



reverses sign is  $R_c = 2430$  MV for these model parameters. This value is related to the latitudinal dependence of the drift velocity and is discussed in section 5.2.2.

The rigidity dependent time parameter  $\tau = \tau_0 (R/R_H)^{-\gamma}$ ; (see section 3.3.2) yields a value of 0.9 years for mid-value 800 MV particles, which is similar to the values found in Table 3.3.1. At  $R = 119$  MV  $\tau$  is 4.8 years, short compared with the 5- to 10- MeV proton fits, and for  $R = 3284$  MV,  $\tau$  is 0.24 years, also shorter than the comparable 1-year values from section 3.3.1. (The difference between the form of the present model  $\exp(-c(1 + e^{-t}))$  and the initial recovery portion of the fit function  $1 - e^{-t}$  is noted; however,  $\tau$  still provides a scale for the initial recovery, and in any case, the phenomenological form approaches a form similar to the recovery factor  $(1 - e^{-t})^c$  for times long compared to the  $e$ -folding time.)

The power-law dependence  $r^{-a}$  of the radial gradient yielded an index value of  $a_1 = 1.5$ . This is similar to the 1.7 value determined by Cummings *et al.* (1995) in using data from five spacecraft to fit 10 MeV/nuc ACR oxygen observations in 1993 from 1 to 60 AU. Note that the reference time  $t_0$  and the source radius  $r_s$  were fixed in the final version of the model fit as this was found to produce the best fit with parameters that were at all reasonable (i.e., fits with source radii in the thousands of AU and the like were discarded). The value of  $r_s$  was set to 100 AU, a typically estimated value, as discussed below. Note that one and then both of these parameters are free for the model results presented in Figure 3.3.5 and 3.3.6, respectively.

The spatial gradients determined by this model are given in Table 3.3.2 and in Table 3.4.1., where they are compared with the gradients resulting from direct

observations. For 3284 MV ions (such as  $\sim 20$  MeV/nucleon O) the model results in a radial gradient,  $g_r = 1.2$  %/AU and a latitudinal gradient,  $g_\lambda = 0.9$  %/degree, for model particles in the vicinity of V1 and V2 (see section 3.3.3). These compare reasonably well with the 1996, 8- to 18-MeV/nucleon ACR oxygen gradients of  $1.9 \pm 0.6$  %/AU and  $0.2 \pm 0.6$  %/degree calculated from Pioneer 10, Voyager 1, and Voyager 2 measurements (McDonald, Lal, and McGuire, 1998) and the  $2.2 \pm 0.8$  %/AU and  $1.3 \pm 0.4$  %/degree gradients from the five-spacecraft study mentioned above (Cummings *et al.*, 1995a). There are differences between the particle energies, times and locations associated with these gradients, but they should nevertheless be comparable, and they are. (Note that measured gradients with uncertainties issuing from the present work are presented systematically and listed in Table 4.4.1.) As discussed in section 3.3.2, the gradients quoted (Figure 3.3.4q and Table 3.3.2) are determined by performing non-local gradient calculations with the modeled intensity. That is, the model provides an analytical value for  $j(r, \lambda, t, R)$  given by Eq. 3.3.5, from which the time-asymptotic, non-local radial gradient between two radii  $r_1$  and  $r_2$ , at a fixed latitude  $\lambda_o$ , for particles with rigidity  $R_o$ , can be calculated:

$$g_r = \ln[j(r_2, \lambda_o, \infty, R_o) / j(r_1, \lambda_o, \infty, R_o)] / (r_2 - r_1).$$

Note that the normalization intensity  $j_{si}$  from Eq. 3.3.5 drops out of the calculation, and therefore the index  $i$  was dropped. Similarly, the time-asymptotic non-local latitudinal gradient at a fixed radius  $r_o$  between two latitudes  $\lambda_1$  and  $\lambda_2$  can be calculated for particles with a rigidity  $R_o$  from,

$$g_\lambda = \ln[j(r_o, \lambda_2, \infty, R_o) / j(r_o, \lambda_1, \infty, R_o)] / (\lambda_2 - \lambda_1).$$

It should therefore be checked that these values agree with the analytical expectations for the steady state case,  $g_r(r,R) = g_r^{\circ} V \exp(-\gamma_1 R/R_L) r^{-\alpha}$  and  $g_{\lambda}(R) = g_{\lambda}^{\circ} V (1-\gamma_4(R/R_L)^{\gamma_5})$ , from Eqs. 3.3.3 and 3.3.4. Inserting the parameters from Figure 3.3.4 we find  $g_r(60 \text{ AU}, 3284 \text{ MV}) = 1.13\%/AU$  and  $g_{\lambda}(3284 \text{ MV}) = 0.94\%/degree$ , which agree excellently with the non-local model values in Table 3.3.2. For low rigidities, we find  $g_r(60 \text{ AU}, 119 \text{ MV}) = 22.6\%/AU$  and  $g_{\lambda}(119 \text{ MV}) = -15.1\%/degree$  and note that the  $g_{\lambda}$  agrees well and  $g_r$  is not too far from the 18.8%/AU value listed on the figure. The discrepancy for the low-rigidity radial gradient is discussed in terms of non-local gradient calculations in section 3.4.1.

**Table 3.3.2 Radial and Latitudinal Gradients from the Phenomenological Model**

Species <sup>a</sup>	H <sup>+</sup>	H <sup>+</sup>	He <sup>+</sup>	O <sup>+</sup>	He <sup>+</sup>	O <sup>+</sup>	O <sup>+</sup>
<i>E (MeV/muc)</i>	8	27	6	1.3	25	6	22
<i>R (MV)</i>	119	225	436	804	867	1713	3284
<i>g<sub>r</sub> (%/AU)</i>	18.8	16.3	13.2	9.6	9.1	4.4	1.2
<i>g<sub>λ</sub> (%/degree)</i>	-15.1	-10.8	-7.1	-4.1	-3.8	-1.2	+0.9

<sup>a</sup> This model is not species dependent, so ions representative of a given *R* are shown.

The appearance of negative latitudinal gradients having been noted above, the next model result (Figure 3.3.5) addresses whether the data can be represented well with a purely positive latitudinal gradient, at all rigidities. To pursue this possibility the parameters  $\gamma_4$  and  $\gamma_5$  associated with the sign of the latitudinal gradient were fixed to prevent the gradient from being negative. The data and fits in panels (a) and (b) agree almost as well in the  $g_{\lambda} > 0$  case as in the previous case (Figure 3.3.4), except at the start of the recovery. What is more significant is the scale of the heliosphere in the model. The  $r_s$  and other parameter initial values were varied and both the Marquardt

and grid search fitting algorithms were used to arrive at the fit here (the former succeeding in this case). To best model the data the source radius had to be fixed at 240 AU, to prevent the source radius from being drawn to values orders of magnitude larger (an adequate fit could not be obtained for smaller values of  $r_s$ ). The model that provided positive gradients was nearly spherically symmetric except at higher rigidities, as can be seen in panels (k) and (l), or in the latitudinal gradient values in panel (q), which range from 0.27 to 1.55%/degree. The time profiles in panels (h) and (i) and the radial profile in panel (j) indicate a dichotomy that was also seen in section 3.2.3. The ACR recovery data that are the focus of this study can essentially be well-described by either one of two cases: the case of weak temporal variations late in the recovery and significant radial gradients, with some negative latitudinal gradients, or the case of large temporal variations with small positive radial and latitudinal gradients. Comparing these three panels (h) – (j) in Figures 3.3.4 and 3.3.5 shows these features well since the radial profile in the former case is steep, but is shallow in the later case, and the temporal dependence is flat after the initial recovery in the former case, but continually increasing in the later case.

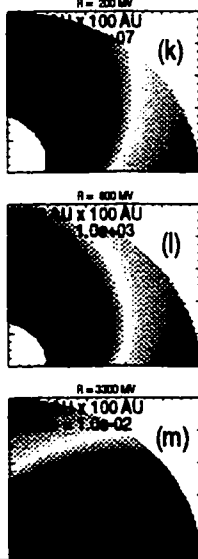
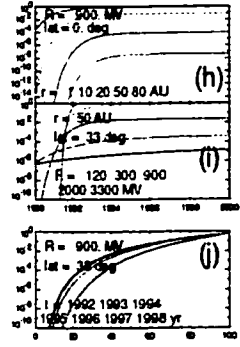
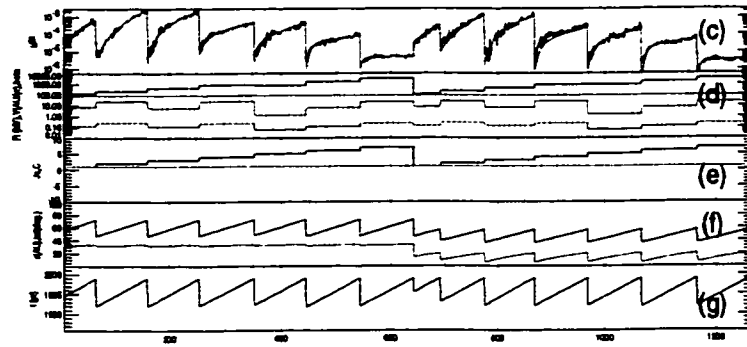
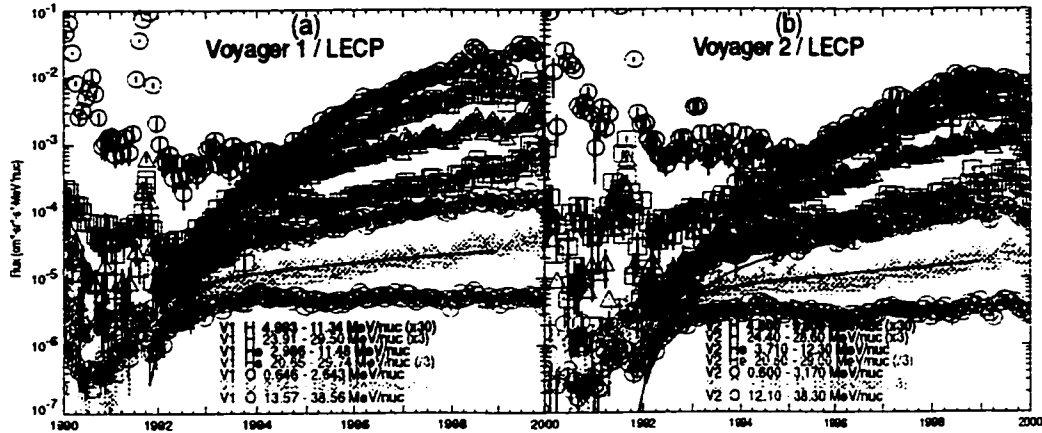
The time constants range from 3.5 to 4.4 years for 119 to 3284 MV rigidities, respectively. The weak dependence on rigidity is a feature that is not inconsistent with the dependence observed in Figure 3.3.3g, ignoring protons, but the magnitudes are roughly four times higher than those found by the fits of section 3.3.1. The latitudinal and radial gradients are in rough agreement with those of McDonald, Lal, and McGuire (1998) for 8- to 18-MeV/nucleon O, 6- to 10-MeV/nucleon He, and 10- to 20-MeV/nucleon He. The conclusion to be drawn from this version of the model is

that it can represent the ACR transport with the requirement that latitudinal gradients are positive, but that the source radius at 240 AU is significantly larger than is presently expected. For example Stone and Cummings (2001) summarize a number of studies which estimate termination shock radii that cluster in the 80- to 100-AU range. Also the initial recovery is somewhat more poorly matched with the  $g_{\lambda} > 0$  model, but the resulting gradients generally agree with those of McDonald, Lal, and McGuire (1998).

In the final version of this model (Figure 3.3.6) an attempt to model the anomalous cosmic ray source spectrum is made. Using the parameterized form of Steenberg and Moraal (1999) given by Eq. 3.3.6 the relative intensities between particles of different energies are linked with parameters common to all three ACR species. The resulting fits were obtained by grid search as the gradient-expansion method was producing poor fits or not converging at all. When the fit routine with initial parameters listed in Figure 3.3.6 was iterated for more times than for this output the reduced  $\chi^2$  could be reduced from 11.5 to about 9.5, but these fits began to represent the data less well in all but the technical sense. The resulting fits shown in panels (a) and (b) are of noticeably poorer quality than for the two previous versions of the model, although the general features are still represented to a large degree as the display in panel (c) demonstrates. Many of the parameters are more similar to the Figure 3.3.4 model than the Figure 3.3.5 model. For instance, the  $e$ -folding times vary from 0.14 to 6.1 years which is similar to the former model, but with an even larger range, unlike the latter model which had a narrower range of times. The source radius  $r_s$  and time reference  $t_0$  are both free but stayed near the starting values with  $r_s = 98$

**AU. The gradients in panel (q) are similar to the first model, but the latitudinal gradient sign reversal occurs at a somewhat lower rigidity of 1830 MV (vs. 2430 MV). The source characteristics are as follows. The power law index in energy  $\gamma$  (-nn) is -1.5 and the rigidity index  $\eta$  (gamma) is -0.3 (see comments on notation in section 3.3.3). Also the cutoff energy is 57 MeV. The inability to obtain a higher quality fit leaves the interpretation of these source parameters a bit in question, so discussion of these values is postponed until section 3.5.4 when a comparison is made with the spectral properties obtained by solving the cosmic ray transport equation.**

**A Phenomenological Intensity-Gradient Model of ACR Recovery**  
 Best fit, source radius and reference time fixed, no model for ACR source.



$gr\_CVRbeta = grinf * C * V * exp(-gamma * (R/Rreflo))$   
 $gr\_tR = 1. + delta * exp(-(t-to)/tauo) * ((R/Rrefhi)^{gamma2})$   
 $INTgrdr = (hrTS * (1-a1) - hr * (1-a1)) / (1-a1)$   
 $gl\_CVRbeta = glo * C * V * (1 - gamma4 * (R/Rreflo)^{gamma5})$   
 $gl\_hr = 1$   
 $j = js * exp(-gr\_CVRbeta * gr\_tR * INTgrdr + gl\_CVRbeta * gl\_hr * t)$

**No Model for ACR Source**

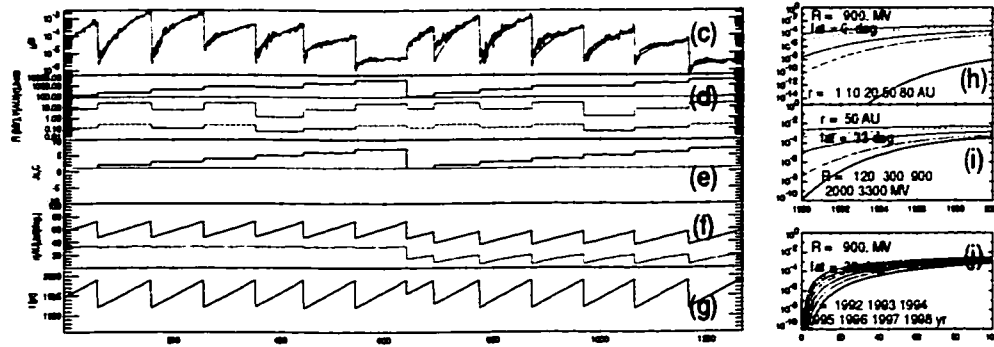
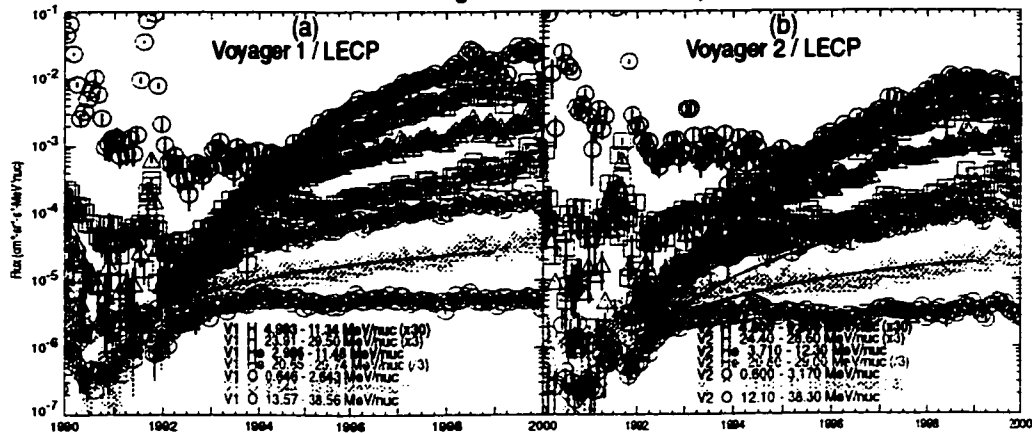
hrTS	Js1	Js2	Js3	Js4	Js5	Js6	Js7
1.00E+02	1.29E-01	1.39E-01	2.72E-02	1.76E-03	1.93E-03	1.93E-04	5.36E-06
1.00E+02	1.99E+00	1.30E+00	2.14E-01	7.71E-03	7.27E-03	2.34E-04	4.53E-06
grinf	glo	delta	to	tauo	Rreflo = 119.0		
8.82E-01	1.33E-04	9.00E-01	1992.57	6.50E-01	Rrefhi = 3335.0		
1.09E+00	1.41E-03	3.31E-01	1992.57	2.42E-01	gamma1/Rreflo = 8.56e-04		
1.00E-01	1.00E-01	1.90E+00	1.20E+01	1.30E+00	Tao * Rrefhi^gamma2 = 353.6		
1.02E-01	8.98E-01	1.90E+00	2.27E+00	2.72E-01	Rreflo^gamma4 * (1/gamma5) = 2428.7		
a1	a2	a3	b1	b2	b3		
1.71E+00	9.44E-01	1.18E+01	0.00E+00	3.47E-01	1.00E+00		
1.51E+00	9.44E-01	1.18E+01	0.00E+00	3.47E-01	1.00E+00		



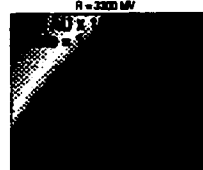
red. chisq, iter = 3.18 82  
 $gr(50 \rightarrow 70 \text{ AU}, 0 \text{ deg}) = 18.77 \ 16.26 \ 13.22 \ 9.61 \ 9.10 \ 4.41 \ 1.15 \ \%/AU \ \text{in } 1999.0$   
 $gl(60 \text{ AU}, 0 \rightarrow 35 \text{ deg}) = -15.06 \ -10.78 \ -7.06 \ -4.16 \ -3.83 \ -1.18 \ 0.93 \ \%/deg \ \text{in } 1999.0$   
 $R(MV) = 119 \ 225 \ 436 \ 804 \ 867 \ 1713 \ 3264$

Thu Oct 25 15:54:35 2001

**Figure 3.3.4 Phenomenological Model Summary—Best Fit Without Source Model**  
 A summary of the best fit model without an ACR source model. See section 3.3.3 for a complete description of this format. The source radius and reference time are fixed.

**A Phenomenological Intensity-Gradient Model of ACR Recovery**  
**Best fit with latitudinal gradient forced to be positive.**



$gr\_CVRbeta = grint * C * V * exp(-gamma1 * (R/Rreflo))$   
 $gr\_tR = 1. + delta * exp(-(t-to)/tauo) * ((R/Rrefhi)^{gamma2})$   
 $INTgrdr = (hrTS * (1-a1) - hr^{(1-a1)}) / (1-a1)$   
 $gl\_CVRbeta = glo * C * V * (1 - gamma4 * (R/Rreflo)^{gamma5})$   
 $gl\_hr = 1$   
 $j = js * exp(-gr\_CVRbeta * gr\_tR * INTgrdr + gl\_CVRbeta * gl\_hr * t)$

**No Model for ACR Source**

hrTS	Js1	Js2	Js3	Js4	Js5	Js6	Js7
2.40E+02	4.55E+00	2.67E+00	4.16E-01	1.31E-02	1.26E-02	3.25E-04	4.97E-06
2.40E+02	4.36E-03	1.15E-02	7.14E-03	1.04E-03	8.00E-04	1.04E-04	4.35E-06
grint	glo	delta	to	tauo	Rreflo = 119.0		
7.71E-01	1.93E-03	2.54E-01	1992.57	2.54E-01	Rrefhi = 3335.0		
7.96E-02	3.16E-04	4.86E-02	2008.63	4.42E+00	gamma1/Rreflo = 5.55e-04		
9.73E-02	7.79E-01	1.90E+00	9.00E-01	2.31E-01	Tao*(Rrefhi)^{gamma2} = 2.6		
6.61E-02	-6.73E-02	1.90E+00	9.00E-01	2.31E-01	Rreflo^{gamma4}/(1/gamma5) = 75.4		
a1	a2	a3	b1	b2	b3		
1.41E+00	9.44E-01	1.16E+01	0.00E+00	3.47E-01	1.00E+00		
1.38E+00	9.44E-01	1.16E+01	0.00E+00	3.47E-01	1.00E+00		

**red. chisq, iter = 3.89 151**  
 $gr(50 \rightarrow 70 \text{ AU}, 0 \text{ deg}) = 3.89 \ 3.50 \ 2.98 \ 2.34 \ 2.25 \ 1.36 \ 0.55 \ \%/AU \text{ in } 1999.0$   
 $gl(60 \text{ AU}, 0 \rightarrow 35 \text{ deg}) = 0.27 \ 0.58 \ 0.89 \ 1.12 \ 1.15 \ 1.37 \ 1.55 \ \%/deg \text{ in } 1998.0$   
 $R(MV) = 119 \ 225 \ 436 \ 804 \ 867 \ 1713 \ 3284$

**Figure 3.3.5 Phenomenological Model Summary—Best Fit with  $g_\lambda > 0$**   
 A summary of the best fit model with the latitudinal gradient forced to be positive. See section 3.3.3 for a complete description of this format. The source radius is fixed.



**A Phenomenological Intensity-Gradient Model of ACR Recovery  
Best fit with an ACR source model.**

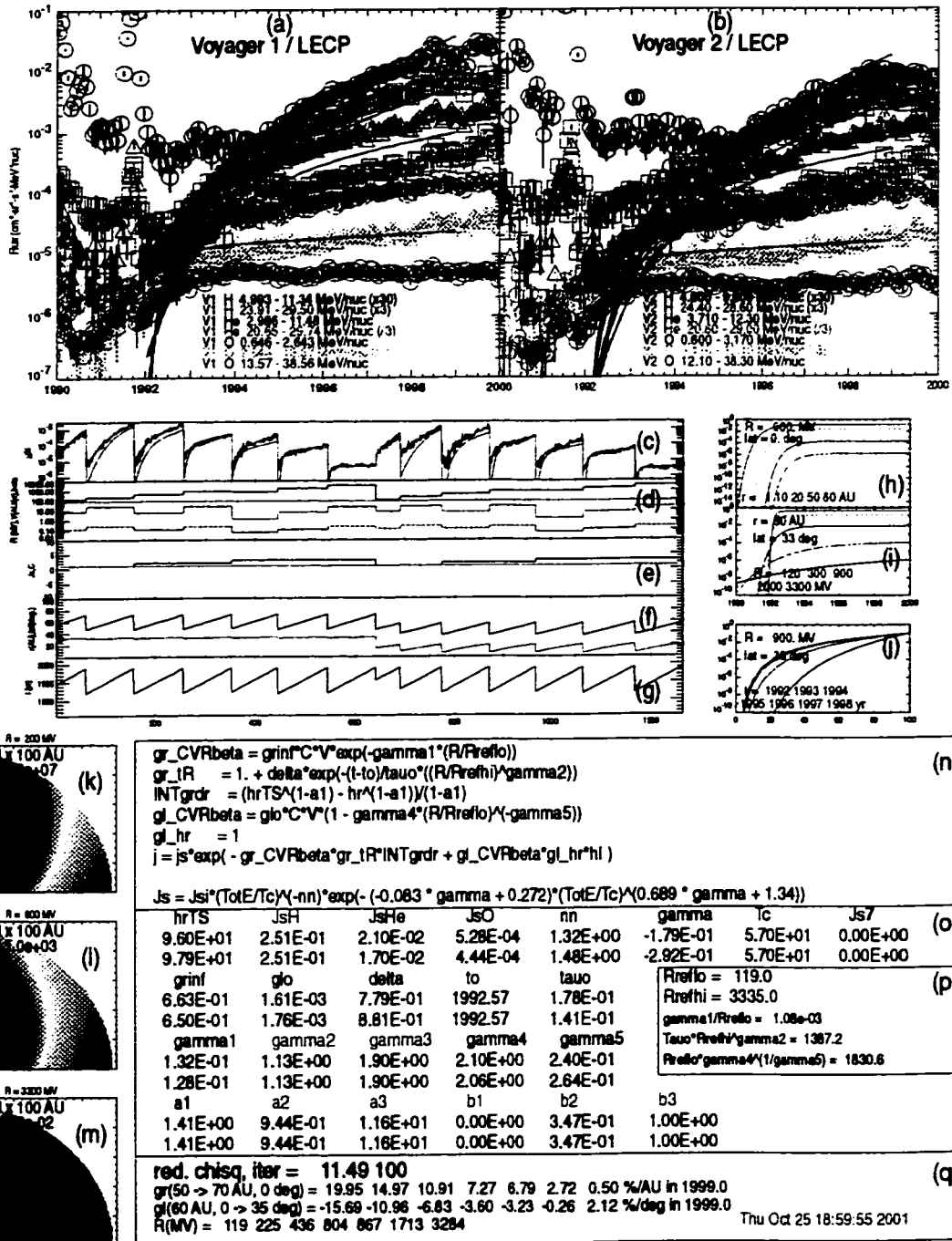


**Figure 3.3.6 Phenomenological Model Summary—Best Fit with Source Model**  
A summary of the best fit of the version of the model that includes a parameterized ACR source spectrum. See section 3.3.3 for a complete description of this format.

### **3.4 – Radial and Latitudinal Intensity Gradients**

The understanding of particle populations in the heliosphere requires a method to measure the manner in which the particle intensities vary with position. The notion of intensity gradients addresses this issue. Were there swarms of spacecraft surveying the heliosphere, a simple way to proceed would be to plot intensities at a given time against some spatial variable, say,  $x$ . Then an analytical fit  $j(x)$  to these data would allow the subsequent differentiation  $\partial j/\partial x$  to provide the information sought. Of course in this fantastic scenario the multiplicity of measurements would render such a crude estimate of spatial morphology unnecessary. In reality there are seldom more than a few spacecraft and, in the outer heliosphere, the distances are sufficiently enormous to provide added complications. What follows is a discussion of the traditionally employed non-local intensity gradient method, an apparently novel “quasi-local” intensity gradient method, and the results of their use as applied to the anomalous cosmic ray problem.

#### **3.4.1 – Non-local Intensity Gradients**

In the case of two spacecraft sharing a common position in two (physically meaningful) dimensions, such as heliolatitude  $\lambda$ , and heliolongitude, but differing in another such dimension, such as helioradius  $r$ , there is a straightforward way to proceed with a gradient measurement. (Note by physically meaningful it is meant to distinguish an arbitrarily defined coordinate system from one that is related to the symmetry of the system under study. In the case of the heliosphere, spherical coordinates are an obvious choice, although cylindrical and elliptical coordinates, for example, could also have their uses. Also note that azimuthal symmetry is assumed in

what follows, so no mention of longitude will be made.) The relevant measured quantities are the intensities  $j_1$  and  $j_2$ , (where the subscripts label the observation points throughout this section), the radii  $r_1$  and  $r_2$ , and the latitudes, in this case equal,  $\lambda_1 = \lambda_2 \equiv \lambda_0$ . If the relative gradient at a given intensity level is desired, one would like to calculate the theoretical radial gradient  $g_r^{\text{th}} \equiv (1/j)\partial j/\partial r = \partial \ln j/\partial r$ . For the case of the two spacecraft this can be estimated by

$$g_r \equiv \frac{\ln(j_2/j_1)}{r_2 - r_1}, \quad (3.4.1)$$

since there is no difference in the latitudes, by assumption. (Henceforth the *th* superscript will be omitted.) This measurement  $g_r$  is the gradient neither (necessarily) at the point  $(r_1, \lambda_1)$  nor  $(r_2, \lambda_2)$ , but is a *non-local* gradient determination between the two positions (see Potgieter, le Roux, and Burger, 1989). This formulation can be rewritten alternatively, for  $j = j(r)$  as,

$$\frac{dj}{j} = \frac{1}{j} \frac{\partial j}{\partial r} dr = \frac{\partial \ln j}{\partial r} dr \equiv g_r dr, \quad (3.4.2)$$

where the radial gradient is defined implicitly in the last step, and reduces in the same way as above to Eq. 3.4.1 in the discrete case.

The formulation of Eq. 3.4.2 suggests a generalization to the case of three or more spacecraft having more than one dimension with non-equal coordinates. For two-dimensions with radial and latitudinal coordinates this becomes, for  $j = j(r, \lambda)$ ,

$$\frac{dj}{j} = \frac{1}{j} \frac{\partial j}{\partial r} dr + \frac{1}{j} \frac{\partial j}{\partial \lambda} d\lambda = \frac{\partial \ln j}{\partial r} dr + \frac{\partial \ln j}{\partial \lambda} d\lambda \equiv g_r dr + g_\lambda d\lambda.$$

This form, which, as discussed in section 3.3.2 remains strictly consistent for  $g_r = g_r(r)$  and  $g_\lambda = g_\lambda(\lambda)$ , is relevant to much of the work in sections 3.3 and 3.4 and, will therefore be rewritten succinctly as,

$$\frac{dj}{j} = g_r dr + g_\lambda d\lambda, \quad (3.4.3)$$

for easy reference. For a three-spacecraft array with  $g_r$  and  $g_\lambda$  assumed to be constants, we integrate Eq. 3.4.3 between any two spacecraft pairs, obtaining the set of two equations in the two variables  $g_r$  and  $g_\lambda$ , given below:

$$\begin{aligned} \ln(j_2 / j_1) &= g_r (r_2 - r_1) + g_\lambda (\lambda_2 - \lambda_1) \\ \ln(j_3 / j_2) &= g_r (r_3 - r_2) + g_\lambda (\lambda_3 - \lambda_2) \end{aligned} \quad (3.4.4)$$

The number of spacecraft (or other observers) needed is always one more than the number of constants since the intensities enter as ratios between pairs of spacecraft. The forms of Eqs. 3.4.3 and 3.4.4 and the general method of non-local gradients have been used by many investigators to great effect for years (e.g., McKibben, 1989, and references therein; McDonald *et al.*, 1997; Cummings, Stone, and Webber, 1987). It can be generalized to variable gradients given sufficiently numerous spacecraft, and yields gradient measurements for each chosen time interval, without reference to the time variable, therefore in addition to being non-local the method is *time-independent*, which is a considerable freedom.

The non-local gradient method is appropriately used under a common set of circumstances, in which a number of suitable spacecraft are available, the gradients (or the spatial separations) are relatively small, and the form of the spatial gradients are well understood. The problem of an insufficient number of spacecraft is self evident,

and depends on the application. The problems caused by a complicated variable form of the spatial gradients are also rather understandable, and related to the previous problem in that more complicated non-constant gradient forms can be modeled with additional free parameters, requiring additional spacecraft. This issue is also related to the need for a small gradient, or close separation. These conditions essentially require, in the cases when the gradients have a complicated form, that the spacecraft separation be of order or less than the scale length (or scale-angle) over which significant change in the intensity level occurs. This is essentially a statement of the mathematical problem of estimating the derivative of a continuous curve by a difference quotient between discrete points; clearly a “slowly” varying function can be reasonably represented this way, while a rapidly changing function would require the discrete points to be closer together for there to be a sensible estimate. Another manifestation of this scale-length problem involves spatial profiles that are potentially time dependent. When the non-local method is applied outside of its regime of validity a result indicating an apparent temporal variation can in actuality be due to a spatial variation resulting from the motion of the spacecraft. In section 3.4.4, the discussion of Figure 3.4.11 and Table 3.4.2 addresses this very problem.

For cosmic rays with energies above that of the LECP instruments, these three conditions are generally met. Galactic cosmic rays and higher-energy anomalous species typically have relatively small gradients (in cycle 22, and the spacecraft were more closely spaced in cycle 21). These gradients can self-consistently be determined, and there are measurements during previous solar cycles to fill in some gaps. During at least part of solar cycle 22 there were four outer heliospheric spacecraft with

instruments capable of measuring the higher-energy particles, the two Voyagers, Pioneer 10 and 11. The inner heliosphere is well-covered as well, with Ulysses, ACE, SAMPEX, Wind, and the IMP satellites all suitable for these measurements. Moreover the theory of cosmic ray modulation is somewhat simpler at higher energies, amenable to limiting solutions of the cosmic ray transport equation (Parker, 1965) such as the force field approximation (Gleeson and Axford, 1968; see section 3.5.2), providing a greater understanding of the form of the spatial gradients.

Compare these high-energy cosmic ray conditions with those of ACRs, particularly at the lowest energies, and one begins to see the possibility that the non-local method is not appropriate to much of the present study. ACR particles at lower energies often undergo substantial modulation compared to GCRs and thus typically have large spatial gradients. This result can also be found self-consistently with the method described in section 3.4.2. Fewer spacecraft have instruments with energy ranges comparable to LECP. The author presently has access only to ACR data from the three positions (V1, V2, and 1-AU) included in this study (although the Ulysses spacecraft might provide suitable measurements as well). In fact, until recently (Hill *et al.*, 2001), low-energy time-intensity measurements at the third, near-Earth region were unavailable throughout the recovery period due to the difficulty of measuring the typically low ACR intensities amidst the residual interplanetary ions prevalent at 1-AU even at solar minimum. Moreover these spacecraft are widely separated from one another, and there is very little information on the form of the intervening spatial morphology. Finally the transport theory of low-energy anomalous cosmic rays is complicated, lacking the approximations useful at higher energies.

An example from section 3.3.4 in discussing the model results shown in Figure 3.3.4 demonstrates the problems associated with the non-local gradient when applied outside of the conditions of validity. The disagreement between the empirically determined non-local gradient and the analytically determined gradients for the case of the low rigidity radial gradient is precisely the expectation resulting from the discussion presented above; i.e., that the non-local gradient method (when restricted to three spacecraft) works well when the spatial gradient is small or well-understood (like the high-rigidity gradients or constant low-rigidity latitudinal gradient in section 3.3.4) and works less well when the gradient has a more complicated form (i.e., the low-rigidity, large radial gradient with power law dependence on radius in the same section). It is emphasized that the comparison is peculiar to the V1, V2, and 1-AU array accessible to the author, as discussed above, since with other sets of spacecraft or species the non-local method has quite properly been used to determine variable gradients (see the example of  $g_r = G_0 r^{-a}$  in section 3.4.2, and references therein).

These considerations have necessitated a search for alternative means through which to measure the ACR spatial gradients. In particular, the ability to measure both the radial and latitudinal intensity gradients of ACRs with just the two Voyagers is desirable, but unattainable with the time-independent, non-local gradient method. Even though V1 and V2 are themselves widely separated from each other, the oft used simplifications of azimuthal and north-south symmetry bring the two spacecraft effectively into reasonably close proximity. Ignoring longitudinal variations is an assumption the present work shares with most cosmic ray studies (see Fichtner, de Bruijn, and Sreenivasan, 1996 for an exception) and is justified for 26-day averaged

data since variations on time-scales shorter than the solar rotation period, effects of which propagate throughout the heliosphere, are averaged. Also, for V1 and V2, both spacecraft are similarly positioned with respect to the heliospheric apex, so non-spherical global heliospheric effects should be relatively small between these two probes. The assumption of north-south symmetry is as well frequently used, and although some evidence of an asymmetry exists (Simpson, Zhang, and Bame, 1996), it is not clearly established (Cummings et al., 1997), and assuming symmetry is the best starting assumption in any case. With these considerations in mind, use of the V1-V2 pair avoids most of the difficulties specified for ACRs above, but the vast separation from 1-AU to the Voyagers is still problematic. In the next section a solution to the problem of using fewer than three spacecraft to measure two simultaneous gradients is presented which additionally provides a “quasi-local” quality to the gradients, but at the expense of time-independence.

### **3.4.2 – Quasi-local Intensity Gradients**

The validity of the non-local method to measure some of the anomalous cosmic ray intensity gradients under the conditions present for this study is placed into question in section 3.4.1. All of the problems stem from one notion, that of making necessary spatial assumptions to enable the gradient calculation (that the radial gradient  $g_r$  should remain constant throughout the region probed by the spacecraft is a direct example). Although calculating spatial gradients based on a foundation of spatial assumptions is a natural choice, it is not the only choice—temporal assumptions may analogously be made. Indeed when the time dependence of the



particle distribution is better-understood than the spatial dependence, one should rely more heavily on assumptions concerning the former than the latter, and vice versa.

First we shall consider the steady-state case. It will be argued below that this considerable simplification is a quite reasonable choice during much of the recovery period, but the general method does not rely on the steady-state assumption.

Successful application of the following method requires that at least one of the spacecraft involved be moving in each of the dimensions of interest. For the case of constant radial and latitudinal gradients one of Eqs. 3.4.4 may be written,

$$\ln\left(\frac{j(r_2, \lambda_2)}{j(r_1, \lambda_1)}\right) = g_r \Delta r + g_\lambda \Delta \lambda,$$

where  $\Delta r = r_2 - r_1$  and  $\Delta \lambda = \lambda_2 - \lambda_1$ . Unlike Eqs. 3.4.4 however, here the steady-state assumption allows the numerator and denominator to be intensities at different times, as well as positions. Inserting this explicitly and dividing by  $\Delta r$ , we get,

$$\frac{1}{\Delta r} \ln\left(\frac{j(r_2, \lambda_2, t_2)}{j(r_1, \lambda_1, t_1)}\right) = g_r + \frac{\Delta \lambda}{\Delta r} g_\lambda. \quad (3.4.5)$$

It should be emphasized that the left-hand side is not a radial gradient in general, although its dimensionality is such, because the latitudes are generally different.

Equating  $y$  with the left hand side of Eq. 3.4.5 and  $x$  with the ratio  $\Delta \lambda / \Delta r$ , a simple linear relationship obtains:

$$y = g_\lambda x + g_r. \quad (3.4.6)$$

So, for each pair of events,  $(r_1, \lambda_1, t_1)$  and  $(r_2, \lambda_2, t_2)$ , in the heliosphere an associated point in the  $xy$  plane can be calculated from the intensities and coordinates. It has recently come to our attention that Paizis *et al.* (1995) have independently employed a

method based on Eq. 3.4.6 to analyze Ulysses/KET data. Given a set of observations  $j_i = j(r_i, \lambda_i, t_i)$  it is then possible to construct an  $xy$  scatter plot from various pairs of measurements and to observe the correlation. Note, importantly, that a particular pair of observations need not be from separate spacecraft, since it is events not spacecraft that are paramount here. For this reason, the name *quasi-local* is suggested for the gradients described here since some of the constituent pairs are between points lying along the trajectory of a single vehicle, with a minimum separation in space prescribed only by the sampling period of the data. Yet even to this level of resolution the method does not yield spatial gradients that are purely local since some pairs may be separated by a long distance along a trajectory or perhaps a greater distance between spacecraft. This method is also time dependent in the sense that the results provide an average over a period of time that is large compared to the intensity averaging period. It is in this sense that the non-local gradients have been considered time-independent since merely the duration of a single sampling period is required, without direct involvement of time. However the time dependent term seems liable to confuse since it might suggest that the time dependence of a temporally varying gradient is measurable with the method described in this section.

To bring the comparison into sharper relief, consider that the non-local gradient is a time-independent method that relies primarily on spatial assumptions to provide fine time resolution gradients that are however averaged over a large distance. Conversely, the quasi-local method is a time-dependent method that relies primarily on temporal assumptions to provide finer spatial resolution gradients that are however averaged over a longer period of time.

For the two-spacecraft case of V1 and V2, pairs of measurements could be selected randomly arriving at a subset of possible pairs from which to generate the  $xy$  data, but the method used here was simply to calculate  $x$  and  $y$  for every possible combination of pairs (since present desktop computer speeds make this calculation a painless procedure). Then a linear least-squares fit is performed, and the gradients are extracted as the slope ( $g_\lambda$ ) and intercept ( $g_r$ ) of the fit line. The method is essentially self-checking in that a non-linear cluster of data points would indicate that the assumptions, (here the constancy of both gradients), need adjustment. A strength of this quite simple procedure is that more general forms for the gradient can be accommodated. For example, for  $g_r = G_0 r^{-a}$  (Cummings *et al.*, 1995a; Fujii and McDonald, 1997; and references therein) and with a constant time dependence  $g_t$ , we integrate just as we did in arriving at Eq. 3.4.4, and get:

$$\ln\left(\frac{j_2}{j_1}\right) = G_0 \frac{r_2^{1-a} - r_1^{1-a}}{1-a} + g_\lambda \Delta\lambda + g_t \Delta t.$$

Clearly this is more complicated than Eq. 3.4.6, but is in principal no different than before. Here, define  $f = \ln(j_2/j_1)$ , where a multivariate fit to  $f = f(r_1, r_2, \Delta\lambda, \Delta t)$  can be performed to obtain the parameters  $G_0$ ,  $a$ ,  $g_\lambda$ , and  $g_t$ . For any reasonably sized data set there will be sufficient degrees of freedom since the number of pairs goes as the square of the number of data points.

Having already treated the ACR problem with a method involving a sizable number of parameters (§3.3), simplicity is opted for here, although not quite the simplest, steady-state case discussed above. It is desirable to remove the temporal dependence from the recovery profiles discussed in section 3.3.1. During solar cycle

22 there is ample evidence to suggest that cosmic ray phenomena resulting from transport and solar cycle variations are well-represented by the  $1 - e^{-r}$  form (referred to as the recovery or initial recovery factor in section 3.3.1). Essentially all cycle 22 anomalous and galactic cosmic rays—over the large range of energies for which modulation is significant—that have been discussed in the literature are of this recovery form (McDonald et al., 2000b; Selesnick et al., 2000; Stone et al., 1999; Krimigis et al., 1997). This includes cosmic rays studied at spacecraft from the outer to the inner heliosphere and ground-based observations as well. During cycle 22, cosmic rays are nearly universally seen to recover rapidly at first and then slowly, often approaching an asymptotic intensity value. The prevalence of this form, although quite suggestively general, is not conclusively known to persist down to the low energies we have analyzed. However, the distinct transitions of the ACR recoveries in section 3.3.1 from the initial recovery forms to the sustained exponential growth forms, even down to rarely studied low energies, also support the hypothesis that the two periods are controlled by different phenomena: temporal and spatial, respectively. Moreover, the exponential growth form is a well known solution ( $\sim e^{Vr/\kappa}$ ) to both the simple steady state convection-diffusion transport equation and the more realistic ( $\sim e^{CVr/\kappa}$ ) force field approximation of the Fokker-Planck equation (Gleeson and Axford, 1968; see section 3.5.2) and is observed in solutions to sophisticated numerical models (e.g., Potgieter, le Roux, and Burger, 1989; Jokipii, 1990; Potgieter and Moraal, 1985). In section 3.5.4 it is directly seen that spatial-gradient-induced exponential profiles following a short initial recovery quite naturally arise in the spherically symmetric solution. Also, the reproduction of such time-profiles (with

recovery and growth phases) by the physically based phenomenological model (§3.3.3) lends further support. Finally *a posteriori* it is seen that the assumption is consistent across all of the techniques used herein, all of which have similar quantitative results.

Therefore, the procedure we adopt is to first apply the quasi-local gradient method to the late period of the recovery, when temporal effects are at a minimum, and then to apply this method to data that have had the  $1 - e^{-t}$  dependence subtracted. In this way it is possible to ascertain to what degree the gradient determination is dependent on this subtraction. In both cases the steady-state method is applied; no more complicated form than this was found to be needed, an encouraging result in and of itself.

### **3.4.3 – Analysis and Format of Gradient Results**

Section 3.4.4 contains summary plots presenting the results of the quasi-local gradient analysis. In Figures 3.4.1 to 3.4.9 the unmodified and “time-subtracted” flux profiles are presented along with five  $xy$  plots as in Eq. 3.4.6, and calculated gradient values and statistics. The format of the summary plots is described below, along with some of the details of the analysis.

Panels (a) and (b) are flux vs. time plots, as indicated. Four types of profiles are displayed in each panel, for the particles with energies labeled above each panel. (The color is coded to the species: green for oxygen, blue for helium, and red for protons.) The colored symbols are the unmodified data, just as they appear in section 3.2.1. Overlaid on these data is a black solid line which is simply an exponential fit to the data over the period indicated by the fit line itself and by colored bars at the

bottom of the plot, just above the time axis. Below the unmodified data and exponential fit are black symbols. These symbols are the modified, time-subtracted data, which are additionally divided by ten to reduce a cluttered appearance. By time-subtracted what is meant is that the unmodified data  $j$  are divided by the initial recovery portion of the fitted functions from section 3.3.1,  $1 - \exp(-(t-t_i)/\tau)$ , extrapolated to cover the entire recovery period, removing the time-dependence of the recovery (by assumption, see 3.4.2) and leaving only the intensity variation due to spacecraft motion. Finally the colored line overlaying the time-subtracted data is the exponential growth factor  $\exp((t-t_i)/T)$ . In all cases where reference is made to the recovery fit function or its constituent factors, the parameters in Table 3.3.1 are those which are used. These parameter values are also listed below panels (a) and (b), to the right of the “params =” label, and associated with the parameters by the following order, from left to right,  $V1-j_a$ , 1.0,  $V1-t_i$ ,  $V1-\tau$ ,  $V1-T$ ,  $V2-j_a$ , 1.0,  $V2-t_i$ ,  $V2-\tau$ , and  $V2-T$ . The unit values in the second and seventh positions are the coefficients  $\Delta$  of the “ $\tau$ -exponent” in the recovery fit function from section 3.3.1; i.e., this coefficient is always unity and can be ignored henceforth in this section (note that a similar coefficient appears in section 3.3.2, wherein it is not unity). The “spatial =” and “removetime =” labels below the parameter line are not used here.

Panels (c) - (g) are  $xy$  plots, or quasi-local gradient (QLG) plots, as in Eq. 3.4.6. The ordinate has units of radial gradient (%/AU) but is in fact the ratio of the intensities at two space-time events (which in general do not have any coordinates that are equal) divided by the radial separation. The abscissa is the ratio of the latitudinal and radial separations. As shown in section 3.4.2 the slope of a line in this plane

represents the latitudinal gradient and the  $y$ -intercept is the radial gradient. Since all possible pairs of events have been used, there are many thousands of data points. To prevent overexposure, a two-dimensional histogram has been employed with 0.02 degree/AU bins along the  $x$ -axis and 2%/AU bins along the  $y$ -axis, as listed below panel (g). Note that a one-bin-wide frame around these QLG plots, representing the end-most bin along each side of the plot, contains overflow counts for points that are outside the plot range. Note also that this is *not* the cause of the thin peak very near the left-hand side of most of these plots. This peak is dominantly due to the pairs of events purely along the Voyager 1 trajectory, since  $\Delta\lambda$  is very small (see Table 2.1.1) at that spacecraft. The period of time from which the event-pairs are drawn is listed at the bottom of each QLG plot.

Each of the QLG plots involve data used in different ways. In panel (c) the unmodified data—colored symbols in panels (a) and (b)—are used to calculate all event pairs within the period prescribed by the colored bars at the bottom of panels (a) and (b), and the resulting QLG plot is plotted. The data in this panel typically display a clear linear correlation between  $x$  and  $y$ , but also have quite a bit of spread in two separate areas near 0.05 and 0.5 degrees/AU. These regions are dominantly V1 and V2 self-pair data (written V1-V1, and V2-V2), and the spread is expected, as it is due to the high-frequency variations (see Chapter 4), which have not been removed from the data in this plot. These raw data have been retained because if short time-scale variations are the cause of the spread as is expected, the average over these variations should still display a trend that indicates the spatial gradients (if the constant gradient assumptions leading to Eq. 3.4.6 hold, which they seem to quite well). It will be seen

in general that the unmodified data in panel (c) do result in gradient values that are similar to the computations resulting from the trend-only data, and this lends added support to the analysis.

The inset panel (d) is related to panel (f) and will be discussed at that time. Panel (e) is based on the exponential fits to the raw data—black lines in panels (a) and (b)—and is the first example of QLG analysis of the data trend. The calculation is just like the standard one described above, except that, rather than using the observed intensity at a given time, the intensity is substituted with the value of the exponential fit to the data at that time. As should be the case, the large spread apparent in panel (c) is not seen here. The data in this panel are typically associated with quite good fits with higher correlation coefficients.

Panel (f) is associated with the time-subtracted data—black symbols in panels (a) and (b)—and includes a larger time period since the time-subtraction minimizes the need to avoid the time-varying early recovery period. Since the panel (a) and panel (b) data include only times from later in the recovery when spatial effects dominate, the gradient determinations for the unmodified and time-corrected data should agree reasonably well, and this is seen as is discussed below. Panel (d), the inset in panel (c), is a subset of the QLG plot in panel (f). In (d) only event-pairs involving both spacecraft are plotted, such that every pair involves a V1-V2 intensity ratio (explaining the label on the bottom). This data subset provides a check on the possibility that the self-pair data, particularly the V1-V1 data, are skewing the fits. That is, it would be preferable if the fit to the V1-V2 data agrees with the fit to all of the data, since this would indicate that the alignment of the fit curve with the V1-V1



peak is not *merely* due to the weight of the V1-V1 data but to a more fundamental alignment, suggesting the constant-gradient assumption is reasonable over the effective distance between the spacecraft. It should be pointed out that linear correlations are not seen in general when the QLG method is used on potentially time-varying periods, as is seen in Figure 3.4.10, in which such a period is analyzed for illustrative purposes.

The last panel (g) is another form of the fit-to-trend used in panel (e). This time the exponential growth fit—the colored lines in panels (a) and (b)—is used directly to generate event-pairs and the QLG plot. That is, the calculation is made as usual except that the value of the exponential growth factor fit from section 3.3.1 replaces the observed intensity at each given time. This results in a narrower peak than in panel (f) and larger correlation coefficients, but typically gradient measures are near those of the other methods.

To the right of each of the five panels (c) – (g) are five sets of text, each with six constituent lines. Each of these five groups has the same format, as follows. Line (1) lists the radial gradient and uncertainty resulting from a linear least-squares fit to the QLG data in the adjacent plot. On line (2) the latitudinal gradient and error are similarly listed. The reduced  $\chi^2$  statistic and the linear correlation coefficient are given in line (3). Line (4) is again the radial gradient, but this time determined by a least absolute deviation method that is less dependent on outlier data. Below, in line (5) of each group of text is the latitude gradient from the least absolute deviation method along with “N” the number of data points at each spacecraft (i.e., the same

number of data points exist at each spacecraft). On the last row, line (6), the least absolute deviation statistic and the total number of degrees of freedom are listed.

Below the text described above, in the lower right corner of the figure, is the last five line block of text, supplying a summary. Line (1) is a summary title indicating the averages below include both the linear least-squares and the least absolute deviation results from panels (c), (e), (f), and (g). Line (2) gives the mean radial gradient derived from the four listed above, along with the associated standard deviation. The midpoint and half spread of the radial gradients are listed in line (3). On line (4) the mean latitudinal gradient and standard deviation are listed, and the midpoint and total spread of the latitudinal gradients is shown in line (5).

#### **3.4.4 – Observed Intensity Gradients**

Quasi-local intensity gradients are calculated for five ACR oxygen energy ranges from 0.6 to 39 MeV/nucleon, for two ACR helium energy intervals from 3.1 to 21 MeV/nucleon, and two ACR hydrogen energy ranges from 4.8 to 30. MeV, the results of which are summarized in Figures 3.4.1 to 3.4.9. These gradients are determined from Voyager 1 & 2 data during the solar cycle 22 recovery period. In addition non-local gradients are calculated for ACR O with energies from 1 to 5 MeV/nucleon, and 7 to 29 MeV/nucleon, utilizing Voyager 1 and 2 data along with 1-AU observations, which include SAMPEX, ACE, and WIND spacecraft data (Figure 3.4.11). The results of these measurements are provided in Tables 3.4.1 and 3.4.2, which should be consulted as the individual Figures 3.4.1 to 3.4.9 are considered below.

The Quasi-Local Gradient (QLG) plots for 0.6- to 14-MeV/nucleon oxygen (Figures 3.4.1-3.4.3) are similar and will be discussed together. The overlapping energy intervals are those described in Table 2.3.1. The Low<sub>2</sub> and High<sub>2</sub> energy ranges are used to match the LECF data with the data from 1-AU, as in Figure 3.4.1. In all three cases positive radial and negative latitudinal gradients are determined. The “time-subtraction” in which the data are divided by the initial recovery factor from section 3.3.1 (as discussed in section 3.4.3) in each case results in an essentially exponential form, with more short-term fluctuations early in the recovery. The gradient determinations from the various methods (panels (c) – (g) of the QLG plots; see section 4.4.3) are all comparable, but the differences are larger than the statistical uncertainties would suggest. With this method it is not the statistical quality of the fit that controls the uncertainty, but the systematics of subtracting the assumed temporal dependence. For this reason the larger systematic variations (obtained by comparing the various methods) are used to estimate the uncertainties in Table 4.4.1. It is encouraging that the V1-V2 pair-only results (d) agree well in all three cases with the modified, time subtracted fit (f), for the reasons discussed in section 4.4.3. In the first two cases (Figures 3.4.1 and 3.4.2) the highest correlation coefficients was found for the simple exponential fits (e), and were -0.84 and -0.86, respectively. In the remaining example (Figure 3.4.3), panel (g) representing event-pairs drawn from the exponential fit function, has the highest correlation at -0.90. The fact that the “low pass filtered” fits (e) and (g), do not disagree with the unfiltered fits (c) and (f), respectively, suggests that the high frequency variations are indeed not affecting the analysis, despite the associated spread in the data in the portions of (c) and (f) that are

dominated by V1-V1 event pairs (0.05 degree/AU) and V2-V2 event pairs (0.5 degree/AU). Note (from left to right), the upward arching distribution of data points in Figure 3.4.3f above and to the right of the V2-V2 peak, at about 1 degree/AU for positive ordinate values. This is due to residual time variations that were not completely removed with the time-subtraction, and should be compared to Figure 3.4.10 in which the quasi-local method is purposely used with data for which the assumptions do not hold, to indicate the built-in consistency check of the method; i.e., analysis of time-dependent periods yields QLG scatter plots with non-linear distributions of data (for the particular form of the quasi-local method that we use here).

In Figures 3.4.4 and 3.4.5 ACR oxygen above 7 MeV/nucleon is discussed. In both of these cases the results are smaller radial gradients than the previous three cases, and small positive latitudinal gradients. The magnitudes and signs of these gradients are in rough agreement with the calculations of other investigators, as is discussed in section 3.3.4, in the context of the phenomenological model gradients, with small positive radial and latitudinal gradients in all cases. The high energy oxygen data should be equally well analyzable by both the non-local, and quasi-local methods since they exhibit small temporal and spatial variations over large stretches of time and space. Note that the 12- to 39-MeV/nucleon O radial gradient (Table 3.4.1) of  $-0.2 \pm 0.5$  %/AU is consistent with zero. The gradients at this energy deserve some additional attention. The essentially zero QL radial gradient and a latitudinal gradient of about 3 %/degree are strong indications that this method is yielding robust results, even though these figures disagree in detail with both the work of other investigators

(McDonald, Lal, and McGuire, 1998; Cummings *et al.*, 1995a, see section 3.3.4), who quote larger radial gradients ( $\sim 2\%/AU$ ) and smaller latitudinal gradients (0.2 to 1.3  $\%/degree$ ), and the phenomenological model results (Table 3.4.1). Despite the differences (which are not surprising due to some differences in the times, locations and energies studied) the Figure 3.4.5 results reproduce unmistakable features of the data, analyzable in an elementary way. The 14- to 39-MeV/nucleon data are remarkably constant over the seven years following 1994 at both V1 and V2, therefore this is strong evidence for a nearly zero radial gradient at these energies for V1 and V2 (since there are no candidate *counterbalancing* phenomena to mask a radial gradient and any such balancing effect would be unlikely in any case to result in such constant intensities for so long a time and at both spacecraft). And the fact that (under the symmetry assumptions in use) a positive latitudinal gradient must exist to explain the V1:V2 intensity ratio of about 1.7 is clear (cf., the  $j_a$  column in Table 3.3.1). The QLG value for  $g_\lambda$  is about 3  $\%/degree$ , which, from a typical V2 absolute latitude of about 15 degrees to V1 at 33 degrees, implies a resulting intensity ratio due to the latitudinal variation alone of  $\exp(g_\lambda \Delta\lambda) = \exp(0.03 \cdot 18) = 1.7$ , in agreement with the data.

The helium and proton results (Figures 3.4.6 - 3.4.9) are also indicated in Table 3.4.1. Notwithstanding the warning about the ambiguity involved in parameterizing the proton recovery (§3.3.1), there are no indications of significant problems with either protons or helium, except that the systematic uncertainties of the proton radial gradients are reasonably large ( $18 \pm 6 \%/AU$  for  $\sim 8$ -MeV protons vs.  $11 \pm 1 \%/AU$  for  $\sim 2$  MeV/nucleon oxygen). It is worth discussing a feature, visible

but less pronounced for oxygen (Figures 3.4.1e and 3.4.2e), that is seen for both H and He in panel (e) of Figures 3.4.6 –3.4.9. It is the V2-V2 peak, which appears as a short horizontal line segment (i.e., a single-bin-width peak) in the vicinity of 0.5 degrees/AU that is found to be noticeably above the fit line. This could be a case in which the self-consistency-check property of the quasi-local method is in evidence. The horizontal V2-V2 peaks (less so for H than for He and O) indicate that the quasi-local determination of the latitudinal gradient at V2 is near zero. This suggests that the latitudinal gradient is latitude-dependent, which is not included in this application of the QLG method (see discussion surrounding Eq. 3.4.6). It may be that the magnitude of the negative latitudinal gradient is smaller near the heliographic equator and increases at higher latitudes, producing a latitudinal profile reminiscent of a shallow inverted bowl. This is not an unexpected potentiality. For example Steenberg (1998) finds such profiles in his no-drift solutions of the cosmic ray transport equation (in two spatial dimensions) that were fit to outer heliospheric ACR and GCR data. Incidentally, he points out that it is the no-drift solution (rather than the drift solution) that fits the data almost perfectly, and finds negative latitudinal gradients for the lower energy ions in this version of his model.

It is of note that quasi-local gradients and the model gradients compared in Table 3.4.1 for He and H are in rather good agreement (and somewhat less so for oxygen). The results of this section and those of section 3.3.4, however, are independent in the following senses. The two methods are markedly different, the phenomenological model involving many assumptions about the form and dependencies of the transport of ACRs during the solar cycle 22 recovery, using

numerous parameters, while the quasi-local gradient method makes few assumptions and is quite simple, with two parameters obtained directly from a linear fit to uncomplicated quantities calculated directly from the observations. Moreover there was no attempt to adjust the initial parameters in the model to bring the gradients into better agreement with the measured gradients, and indeed the final results of each of these methods were settled upon before the comparison was made. The agreement of these two methods is taken to indicate that the level of confidence in each should be appropriately increased. It is also found in section 3.5.3 and 3.5.4, in application of the numerical solution to the transport equation, that the rates of recovery and relative intensities between ACRs of differing energies are reproduced rather well with only the barest adjustment of a few well-understood parameters (see in particular the end of section 3.5.3). Together with such notions as both the theoretical expectation of an exponential growth form of intensity for spacecraft motion through a radial gradient and the observed prevalence of weak, late-recovery temporal dependence for many cosmic ray species in cycle 22, the threefold convergence (including section 3.5) of the varied methods used here towards the same conclusion suggests that the interpretation herein (see Chapter 5) is a good approximation of reality.

There are ACR oxygen observations available at three locations, Voyager 1, Voyager 2, and the several 1-AU spacecraft. Therefore, 3-point non-local gradients may be calculated from these data by simultaneously solving both of Eqs. 3.4.4 during each averaging interval. In Figure 3.4.11 the result of this analysis is displayed. The 1-AU data have been interpolated to match the Voyager 26-day averaging periods. The (a) radial and (b) latitudinal intensity gradients are plotted against time for

(squares) low<sub>2</sub>- and (circles) high<sub>2</sub>-energy data, in addition to a half-year-smoothed curve (solid line) which is overlaid to highlight the trend. The large changes seen beginning in 1997 in both panels are due to increasing solar modulation in the inner heliosphere and are shown for completeness, although this period following the onset of increasing modulation is beyond the scope of the present work. From 1992 to 1996 the 7- to 29-MeV/nucleon radial gradient decreases steadily from 6 to 1 %/AU. This occurs despite the fact that, at the Voyagers after 1994, there is very little change in the intensity of the high<sub>2</sub>-energy ACR oxygen, indicating locally that there are very small radial gradients in the outer heliosphere. The apparent time-dependence of the high<sub>2</sub>-energy radial gradient (a) is due to the increasing separation of the Voyager spacecraft from the Earth and not to temporal variations in the global heliosphere. This is an example of how a non-local gradient, when applied inappropriately, can lead to misleading results. (This is the scenario described in section 3.4.1.) The 1- to 5-MeV/nucleon ACR O radial gradients are consistent with a somewhat stable 3- to 4- %/AU gradient, although with significant scatter, from 1993 to 1996, and both the low<sub>2</sub>- and high<sub>2</sub>-energy latitudinal gradients exhibit scattered values clustering in the -1 to +4 %/degree range. In these cases, due to the uncertainty in the form of the latitudinal and radial flux profiles, and the large distance from Earth to the outer heliospheric probes, these gradients provide some measure of the bulk variation from the inner to the outer heliosphere, but very little information about the spatial distribution of intensity in the vicinity of the Voyager spacecraft. Table 3.4.2 summarizes the range of spatial gradients determined by his method for the 1993 to 1996 period.



**Table 3.4.1 Spatial Intensity Gradients of Outer Heliospheric ACRs**

Ion <sup>a</sup>	$E^b$ (MeV/nuc)	$R^c$ (MV)	Quasi-Local Gradient Measurements		Phenomenological Model Results <sup>c</sup>	
			$g_r^d$ (%/AU)	$g_\lambda^d$ (%/deg.)	$g_r$ (%/AU)	$g_\lambda$ (%/deg.)
O <sup>+</sup>	0.6 – 3	800	11.2 ± 1.1	-5.5 ± 1.2	9.6	-4.2
O <sup>+</sup>	1 – 5	1000	10.8 ± 0.9	-5.3 ± 1.2	...	...
O <sup>+</sup>	3 – 14	1700	6.8 ± 0.8	-2.6 ± 0.8	4.4	-1.2
O <sup>+</sup>	7 – 28	2600	0.9 ± 0.9	+2.8 ± 0.8	...	...
O <sup>+</sup>	12 – 39	3300	-0.2 ± 0.5	+2.9 ± 0.3	1.2	+0.9
He <sup>+</sup>	3 – 12	440	13.3 ± 1.6	-7.5 ± 1.6	13	-7
He <sup>+</sup>	21 – 30	870	8.1 ± 1.3	-3.9 ± 1.6	9.1	-3.8
H <sup>+</sup>	5 – 11	120	18 ± 6	-13 ± 5	19	-15
H <sup>+</sup>	24 – 30	230	16 ± 3	-10. ± 2	16	-11

<sup>a</sup> Particles observed at both Voyager 1 and Voyager 2 from 1992 to 1999.

<sup>b</sup> Energy ranges do not match exactly at the two spacecraft, see Figures 3.4.1 to 3.4.9.

<sup>c</sup> Typical mean value for specified ion.

<sup>d</sup> Error estimates include statistical and systematic uncertainties.

<sup>e</sup> See Figure 3.3.4, Table 3.3.2, and section 3.3 for details of the model.

**Table 3.4.2 Non-Local Gradient Ranges for ACR O<sup>+</sup> in 1993 to 1996**

$E$ (MeV/nucleon)	$g_r$ (%/AU) <sup>a</sup>	$g_\lambda$ (%/degree) <sup>a</sup>
1 to 5	+3 to +4	-1 to +4
7 to 29	+1 to +6	-1 to +4

<sup>a</sup> Estimated from V1-V2-1AU gradients in Figure 3.4.11 from 1993 to 1996.

Measurements of cosmic ray intensities from the Ulysses spacecraft during its 1994 - 1995 fast latitude scan have indicated an apparent latitude of reflective symmetry at 10° S (Simpson, Zhang, and Bame, 1996; McKibben *et al.*, 1996), and a 7° S latitude of symmetry is reported by Heber *et al.* (1996). In contrast, symmetry about the heliographic equator ( $\lambda = 0^\circ$ ) has been heretofore assumed in this work. We have performed quasi-local gradient calculations under the alternate assumption that the latitude of symmetry is 10° S to examine the effect such an assumed offset would have on the intensity gradient determinations (Table 3.4.1). The results of these

calculations (along with the equatorially symmetric intensity gradients, for comparison) are listed in Table 3.4.3. The determined radial gradients are the same under both assumptions, except for small statistical differences. As expected, the latitudinal gradients are significantly changed when the offset latitudinal symmetry is assumed; i.e., the offset latitudinal gradients all have smaller magnitudes than the previously discussed latitudinal gradients, but none of the signs changes. The smaller magnitudes are primarily due to the fact that the latitudinal separations  $\Delta\lambda$  are larger for the V1-V2 event pairs in the QLG plots under the offset coordinate system.

In Figure 3.4.12 an example of the QLG plot for the offset symmetry case is shown for ~3- to 14-MeV/nucleon ACR Oxygen (cf., Figures 3.4.3 and 3.4.10). The 10 degree offset has the effect of increasing the calculated abscissa values, thus decreasing the magnitude of the slope of the fit lines and subsequently decreasing the offset latitudinal gradients relative to the equatorially symmetric latitudinal gradients, as seen in Table 3.4.3. Except for features resulting directly from this change in slope, panels (c) – (e) and (g) are quite similar in both figures. Although the distribution of data points between 0 and 1 degree/AU in Figure 3.4.12f is different than that in Figure 3.4.3, the quality of the fits is comparable. Due to the crossing of the (10° S) symmetry latitude by Voyager 2, the V1-V1 peak (~ 0.05 degree/AU) and the V2-V2 peak (~ 0.5 degree/AU) in panel (f) of Figure 3.4.12 are *bridged* by a cluster of data points that straddle the fit line. The offset QLG plots for the other ACR species (not shown) show no significant features indicating qualitative differences between the offset and non-offset cases. The smaller magnitudes of the latitudinal gradients resulting from the 10° S offset calculations may be easier to interpret, simply because

weaker physical mechanisms would be required to explain the results. Nevertheless, we do not see a way to experimentally distinguish between the equatorially symmetric and the 10° S latitudinal offset cases based on the comparative quality of the quasi-local gradient fits.

**Table 3.4.3** Quasi-Local Gradients with 10° S Latitude of Symmetry

Ion <sup>a</sup>	<i>E</i> (MeV/nuc)	<i>R</i> (MV)	Without Offset of $\lambda$ Symmetry <sup>b</sup>		10° S Offset of $\lambda$ Symmetry <sup>c</sup>	
			<i>g<sub>r</sub></i> (%/AU)	<i>g<sub>λ</sub></i> (%/deg.)	<i>g<sub>r</sub></i> (%/AU)	<i>g<sub>λ</sub></i> (%/deg.)
O <sup>+</sup>	0.6 – 3	800	11.2 ± 1.1	-5.5 ± 1.2	11.0 ± 0.5	-2.4 ± 0.5
O <sup>+</sup>	1 – 5	1000	10.8 ± 0.9	-5.3 ± 1.2	10.5 ± 0.5	-2.4 ± 0.4
O <sup>+</sup>	3 – 14	1700	6.8 ± 0.8	-2.6 ± 0.8	6.5 ± 0.8	-1.1 ± 0.4
O <sup>+</sup>	7 – 28	2600	0.9 ± 0.9	+2.8 ± 0.8	1.3 ± 0.8	+1.2 ± 0.4
O <sup>+</sup>	12 – 39	3300	-0.2 ± 0.5	+2.9 ± 0.3	0.1 ± 0.4	+1.2 ± 0.2
He <sup>+</sup>	3 – 12	440	13.3 ± 1.6	-7.5 ± 1.6	13.0 ± 1.7	-3.3 ± 0.6
He <sup>+</sup>	21 – 30	870	8.1 ± 1.3	-3.9 ± 1.6	8.1 ± 1.0	-1.9 ± 0.6
H <sup>+</sup>	5 – 11	120	18 ± 6	-13 ± 5	17 ± 5	-5.5 ± 1.9
H <sup>+</sup>	24 – 30	230	16 ± 3	-10. ± 2	15 ± 3	-4.6 ± 0.9

<sup>a</sup> ACRs observed at both V1 and V2 from 1991 to 1999, see Table 3.4.1.

<sup>b</sup> The assumed latitude of symmetry is 0° for these calculations, as in Table 3.4.1.

<sup>c</sup> The assumed latitude of symmetry is 10° S rather than 0° for these calculations.

# Quasi-Local Intensity Gradients V1/V2-O-Low (gradplot.pro)

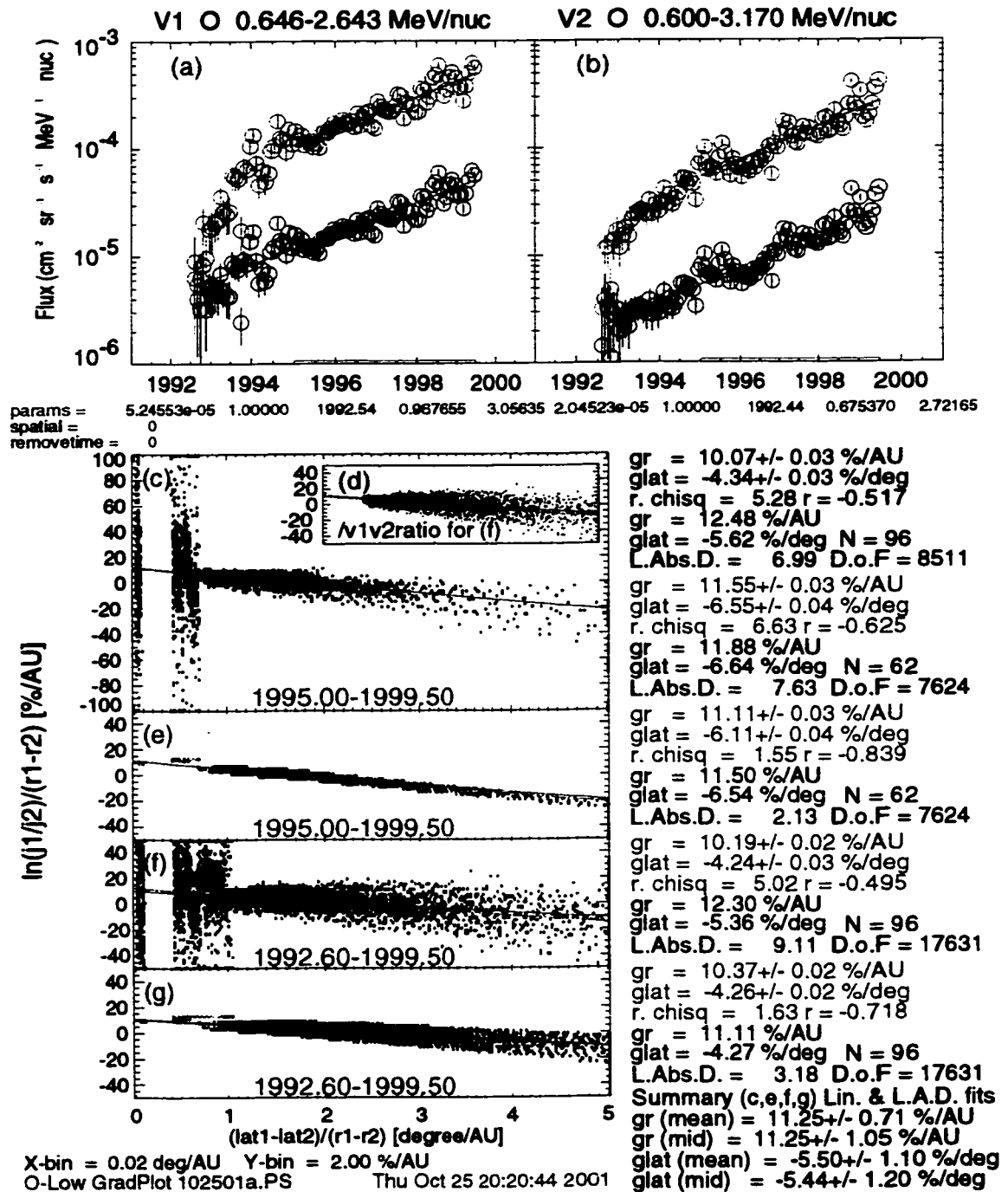


Figure 3.4.1 Quasi-Local Intensity Gradient Fits for 0.6- to 3-MeV/nucleon  $\text{O}^+$  Voyager 1 and Voyager 2 ACR oxygen observations are used to determine radial and latitudinal gradients. See section 3.4.3 for a description of the layout of this figure.

# Quasi-Local Intensity Gradients

## V1/V2-O-Low2 (gradplot.pro)

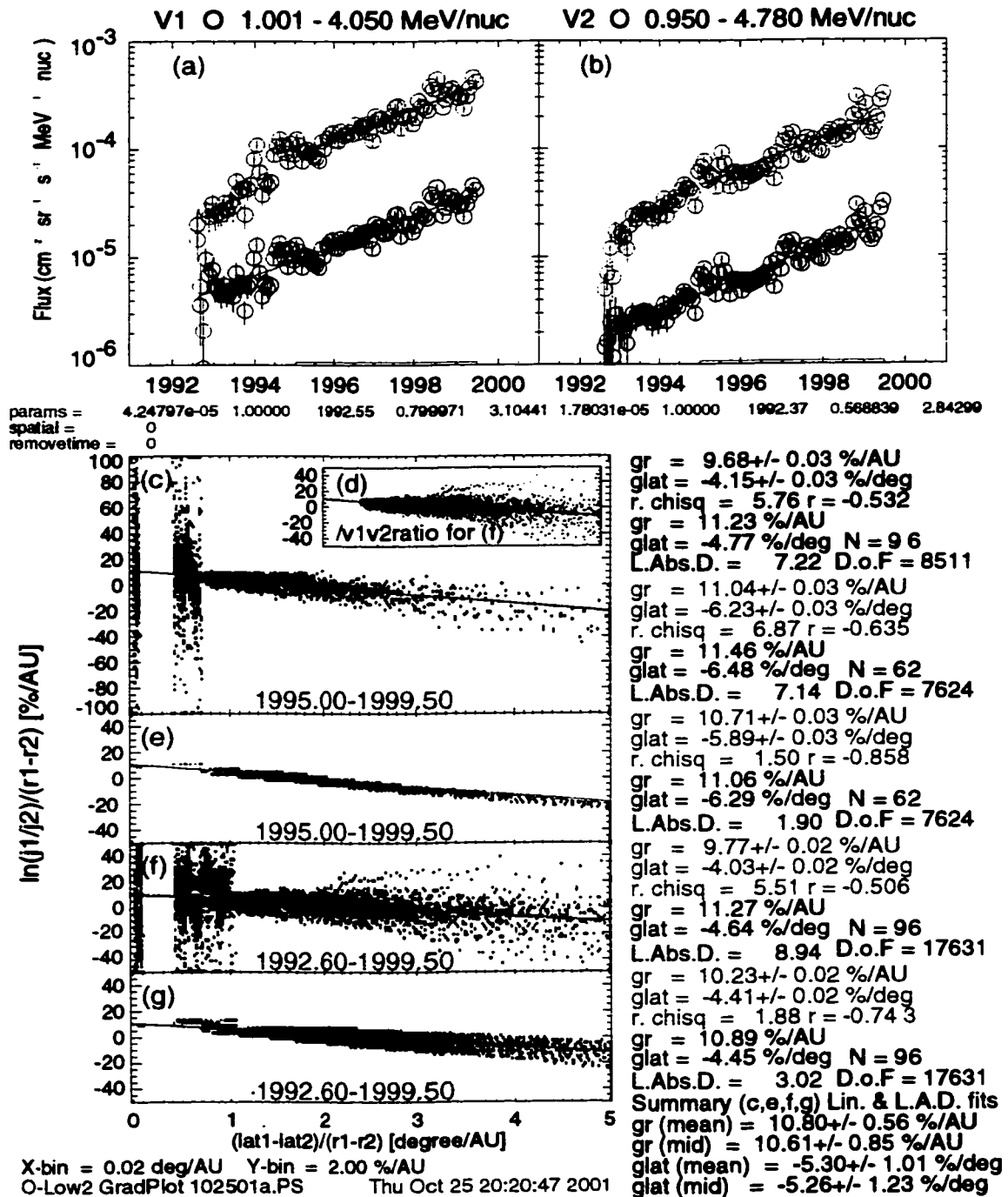


Figure 3.4.2 Quasi-Local Intensity Gradient Fits for 1- to 5-MeV/nucleon O<sup>+</sup>. Voyager 1 and Voyager 2 ACR oxygen observations are used to determine radial and latitudinal gradients. See section 3.4.3 for a description of the layout of this figure.

# Quasi-Local Intensity Gradients V1/V2-O-Med (gradplot.pro)

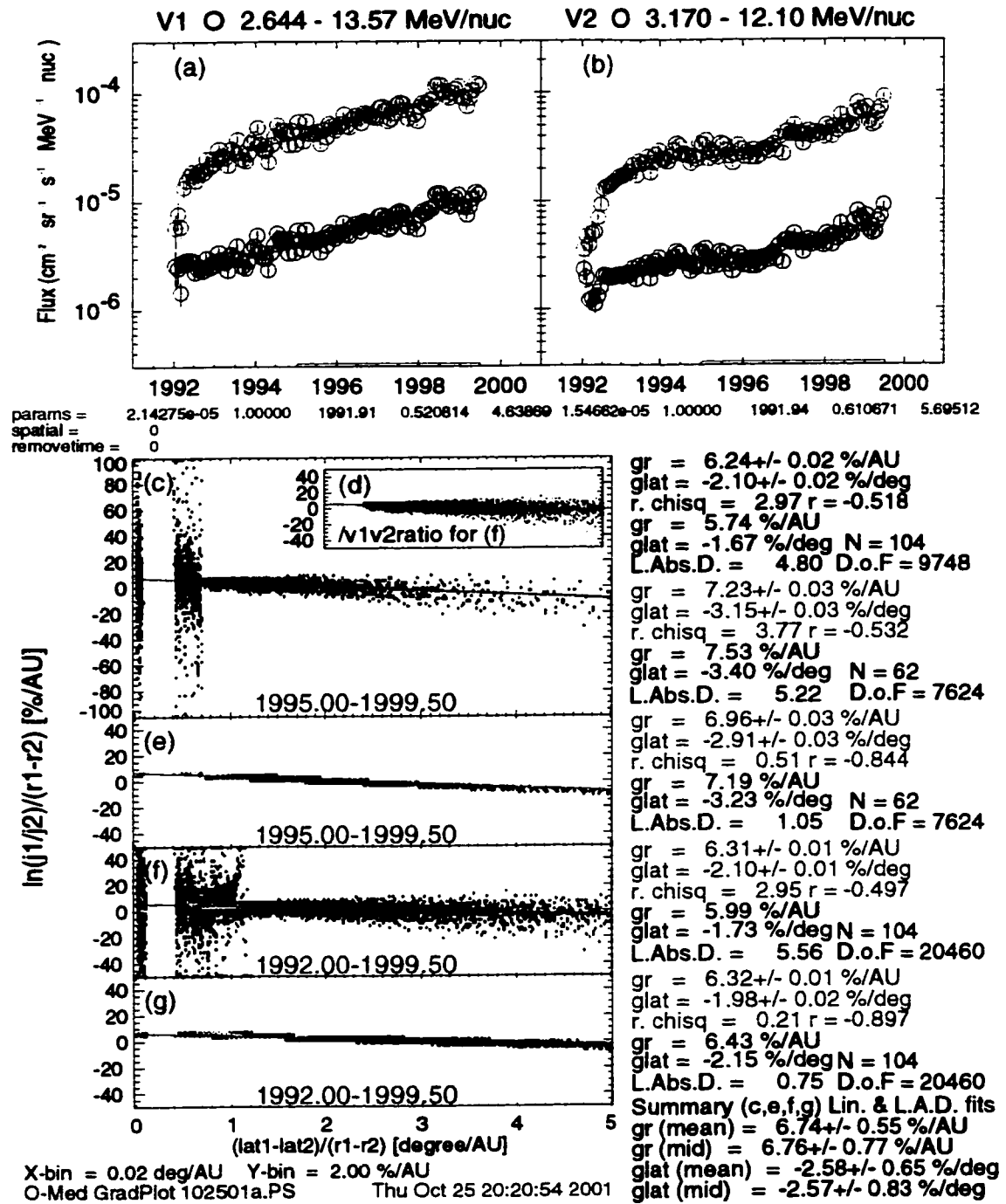


Figure 3.4.3 Quasi-Local Intensity Gradient Fits for 3- to 14-MeV/nucleon O<sup>+</sup> Voyager 1 and Voyager 2 ACR oxygen observations are used to determine radial and latitudinal gradients. See section 3.4.3 for a description of the layout of this figure.

# Quasi-Local Intensity Gradients

## V1/V2-O-High2 (gradplot.pro)

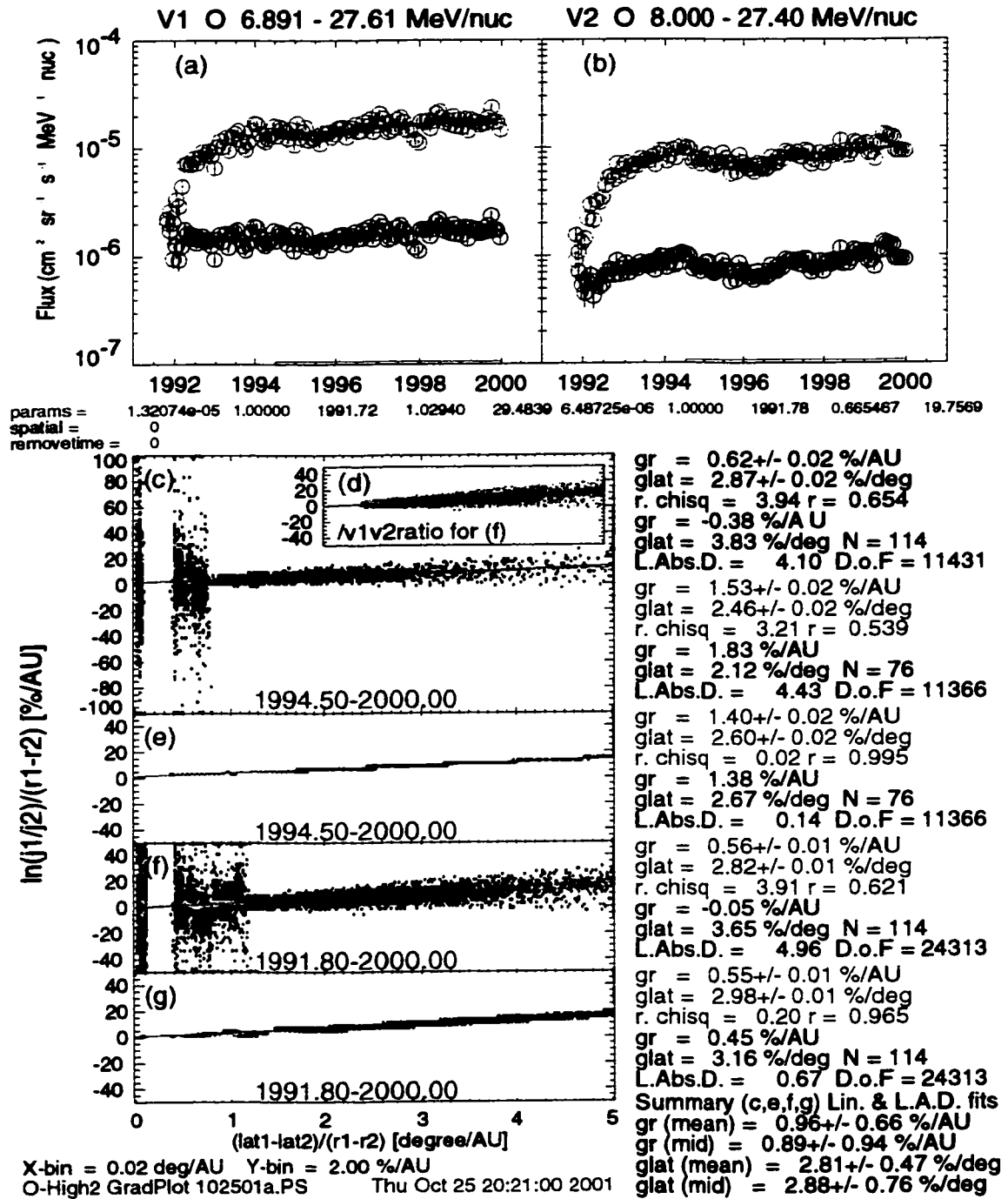


Figure 3.4.4 Quasi-Local Intensity Gradient Fits for 7- to 28-MeV/nucleon  $O^+$  Voyager 1 and Voyager 2 ACR oxygen observations are used to determine radial and latitudinal gradients. See section 3.4.3 for a description of the layout of this figure.

# Quasi-Local Intensity Gradients

## V1/O-2-High (gradplot.pro)

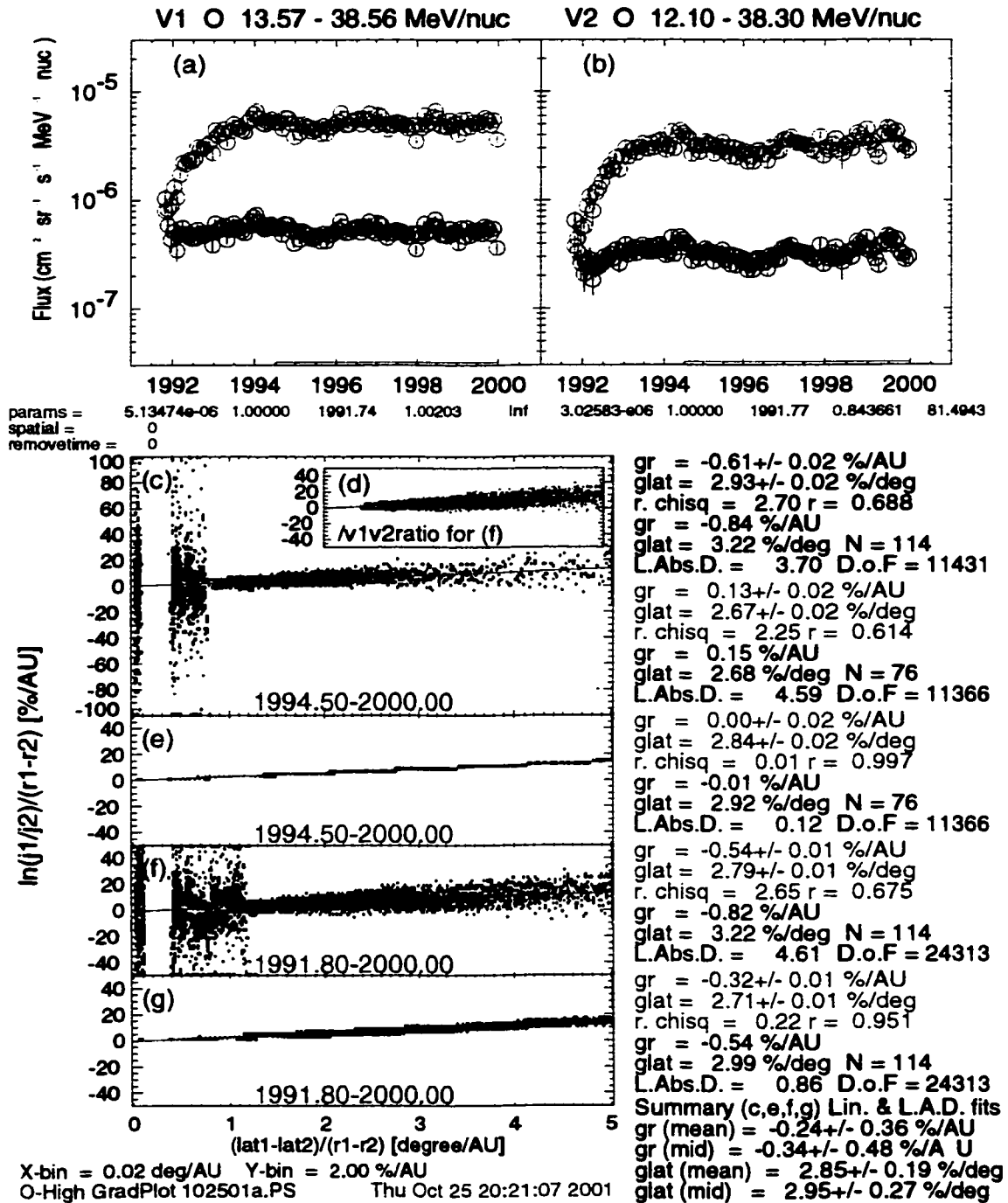


Figure 3.4.5 Quasi-Local Intensity Gradient Fits for 12- to 39-MeV/nucleon  $O^+$  Voyager 1 and Voyager 2 ACR oxygen observations are used to determine radial and latitudinal gradients. See section 3.4.3 for a description of the layout of this figure.



# Quasi-Local Intensity Gradients V1/V2-He-Med (gradplot.pro)

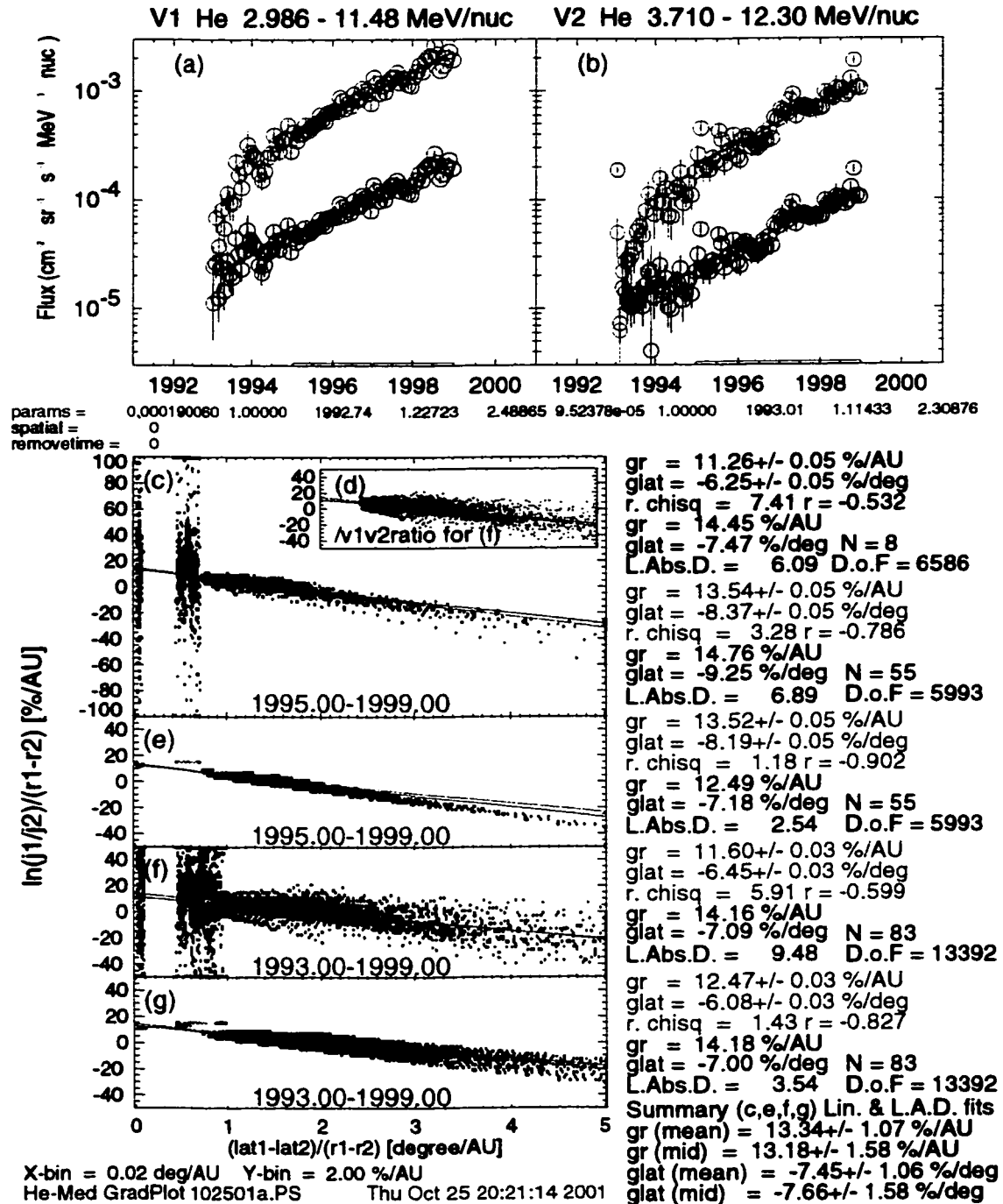


Figure 3.4.6 Quasi-Local Intensity Gradient Fits for 3- to 12-MeV/nucleon He<sup>+</sup> Voyager 1 and Voyager 2 ACR helium observations are used to determine radial and latitudinal gradients. See section 3.4.3 for a description of the layout of this figure.

# Quasi-Local Intensity Gradients

## V1/V2-He-High (gradplot.pro)

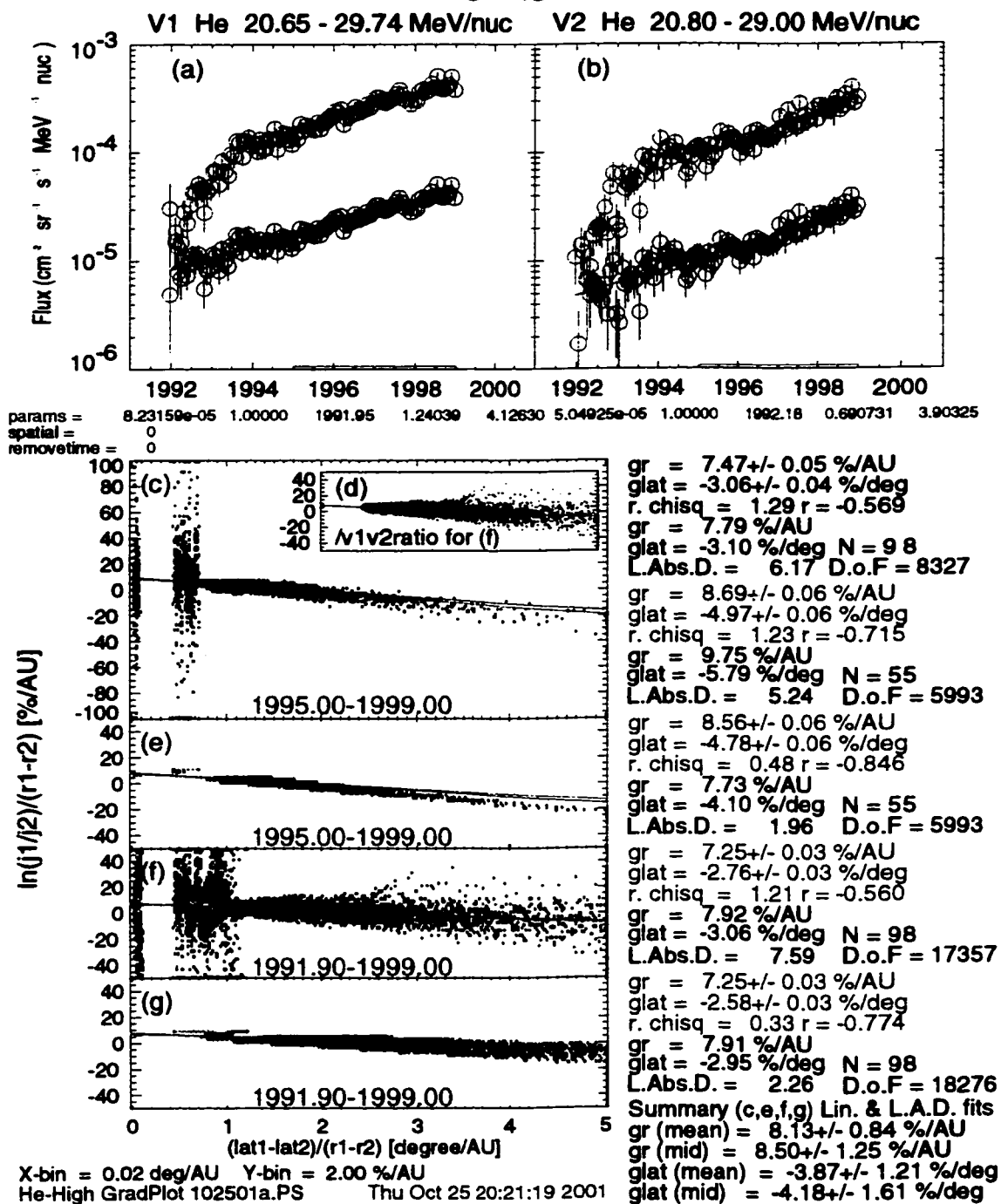


Figure 3.4.7 Quasi-Local Intensity Gradient Fits for 21- to 30-MeV/nucleon  $\text{He}^+$ . Voyager 1 and Voyager 2 ACR helium observations are used to determine radial and latitudinal gradients. See section 3.4.3 for a description of the layout of this figure.

# Quasi-Local Intensity Gradients V1/V2-H-Med (gradplot.pro)

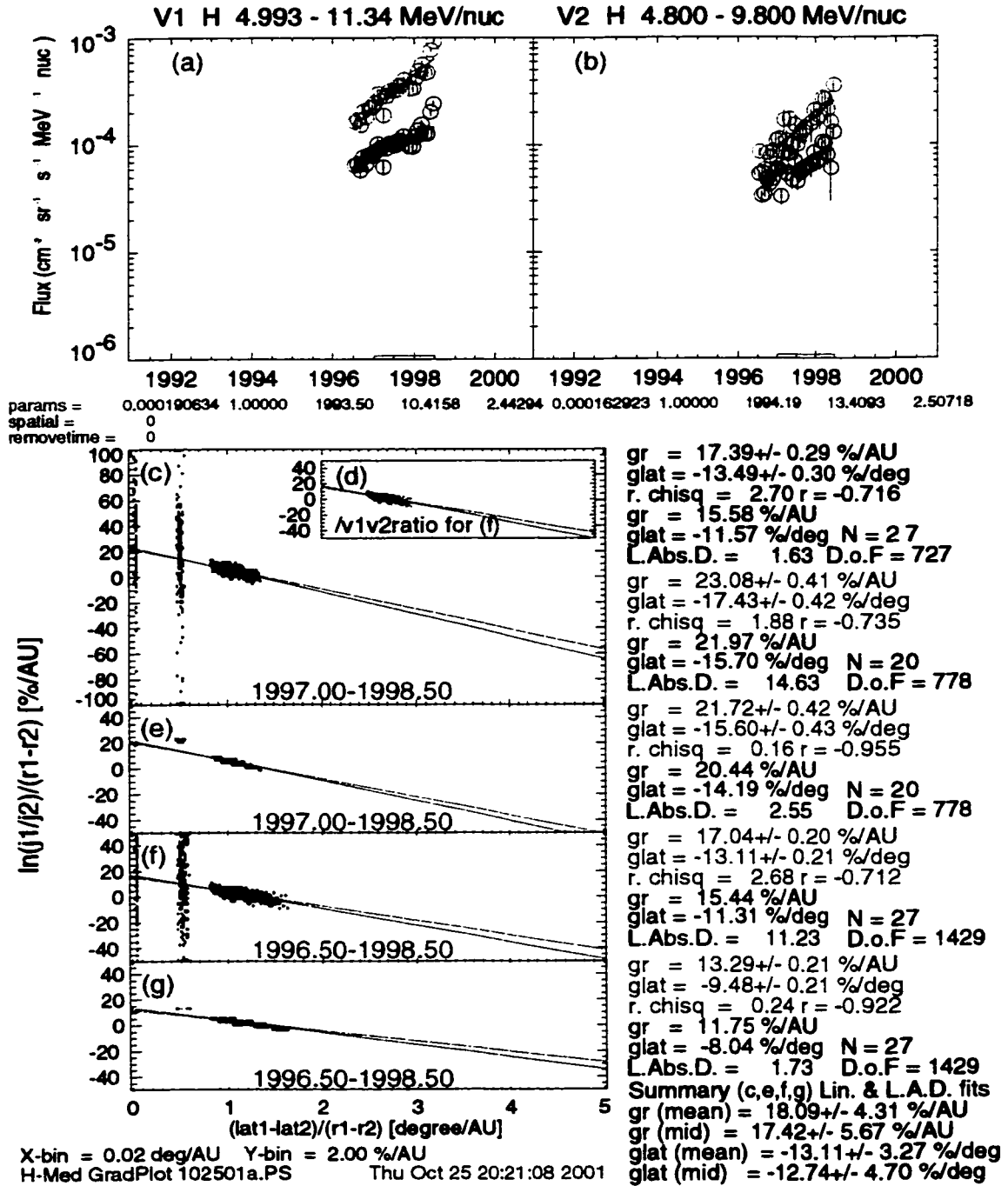


Figure 3.4.8 Quasi-Local Intensity Gradient Fits for 5- to 11-MeV H<sup>+</sup>  
 Voyager 1 and Voyager 2 ACR proton observations are used to determine radial and latitudinal gradients. See section 3.4.3 for a description of the layout of this figure.

# Quasi-Local Intensity Gradients

## V1/V2-H-High (gradplot.pro)

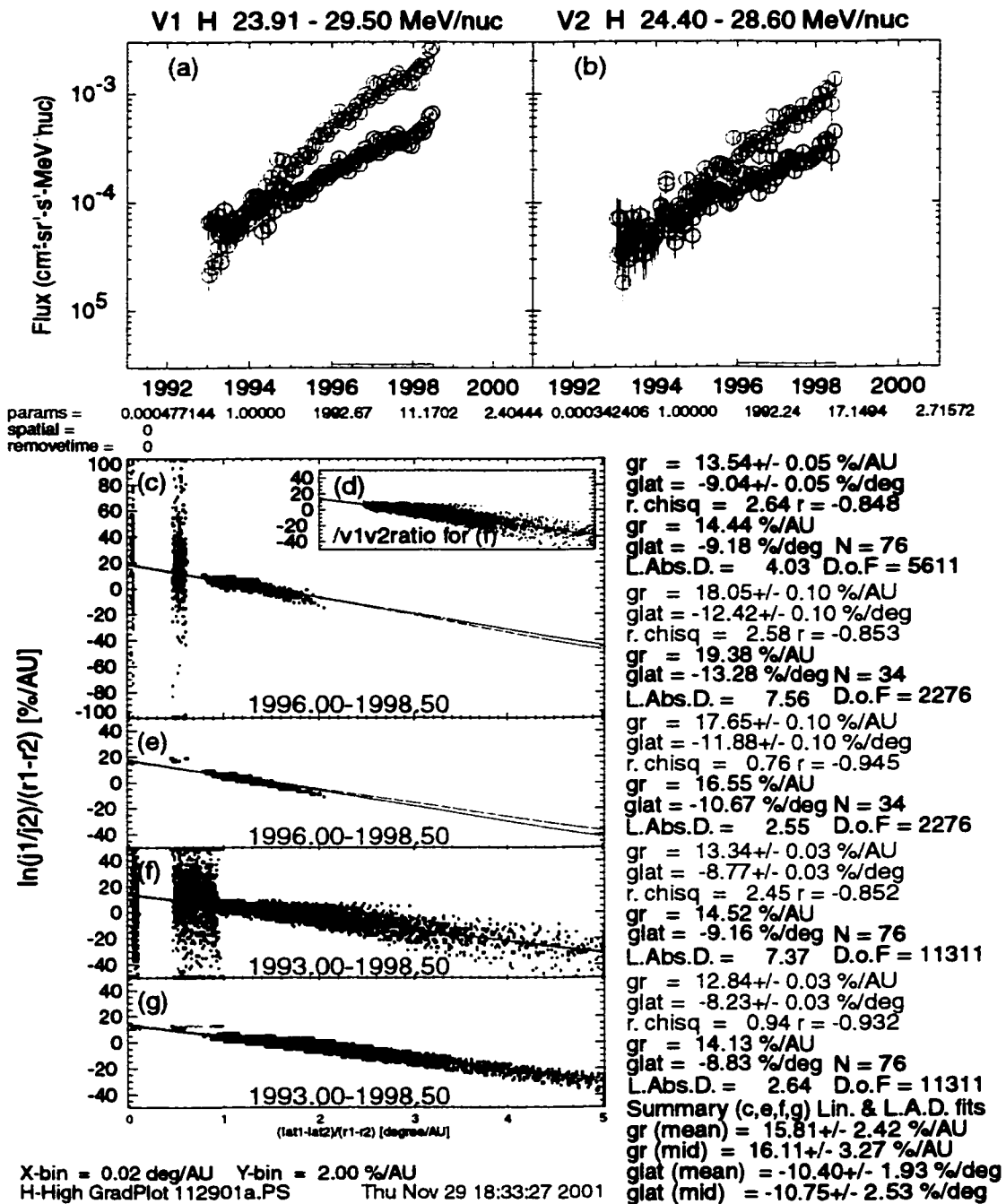
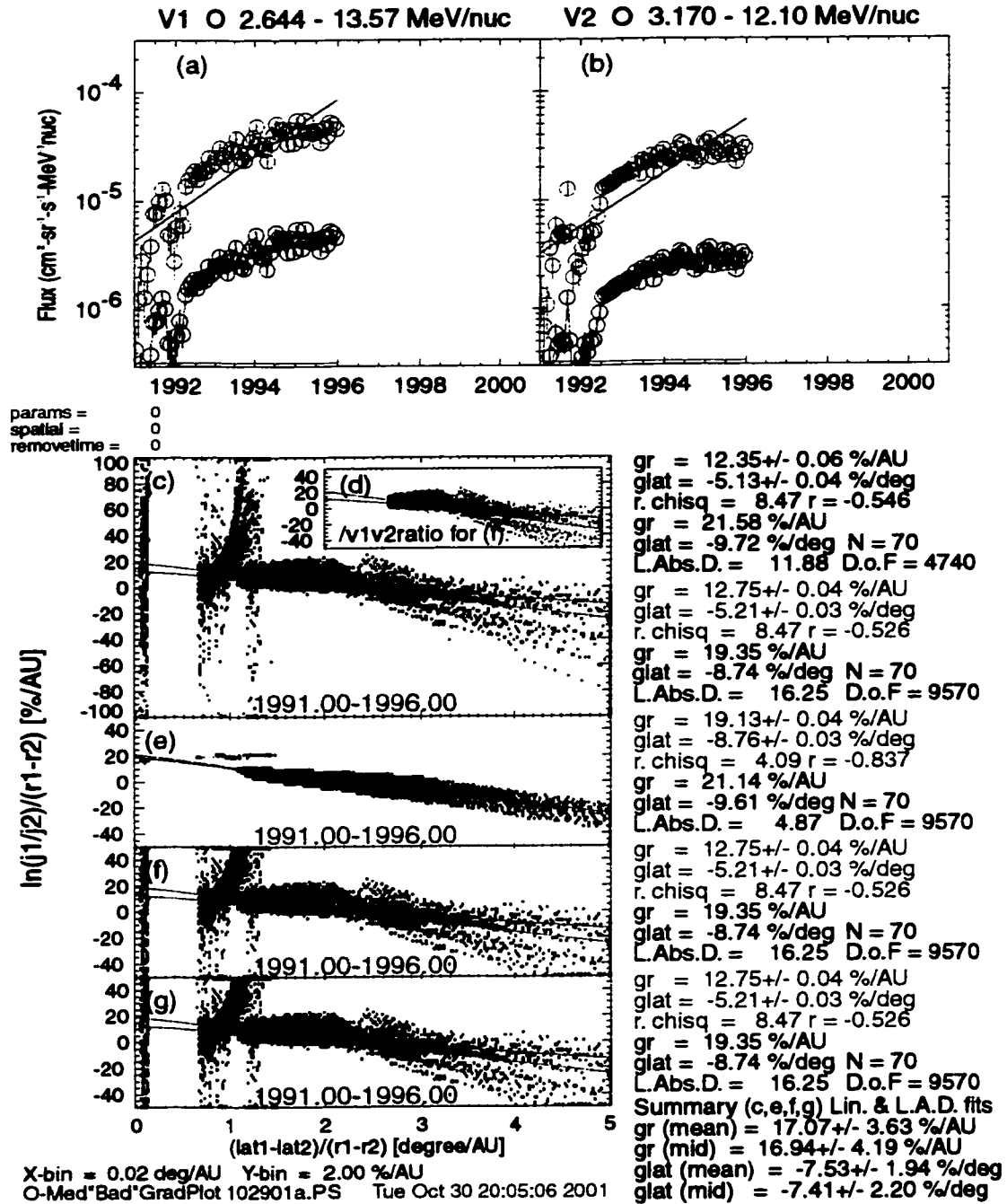


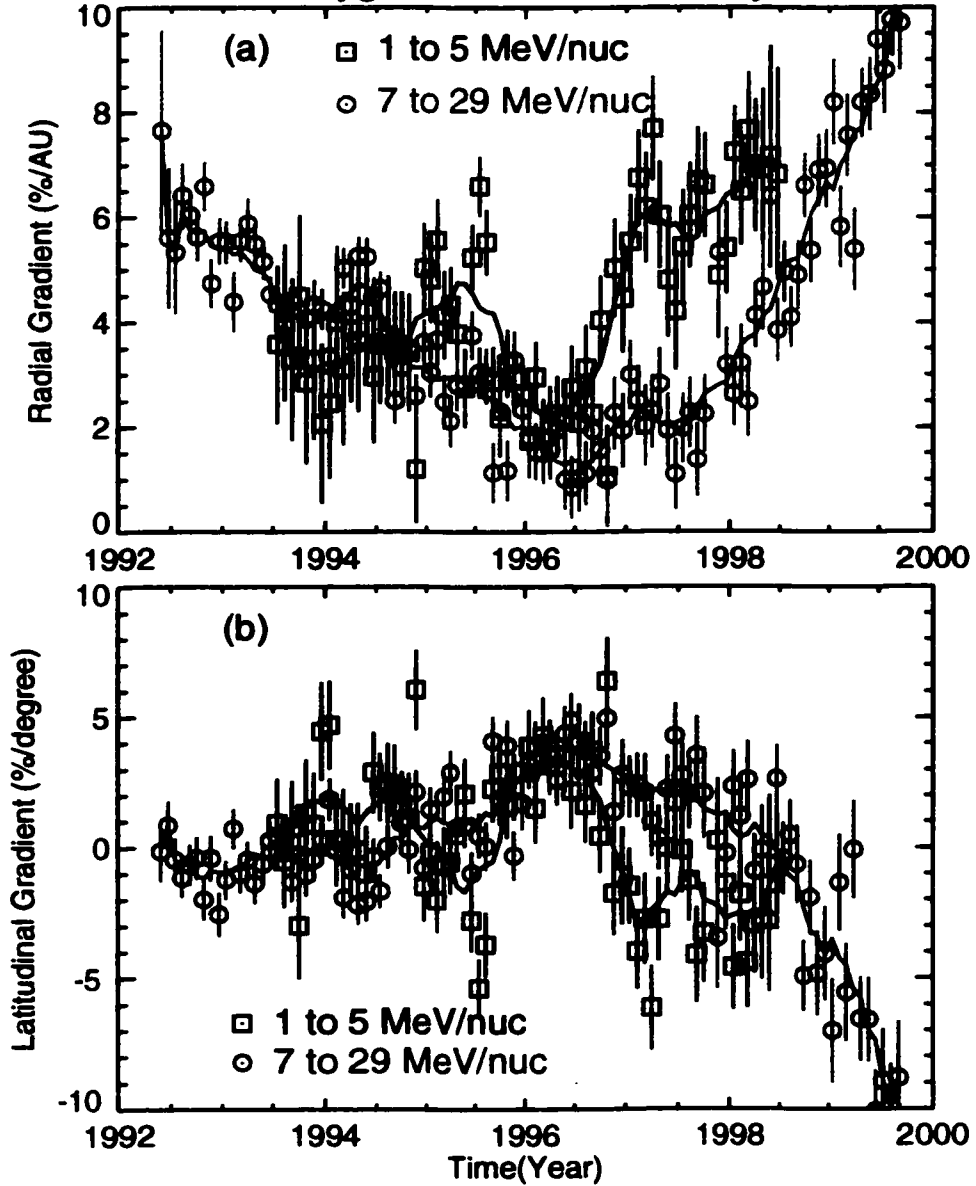
Figure 3.4.9 Quasi-Local Intensity Gradient Fits for 24- to 30-MeV H<sup>+</sup> Voyager 1 and Voyager 2 ACR proton observations are used to determine radial and latitudinal gradients. See section 3.4.3 for a description of the layout of this figure.

# Quasi-Local Intensity Gradients V1/V2-O-Med (gradplot.pro)



**Figure 3.4.10 Quasi-Local Intensity Gradient—Large Time Variations**  
As a demonstration of a case when the QLG plots are not fit well by a line, a period with a large temporal variation is studied. The V2-V2 peak around 1 degree/AU is clearly not aligned with the V1-V2 peak to the right.

### V1-V2-1AU Oxygen Non-Local Intensity Gradients



Smoothing Window = 7 Periods

V1-V2-1AU O Non-L Grad.PS

Tue Nov 6 16:55:35 2001

**Figure 3.4.11 Non-Local Intensity Gradients of ACR Oxygen**  
 Non-local (a) radial and (b) latitudinal intensity gradients for (circles) Low- $\gamma$ - and (squares) high- $\gamma$ -energy  $O^+$  are shown. Voyager 1, Voyager 2, and 1-AU data from Figure 3.3.2 are used for the calculations, for which the 1-AU data are interpolated.

# Quasi-Local Intensity Gradients

V1/V2-O-Med (gradplot.pro)

(10 deg. S offset)

V1 O 2.644 - 13.57 MeV/nuc    V2 O 3.170 - 12.10 MeV/nuc

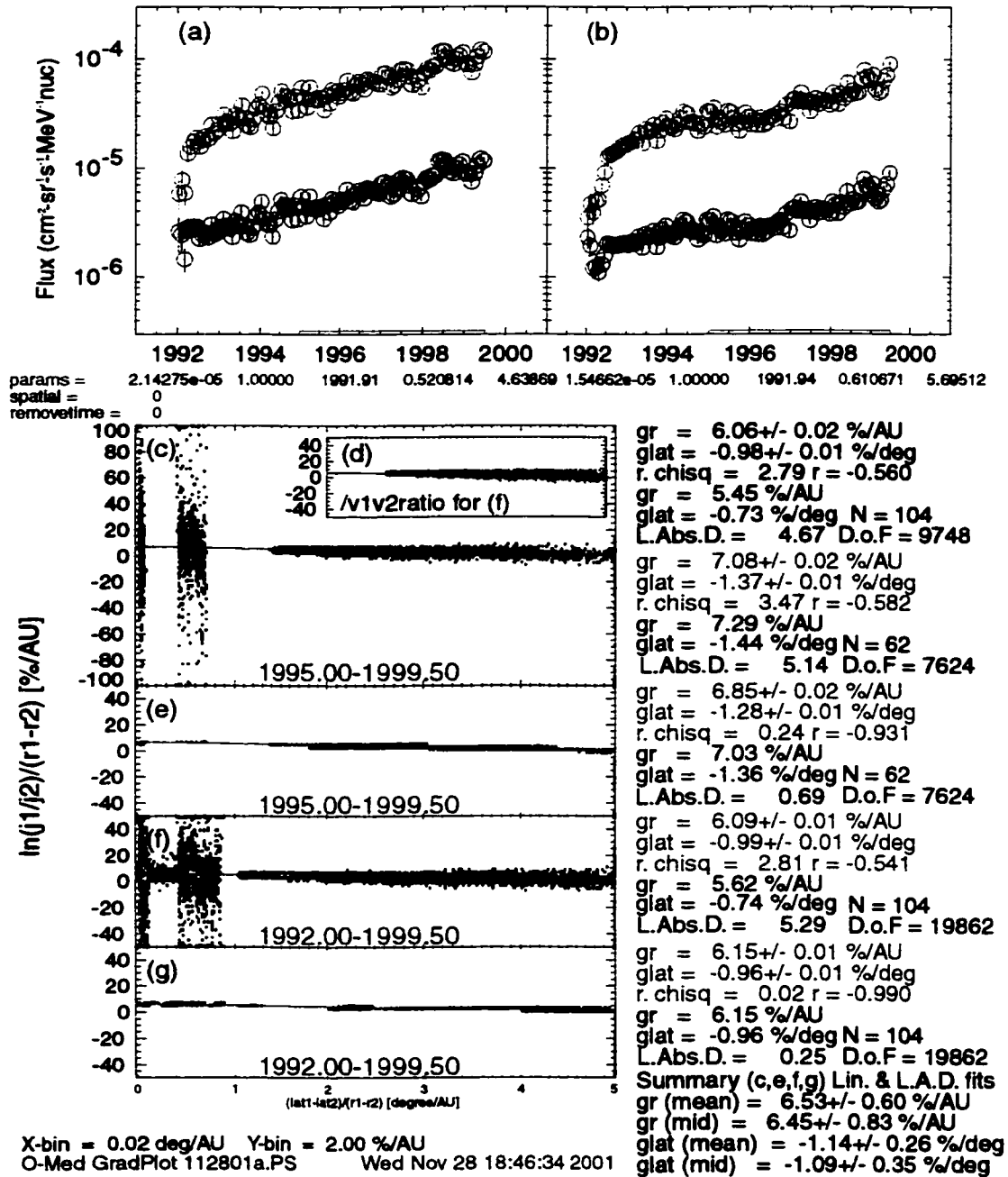


Figure 3.4.12 Quasi-Local Gradient Fits with Latitudinal Symmetry Offset  
 As an example, Voyager 1 and Voyager 2 3- to 14-MeV/nucleon ACR O<sup>+</sup> (cf. Figures 3.4.3 and 3.4.10), with the assumed latitude of symmetry offset to 10° S. See Table 3.4.3 for intensity gradient values for this and other ACR species.

### 3.5 – Numerical Solutions to the Transport Equation

#### 3.5.1 – The Cosmic Ray Transport Equation

Parker (1965) first wrote the Fokker-Planck equation in a complete form useful for solving the problem of cosmic ray transport in interplanetary space, most notably including the adiabatic cooling term arising from the expansion of the radially convecting solar wind. This cosmic ray transport equation (CRTE), to the present day, is widely believed to embody the essential physics of cosmic ray acceleration and propagation through the heliosphere. Formal derivations are available in the literature (e.g., Jokipii, 1971; Jones, 1990); however, a heuristic argument, intended to highlight the essential physics, is provided in Appendix C, wherein the CRTE is given as,

$$\frac{\partial f}{\partial t} = \nabla \cdot \kappa \cdot \nabla f - V \cdot \nabla f + \frac{1}{3}(\nabla \cdot V)p \frac{\partial f}{\partial p},$$

where  $f=f(\mathbf{r},p,t)$  is the omnidirectional distribution function in terms of position  $\mathbf{r}$ , scalar momentum  $p$ , and time  $t$ , and  $V$  and  $\kappa$  are the vector solar wind velocity and diffusion tensor, respectively. The differential number density  $U$  is related to  $f$  by  $4\pi p^3 f = \alpha T U$ , where  $T$  is the total cosmic ray kinetic energy and  $\alpha$  is defined by  $\alpha = (T+2E_0)/(T+E_0)$ , where  $E_0 = mc^2$  is the rest energy. Using  $p\partial/\partial p = \alpha T\partial/\partial T$  the CRTE becomes, in terms of kinetic energy and  $U$ :

$$\frac{\partial U}{\partial t} = \nabla \cdot (\kappa \cdot \nabla U - \mathbf{V}U) + \frac{1}{3}(\nabla \cdot \mathbf{V}) \frac{\partial}{\partial T} \alpha T U.$$

In the non-relativistic limit ( $\alpha=2$ ) with spherically symmetric geometry and a constant radial solar wind, and rewriting in terms of the flux  $j = vU/4\pi$  and energy per nucleon  $E = T/A$  (where  $A$  is the nucleon number and  $v$  is the ACR velocity) we get:



$$\frac{\partial j}{\partial t} = \kappa \frac{\partial^2 j}{\partial r^2} - \left( V - \frac{2\kappa}{r} - \frac{\partial \kappa}{\partial r} \right) \frac{\partial j}{\partial r} - \frac{4V}{3r} \left( 1 - \frac{\partial \ln j}{\partial \ln E} \right) j. \quad (3.5.1)$$

With the diffusion velocity  $V_\kappa = 2\kappa/r + \partial\kappa/\partial r$  so defined, an effective radial velocity  $V_{\text{eff}} = V - V_\kappa + V_d$  can be defined to replace the parenthetical coefficient of the first radial derivative, where  $V_d$  is an *ad hoc* drift speed added to phenomenologically represent the radial component of curvature and gradient drift velocities in this spherically symmetric model. If we write the Compton-Getting factor as  $C(j,E) = 2/3(1 - \partial \ln j / \partial \ln E)$  and represent radial and temporal derivatives with subscripts, Eq. 3.5.1 becomes simply  $j_t = \kappa j_{rr} - V_{\text{eff}} j_r - 2VC/r j$ . Eq. 3.5.1 is the form of the CRTE that is considered here with the dependence  $\kappa = \kappa(E)$ , (resulting in  $V_\kappa = 2\kappa/r$ ), and the solar wind bulk speed  $V$  is a constant.

### 3.5.2 – The Numerical Solution

Solving Eq. 3.5.1 analytically is not possible in general; consequently a numerical solution has been sought. Since the temporal and spatial dependencies of anomalous cosmic ray spectra are of interest, the equation must be solved in a time-dependent form, i.e., retaining all three dimensions  $(r,E,t)$ . To that end, the following parabolic linear partial differential equation was solved numerically:

$$\frac{\partial \psi}{\partial t} = A \frac{\partial^2 \psi}{\partial x^2} + B \frac{\partial \psi}{\partial x} + C \psi + D \frac{\partial \psi}{\partial y}, \quad (3.5.2)$$

where  $\psi$ ,  $A$ ,  $B$ ,  $C$ , and  $D$  may each depend on  $x,y$ , and  $t$  (in this subsection  $C$  does not represent the Compton-Getting factor). A difference equation was generated corresponding to Eq. 3.5.2, suitable for solving with a computer. An operator splitting technique was used to alternately step forward in time in the  $x$  and  $y$  dimensions. The

$x$  and  $y$  dimensions were solved using the usually stable Crank-Nicholson scheme (Press *et al.*, 1989; Kreyszig, 1993) and explicit forward differencing, respectively. An option to apply the Lax method (see Press *et al.*, 1989) to both the  $x$  and  $y$  operations was included to add stability for certain cases, but was infrequently used. To acquire confidence in the computer program that solves Eq. 3.5.2, several limiting forms of the equation that are amenable to analytical solution were solved both analytically and numerically, and comparisons were made of the solutions. The following steady-state and time-dependent limits were tested with universal success: (1)  $0 = x\psi_{xx} + 3\psi_x$ , (2)  $0 = \psi_{xx} - \psi_x$ , (3)  $0 = \psi_{xx} + (2/x)\psi_x$ , (4)  $0 = \psi_{xx} + 2\psi_x + \psi$ , (5)  $\psi_t = 1/4\psi_{xx} + 1/(2x)\psi_x$ , (6)  $\psi_t = 1/4\psi_{xx} - \psi_x$ , (7)  $0 = -\psi + \psi_y$ , and (8)  $\psi_t = -\psi_y$ . In the steady-state limits, (1) – (4) and (7), the numerical solution approached the static analytical solution as the program stepped forward in time. For the remaining time-dependent cases agreement was sought for all times. There were essentially no disagreements between the numerical and analytical solutions (the maximum estimated discrepancy was less than 0.2 %).

Although the success of the tests lends a high degree of confidence in the model, a final comparative test is performed below for the case when the coefficients in Eq. 3.5.2 are chosen to yield Eq. 3.5.1 with  $x, y$  corresponding to  $r, E$ . First, a description of the parameters and boundary conditions used to solve the CRTE is given. The diffusion coefficient is given the form  $\kappa = \kappa_0(E/E_0)^j$  where  $E_0$  is an adjustable energy scale in units of MeV/nucleon and  $\kappa_0$  has the value of the diffusion coefficient at  $E = E_0$ , in units of AU<sup>2</sup>/year. The solar wind velocity  $V$  is held constant in each run, unless otherwise noted.

The outer radial Dirichlet boundary condition (BC), representing the ACR source spectrum, has the general form  $j(r_{\max}, E) = j_s(E)$ , equaling either a power law  $j_s(E) = (E/E_s)^\gamma$ , or a power law with an exponential roll-over  $j_s(E) = (E/E_s)^\gamma \exp(-b(E/E_c)^a)$ . The latter form was that suggested by Steenberg and Moraal (1999), utilizing a sophisticated acceleration model, to be an appropriate parameterization of the termination shock spectrum in terms of the cutoff energy  $E_c$ , the energy at which the diffusive length scale is of order the radius of curvature of the ACR source surface. It follows that this effect is referred to as the curvature cutoff. The parameters,  $a$  and  $b$  were determined by Steenberg and Moraal (1999) in terms of the power-law rigidity dependence  $\eta$  of the scattering mean free path, i.e.,  $a = 0.689\eta + 1.34$  and  $b = -0.083\eta + 0.272$ . The assumed form of the mean free path  $\Lambda = \Lambda_0(R/R_0)^\eta$  is written in terms of the rigidity  $R$ , where  $\Lambda_0$  and  $R_0$  are constants with units of AU and MV, respectively. In the non-relativistic limit, (which is acceptable for ACRs and is used throughout),  $\eta$  is related to  $\gamma$  by the relation  $\eta = 2\gamma - 1$ , where the classical result  $\kappa = v\Lambda/3$  has been used (see Eq. 3.5.3 and Appendix C).

On the inner radial boundary, unless stated otherwise, is the Neumann condition,  $\partial j / \partial r |_{r_{\min}} = 0$ . The vanishing derivative approximates a reflective boundary which is perhaps more appropriate than an absorptive boundary; the ACRs that approach the inner heliosphere may experience significant latitudinal transport, which tends to extend the length of time a given ACR spends inside of 1 AU compared with the scenario in which the cosmic ray streams directly into the sun. The expectation of increased latitudinal transport arises from Ulysses observations; e.g., that recurrent

energetic particles seemingly originating at low latitudes are magnetically well-connected or otherwise efficiently transported to high latitudes (Jokipii et al., 1995; Fisk, 1996). In any case this work is concerned primarily with the outer heliosphere, where it is more likely that the spherically symmetric model will capture the significant physics so details of the inner boundary are not important. Moreover, it was found that the Neumann condition resulted in solutions that better matched the force field approximation than did other boundary conditions.

The boundary conditions used at the lowest and highest energies of the solution are “extrapolated BCs” in which the spectral slope at a grid-point adjacent to the boundary point is used to extrapolate the spectrum and thus determine the boundary value. This simple condition was found to introduce the fewest unusual features into the spectra and consequently allowed the energy range to be somewhat shorter, since there was less of a need to isolate the energy range of interest from spurious boundary effects.

The initial condition used is the simplest one possible; i.e., the intensity function is zero at all radii and energies. This empty model heliosphere is a reasonable, if coarse, approximation of the state of the heliosphere during and shortly after solar maximum, since it is observed that ACR ions are nearly universally at undetectable levels during this period, (in 1990-1991, for example). Moreover the model used here excludes important effects (non-radial diffusion, drifts, heliospheric current sheet, to name a few) and is not expected to model all of the relevant physics. In particular, the fast initial ACR recovery, occurring shortly after the heliomagnetic polarity reversal, and coinciding with significant, though declining, solar activity is

not expected to be well-modeled in detail without arbitrarily modifying the model. In light of the limitations of the model, the simple initial condition is justified since the solution rapidly relaxes to a physically reasonable form.

The radial steps used to discretely represent the heliosphere are linear with a typical grid spacing of 1AU, and a logarithmic energy grid is used with logarithmic steps spaced at intervals of 0.1, corresponding to energy steps of about 25%. The time steps are linear with a typical step size of 0.003 years. These step sizes were adjusted to maintain stability and efficiency as the transport parameters were varied. It was confirmed that stable solutions were not dependent on the step sizes, and in particular as the grid was made finer, the solutions converged, and usually did so rapidly.

The final test of this model was to compare the numerical solution of Eq. 3.5.1 to a useful approximation first derived by Gleeson and Axford (1968; see also the review by Jokipii, 1971). This well-known approximation is termed the force field approximation because of the resemblance the solution has in a certain limiting form to that of a charged particle in an electrostatic field. The approximation is valid for small  $rV/\kappa$ , which is usually appropriate for high energy cosmic rays above the LECF energy range. As Figure 3.5.1 shows, the analytic approximation and the numerical solution agree well in the higher end of the energy range. In this figure of intensity versus radius, the energy spacing between adjacent lines is about 25%, with reference energies given on the right axis. The colored lines are the force-field approximation solutions and the black lines are the numerical solutions. The lines at the bottom of the figure represent higher energy particles, where the approximation is expected to be most accurate. At the top of the figure the differences between the numerical solution

and the force field approximation can be seen. At large radii the numerical solution shows the expected convection-diffusion dominance, as evidenced by the steep gradients due to the inability the low energy particles to diffuse inward significantly. At smaller radii the adiabatic deceleration is important and the low-energy intensities there are due to the cooling of higher energy particles. The force-field model does not include the variation of adiabatic acceleration with radius, and so the gradients of the low-energy particles in the outer heliosphere according to the force-field approximation are very different from the numerical solution. The force field approximation is valid for  $Vr/\kappa \ll 1$ , which in this case corresponds to the higher energies, for which agreement with the numerical solution is seen in Figure 3.5.1. We also note that the general shape and scale of the approximate and numerical spectra agree except down to lower energies.

Another feature of the numerical solution that supports its validity is the approach of the spectra to the  $j \propto E$  form at low energies, particularly near the Sun (Figure 3.5.2c). In this panel, spectra are shown at various radii, separated by 10 AU, with the black and blue lines at small radii and the red lines at and near the outer source. At 1 AU it is clear that the  $j \propto E$  form is precisely reproduced by the model. This form is due to the adiabatic cooling that is responsible for the relatively high intensity of low-energy ions near the Sun relative to the paucity of these ions that would be expected with just convection and diffusion (Rygg and Earl, 1971). The  $j \propto E$  form is not seen in the outer heliospheric spectral solutions as also has been seen by others who have modeled these spectra (e.g., Reinecke and Moraal, 1992), since diffusion is more important than adiabatic energy loss at large radii (§1.1.5).

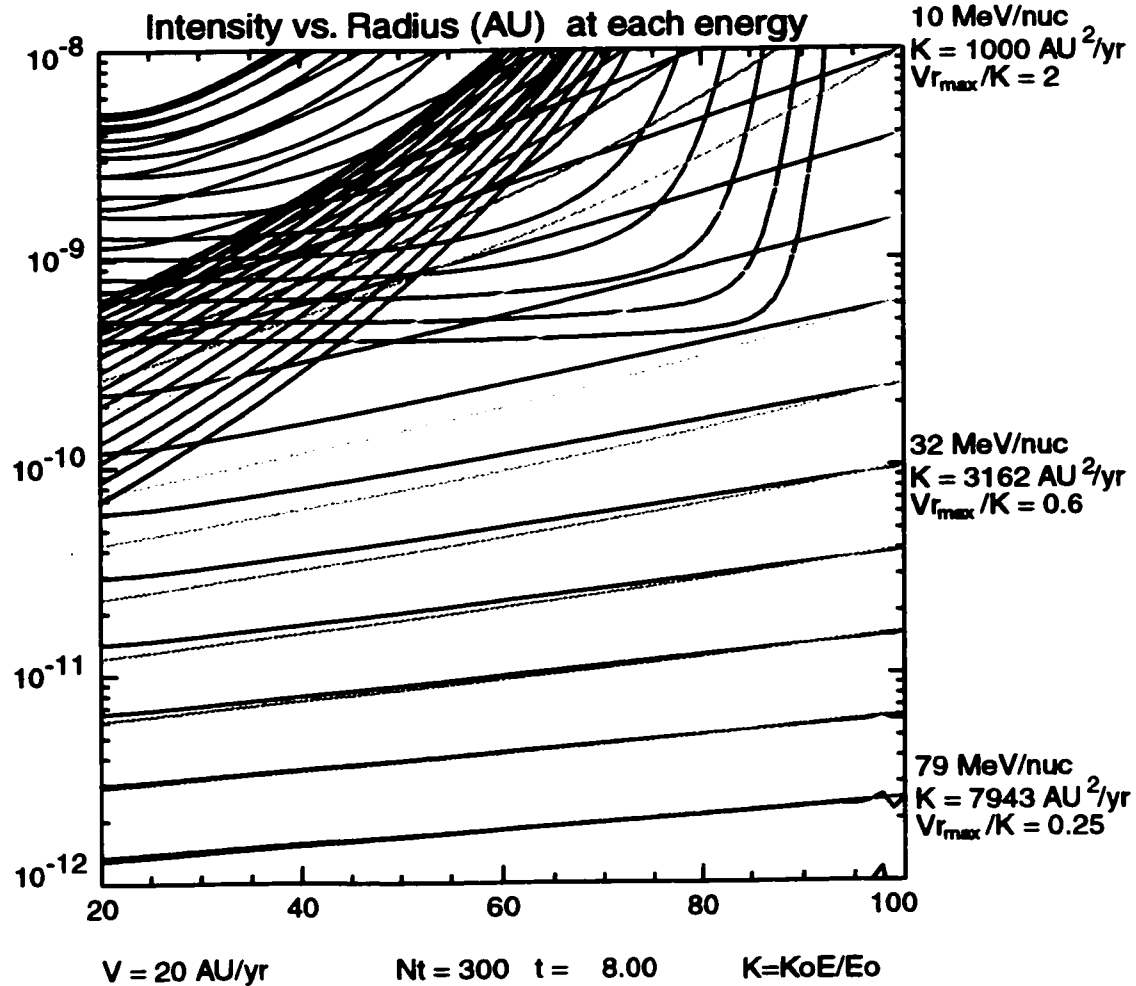


*Figure 3.5.1 Numerical Solution Compared with Force Field Approximation*  
*Intensity (in arbitrary units) is plotted against radius (AU) for the numerical model (black) and the force field approximation (color). Note the good agreement for the bottom, higher energy curves, where the approximation is most valid.*

### 3.5.3 – Format of Model Comparisons with Observations

Figure 3.5.2 shows the standard display format used in the comparison between observations and the numerical solutions. The block of parameters listed at the top of the figure is mostly for reference, as the important parameters of a particular numerical solution will be highlighted elsewhere. In the first line of parameters, in red, “Nx, deltax,” etc. refers to the number of grid points in the  $x$ ,  $y$ , or  $t$  direction (corresponding to  $r$ ,  $\log E$ , or  $t$ ) and the grid spacing for each dimension (unless the “NoEloss” parameter, see below, is equal to one, all of the  $y$ -parameters refer  $\log E$ ). The “min” and “max” values listed on the right hand side of lines one, three and four indicate the minimum and maximum value of the associated variable. In the second line, “Neumann, BCy” indicates the status of the boundaries. The status “Neumann = 1” indicates the inner radial BC discussed in section 3.5.2, while “Neumann = 0” indicates the  $j = 0$  BC at  $r = r_{\min}$ . When “BCy = 1” is displayed the aforementioned extrapolated BCs are used at the energy boundaries. The next set of parameters on the second line indicates whether the Lax method is used (“Lax = 1”) or not (“Lax = 0”) in the  $x$  or radial direction and whether this method is used (“NOyLax = 0”) or not (“NOyLax = 1”) in the  $y$  or energy direction. If “noEloss” (“yOnly”) is set to 1, this indicates that the energy (radial) dimension is turned off, otherwise all dimensions are active. “FUNCTION\_NAME” indicates the source code file containing the model specifications. The parameter “tyear0” indicates the calendar year to associate with the zero time in the solution and “tyear1, tyear2” indicate the minimum and maximum years displayed for the time profiles in panels (b), (e), and (g). The “halfyears” parameter indicates when zero that yearly model spectra are



shown in panels (a), (d), and (f), and when set to one, this indicates that semiannual spectra are displayed. The “nomidyear” parameter is zero when the annual spectra are plotted at the middle of each year and is one when each annual spectrum is shown at the start of each year. In line four, the SCALE parameter indicates the multiplication factor applied to the (arbitrary) intensity scale generated by the numerical solution. The next three scales “V1scale, V2scale, Earthscale” are multiplication factors that can be used to offset the normalization of the numerical solution shown at the V1, V2, or Earth positions. When all of these are equal to one, no relative offsets exist between the three positions. The numbers listed to the right of the “Energies(MeV/nuc)” label, on the fifth line, indicates the energies of the model particles shown in the time profile panels (b) and (e) and are selected to approximately equal the average energy of the data shown. The sixth line provides analogous information to the above, but is associated with panel (g).

The important parameters in blue on line seven, “V”, “Kappa\_o,Eo,GammaK”, and “Es,GammaS” refer to the symbols discussed in section 3.5.2, namely  $V$ ,  $\kappa_o$ ,  $E_o$ ,  $\gamma$ ,  $E_s$ , and  $\gamma_s$ , respectively (Figure 3.5.2). The cutoff energy,  $E_c$ , is indicated by the “cutoff” parameter shown in blue on the right side of the eighth line, and is equal to zero when the exponential roll-off is turned off at the outer source. The other parameters on line eight can be ignored. On line nine, the “Static” parameter indicates a time-saving feature that allows the numerical model to stop iterating after the time listed, but still allows the spatial motion of the spacecraft through the model heliosphere to be displayed. This feature is off when set to zero and is only used in

cases when the system is known to approach the steady state value early to save computational time.

In panels (a), (d) and (f) of Figure 3.5.2 energy spectra are shown. The annual observations for the three years, 1992, 1995, and 1999 are shown by the symbols (colored black, green, and red, respectively). The numerical solution is shown by solid lines at the time and position of the Voyager 1 and Voyager 2 spacecraft to facilitate direct comparisons, and are shown mid-year for 1992, 1995 and 1999 (colored black, green, and red, respectively). The same format is used for the numerical solution in panel (f), the inner heliosphere ( $r = 1$  AU), but the measurements are SAMPEX data averaged from 1993 to 1998 below 10 MeV/nuc, and are from late 1995 at and above this energy (§3.2.3).

In panels (b) and (e) of Figure 3.5.2 the model and observed time-intensity profiles are compared similarly to the spectral comparisons. Again the symbols represent the data and the lines indicate the model (with black, green-to-blue, and red indicating the low, medium and high energy listed with “Energies” parameter discussed above). In addition to showing the numerical solution along the spacecraft trajectory, the flat dashed curve (below each of the other usually increasing curves) shows the time profile at the fixed position occupied by the spacecraft at the initial time. In this way the differences between spatial and temporal features of the numerical solution can easily be distinguished. Panel (g) is analogous but for the inner heliospheric location. The “1AU Energies” parameter discussed above lists the low<sub>2</sub> and high<sub>2</sub> energies, shown in black and green, respectively. Of course since this panel shows a fixed position, only a single solid curve is plotted for each energy.

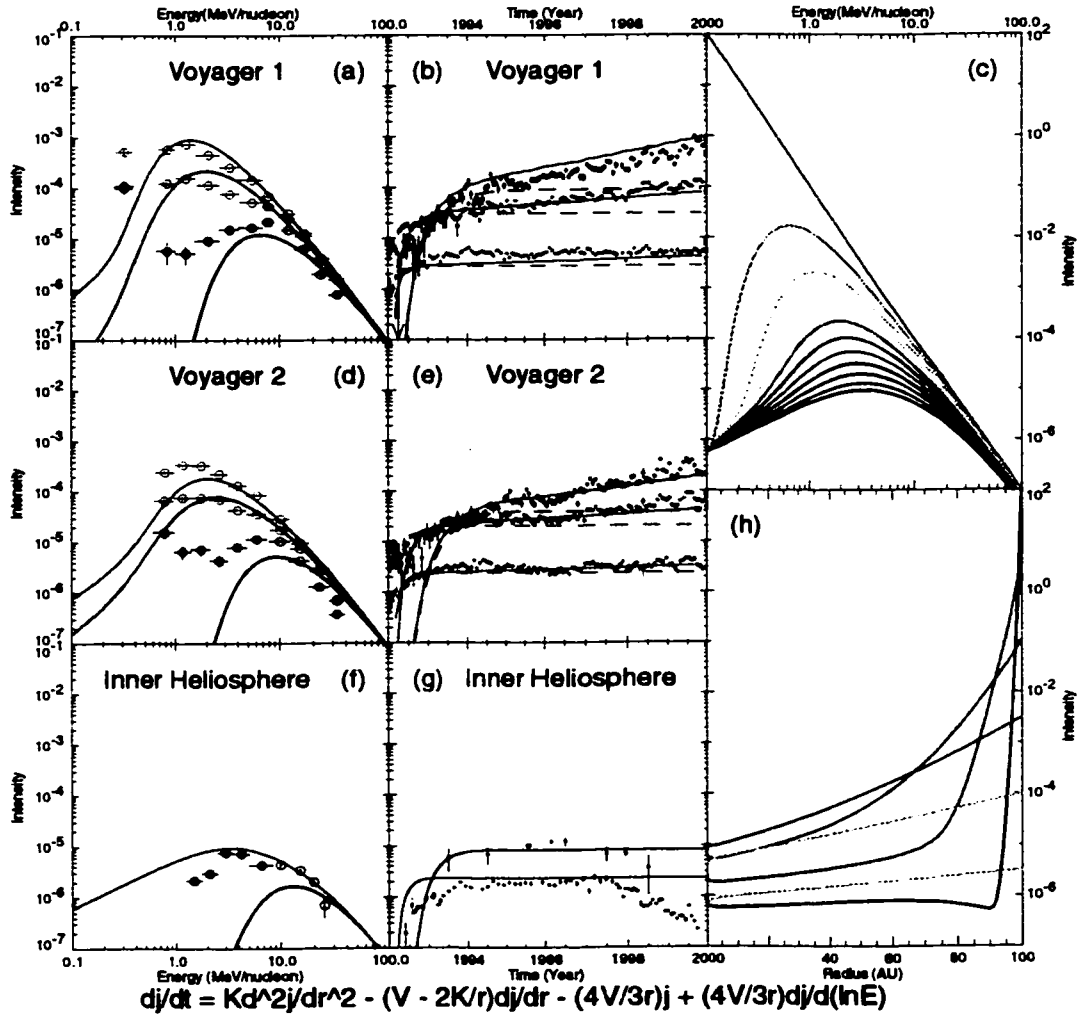
In the rightmost panels of Figure 3.5.2, (c) and (h), the numerical solution is displayed in a format that is not connected to the data, and in both cases, is at the final time  $t=t_{\max}$ , which in nearly all cases is indistinguishable from the steady state solution. Panel (c) contains a plot of the energy spectra at various radii, with the black line indicating the spectrum at  $r_{\min}$  and the red line, at  $r_{\max}$ , with 10-AU spacing between adjacent lines. In the final panel (h) radial profiles are presented at various energies, with the black curve showing the low-energy profile (at  $E_{\min}$ ) and red the high-energy ( $E_{\max}$ ) profile, as a function of radius. This display is useful for understanding the spatial intensity gradients of anomalous cosmic rays.

As a precursor to the next section, note the following interesting features of the specific numerical solution shown in this demonstration section (Figure 3.5.2). The four parameters,  $V$ ,  $\kappa_0$ ,  $\gamma$ , and  $\gamma_s$  were all selected before any data were directly compared with the model and were picked for the following general reasons. The outer source index was taken to be an integer that roughly matched the ACR oxygen spectra,  $\gamma_s = -3$ . The energy dependence of the diffusion coefficient was picked to depend on  $E$  in a simple manner,  $\gamma = 1$ , which follows from the commonly used  $\kappa \propto vR$  form of the diffusion coefficient. The solar wind speed and diffusion coefficient were picked to place the spectral peak at an energy with the right scale (1 MeV/nuc) and to yield a recovery time of one to two years, a general feature of the observed ACR recovery in solar cycle 22. These features were easily reached with the combination  $V = 20$  AU/year (95 km/s) and  $\kappa_0 = 100$  AU<sup>2</sup>/year ( $7.1 \times 10^{20}$  cm<sup>2</sup>/s). The surprising result of the first comparison with the data (Figure 3.5.2) was that the scale and general appearance of the numerical solution agreed reasonably with the data. In

particular, the data and model time profiles in panels (b) and (e) display similar slopes and the relative intensity offset between different energies has the right scale. The V1 1992 and 1999 observed spectra in panel (a) agree roughly with the numerical result in both intensity and peak energy and V2 has a fair agreement up to a small normalization. The general shape and scale of the SAMPEX spectrum in panel (f) is consistent with the model except at the lowest energies and finally, the intensities of both the low and high energy data at 1 AU in panel (g) are in surprisingly good agreement. The purpose of this discussion is not to rejoice in good luck but to make the following point. To the extent the agreement between the present simple numerical model and the data is considered good, it is emphasized that this is not the result of an exhaustive search of parameter space, but rather this results from the fact that this simple model appears to possess enough of the physics to naturally explain the bulk features of ACR transport during the most recent recovery period.

# Model Comparison with Data -- PDEplot.pro

Oxygen  
 Nx,deltax = 101, 0.995; Ny,deltay = 61, 0.050; Nz,deltaz = 2500, 0.003 ;tmin,tmax = 0.010, 8.000  
 Neumann,BCy = 1,0; Lax,NOyLax = 0,1; noEloss,yOnly = 0,0; FUNCTION\_NAME = PDE\_funct  
 tyear0,tyear1,tyear2 = 1992.00,1992.00,2000.00; halfyears,nomidyears = 0,0 xmin,xmax = 0.500,100.000  
 SCALE,v1scale,v2scale,Earthscale = 1.00E+02, 1.00E+00, 1.00E+00, 1.00E+00 ymin,ymax = -1.000, 2.000  
 Energies(MeV/nuc) = 1.70000 8.00000 25.00000  
 1AU Energies(MeV/nuc) = 2.00000 17.00000  
 V = 20.00; Kappa\_o,Eo,GammaK = 100.00, 1.00, 1.000; Es,GammaS = 0.10, -3.000; NologE = 0  
 testlimit = 0; A,B,C,D = 0.00, 0.00, 0.00, 0.00; noA,B,C,D = 0,0,0,0 cutoff = 0.00 MeV/nuc  
 Static = 6.00



$$K = K_0(E/E_0)^{\gamma_K}, j(r_{max}, E) = (E/E_s)^{\gamma_S}, \text{ \& } dj/dr|_{r_{min}} = 0$$

Fig 3-5-2 meh diss.EPS

Mon Oct 29 13:49:00 2001

**Figure 3.5.2 Demonstration Solution to the Cosmic Ray Transport Equation**  
 This figure represents the initial fit of the model to the data using parameters selected merely to obtain the proper scale. The format is described in section 3.5.3.

### 3.5.4 – Model Comparisons with Observations

The general agreement that is seen in the demonstration solution of Figure 3.5.2 has a problem, namely the value for the solar wind speed  $V = 20$  AU/yr (95 km/s) is at least a factor of four smaller than typical (low latitude) solar wind speeds. By scaling this solution in such a way that a more reasonable solar wind speed obtains either the temporal or spatial scale of the solution (or a combination of the two) must be altered. For example, by increasing the length scale by a factor of 4, the new transport parameters become,  $V = 80$  AU/yr (380 km/s),  $\kappa_0 = 1600$  AU<sup>2</sup>/yr ( $1.1 \times 10^{22}$  cm<sup>2</sup>/s),  $t_{\max} = 8$  yr, and  $r_{\max} = 400$  AU. This scaling retains the ~2-year initial recovery time-scale seen in the measurements, but the comparisons at the spacecraft are no longer valid due to the change in the length-scale, and the size of the heliosphere becomes much larger than the ~100 AU size expected (see section 3.4.4 for a discussion of the heliospheric size). By changing the temporal scaling by one-fourth a similar comparison could be made, but the relative agreement of the demonstration solution during the initial recovery period would be lost. The present model assumes an empty heliosphere and transport with a constant diffusion coefficient. In reality a better model would be to start with a nearly empty heliosphere and gradually change the diffusion coefficient from the solar maximum to the solar minimum value, which might change by an order of magnitude (see section 5.2.1). However, since it is not the intent of this work to model the details of the initial recovery, but rather primarily to understand the distinct temporal and spatial variations after this period ends (i.e., after ~1994), the modeling goal becomes to find agreement

with the spectra and time-intensity profiles after the initial recovery period ends. This has been done with reasonable values for the source radius and the solar wind speed and the summary is displayed in Figure 3.5.3.

Roughly speaking, the Figure 3.5.3 solution (hereafter the second solution), is a modification of the first demonstration solution with a time re-scaling factor of 1/4, i.e., substitute the time unit everywhere with a unit 1/4 as large (e.g., substitute 1 year with 1/4 year in all quantities containing units of time, like  $V$  and  $\kappa_0$ ). In this way, in the new scaling, the values of the solar wind speed and diffusion coefficient both increase by a factor of four, which is roughly what we have done for the second solution. In addition, the other transport parameters were adjusted to try to improve the quality of the late-recovery spectral fit and time-intensity profiles at Voyager 1. The power-law energy index of the diffusion coefficient was kept at one yielding  $\kappa = \kappa_0 E/E_0$ , with  $E_0 = 1$  MeV/nucleon (in this case the rigidity index  $\eta$  of the scattering mean free path  $\Lambda$  is also unity). The source spectrum used has the form provided by Steenberg and Moraal (1999)  $j_s(E) = (E/E_s)^{\gamma_s} \exp(-b(E/E_c)^a)$  as discussed above (§3.5.2), with  $\gamma_s = -2.4$  and  $E_c = 20$  MeV/nucleon chosen based purely on the quality of the fit ( $E_s = 0.10$  MeV/nucleon provides an arbitrary normalization). The solar wind speed is  $85 \text{ AU/yr} = 400 \text{ km/s}$ , a typical value, and the diffusion coefficient for 1-MeV/nucleon particles  $\kappa_0$  is  $450 \text{ AU}^2/\text{yr}$  ( $3.2 \times 10^{21} \text{ cm}^2/\text{s}$ ), also selected to achieve a good fit to the data.

First it should be noted that the second solution shares all of the general features of agreement with the data that the demonstration solution has, as discussed at the end of section 3.5.3, except for the time-scale of the initial recovery. In addition

the agreement of the post-1994 V1 time-intensity profiles (Figure 3.5.3b) is significantly improved, as the relative intensities between the 1.7-, 8.0-, and 25-MeV/nucleon profiles are much closer to the data, while the agreement of the rates of increase is just as good. (As with the first solution, no normalization between spacecraft has been used here.) The 1999 V1 spectrum (a) agrees about as well as in the first solution, but the second solution reproduces the flatter spectral shape just above the peak energy, as well as the steeper slope above 10 MeV/nucleon. As in the first solution, the 1995 V1 model spectrum does not well-reproduce the similar, but more pronounced, flattening above the peak. Since the recovery is much more rapid in this model, the 1992 model spectrum does not fit the observations as well as the demonstration solution. (As discussed in section 3.2.2, no attempt has been made to match the model to the lowest-energy V1 oxygen point.) The agreement with the SAMPEX data at 1-AU is a bit worse for the second solution (Figure 3.5.3f and g), than for the first (Figure 3.5.2f and g) but is still remarkably good considering the simplicity of the model.

The comparison between this model and the analyses of sections 3.3.4 and 3.4.4 is interesting. The non-local radial gradients for the steady state numerical solution were calculated at three energies, from 50 to 70 AU, to be directly comparable with those listed in Table 3.4.1, and the agreement with the quasi-local gradient measurements (§3.4.4) was fair, and reasonably good with the phenomenological model results (§3.3.3, Table 3.3.2), as shown in Table 3.5.1. It should be emphasized that the radial gradients determined from the numerical models (the first model is not dissimilar to the second, as a comparison of panel (h) of Figure



3.5.2 and 3.5.3 shows) were not based on any assumptions concerning the relative importance of temporal vs. spatial variations, and indeed once the solar wind speed was fixed to a nominal value (400 km/s) and it was decided to keep the diffusion coefficient simple by using  $\gamma = \eta = 1$ , effectively the only free parameters were  $\kappa_0$ ,  $\gamma$  and  $E_c$ . Given this independence from the other methods (both of which do assume that the temporal dependence becomes weaker with time), the reasonable agreement of the radial gradients supports the assumptions and methods used in the previous sections.

**Table 3.5.1 ACR O<sup>+</sup> Radial Gradients (%/AU) Calculated by Three Methods**

	$E$ (MeV/nuc)	Numerical Model <sup>a</sup>	Phenomenological Model <sup>a,b</sup>	Quasi-Local Measurement <sup>a,c</sup>
O <sup>+</sup>	1.3	8.3	9.6	11.2 ± 1.1
O <sup>+</sup>	6	3.5	4.4	6.8 ± 0.8
O <sup>+</sup>	21	1.7	1.2	-0.2 ± 0.5

<sup>a</sup> Radial gradients from ~50 to 70 AU.

<sup>b</sup> See section 3.3., Table 3.3.2.

<sup>c</sup> See section 3.4, Table 3.4.1.

The relation between the diffusion coefficient and the scattering mean free path,  $\kappa = v\Lambda/3$ , when expanded in terms of the assumed dependencies becomes  $\kappa_0(E/E_0)^\gamma = v/3 \Lambda_0(R/R_0)^\eta$ . Using  $R/R_0 = 43.3A(E/E_0)^{\eta/2}/z$  and  $v = (2c/43.3)(E/E_0)^{1/2}$ , where  $E_0 = 1$  MeV/nucleon and  $R_0 = 1$  MV define the units, and the value 43.3 is the square root of twice the nucleon rest energy in units of MeV, we obtain,

$$\kappa = \kappa_0 \left( \frac{E}{E_0} \right)^\gamma = \Lambda_0 \frac{2c/3}{43.3} \left( 43.3 \frac{A}{z} \right)^\eta \left( \frac{E}{E_0} \right)^{\frac{1-\eta}{2}} = \frac{v\Lambda}{3}, \quad (3.5.3)$$

from which we get  $\eta = 2\gamma - 1$  and  $\Lambda_0 = (\kappa_0/974 \text{ AU/yr})(43.3 A/z)^{-\eta}$ . For the case where  $\gamma$  and  $\eta$  are unity we have  $\Lambda_0 = (\kappa_0 z/A)2.37 \times 10^{-5}$  AU, where  $\kappa_0$  is in units of

$\text{AU}^2/\text{yr}$ . With this we can calculate the implied scattering mean free path for ACR oxygen ( $A=16$ ,  $z=1$ ) at selected rigidities for the present case of  $\kappa_0 = 450 \text{ AU}^2/\text{yr}$ , from the relation,

$$\Lambda = 0.67 \text{ AU R/GV}. \quad (3.5.4)$$

For anomalous  $\text{O}^+$  at 800, 1700, and 3300 MV (1.3, 6, and 22 MeV/nucleon), the scattering mean free paths in the interplanetary medium are found to be 0.54, 1.1, and 2.2 AU, respectively. These figures happen to agree rather well with the analogous values (0.54, 1.0, and 2.0 AU) calculated from the piecewise rigidity dependence Steenberg (1998) used to best fit ACR and GCR spectra from 1997 with a time dependent drift model.

The cutoff energy  $E_c$  characterizes the exponential roll off of the power law source spectrum. Although the data do not heavily constrain the selection of this energy, it was nevertheless selected, along with the other parameters, to best match the observations, as described above. Since the initial recovery is completed within about two years of the start of the recovery and the ACR source is constant for several years after this time, this cutoff energy is not due to the acceleration time, but is likely to be the cutoff due to the local curvature of the termination shock, (as discussed by Drury, 1983), which occurs where the diffusive length scale  $\kappa/V$  is approximately the radius of curvature of the shock front  $r_s$ . For  $E_c = 20 \text{ MeV/nucleon}$  with  $\kappa = \kappa_0 E/E_0$ , and the parameter values given above, the ratio of the length scales is found to be  $Vr_s/\kappa = 0.94$ , just what would be expected were this cutoff due to the geometry of the source shock. It is noted that this disagrees with the work of Steenberg and Moraal (1999) who find that the cutoff energy should occur when the ratio  $Vr_s/\kappa$  is approximately 10. It is not

ruled out that a solution could be found with the present model that meets the  $Vr_s/\kappa \approx 10$  criterion, but it is seen that this condition is not a necessary one. The 20-MeV/nucleon cutoff is slightly higher than, but closer to that of Stone, Cummings and Webber (1996), who observe a roll-off in ACR oxygen above 10-15 MeV/nucleon in 1993 and 1994 Voyager and Pioneer spacecraft observations. It cannot be ruled out based on this analysis that the cutoff energy could be due to the maximum allowable energy per charge ( $\sim 240$  MeV/charge) expected for particles drifting from the heliospheric polar region to the equatorial plane (Pesses, Jokipii, and Eichler, 1981), since the cutoff energy  $E_c$  corresponds to 320 MeV/charge for singly ionized oxygen and 160 MeV/charge for double ionized oxygen (see section 1.1.4). If doubly charged oxygen is negligible in ACRs then the present observations strain the 240 MeV/charge interpretation, but the possible existence of such multiply charged ions (Mewaldt *et al.*, 1996) makes this interpretation a possibility.

Diffusive shock acceleration theory (Drury, 1983) predicts the momentum dependence of the distribution function to be  $\partial \ln f / \partial \ln p = -3V_U / (V_U - V_D)$ , where  $V_U$  and  $V_D$  are the solar wind velocities immediately upwind and downwind of the termination shock, respectively. It is customary to define a compression ratio  $s = V_U / V_D$  in terms of which the energy power-law index of the source spectrum can then be written  $\gamma_s = -(s + 2) / (2s - 2)$ , or likewise  $s = 2(\gamma_s - 1) / (2\gamma_s + 1)$ , in the non-relativistic limit. As the compression ratio is one of the key characteristics of a shock, it is of interest to determine what the source spectrum ( $\gamma_s = -2.4$ ) of the second model yields. For this case the compression ratio is  $s = 1.8$ , a so-called *weak* shock, where  $s = 4$  is considered a strong shock (see Eq. 2.46 of Drury, 1983). The source index found with the third

phenomenological model (Figure 3.3.6) was  $\gamma_s = -1.5$ , for which the compression ratio would be  $s = 2.5$ , still a weak shock. Stone, Cummings and Webber (1996) also determined the existence of a weak shock ( $s = 2.63 \pm 0.14$ ) when they fit 1993 and 1994 outer heliospheric ACR spectra with a spherically symmetric equilibrium model of ACR propagation.

More qualitatively, but importantly, an examination of the model comparisons with the Voyager 1 and the Voyager 2 data provides information concerning the latitudinal gradients. Since the model employed is spherically symmetric and the parameters were chosen to fit the V1 data (since the latitudinal variation there is negligible) the V1 and V2 model spectra (Figure 3.5.3a and d) are for absolute latitudes of  $\sim 33$  degrees. Therefore, the V2 data need to be compared to the V2 model spectra with this in mind. The 1999 spectral data at V2 are seen to be higher than the model values below about 4 MeV/nucleon and the data are lower the model above  $\sim 20$  MeV/nucleon. A positive latitudinal gradient at the higher energy range would explain the disagreement there, since the data are at a lower latitude than the model and therefore have a lower intensity level. For the low-energy discrepancy a negative latitudinal gradient of a magnitude larger than the higher-energy case would bring the model into closer agreement with the data, by increasing the lower-latitude V2 model to a higher flux level compared with the nominal 33 degree latitude baseline. These qualitative observations, of course, are just what has been seen in the two latitudinal gradient determinations already made (Table 3.4.1); namely, a positive latitudinal gradient of 0.9 to 2.9 %/degree for 12-29 MeV/nucleon O, and negative latitudinal gradients of -4.2 to -5.5 %/degree for 0.6- to 3-MeV/nucleon O. The factors by which

the model data should be multiplied to account for the latitudinal gradients from 33 to 20 degrees, i.e.,  $\Delta\lambda = -13$ , are 0.69 and 2.0 for the high and low energies, respectively (where the best agreement was found when the larger magnitude of the given gradient ranges were used). These factors are just about the same as the factors separating the model and data at the specified energies in Figure 3.5.3d. This independent, if rough, confirmation of the latitudinal gradients from sections 3.3 and 3.4, along with the analogous comparison of the radial gradients dealt with in Table 3.5.1, constitutes the final bit of evidence composing the threefold agreement of the procedures we used to distinguish between the spatial gradient and temporal variation effects on the Voyager ACR intensities.

The methods all agree that the higher energy ions, specifically ACR oxygen above about 10 MeV/nucleon, have small positive latitudinal and radial gradients during the solar cycle 22 recovery phase. As has been addressed, this result agrees with the results of other investigators for similar ions. All three methods also find negative latitudinal gradients for the lower energy ions except in cases where certain parameters are given unreasonable values (such as the too-large 240 AU source radius in section 3.3.4 and the too-small 20 AU/yr (95 km/s) solar wind speed of section 3.5.3 and this section).

## Model Comparison with Data -- PDEplot.pro

**Oxygen**

Nx,deltax = 81, 1.238; Ny,deltay = 41, 0.075; Nt,deltat = 6000, 0.001 ;tmin,tmax = 0.010, 8.000  
 Neumann,BCy = 1,0; Lax,NOyLax = 0,1; noEloss,yOnly = 0,0; FUNCTION\_NAME = PDE\_funct  
 tyear0,tyear1,tyear2 = 1992.00,1992.00,2000.00; halfyears,nomidyears = 0,0 xmin,xmax = 1.000,100.000  
 SCALE,v1scale,v2scale,Earthscale = 8.00E+00, 1.00E+00, 1.00E+00, 1.00E+00 ymin,yymax = -1.000, 2.000  
 Energies(MeV/nuc) = 1.70000 8.00000 25.00000  
 1AU Energies(MeV/nuc) = 2.00000 17.00000  
 V = 85.00; Kappa\_o,Eo,GammaK = 450.00, 1.00, 1.000; Es,GammaS = 0.10, -2.400; NologE = 0  
 testlimit = 0; A,B,C,D = 0.00, 0.00, 0.00, 0.00; noA,B,C,D = 0,0,0,0 cutoff = 20.00 MeV/nuc  
 Static = 1.70

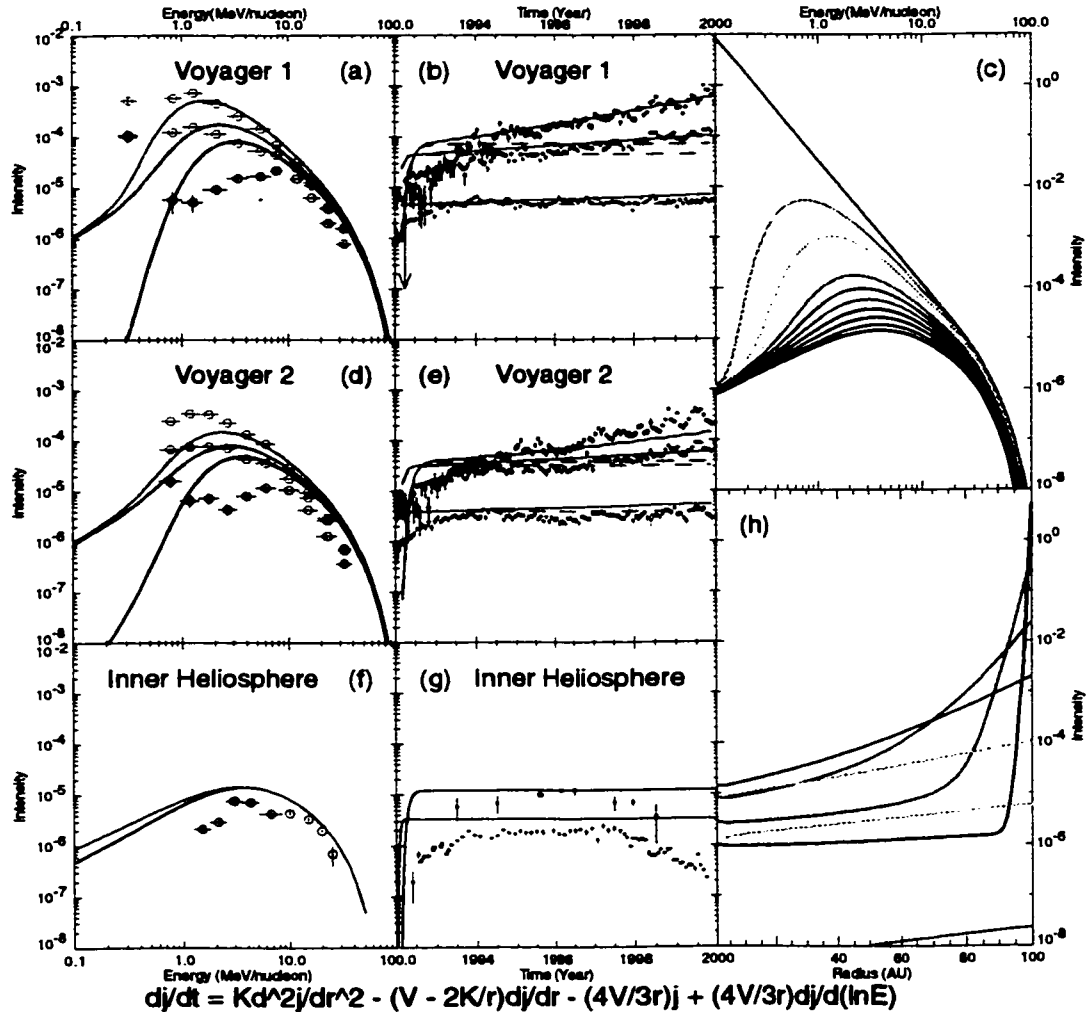


Fig 3.5.3 meh diss.EPS

Mon Oct 29 14:25:25 2001

*Figure 3.5.3 Numerical Solution with Optimized Late-Recovery Agreement*  
 The solution represented above has been optimized to match the Voyager 1 observations. The format is discussed in section 3.5.3.

## **Chapter 4 – Periodic ACR Phenomena**

Statistically significant variations have been observed in the differential flux of ~27-MeV anomalous cosmic ray (ACR) oxygen, helium, and protons at the Voyager 1 spacecraft during 1998 and 1999 (at a helioradius of ~73 AU). The quasiperiodic variations are in phase, with oxygen and helium having periods near 151 days, while protons exhibit a period of ~146 days. The Voyager 1 ACRs vary by ~30% with respect to the trend, and similar galactic cosmic ray variations, if they exist, must be less than ~5%, probably much less. No similar, significant periodicities have been detected for these same ACR species at Voyager 2 (at 57 AU) during this period. We report on these and other periodicities in the Voyager Low Energy Charged Particle experiment measurements and address the possible connection between this ~151-day ACR periodicity and the previously discovered ~154-day periodicities in solar flares, the interplanetary magnetic field, and other phenomena. Most of the work from this chapter was first presented in a paper by Hill, Hamilton, and Krimigis (2001).

### **4.1 – Introduction**

Many authors during the previous two decades have observed periodicities ranging from ~150 to 158 days in a variety of solar and heliospheric measurements. Rieger *et al.* (1984) first identified such a variation in their report of a 154-day periodicity in the occurrence rate of solar gamma ray flares measured by the Solar Maximum Mission during 1980-1983. Subsequently, similar periodicities have been observed in other solar flare phenomena, such as X-ray measurements (Bai and Sturrock, 1987; Brueckner and Cook, 1990; Dennis, 1985), H $\alpha$  flares (Ichimoto *et al.*,

1985), 10.7-cm radio flux (Lean and Brueckner, 1989; Kile and Cliver, 1991), other microwaves (Bogart and Bai, 1985), solar flare electron events (Droge *et al.*, 1990), proton flares (Bai and Cliver, 1990), and various solar flare indices (Bai and Sturrock, 1993; Ozguc and Atac, 1989). In addition to these flare measurements, similar periodicities were also found in historical and modern sunspot measurements (Lean and Brueckner, 1989; Lean 1990; Carbonell and Ballester, 1990), solar diameter observations (Delache *et al.*, 1985; Ribes *et al.*, 1989), and auroral data (Silverman, 1990). These investigations have confirmed the existence of this periodicity as a more general solar oscillation during solar cycle 21 (1976-1986) and suggest that similar periodicities exist in other recent solar cycles and historical data, although the status for other solar cycles is less certain than for cycle 21 (see, e.g., Bai and Cliver, 1990, Table 4). Apart from these phenomena, observations have been made that indicate roughly 154-day periodicities in the near-Earth interplanetary magnetic field strength and solar wind speed (Cane *et al.*, 1998) and in solar proton events (Gabriel *et al.*, 1990). Recently, recurrences in Ulysses spacecraft measurements of MeV proton fluxes and anisotropies were reported (Dalla and Balogh, 2000; Dalla *et al.*, 2001) that may also be related to these periodicities.

Cosmic ray measurements indicating periodicities near 154 days, however, have not yet been fully explored. Kudela *et al.* (1991) did analyze 3- and 6-month periodicities in data from the Calgary and Deep River neutron monitors but did not address periodicities near 154 days. Cosmic ray intensity measurements made at the Deep River neutron monitor and Huancayo ion chamber during 1947-1990 were examined spectrally by Valdes-Galicia *et al.* (1996), and a ~154-day peak is evident in



their solar cycle 21 analysis, but, although aware of the work of Ichimoto *et al.* (1985), they did not investigate a relationship between the solar flare and cosmic ray periodicities. Likewise, three roughly 1/4-year-wide intensity variations were observed by Decker *et al.* (1999) in anomalous cosmic ray (ACR) H and He measurements at the Voyager 2 spacecraft in 1995, but no connection was examined between these small-amplitude variations and the 154-day solar periodicity. The cause of the 154-day solar and heliospheric oscillations is not yet known, although physical mechanisms that might explain the periodicities have been explored, such as (1) the global solar “clock” model of Bai and Sturrock (1993), (2) the suggestion that the period may be a manifestation of the timescale required for storage and emergence of magnetic flux through the solar surface (Ichimoto *et al.*, 1985; Carbonell and Ballester, 1990; Cane *et al.*, 1998), and (3) the beat frequencies of rotational rates proposed by Wolff (1983) to be due to solar “g-mode” oscillations.

In the present paper, 1998 and 1999 measurements from Voyager 1 (V1) and Voyager 2 (V2) are both visually and harmonically analyzed, revealing statistically significant variations in V1 ACR O, He, and H fluxes, all in phase with periods of ~151 days. This work appears to be the first to present evidence relating cosmic ray variations or outer heliospheric (>5 AU) measurements to the established 154-day solar and heliospheric periodicities. The lack of such a periodicity is noted for V2 anomalous cosmic rays, although some other periodicities at V2 and V1 exist. In sections 4.2 and 4.3 the details of this analysis and the numerical observations are presented, followed by a discussion in section 4.4 of the physical implications of the anomalous cosmic ray periodicities.

## **4.2 – Data Analysis**

### **4.2.1 – Residual Intensity Variations**

The Low Energy Charged Particle (LECP) experiments aboard the two Voyager spacecraft (Krimigis *et al.*, 1977) return composition and differential flux measurements of energetic ions ( $\sim 0.3$  to 30 MeV/nucleon) in the distant heliosphere. From the first day of 1998 to the last day of 1999 the helioradii of V1 and V2 increased from 68.9 to 76.3 AU and from 53.7 to 59.9 AU, respectively. During this period the heliolatitudes of the Voyagers changed from  $33.3^\circ$  to  $33.6^\circ$  N for V1 and from  $18.4^\circ$  to  $21.1^\circ$  S for V2. We use these LECP measurements (derived from  $dE/dx$  versus  $E$  pulse height data) to investigate the periodic behavior of the three ACR species for which we have sufficient counting statistics during 1998 and 1999 to allow meaningful periodogram analysis (see below). The kinetic energy ranges studied for these ACR protons, helium, and oxygen at V1 are 23.9-29.5, 2.99-11.5, and 0.65-2.64 MeV/nucleon, respectively, and 24.4-28.6, 3.71-12.3, and 0.60-2.13 MeV/nucleon, respectively, at V2. These energy ranges were selected to correspond with the ACR flux peaks (at  $\sim 27$  MeV for each species) observed in the energy spectra of these particles during the period of 1994-1999 (Hamilton *et al.*, 1999).

Although the  $\sim 150$ -day flux variations of  $\sim 20$ -50% with respect to the trend were initially observed in 26-day averaged data (Figure 4.1a), 5-day averages are used for the bulk of our analysis, as these finer time-resolution data afford a high level of

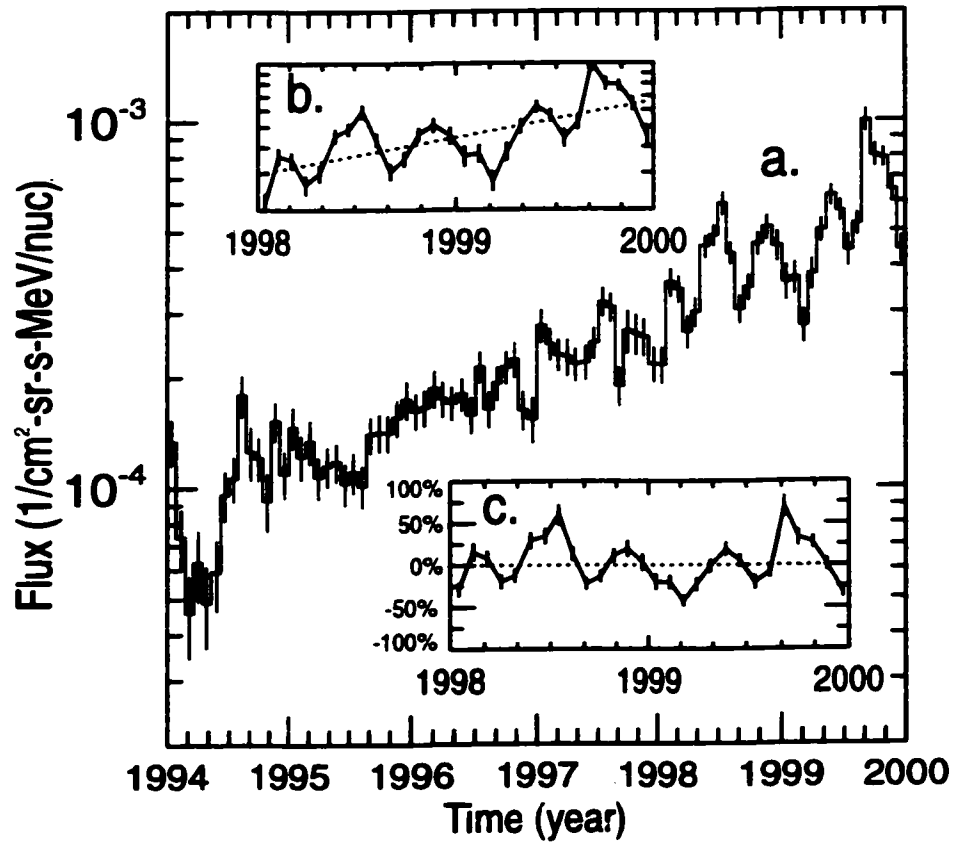


**Figure 4.1 Periodicity in the Voyager 1 Oxygen Time-Intensity Profile**  
 (a) The 26-day averaged flux of 0.65 – 2.64 MeV/nucleon V1 ACR Oxygen, (b) The same data in 1998-1999 with the trend (dotted line). (c) The percentage residual intensity variation.

confidence in the statistical significance of the periodicities. The 1998-1999 period exhibited more nearly periodic ~150-day oscillations and larger-amplitude variations than other time periods in the 1994-1999 interval. Therefore this 2-year period was selected as the primary period of interest for this study; however, in 1997, although the “period” varies (Figure 4.1a), there are two or three additional cycles with a roughly 150-day period preceding the five cycles in 1998-1999. The approach to the analysis of these variations has been to first determine the trend function for the data (Figure 4.1b) and then to remove this trend, yielding the residual variations from the trend (Figure 4.1c). A linear least squares fit to the log of the flux,  $\log j(t)$ , was used to determine the trend function,  $f(t)$ , having the form  $f(t) = N \exp[(t-t_0)/\tau]$ , where  $t_0$  is the year 1998 throughout and  $N$  and  $\tau$  (which correspond to the flux levels at the beginning of 1998 and the e-folding times, respectively) are determined by the fitting procedure. The residual intensity variation,  $J(t)$ , is defined by the relation,  $J(t) = [j(t) - f(t)]/f(t)$ . Residuals are plotted for both 26-day averaged (solid line) and 5-day averaged (open symbols) data in Figure 4.2. Before implementing the periodogram analysis, the data are further prepared by transforming to zero-mean time series.

#### 4.2.2 – Periodogram Analysis

The periodogram analysis method of Scargle (1982) has been used to harmonically analyze the periodicities in question, as it permits a straightforward interpretation of the statistical significance of a given periodicity and easily accounts for the few short data gaps in the 5-day averaged data. With this method the periodogram is determined, giving the spectral power,  $P(\nu)$ , at a given frequency  $\nu$ .

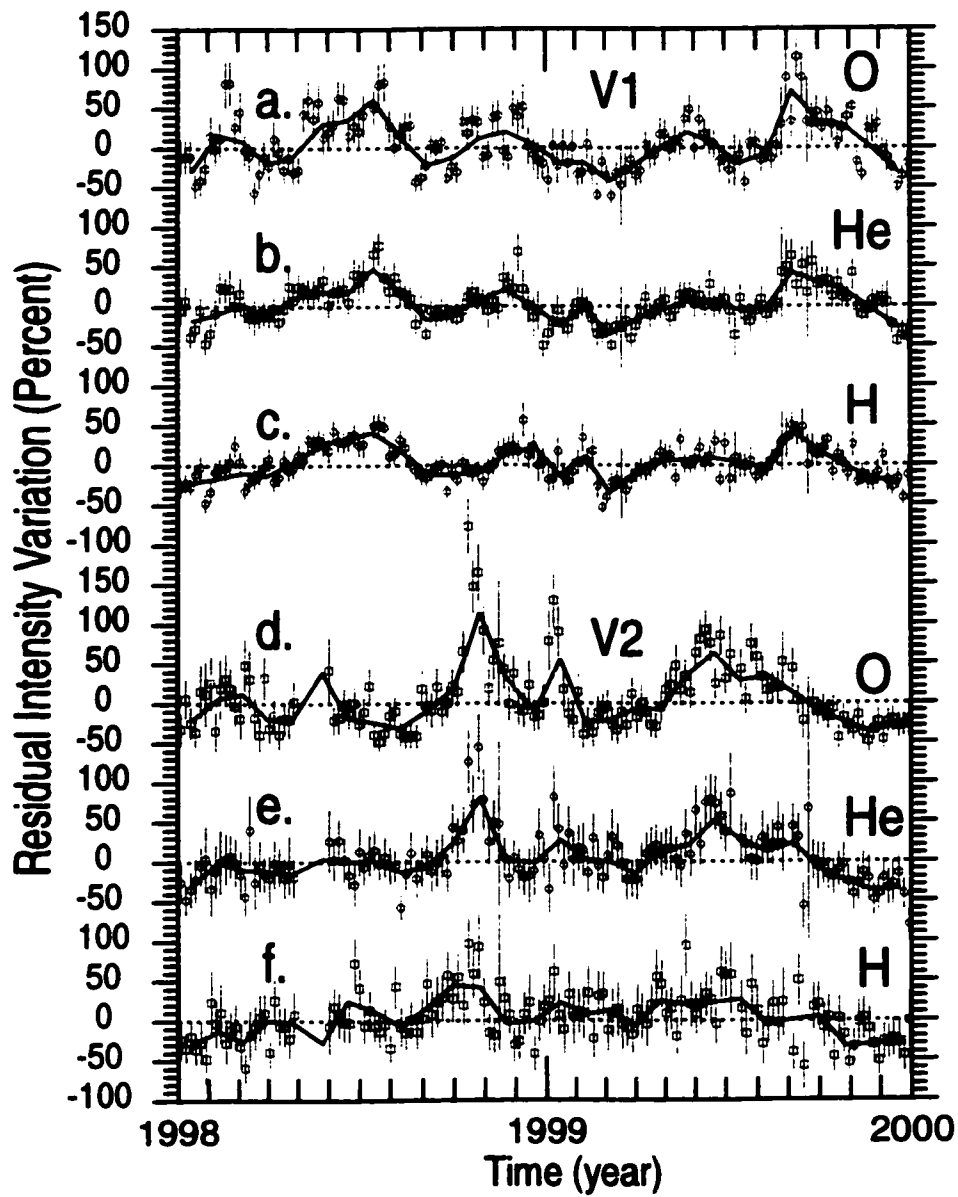


**Figure 4.2 Residual Intensity Variations of H, He, and O in 1998-1999**  
 The 26-day (solid line) and 5-day (open symbols) ACR residuals for V1 (a) O, (b) He, and (c) H, and V2 (d) O, (e) He, and (f) H with respective mean energies of 1.6, 7.2, 2.7, 1.4, 8.0 and 27 MeV/nucleon.

When normalized by the total statistical variance,  $\sigma_o^2$ , of the data (see Horne and Baliunas, 1986), the periodogram of Scargle (1982) has the useful property that the statistical significance at a single preselected frequency,  $\nu$ , is determined by  $\exp(-z)$ , where  $z = P(\nu)/\sigma_o^2$  is the normalized power, a dimensionless quantity. We indicate the statistical significance with the notation  $n\sigma$ , where  $\sigma$  is the Gaussian standard deviation,  $n$  is a numerical coefficient, and  $p_{\text{sig}}(n\sigma)$  (the integral of the Gaussian distribution,  $\exp(-x^2/2\sigma^2)/(2\pi\sigma^2)^{1/2}$ , from  $x = -n\sigma$  to  $x = +n\sigma$ ) is equal to the statistical significance. Therefore the normalized power is related to the statistical significance by  $1-e^{-z} = p_{\text{sig}}(n\sigma)$ , as the  $\sigma$  labels on the right side of Figure 4.3 illustrate. Another useful measure provided by Scargle (1982) is the false alarm probability,  $F=1-(1-e^{-z})^M$ , which, for a periodogram with  $M$  independent frequencies, determines the probability of observing a single peak at or above a given height,  $z$ , assuming the data were pure noise;  $p_o = 1-F$  therefore gives the probability that a given peak with a maximum normalized power of  $z$  or higher is the result of a signal rather than noise. This probability,  $F$ , supplements the statistical significance by taking into account that a larger number of searched independent frequencies implies a larger probability for statistical fluctuations to generate an erroneous periodogram peak with power of a given level. With  $p_o = 99.7\%$  and  $z = -\ln(1-p_o^{1/M})$ , we found  $z = 9.0$  to be the false alarm threshold for the periodograms shown in Figure 4.3. This threshold uses  $M = 24$ , where  $M$  has been determined by calculating the number of Fourier frequencies (see Scargle, 1982, Appendix D) that lie within the 40- to 400-nHz frequency range (see below) of the periodograms in Figure 4.3. The frequency resolution, defined by the spacing,  $\delta\nu =$

15.8 nHz, between independent frequencies, is the inverse of the total analysis period, in this case two years. Therefore it follows that  $M = \Delta\nu/\delta\nu + 1 = 24$ , where  $\Delta\nu = (400-40) \text{ nHz} = 360 \text{ nHz}$  is the frequency range interval. The alternate use of the empirical method of Horne and Baliunas (1986) to estimate the number of independent frequencies rather than that of Scargle (1982), results in a higher value for  $M$  since in this case the frequency spacing,  $\delta\nu_{\text{EB}}$ , is smaller than that given above. This is determined from  $\delta\nu_{\text{EB}} = \Delta\nu'/(M'-1) = 6.07 \text{ nHz}$ , where  $\Delta\nu' = (1157.4-15.8) \text{ nHz} = 1141.6 \text{ nHz}$  is the unrestricted frequency interval defined by the Nyquist frequency and the inverse of the 2-year analysis period and  $M' = 189$  is the number of independent frequencies obtained with the *Horne and Baliunas* [1986] method for time series with 146 data points (the number of data points in a 2-year series recorded at 5-day intervals). With this we find  $M_{\text{EB}} = \Delta\nu/\delta\nu_{\text{EB}} + 1 = 60$ , resulting in the somewhat higher false alarm threshold of  $z = 9.9$ , but this is an unimportant distinction for our purposes, so we retain the previously determined threshold. Although we show only the results of periodogram analysis of the 5-day averages in Figure 4.3, we also performed power spectral density analysis (see Press *et al.*, 1989), based on a discrete Fourier transform, as well as periodogram analysis, on the 26-day averages, finding essentially the same results, with nearly identical peak centers and widths.

It is important to note that although a fine-frequency grid has been employed, resulting in the smooth appearance of the periodograms in Figure 4.3, the meaningful frequency resolution remains, nevertheless, constrained by the independent, or Fourier, frequencies. We have  $\delta\nu = 15.8 \text{ nHz}$ , which is comparable to the typical peak widths and peak spacing in the periodograms in Figure 4.3. This somewhat coarse

frequency resolution, due to the relatively short 2-year analysis period relative to the 151-day period, limits our ability to distinguish between pure and quasiperiodicities, on the basis of the periodogram, unless the scale of the peak or spectral feature is significantly larger than 16 nHz. However, one may still return to the time domain and obtain a measure of the pure or quasiperiodic nature of a variation by comparing features in adjacent cycles of the time series, as is done in section 4.4. The lower limit of the 40- to 400-nHz frequency range in Figure 4.3 was selected as a compromise choice between requiring either two or three complete cycles during the 2-year analysis period. The 2-cycle (32 nHz) threshold is of use since, with fewer than two cycles of repetition, an accidental coincidence of two time-intensity features cannot reliably be distinguished from a true periodicity, while the 3-cycle (48 nHz) minimum provides added confidence by ensuring agreement among two or more periods between adjacent, repeated time-intensity features. The 400-nHz upper limit was chosen so as to yield an order-of-magnitude range as well as to exclude frequencies higher than a frequency (445 nHz) defined by our customary 26-day averaging interval.

#### **4.2.3 – Galactic and Interplanetary-Accelerated Particles**

In addition to ACRs we analyzed two other particle populations accessible to the LECP instrument to see if they also exhibited ~150-day periodicities: interplanetary (IP) accelerated particles and galactic cosmic rays (GCRs). Conditions in the outer heliosphere for IP ions such as ~1-MeV protons are still quiet during 1998



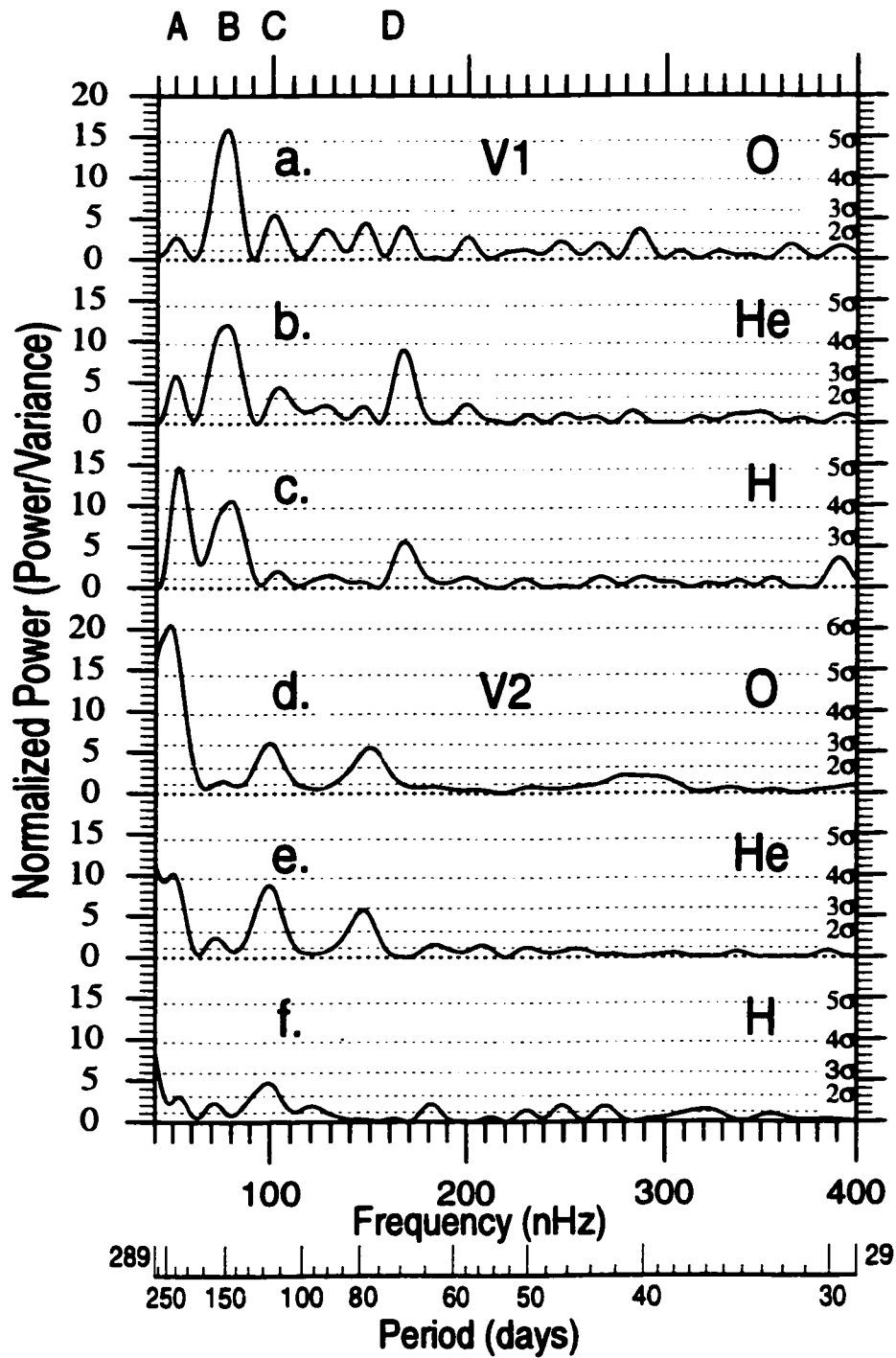


*Figure 4.3 Periodogram Analysis of Outer Heliospheric ACRs*  
 Periodograms of ACRs in the same form as as Figure 4.3. A, B, C, and D above Figure 4.3a indicates the peaks labeled in Table 4.1.

and 1999, so statistical limitations are significant. Therefore despite the fact that hints of an anti-correlation between (0.63-1.39 MeV) IP H and ACR O are seen at V1, a periodicity in interplanetary accelerated particles cannot be concluded on the basis of visual inspection of the 26-day averaged IP H time-intensity profile (not shown). Periodogram analysis of 5-day averaged V1 IP H (not shown) does reveal a very broad, barely significant spectral feature near 160 days. To study GCRs, we visually and harmonically analyzed the LECP E $\beta$ 05 counting rate provided by R. B. Decker (private communication, 2000), which is sensitive to protons with energies greater than 70 MeV, as well as other high-energy ions. The 5-day averaged E $\beta$ 05 time profiles (not shown) are very similar for both V1 and V2 to the ACR data in Figure 4.2 (although the ~5% E $\beta$ 05 variations are small compared to the ~30% ACR H variations), and periodogram analysis of the V1 data does show a statistically significant ~150-day periodicity. However, an estimate of the relative ACR and GCR contributions to this rate based on the ~2- to 400-MeV H spectrum at V1 during 1998 (Stone *et al.*, 1999) indicates that the ~5% variations in the >70-MeV H data could be due to variations of the higher-energy ACRs (which dominate GCRs up to ~120 MeV) contributing to the E $\beta$ 05 rate. Therefore we can rule out a large-amplitude (> 5%) GCR periodicity, but our inability to separate ACRs from GCRs at these higher energies prevents us from determining whether small-amplitude GCR variations might exist. (We note that independent 1998-1999 Voyager 1 measurements given in Figure 2 of McDonald *et al.* (2000a) do reveal the ~151-day periodic features in 30- to 56-

MeV ACR H but not in 130- to 225-MeV GCR H, although this is not addressed by the authors.) We analyzed V1 150-380 MeV/nucleon GCR He data provided by F.B. McDonald (private communication, 2001.) and found no significant periodicity near 150 days during 1998 and 1999. These results suggest that ACRs most clearly display the ~151-day periodicity during the 1998-1999 time period, other particle populations may exhibit less significant but related variations, and GCRs show no evidence of this periodicity.

### **4.3 – Observations**

#### **4.3.1 – Voyager 1 ACR Periodicities**

At Voyager 1, significant ~151-day periodicities were found for ACR O, He, and H, as evidenced by the large peak near 76-79 nHz in Figures 4.3a, 4.3b, and 4.3c. Oxygen (Figure 4.3a) has a peak at  $151 \pm 12$  days ( $77 \pm 6$  nHz), with a  $5.3\sigma$  statistical significance. (The periodogram peak uncertainties are estimated throughout by the full-width half-maximum divided by 2.35, as their near-Gaussian forms suggest.) In the helium data (Figure 4.3b) a peak is found at  $152 \pm 15$  days ( $76 \pm 7$  nHz) with a  $4.5\sigma$  significance; and the proton periodogram (Figure 4.3c) has a peak at  $146 \pm 15$  days ( $79 \pm 8$  nHz), with a statistical significance of  $4.2\sigma$ . The conclusion that these three significant peaks are related to one another, in addition to the threefold agreement of their periods (within uncertainties), is strongly supported by the fact that the three variations are in phase (Figures 4.2a-4.2c). For oxygen and helium these peaks are the most significant, but there is a proton peak of  $221 \pm 21$  days ( $52 \pm 5$  nHz) that has a higher normalized power than the 146-day H peak, and it is above the  $z=9$  false alarm threshold. There are a few peaks at or below the false alarm threshold that are,

nevertheless, noteworthy, as comparable periods are found in multiple species. The 221-day H peak mentioned above is mirrored by a  $\sim 3\sigma$  helium peak at  $229 \pm 18$  days ( $51 \pm 4$  nHz) and a similar, though nonsignificant, oxygen peak around 231 days (50 nHz). Anomalous protons and helium have peaks with  $\sim 3$ - $4\sigma$  significance at  $69 \pm 2$  days ( $167 \pm 6$  nHz) and  $70 \pm 2$  days ( $166 \pm 5$  nHz), respectively; again, there is also a similar nonsignificant oxygen peak at 70 days (166 nHz). For comparison with potentially related V2 peaks the following small V1 O, He, and H peaks are mentioned:  $115 \pm 5$  days ( $101 \pm 5$  nHz),  $112 \pm 6$  days ( $104 \pm 6$  nHz), and  $112 \pm 5$  days ( $103 \pm 4$  nHz), respectively, with only the oxygen peak nearing  $3\sigma$  and the others being less significant.

#### **4.3.2 – Voyager 2 ACR Periodicities**

For Voyager 2 the situation is different. No significant peaks were found with periods near 151 days, although statistically insignificant peaks at 153 days (76 nHz), 160 days (72 nHz), and 162 days (71 nHz) can be identified in the ACR O, He, and H periodograms, respectively (Figures 4.3d-4.3f); peaks with higher significances, though at or below the false alarm threshold, are evident for oxygen and helium, both at  $116 \pm 8$  days ( $99 \pm 7$  nHz), with  $3\sigma$  and  $\sim 4\sigma$  significance, respectively, along with a less significant H peak at  $117 \pm 9$  days ( $99 \pm 8$  nHz). The largest feature in the V2 periodograms is the oxygen peak of  $243 \pm 41$  days ( $48 \pm 8$  nHz) with a  $6\sigma$  statistical significance, although barely three cycles of this period are analyzable in the 2-year 1998-1999 interval. While there appears to be a more complicated dual-peak structure for He and H, these species show similar peaks at 231 days (50 nHz) and 216 days (54 nHz), respectively. Longer-term analysis of the 26-day averaged V2 oxygen 1994-

1999 time series shows a  $\sim 2.5\sigma$  peak centered on 230 days, indicating that the 243-day O peak is not a sustained, prominent feature. Finally, there are two more subthreshold peaks, with  $\sim 3\sigma$  significance for O and He at the respective peaks of  $77\pm 4$  days ( $150\pm 8$  nHz) and  $79\pm 4$  days ( $146\pm 7$  nHz). These observations for V1 and V2 ACR oxygen, helium, and protons are summarized in Table 4.1. Note that were it assumed that the observed periodic variations are due to disturbances that propagate radially outward from the Sun with a speed of 800 or 400 km/s (for typical “fast” or “slow” solar wind), then the Doppler shift due to the spacecraft motion would result in a 2% or 4% increase, respectively, of the period measured at the spacecraft relative to the true period. Since neither the manner nor the speed of propagation is known and the estimated Doppler corrections are small (relative to the measurement uncertainties), throughout this paper we report the actual periods measured in the spacecraft frames without adjustment.

## **4.4 – Discussion**

### **4.4.1 – The ACR Periodicity and Interplanetary Variations**

It is the primary result of this chapter that a statistically unambiguous periodicity has been identified in multiple outer heliospheric anomalous cosmic ray species, with a period of  $\sim 151$  days, as detailed in sections 4.2 and 4.3. Before addressing the important secondary result that this periodicity is observed only at the higher northern latitude of V1 and not at the lower southern latitude of V2, the issue will be addressed of how these ACR variations might be related to the 154-day solar periodicities first reported by Rieger *et al.* (1984). The most likely medium connecting the “Rieger periodicities” with those in the distant heliosphere is the

interplanetary magnetic field (IMF). Cane *et al.* (1998) have shown that the near-Earth IMF strength exhibited a 153-day periodicity during 1978-1982 (during solar cycle 21) that is in phase with concurrent solar periodicities, in particular, solar energetic particle events. This result provides a plausible mechanism for explaining the periodic ACR variations since it is expected (Burlaga *et al.*, 1985) that a strong anti-correlation should exist between the IMF and cosmic ray intensities (although the very weak magnetic field in the vicinity of V1 will probably make it difficult to directly detect the expected IMF periodicity).

Returning to the comments from section 4.2, it happens that the extent to which the ACR periodicity is quasiperiodic also provides some support for the IMF interpretation given above. To determine how uniform the periodicity is during 1998 and 1999, V1 oxygen was examined in more detail. To facilitate determination of the time intervals between adjacent local maxima and minima, the 5-day data (Figure 4.2a) were smoothed using several boxcar averages ranging from 25 to 65 days, and then the peak and trough of each cycle were visually identified. The local maximum or peak-to-peak period was found to be  $140 \pm 46$  days, while the local minimum or trough-to-trough period was determined to be  $154 \pm 18$  days. There are two interesting aspects of this result: (1) The intensity minima have an average period that is consistent with the periods observed for the various solar periodicities, while the intensity maxima have a somewhat shorter average period (although the overlapping standard deviations prevent a conclusive determination), and (2) the standard deviation of the minimum period is less than half as large as the maximum-period standard deviation; thus the minima are more uniformly periodic. This is consistent with

variations in the interplanetary magnetic field strength causing the ACR periodicity, as it is the elevated IMF strength that periodically inhibits the flow of the cosmic rays into the high-IMF region, resulting in the decreased particle intensity at the spacecraft.

The LECP E $\beta$ 05 counting rate, sensitive to >70-MeV H, and the GCR measurements of McDonald *et al.* (2000a) constrain potential 151-day variations in GCRs at V1 during 1998-1999 to less than ~5%, probably much less, while the ACRs vary by 20-50%. Therefore it is interesting to consider which physical quantities relevant to cosmic ray transport and modulation might distinguish GCRs from ACRs. The velocities,  $\beta$ , relative to  $c$ , for the ~27-MeV ACR H, He, and O we analyzed are 0.23, 0.12, and 0.06, respectively, and the particle rigidities,  $R$ , are 0.22, 0.45, and 0.87 GV, respectively. For the 180-MeV GCR H and 1280-MeV GCR He observed by McDonald *et al.* (2000a), the values of  $\beta$  are 0.54 and 0.67, respectively, and the values of  $R$  are 0.60 and 1.69 GV, respectively. The overlapping rigidities between the anomalous and galactic cosmic rays suggest that the  $R$  dependence is not the primary factor determining the occurrence of the 151-day periodicity. Conversely, the values of  $\beta$  for the ACRs are quite distinct from the GCR values, as are the total energies, indicating that these parameters may be important in organizing the 151-day periodic phenomenon.

#### **4.4.2 – The Lack of 151-day Periodicities at Voyager 2**

Why is the 151-day periodicity evident only at V1? The heliospheric environments in which the Voyager spacecraft reside are quite different, beyond merely the magnitudes and signs of the respective helioradii and heliolatitudes of the twin spacecraft. As Burlaga and Ness (2000) have pointed out, V2 in 1998 is in the

“sector zone,” (see Figure 5.2.1) meaning that the V2 latitude is less than the tilt angle of the heliospheric current sheet (HCS), and therefore V2 repeatedly crosses and recrosses the HCS as the wave pattern of the HCS ripples past the spacecraft; thus, during each solar rotation period, V2 alternately samples the northern and southern halves of the heliosphere, which have opposing magnetic polarities. This is in contrast to V1, which Burlaga and Ness (2000) show is largely outside the sector zone, and therefore the spacecraft remains predominantly north of the HCS, sampling a single IMF polarity. It is possible that these differences could be related to proposed transport effects of the outer heliospheric HCS (see section 5.2.3). It has been reported (Lean, 1990, and references therein) that the existence of a ~154-day periodicity in the southern solar hemisphere is questionable. A southern periodicity with a different phase or period (or no related periodicity at all) could explain the lack of a 151-day periodicity at V2 in two ways: (1) Complications imposed by the repeated sampling of distinct northern and southern periodicities as Voyager 2 crosses the HCS might obscure the variations, rendering them incoherent or undetectable, or (2) the fact that V2 is primarily south of the HCS might imply that a relevant periodicity is simply nonexistent in that region of the heliosphere. We point out that peaks B and C from Table 4.1 are candidate northern and southern periodicities, with ~151 days for the north and ~116 days for the south. It would be interesting to learn if comparable periods are found in solar phenomena of the northern and southern hemispheres during 1998 and 1999, as this could rule out or support explanation 1. A search for future periodicities after V2 leaves the sector zone can test both explanations 1 and 2 as well.



#### 4.4.3 – Implications for the Sun and Heliosphere

Recent data so far indicate that the Voyager 1, 151-day periodicity appears not to continue into the year 2000. This would imply that the 5- to 8-cycle periodic ACR episode has a 2- to 3-year duration (depending on whether one included the pseudo-periodic start-up phase in 1997), which is consistent with previous work (Lean, 1990) finding typically 1- to 3-year episodes of the periodicity. We also examined 26-day averaged V1 O data from 1994-1999 and found, except for one  $3\sigma$ , high-frequency ( $\sim 370$  nHz) peak, that the only peak significantly higher than  $2\sigma$  was a  $\sim 3\sigma$  peak of  $\sim 160$  days (72 nHz). This shows, as was found by Cane *et al.* (1998) in the IMF, that the periodicity has a period that is dependent on the time interval studied. Some indications consistent with 22-year heliomagnetic variations in the periodicities are found in the literature, such as the lack of a 153-day periodicity in the IMF during the even cycles 20 and 22, compared with the existence of this periodicity during cycle 21 (Cane *et al.*, 1998) and the existence of a 5.1-month periodogram peak in neutron intensity monitor data during cycle 21 but not cycle 20 (Valdes-Galicia *et al.*, 1996). Moreover, Lean (1990) reports disproportionate occurrences of alternating north-south periodicity episodes in sunspot areas during odd solar cycles, and many authors have observed that the power of the Rieger periodicity during cycle 21 is greater than that during 20 and 22, when it is observed at all. The present episode of a 151-day periodicity in the ACR fluxes takes place during the rising phase of solar cycle 23. (Nominal “1 AU” times are used here to relate the present observations to the solar cycle.) It would be interesting to see if other phenomena, particularly IMF and other

cosmic ray measurements, exhibit similar periodic behavior during this period and how they compare with the previous odd solar cycle.

A periodicity in the global solar magnetic field perhaps related to the rate of magnetic flux emergence, such as that discussed by Cane *et al.* (1998) or Ichimoto *et al.* (1985), appears to more naturally explain subsequent ACR variations than the solar flare “exciters” of Bai and Sturrock’s (1993) “clock” model. Yet, it is of note that the three most significant V1 peaks at 70, 151, and 221 days could be interpreted as being subharmonics of the 25.5-day fundamental period of the clock model, with the third, sixth and ninth integer multiples of this period corresponding to subharmonics of 76.5, 153, and 229.5 days, respectively. We feel, however, that it is premature, before confirmation of the 151-day ACR periodicity by additional cosmic ray or outer heliospheric measurements, to draw any conclusion concerning the cause of the Rieger periodicities.

#### 4.5 – Summary

We have presented evidence of statistically significant ~150-day periodic variations in the intensities of three species of ~27-MeV anomalous cosmic rays measured at the Voyager 1 spacecraft during 1998 and 1999. These outer heliospheric ACR oxygen, helium, and proton variations are all in phase, have periods in agreement with one another, and have amplitudes of ~30% with respect to the trend. The most prominent variation is seen in ACR oxygen, with a period of  $151 \pm 12$  days. We interpret the ACR periodicities as being related to the well-known (though not well understood) solar periodicities first detected by Rieger *et al.* (1984), which have comparable periods ranging from ~150 to 158 days. The interplanetary magnetic field

strength, which was shown by Cane *et al.* (1998) to sometimes exhibit this Rieger periodicity, is most likely related to the ACR variations, probably by periodically impeding the transport of anomalous cosmic rays as regions of elevated magnetic field strength propagate past the spacecraft. We find that  $\sim 250$  MeV/nucleon GCR He ions do not show large  $\sim 150$ -day variations. The lack of similar, significant periodicities at Voyager 2 was also reported. This is perhaps due to complications arising from the proximity of Voyager 2 to the wavy and rapidly varying heliospheric current sheet (cf. section 5.2.3 and Figures 5.2.1 and 5.2.2) and to observed differences (Lean, 1990) between periodicities in the northern and southern hemispheres of the Sun.

**Table 4.1** Period (in Days) of Selected Periodogram Peaks From Figure 4.3

Spacecraft	ACR Species	Peak A. 48-54 nHz	Peak B. 71-79 nHz	Peak C, 99-104 nHz	Peak D, 146-167 nHz
V1	oxygen	231	$151 \pm 12^{a,b}$	$115 \pm 5$	70
V1	helium	$229 \pm 18^a$	$152 \pm 15^{a,b}$	$112 \pm 6$	$70 \pm 2^{a,b}$
V1	protons	$221 \pm 2^{a,b}$	$146 \pm 15^{a,b}$	$112 \pm 5$	$69 \pm 2^a$
V2	oxygen	$243 \pm 41^{a,b}$	153	$116 \pm 8^a$	$77 \pm 4$
V2	helium	$231^{a,b}$	160	$116 \pm 8^{a,b}$	$79 \pm 4^a$
V2	protons	216	162	$117 \pm 9$	

<sup>a</sup> Indicates statistical significance at or above the  $3\sigma$  level.

<sup>b</sup> Indicates that the 99.7% false-alarm threshold has been met.

## **Chapter 5 - Discussion**

### **5.1 – Summary of Data Analysis**

#### **5.1.1 – Analysis of ACR Transport**

In Chapter 3 the long-term behavior of anomalous cosmic rays during the recovery phase from 1992 to 2000 was considered (i.e., intensity variations on a timescale greater than one year). The approach to the analysis of the transport of ACRs has been to employ three primary methods to attempt to learn about the processes taking place. The underlying goal of these three methods is to attempt to distinguish phenomena resulting from the motion of the Voyager 1 and 2 spacecraft from intrinsic temporal, solar cycle-related, transport properties. The first method (§3.3) was to model the intensity gradients of ACRs and simultaneously fit H, He, and O at several energies and both spacecraft in an attempt to disentangle the dependence on helioradius, heliolatitude, rigidity, and time. The second method (§3.4) treated each species and energy range independently to calculate spatial intensity gradients directly by using the quasi-static phase of the recovery and apparently well-understood time dependence of cosmic rays to make two-dimensional measurements with only the two Voyager spacecraft. The third method (§3.5) was to numerically solve the Fokker-Planck equation appropriate to the transport of ACRs through the interplanetary medium and to match the solutions to the available oxygen data in the inner and outer heliosphere. The general agreement among these three methods, which are nearly independent, is an encouraging signal of their validity. The

similarities and differences between these methods will be discussed followed by a more detailed review of the each method in turn.

Method (1), the phenomenological model of intensity gradients (§3.3) and method (2), the quasi-local gradient method (§3.4), share some common features that method (3), the numerical model (§3.5) does not have. Firstly (1) and (2) both deal directly with intensity gradients, but in different ways. Secondly, both methods make similar assumptions about the temporal dependence of ACR recovery. Thirdly, both methods involve time-series data alone (i.e., no direct spectral measurements are used). Fourthly, both methods rest on a fitting procedure. Fifthly, latitudinal and radial variations are treated by both (1) and (2). Method (3) shares none of these features as it does not rely on the notion of gradients or of a particular time dependence, it utilizes both spectra and time-profile data without fitting, and is spherically symmetric. The first two methods are also dissimilar in that (1) simultaneously analyzes *all* of the data while (2) treats small subsets of the data separately. Related to this is the difference that (1) uses many parameters, while (2) has but two parameters. Moreover, method (1) involves assumptions about global properties of the heliosphere, such as the source radius, while (2) is independent of such assumptions, dealing only with the observations at the two spacecraft and their locations. The third method shares these features of method (1), since (3) simultaneously models a large set of data (all of the studied ACR oxygen observations), has several parameters, and involves global heliospheric properties. Methods (2) and (3) are the most dissimilar, sharing only the most general features. One distinction (1) has from the other two methods is that (1) is more *ad hoc*, while

method (2) in its simplicity, lacks any arbitrary features, and (3) is based on a well-established theory. In these ways the three methods are complimentary, sharing some features but maintaining many important distinctions.

As a prelude to method (1) the data were parameterized (§3.3.1)—comprising a fourth method in a sense, with its own similar and distinct features—the results of which are summarized in Table 3.3.1 and Figure 3.3.3. Primarily this method demonstrated that all of the twenty ACR time series could be fit well with a 4-parameter recovery and growth function, that total kinetic energy and rigidity both organize many of the ACR features well, while energy per nucleon and atomic mass number do so poorly, and that all of the recovery profiles over the relatively large range of rigidities, positions and particle masses are closely related to one another. Method (1) makes use of these results to try to uncover the relationship between the outer heliospheric ACR time profiles. We chose forms for the radial and latitudinal gradients that were as simple as possible while still matching the data, erring on the side of simplicity of form rather than attempting to achieve exact fits. Rigidity alone was selected to parameterize this aspect of ACR properties and did so rather well (although it is certainly possible that total kinetic energy could have done as well or better). The model is based on the notion that the changing radial gradient governs the bulk of the temporal and spatial features of the recovery, along with a latitudinal gradient that depends only on rigidity. The primary result of section 3.3.4 is that a model of the latitudinal gradient with the rigidity-dependent sign seems to best fit the data. Moreover all but the highest-rigidity ACRs were determined to have negative latitudinal gradients, an unexpected result considering the drift theory of cosmic ray

modulation which predicts positive latitudinal gradients (for most cosmic rays) during the so called positive heliomagnetic polarity cycle. The values of the determined gradients are listed in Table 3.3.2.

Method (2) was designed to extract latitudinal and radial gradients from the Voyager measurements alone (§3.4) without appealing to a global transport model. It was shown that the standard non-local gradient is not appropriate for the case of low-energy ACRs observed at V1, V2 and near-Earth during the solar cycle 22 recovery. The problem for most of the ACRs under consideration is that the gradients are too large, the distance from Earth to the outer heliosphere is too vast, and the spatial dependencies are too-poorly understood. Fortunately, the recovery profiles of GCRs and higher-energy ACRs are well-understood, and there is reason to believe that the low-energy ACRs would exhibit similar profiles were it not for the motion of the Voyager spacecraft. Therefore under this milder assumption (compared to the assumptions required for non-local gradients in this case) the latitudinal and radial gradient can be determined by comparing the time-intensity profiles of an ACR species of a given energy at V1 and V2. By comparing all pairs of events, (26-day averaged fluxes at particular positions and times), along the V1 and V2 trajectories, a scatter plot can be constructed to which a linear fit is made, yielding the latitudinal and radial gradient as the slope and y-intercept, respectively. We perform this calculation for all of the ACR recovery profiles and find clear linear relationships in all cases. When the analysis is purposely performed on data that are changing in time, the result is a non-linear distribution of data points, consistent with the fact that the assumptions break down in this period. In this way the method provides an internal check as to the

appropriateness of its use since the linear organization of the data would not be expected in general. The result of this analysis (Table 3.4.1) is consistent with the result of the previous model; namely, negative latitudinal gradients were obtained for most of the ACR, save the high-energy oxygen, as well as sizable radial gradients for all of the lower-energy ACRs. After we developed the quasi-local gradient method we learned that Paizis *et al.* (1995) used a method that relies on the same linear equation (Eq. 3.4.6) to determine spatial intensity gradients.

In method (3) the cosmic ray transport equation is solved numerically for spherically symmetric geometry with a constant source at the outer boundary (§3.5). The intensity is modeled as a function of time, energy, and radius, and the initial condition is an empty heliosphere. The numerical techniques used were standard ones involving the Crank-Nicholson finite differencing scheme and operator splitting of the radial and energy variables. The purpose of using method (3) is to make a connection between the phenomenological and observational analyses and the established theory of particle transport through interplanetary space. Also by selecting a particularly simple arrangement (i.e., spherical symmetry and constant source) it is possible, by comparing the solutions to the data, to gauge to what extent processes beyond convection, diffusion, and adiabatic deceleration are required to explain the behavior of ACRs during recovery. By choosing the few basic parameters to match the model solutions with the observations, information about the transport process can be gained that is not accessible with methods (1) and (2). For instance with method (3) we determined an approximate heliospheric size (100 AU) that is consistent with the observations and were able to estimate the scattering mean free path of anomalous



cosmic rays. For example 1.3-MeV/nucleon anomalous  $O^+$  is estimated to have a mean free path of 0.5 AU, while higher-energy 22 MeV/nucleon- $O^+$  has a mean free path of 2.2 AU. Although negative latitudinal gradients are not explicitly dealt with using this method, we considered the disagreement of the observation with the model and found that latitudinal gradients like those determined in the previous sections (§3.3.4, §3.4.4) would bring the model into better agreement with the data. Moreover radial gradients, which are explicitly derivable from the numerical solution, were found to agree reasonably well with the method (1) and (2) determinations.

### **5.1.2 – Periodicity Analysis**

Intensity variations of a timescale less than a year were analyzed in Chapter 4. These higher-frequency observations were ignored in Chapter 3 where only the trend related to the recovery phase was of interest. In section 4.2.1 the long-term trend is subtracted from the 1998 and 1999 data, which (at Voyager 1) exhibited an unusual variation with a period between a third and half a year. The energy ranges of H, He and O ACRs for which these variations were sufficiently large to analyze correspond with energy ranges which included the peaks of the ACR spectrum. So the residual flux variations with respect to the trend were determined for all three species near the total kinetic energy of 27 MeV, at both Voyager 1 and 2, resulting in six time series. The first part of the analysis of the residual variations was to visually note the amplitudes and common phase of the quasiperiodic V1 data, and the lack of such at the V2 spacecraft.

More quantitatively, the six time series of residual intensity variations were harmonically analyzed to determine frequencies and uncertainties of periodicities with

significant spectral power. The method chosen to accomplish this is the periodogram analysis method of Scargle (1982) which provides a straightforward measure of the statistical significance of the periodicities and allows irregularly sampled data. The necessity to use a method that permits the use of irregularly sampled data was due to the fact that 5-day flux averages were used rather than our customary 26-day averages, and these higher resolution time series contained a few short data gaps. The reason the 5-day data were preferable to the 26-day data is that they afford a higher statistical level of confidence in the measurements of the  $\sim 150$  day periodicity (which was the focus of Chapter 4), because the 5-day sampling period is sufficiently small compared to the  $\sim 150$ -day period to eliminate the possibility that statistical fluctuations were the cause of the variations.

The result of this analysis is a periodogram which relates normalized power to the frequency and period of oscillation. The normalized power is a measure of the statistical significance of a given periodicity rather than a direct measure of the amplitude of the associated intensity variation. Finally the 40- to 400-nHz periodograms from H, He and O at V1 and V2 were compared to identify four notable periodicities in the V1 data, the most significant of which is the periodicity of  $150 \pm 10$  days in the ACR intensities observed at V1 during 1998 and 1999. The periodograms showed that no such periodicity exists for the V2 data of the same time period.

## 5.2 – Theory and Observation

### 5.2.1 – The Scale of Transport Parameters

Cummings, Stone, and Webber (1984) showed that a simple scaling exists between different species of anomalous cosmic rays under the assumption that the ACRs all share the same power-law index for their source spectra and that the diffusion coefficient depends directly on velocity, and on rigidity as a power law,  $\kappa \propto vR^\eta$ . With these conditions one can equate the diffusion coefficients at any characteristic point of two ACR spectra, such as at the intensity peak to get, for particles with mass numbers  $A_i$ , peak energies  $E_i$ , and charges  $z_i e$ , the scaling relationship  $E_2/E_1 = (A_1 z_2 / A_2 z_1)^\theta$ , where  $\theta = 2\eta / (\eta + 1)$ . Therefore for singly ionized particles we get  $\theta = \ln(E_2/E_1) / \ln(A_1/A_2)$ , and  $\eta = \theta / (2 - \theta)$ . We have found that ACR He and O have peak energies at 6.0 and 1.3 MeV/nucleon late in the recovery period (Figure 3.2.6 and 3.2.7), respectively. From Stone *et al.* (1999) the peak energy of ACR H is determined to be 35 MeV, where for all three species the difference in peak energies between the V1 and V2 spectra were too small to consider. With these observations the rigidity dependence  $\eta$  of the mean free path can be determined for each ACR pair,  $\eta_{H/He} = 1.75$ ,  $\eta_{He/O} = 1.23$ ,  $\eta_{H/O} = 1.46$ , the average of which is  $\eta = 1.5 \pm 0.3$ . This dependence is somewhat higher than that used in this study ( $\eta = 1$ ) in solving the cosmic ray transport equation (§3.5), and different than was determined by the third phenomenological model ( $\eta = -0.3$ , Figure 3.3.6), but is lower than the value ( $\eta = 2$ ) found by Cummings and Stone (1998).

Another simple scaling, put forth by Moraal and Steenberg (1999), relates the ACR peak energy to the integral  $\int V dr / \kappa$  from the source to the observation position, for the no-drift case with spherical symmetry. With  $V$  and  $\kappa$  independent of radius, as has worked rather well throughout this paper, the relationship becomes  $E = aV\Delta r / \kappa$ , where  $a$  is an arbitrary constant and  $\Delta r = r_s - r$  is the distance from an observer to the termination shock. With ACR oxygen spectral peak values at 1 AU (SAMPEX) and 63 AU (V1) of 3.3 and 1.3 MeV/nucleon, respectively (Figure 3.2.8) we can equate the ratio  $E_i / \Delta r_i$  at the two positions to get  $r_s = (r_1 - r_0 E_1 / E_0) / (1 - E_1 / E_0) = 103$  AU (where  $i = 0$ , and 1 indicates 1-AU and V1, respectively). This scale agrees with that which has been assumed throughout this work. Using this same scaling and the fact that, we can equate  $E_i \kappa_i / \Delta r_i$  at two times at V1, say, to estimate the relative change in the diffusion coefficient. From 1991 to 1994 the V1 ACR oxygen peak undergoes a significant shift from 10 MeV/nucleon to 1.3 MeV/nucleon as the heliosphere changes from solar maximum to minimum conditions (Figure 3.2.7a). We can determine the ratio of the diffusion coefficient in 1994 to that in 1991 as follows (referencing Table 2.1.1 and the source radius above):  $\kappa_{94} / \kappa_{91} = (E_{91} / E_{94})(r_s - r_{94}) / (r_s - r_{91}) = 6.3$ . Thus, we can estimate that the scattering mean free path near solar maximum in 1991 was about 1/6 that during the extended solar minimum period from 1994 to 1999. For anomalous  $O^+$  with a rigidity  $R$ , the (~1991) solar maximum scattering mean free path is therefore estimated from Eq. 3.5.4 to be:

$$\Lambda = 0.1 \text{ AU } R/GV .$$

### 5.2.2 – Drifts and Intensity Gradients

Gradient and curvature drifts, including the neutral sheet drift are known to be important processes in the transport of cosmic rays and have been studied extensively (Levy, 1976; Jokipii, Levy, and Hubbard, 1977; Pesses, Jokipii, and Eichler, 1981; Potgieter and Moraal, 1985; McDonald, Lal, and McGuire, 1993; Reinecke and Potgieter, 1994). It is of great interest to compare the observations we have made with the expectations established by the drift theory, since we have not explicitly addressed drift effects. Three related comparisons are made between (1) the neutral sheet drift velocity  $V_{ND}$  and the solar wind velocity  $V$ , (2) the latitudinal dependence of the radial component  $V_{Dr}$  of the gradient and curvature drift velocity  $V_D$  and the latitudinal gradient of the solar wind speed  $\partial V/\partial \lambda$ , and (3) the latitudinal dependence of the solar wind speed  $\partial V/\partial \lambda$  and the latitudinal intensity gradient  $g_\lambda$  for a simple diffusion case without drifts.

Using  $V/\Omega r \approx AU/r \ll 1$  in the outer heliosphere, where the solar wind speed  $V$  is taken to be 85 AU/yr, the angular rotation rate of the Sun  $\Omega$  is approximately 90 rad/yr, and  $r$  is a helioradius greater than, say, 40 AU, the neutral current sheet drift velocity can be written approximately as  $V_{ND} = (2v/3r)(R/Bc)$ , which is radially directed. The symbols  $v$  and  $R$  are the ACR velocity and rigidity, respectively, and  $B$  is the absolute magnitude of the magnetic field strength. Terms of order  $(V/\Omega r)^3$  were dropped in the radial component and the azimuthal component (which is third order in  $V/\Omega r$  anyway) was dropped in accordance with the longitudinal symmetry assumption used throughout. In terms of the gyroradius  $\rho = R/Bc$ , the magnitude is written simply

as  $V_{ND} = 2v\rho/3r$ . This is an approximate form of the neutral sheet drift velocity given by Jokipii, Levy, and Hubbard (1977) for a Parker spiral magnetic field and a flat neutral current sheet, and is strictly applicable to particles with guiding centers falling within a gyroradius of the neutral sheet. However, in the presence of scattering, there will be a similar drift for most particles that fall within two gyroradii, with the drift velocity approaching zero as the guiding center approaches a distance of two gyroradii from the sheet (see section 5.2.3). Note that the boundary layer at which the magnetic field reverses is assumed, at this point, to be infinitesimal (see section 5.2.3). For this same heliospheric geometry, the authors (Jokipii, Levy, and Hubbard, 1977) evaluated the curvature and gradient drifts above and below the equatorial plane. In the same outer heliospheric limit, the radial component of this drift velocity becomes  $V_{Dr} = -V_{ND}(V/r\Omega)^2(\sin\lambda/\cos^3\lambda)$ . The relation  $B = A\Omega\cos\lambda/Vr$ , valid in the outer heliosphere, is used to relate the absolute magnitude of the magnetic field strength to the polarity constant  $A$ , which should be distinguished from the atomic mass number (which shares this symbol) by the context. This is needed to write the drift velocities in terms of measurable quantities, as above. We note that the latitudinal and longitudinal components of  $V_D$  are larger than the radial component in much of the heliosphere, but that here only the radial component will be considered to test the possible modification of the effective radial convective velocity. Drifts and other transport in the latitudinal (and longitudinal) direction are not being considered, but the latitudinal variations of radial transport quantities are.

Using Voyager 1 magnetometer measurements (Ness and Burlaga, 2001) the magnetic field strength in the outer heliosphere can be modeled as  $B = B_\odot r_\odot/r$ , with

$B_0 = 0.06$  nT and  $r_0 = 40$  AU, where the sign of the azimuthally directed field is ignored as arbitrary. Rewriting the particle rigidity and velocity in terms of velocity (in the non-relativistic limit) the neutral sheet drift velocity with the given magnetic field becomes,  $V_{\text{ND}} = (0.76 \text{ AU/yr})(T/\text{MeV})/z$ , where  $T$  is the total kinetic energy and  $q = ze$  is the charge of the ion. This relation is used to determine the entries in Table 5.2.1, where a comparison of the neutral sheet drift velocity and the solar wind speed is made for several species. It is notable that  $V_{\text{ND}}$  is also approximately equal to the latitudinal component of  $V_{\text{D}}$ , usually the largest component in the outer heliosphere, so the comparison in Table 5.2.1 is essentially a comparison of neutral drift velocity or the heliospheric drift velocity to the solar wind velocity. The size of the drift velocity compared to the solar wind velocity is an elementary estimate of the relative importance of drifts for a given species, since the drift velocity, in a coarse sense, can be thought of as an additional convective velocity to which the solar wind speed is added vectorially to yield an effective convection velocity (Jokipii, Levy, and Hubbard, 1977).

The fifth column in Table 5.2.1 is interesting in how it compares with the critical rigidity  $R_c$  from section 3.3 and the latitudinal gradient measurements of section 3.4. The values of  $R_c$  for the first (Figures 3.3.4) and third (Figures 3.3.6) phenomenological models in section 3.3.4 are 2400 and 1800 MV, respectively. For  $\text{O}^+$  this corresponds to about 7 to 12 MeV/nucleon, or between the Med and High<sub>2</sub> energy ranges. The two highest energy ranges of oxygen, both above this critical energy range, are the only ACRs we studied for which the derived latitudinal gradients were positive (Table 3.4.1). Likewise Table 5.2.1 shows that 14 and 22 MeV/nucleon

oxygen are the only species with  $V_{ND}/V$  ratios appreciably greater than unity. This suggests that the rigidity (or total kinetic energy) at which  $g_\lambda$  reverses sign is directly related to the particle drifts since it is only the high-energy ACRs for which the drift velocity is considerably greater than the solar wind speed, where drifts are likely to be more important.

**Table 5.2.1** Drift and Solar Wind Velocities for ACR Species

Ion	$E$ (MeV/nuc)	$T$ (MeV)	$V_{ND}$ (AU/yr)	$V_{ND}/V^a$
H <sup>+</sup> - Med	7	7	5.3	0.06
H <sup>+</sup> - High	26	26	20	0.24
He <sup>+</sup> - Med	6	24	18	0.21
He <sup>+</sup> - High	25	100	76	0.89
O <sup>+</sup> - Low	1.3	21	16	0.19
O <sup>+</sup> - Low <sub>2</sub>	2	32	24	0.28
O <sup>+</sup> - Med	6	96	73	0.86
O <sup>+</sup> - High <sub>2</sub>	14	224	170	2.00
O <sup>+</sup> - High	22	352	268	3.15

<sup>a</sup> The solar wind speed is taken to be  $V = 85$  AU/yr = 400 km/s.

A second comparison was made in an attempt to see if equal but opposite balancing between the solar wind latitudinal gradient  $\partial V/\partial \lambda$  and the latitudinal rate of change of  $V_{Dr}$  occurred at an energy that could explain the zero-latitude gradient that exists when  $g_\lambda$  changes sign at a rigidity  $R_c$ . Using a simple linear form for the solar wind velocity  $V = 400$  km/s  $(1 + \lambda/40^\circ)$ , for absolute latitudes below  $40^\circ$ ,  $-\partial V_{Dr}/\partial \lambda$  was equated to  $\partial V/\partial \lambda = 10$  km/s/degree (= 2.1 AU/yr/degree), and the energy at which this relationship held was determined for latitudes similar to the Voyagers. It was found that the reversal energy found by this technique was much too high to explain the sign reversal of the latitudinal gradient.



A third comparison was made to try to ascertain whether the solar wind velocity gradient in latitude is of the right scale to explain the negative latitudinal gradients of the lower-energy ACRs. This was done by assuming the convection-diffusion solution for the intensity, normalized to a source value  $j_s$  at a radius  $r_s$ ,  $j = j_s \exp(-V(r_s - r)/\kappa)$ . With the simple linear dependence of the solar wind velocity on latitude given above,  $\kappa = \kappa_0 E/E_0$  with  $\kappa_0 = 450 \text{ AU}^2/\text{yr}$  (§3.5.4) and  $E_0 = 1 \text{ MeV/nucleon}$ , and the distance to the source  $r_s - r = 40 \text{ AU}$ , we get  $g_\lambda = (1/j)(\partial j/\partial \lambda) = -(r_s - r)\partial V/\partial \lambda / (\kappa_0 E/E_0) = -19\%/deg/(E/E_0)$ . So for low-energy oxygen,  $E = 1.3 \text{ MeV/nucleon}$ , we have  $g_\lambda = -15\%/degree$  and for medium-energy oxygen,  $E = 6 \text{ MeV/nucleon}$ , we have  $g_\lambda = -3.0\%/degree$ . While the low-energy value is somewhat high compared to the measured value  $-5.5 \pm 1.2\%/degree$  in Table 3.4.1, the middle energy gradient is about the same, at  $-2.6 \pm 0.8\%/degree$ . Therefore, it seems that the solar wind latitudinal gradient cannot be ruled out as the cause of the negative latitudinal gradients observed for low-energy ACRs, and is likely a component of this effect.

### 5.2.3 – Neutral Current Sheet Conditions in the Outer Heliosphere

We point out some aspects of energetic particle interactions with the heliospheric current sheet (HCS) that are peculiar to the outer heliosphere and may have effects on cosmic ray transport. It is possible that effects in the vicinity of the HCS, for particles with sufficiently high rigidities, might contribute to the relative lack of predicted  $A > 0$  drift phenomena, such as the smaller than expected latitudinal gradients seen at the Ulysses spacecraft (e.g., McKibben, 1998) and the negative latitudinal gradients of low-energy ACRs reported here. The transport of high-energy

GCRs is potentially effected by the effects discussed below as well. In this section the possible HCS effects are considered. Some of these issues are addressed more observationally in section 5.3.2 as well.

The HCS, or neutral sheet is the reversing layer for the global interplanetary magnetic field (IMF) and is near the heliographic equatorial region during solar minimum (see Figure 5.2.2). In the outer heliosphere at low latitudes the field is essentially azimuthal, according to the ideal Parker field, so it is instructive to consider the half of the meridional plane that is to the right of the Sun's spin axis in Figure 5.2.1, with North being upward. We know that in an " $A > 0$ " positive heliomagnetic solar polarity cycle (such as the cycle 22 recovery phase) the field above the HCS is directed out of the plane, while the IMF is directed into the plane below the HCS. (Of course the azimuthal nature of the field dictates that the directions reverse to the left of the spin axis in Figure 5.2.1.) Notice in Figure 5.2.1 that the Sun's size is greatly exaggerated to a radius of 3 AU, but that the other features are to scale, appropriate to the case of an 85 AU/yr (400 km/s) solar wind speed with the Sun rotating approximately 14 times per year, resulting in a wavelength for the HCS of about 6 AU. The 1996.5 positions of the V1 (circle) and V2 (square) spacecraft are projected onto this plane, as shown.

Briefly, the modified sinusoidal pattern develops from the offset between the plane of symmetry of the solar magnetic field and the heliographic equatorial plane (which is normal to the spin axis). An idealization of this scenario is used here. The short line drawn across the disc of the Sun in Figure 5.2.1 represents the neutral boundary of the Sun's magnetic field, oriented at a tilt angle  $\alpha$  of 20 degrees. As the

Sun spins the latitude of the neutral line (along the limb of the Sun in any fixed meridional plane) varies sinusoidally and this pattern is carried by the radially expanding solar wind into the heliosphere as shown. The region between latitudes of  $\pm\alpha$  is known as the sector zone, in a reference to the sector structure of the IMF first observed at the Earth. In this idealization the large “ballerina skirt” waves in the HCS are ignored, so, for example, Earth would always have two equal IMF sectors, one positive and one negative.

In the inner heliosphere the assumption, consistent with observations, is that the reversing layer is very small compared to the gyroradii of particles of interest (Levy, 1976). While this may or may not be the case in the outer heliosphere, there is another issue which affects the effective reversing layer experienced by particles with sufficiently large gyroradii. The effect arises from the fact that the gyroradii of particles with a constant rigidity increases in proportion to the helioradius, since at large  $r$  the IMF strength decreases as  $1/r$  and the gyroradius is given by  $\rho = R/cB \propto r$ . However not all of the features of the heliosphere increase as  $r$ ; in particular, the HCS. The north-south extent of the HCS is  $2\alpha r$ , but the wavelength is constant with radius, remaining about 6 AU for the typical parameters mentioned above. This results in an average separation of  $\delta r = 3 \pm 1$  AU between adjacent HCS reversing layers inside the sector zone, which does not systematically increase in the outer heliosphere (see Figure 5.2.1). Therefore there is a relevant scale in the outer heliosphere, 3 AU, which enters into the transport process, since at large distances from the Sun, ACRs do have gyroradii comparable to this scale.

As discussed in section 5.2.2 the neutral sheet drift takes place when the guiding centers of particles are within one gyroradius of the neutral sheet. Since, for most of the ACRs under consideration, the scattering mean free path is of the same order as the gyroradius, the gyro-orbits are irregular and particles within two gyroradii are likely to experience the effects of the neutral sheet drift (which is different than the requirement that particles have guiding centers less than one gyroradius from the reversal layer when the scattering is significant). Particles outside of the two gyroradius distance would be required to scatter at least twice before their guiding centers approach within a gyroradius of the neutral sheet, and so a natural scale is set. Particles that pass within two gyroradii of the neutral sheet experience the neutral drift to a significant degree if their scattering mean free paths and gyroradii are of the same order. Of course some particles whose guiding centers are within the strict one-gyroradius range will scatter out of this drift region, so a careful treatment would have to consider this as well.

The previous discussion leads us to the following observation. When the HCS spacing in the sector zone  $\delta r$  is less than four gyroradii  $\rho$  for a particular particle population, those particles will essentially experience a net neutral sheet drift throughout the sector zone. If this is so this would mean that the path along the peaks and troughs of the current sheet would not be simply related to the particle's pathlength since the particles would frequently *radially bypass* significant portions of the HCS path. Particles with sufficiently small gyroradii would not frequently bypass legs of the HSC and would instead drift primarily along the reversing layer in the usual way. For particles with gyroradii greater than half the HCS spacing, a third

regime is entered. For these particles it is impossible to complete one orbit without encountering the reversing layer, so they would experience an efficient non-gyrating motion throughout the sector zone, and would be completely decoupled from the path along the HCS. For increasing gyroradii the particle motion approaches free streaming, and the sector zone effectively becomes a *neutral region* rather than a series of reversing layers. Interestingly, for particles having large gyroradii, the directionality of the drift that the less-rigid particles experience should be lost, except perhaps at the boundaries of the neutral region.

The three regimes that become relevant for anomalous cosmic rays and other energetic particles in the outer heliosphere are summarized below, with both the general inequalities and the values for  $\delta r = 3$  AU given:

$\rho < \delta r/4$	}	(1) Particles drift along the neutral current sheet in the usual way.
$\rho < 0.75 \text{ AU}$		
$\delta r/4 < \rho < \delta r/2$	}	(2) Particles drift throughout the sector zone in the same net direction as the usual neutral sheet drift.
$0.75 \text{ AU} < \rho < 1.5 \text{ AU}$		
$\delta r/2 < \rho$	}	(3) Particles stream freely within the neutral region, in no preferred direction.
$1.5 \text{ AU} < \rho$		

The author is not aware that these concepts have been considered before and recognizes the need for a careful treatment to confirm and quantify the physical interpretation given here, but that treatment is beyond the scope of this dissertation. If effect (3) is a part of energetic particle transport, it is noted that this effect could efficiently transport galactic cosmic rays or an equatorial ACR source from the outer to the middle heliosphere, during both phases of the solar cycle. This would tend to reduce classical drift effects of high-rigidity cosmic rays during  $A > 0$  cycles and enhance these effects during  $A < 0$  cycles. Such a pattern of reduced and enhanced

drift phenomena as compared to expectations has been observed by many investigators, but it is clearly premature to draw any conclusions.

The implications of these effects may be complicated by the fact that the reversal layer itself may be less sharp than in the inner heliosphere due to such processes as field line random walk. If the transition becomes gradual rather than sharp, additional gradient drifts may come into play (Levy, 1976). Also it is conceivable under conditions of a gradual field reversal that the scale at which the non-standard effects discussed above become important could become smaller, therefore lower rigidity particles could experience the neutral region effects due to the general lack of a consistent field over scales comparable to the gyroradius.

Since most ACRs are singly ionized they have relatively high rigidities and some may be subject to the effects discussed above. If we again assume the interplanetary magnetic field model  $B = B_0 r_0 / r$ , with  $B_0 = 0.06$  nT and  $r_0 = 40$  AU (§5.2.2), we can learn for which particle and at what helioradii the neutral region effects may be important. The relations  $\rho = R/Bc = \delta r/4$  and  $\rho = \delta r/2$  provide the information we need. The former reduces, for  $r$  in AU and  $R$  in MV to  $rR = 8 \times 10^4$ . For example at 40 AU the rigidity at which effect (2) may become important is  $R = 2$  GV. In table 5.2.2 we list a few calculated values for convenience. In the LECF energy range, of H, He, and O, only O reaches the range of rigidities in the table, which roughly correspond to ACR oxygen above the spectral peak.

There are a few features in our observations that might be usefully considered in terms of these effects. For example, the intensity of 13 – 38 MeV/nucleon ACR oxygen is remarkably constant at both V1 and V2. This is interesting because V2 is

undergoing a relatively large latitudinal change (cf. Table 2.3.1). Nevertheless the absolute intensity offset between V1 and V2 is approximately a factor of two indicating a positive latitudinal gradient since V1 has a higher flux (see section 3.4). So, we have indications of a latitudinal gradient from the offset and indications of no gradient from the fact that the V2 flux is not changing, despite the latitudinal change. This suggests that V2 is locally in a shallow portion of the latitudinal distribution and that the intensity must change sharply at some absolute latitude between the V2 and V2 latitudes, roughly 20 and 33 degrees, respectively. Figure 5.2.2 shows that the edge of the sector zone defined by the heliospheric tilt angle is between the absolute latitudes of the Voyagers throughout the solar minimum period. Thus the type (2) effects could explain some of this since the modified neutral sheet drift would be generally felt throughout the sector zone, directed outward for  $A > 0$  and inhibiting the transport of ACRs to the V2 latitudes. Conversely V1 is outside of the region of generalized drift and the ACRs propagating from the termination shock to the V1 latitudes do not experience the increased effective convection velocity, so their intensity is higher. If the high-energy ACR oxygen have rigidities sufficient to experience the type (3) effect, than this could make sense in terms of balancing traditional  $A > 0$  positive latitude gradient drifts and inward streaming ACRs at the equator; i.e., effect (3) would be to reduce traditional  $A > 0$  drift effects and increase  $A < 0$  drift effects.

**Table 5.2.2 Minimum Rigidities for Possible Neutral Region Effects**

Condition	$r = 40$ AU	$r = 60$ AU	$r = 80$ AU
Minimum $R$ for effect (2), $\rho = \delta r/4$ .	2000 MV	1300 MV	1000 MV
Minimum $R$ for effect (3), $\rho = \delta r/2$ .	4000 MV	2700 MV	2000 MV

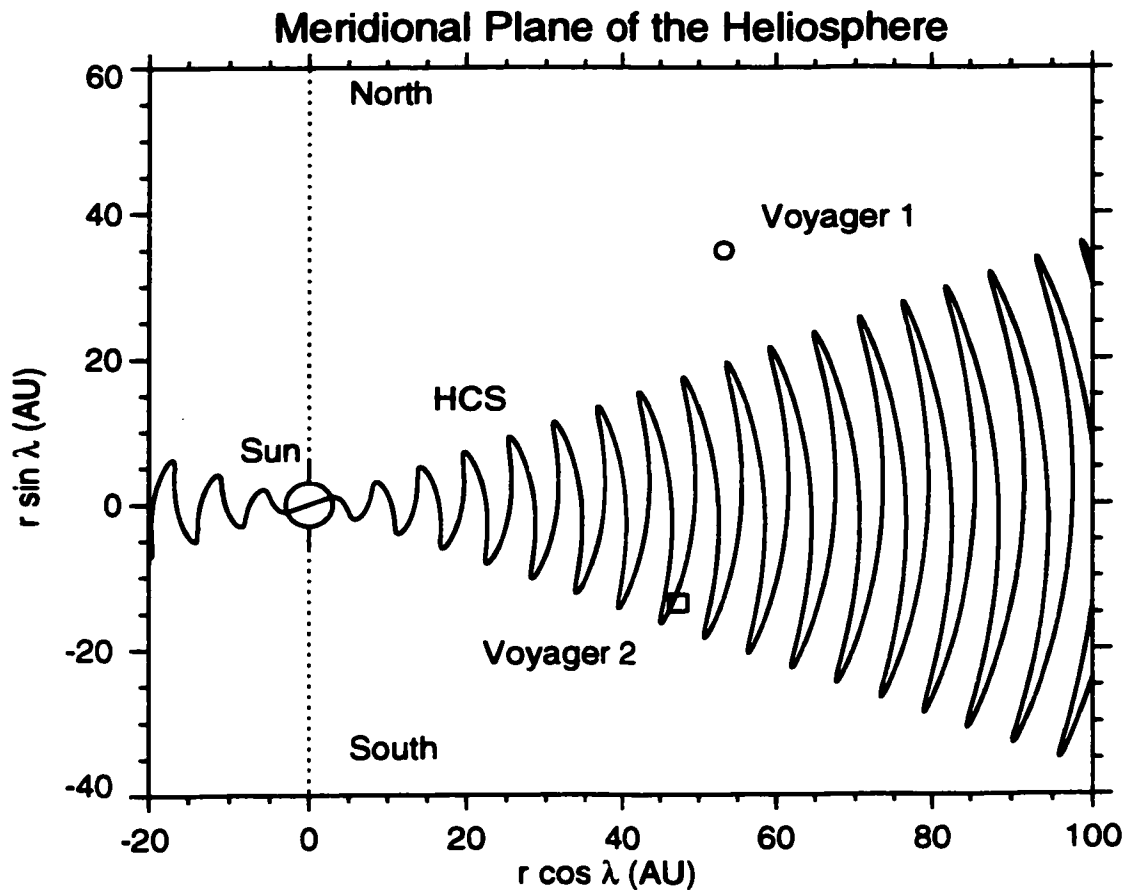


*Figure 5.2.1 Heliospheric Current Sheet in the Meridional Plane  
With the tilt angle of the HCS equal to  $20^\circ$  V2 remains in the sector zone during the recovery phase (the sun is not to scale).*



# HCS Tilt Angle and Voyager Latitudes

Wilcox Solar Observatory data used in this study was obtained via the web site  
<http://quake.stanford.edu/~wso> at 2001:08:02\_13:47:58 PDT  
courtesy of J.T. Hoeksema.

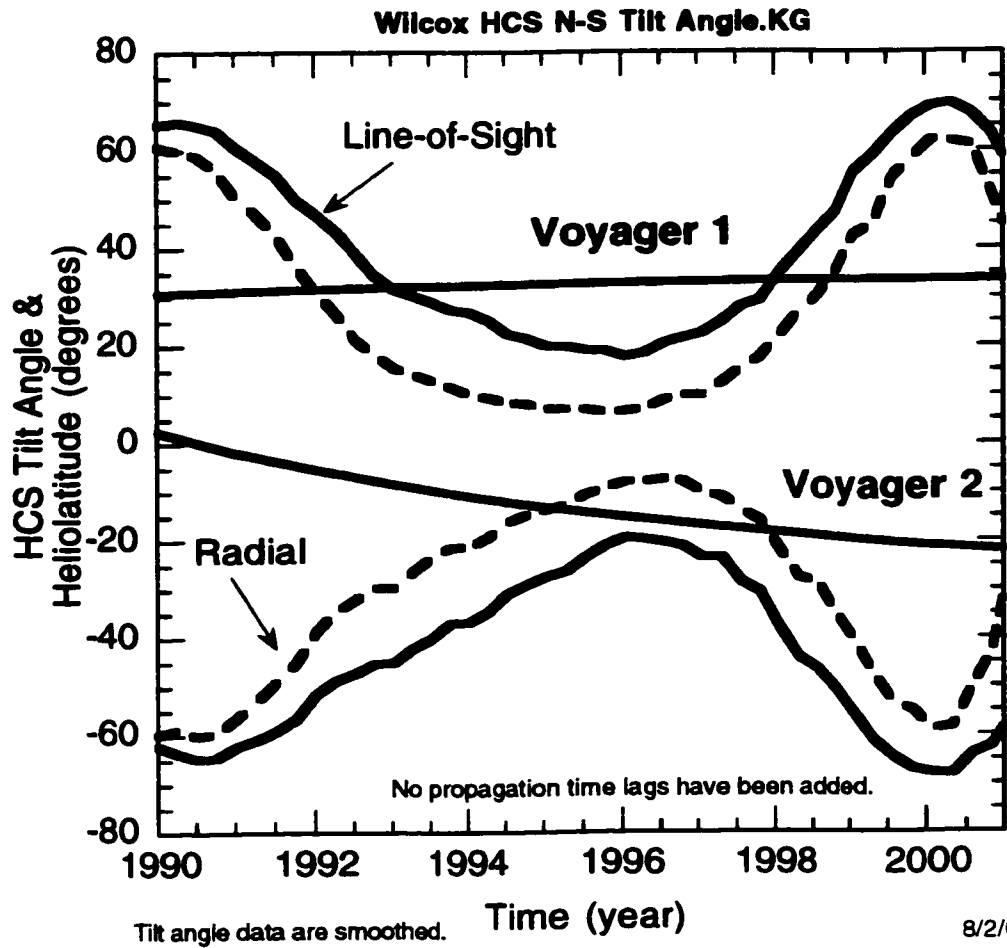


*Figure 5.2.2 Tilt Angle of the HCS and Voyager 1 & 2 Latitudes  
The tilt angle does not drop below  $\sim 20^\circ$  even during solar minimum so V1 and V2 remain in separate regions throughout the recovery phase.*

#### 5.2.4 – Comparison of Intensity Gradient Observations

Although the low-energy, outer heliospheric ACR intensity gradients we have reported (Table 3.4.3) are largely unique, there are a few comparable measurements to be considered from Voyager, Pioneer 10, Ulysses, SAMPEX, and various near-Earth spacecraft (Fujii and McDonald, 1999; McDonald, Lal, and McGuire, 1998; Cummings *et al.*, 1997; Stone, Cummings, and Webber, 1996; Cummings *et al.*, 1995a; Cummings *et al.*, 1995b). In Table 5.2.3 these published, (primarily) outer heliospheric intensity gradients are listed along with our results for comparison and reference. Gradients calculated with the assumption of offset latitudinal symmetry ( $10^\circ$  S) are italicized to distinguish them from the equatorially symmetric gradients (see Table 3.4.3). All of the published gradients are non-local and the non-local gradients from this work are so indicated; all other gradients from this work are quasi-local.

Two quantities in Table 3.4.3 from the present work that were not previously discussed are the annually averaged 1996 1-5 MeV/nucleon  $O^+$  non-local gradients, utilizing V1, V2, and 1-AU data (they are,  $g_r = 2.6 \pm 0.6$  %/AU and  $g_\lambda = 2.5 \pm 0.6$  %/degree). The rigidity of these particles is 1000 MV, which is somewhat higher than the 670 MV rigidity of the 10-22 MeV/nucleon He from 1996 ( $g_r = 3.3 \pm 0.3$  %/AU and  $g_\lambda = 1.6 \pm 0.3$  %/degree; McDonald, Lal, and McGuire, 1998) to which a comparison can be made; the next closest match in rigidity is 2200 MV for the 10-MeV/nucleon Oxygen point from 1994 ( $g_r = 2.6 \pm 0.5$  %/AU and  $g_\lambda = 2.1 \pm 0.6$  %/degree; Cummings *et al.*, 1995b). The 1996 He gradients were calculated from V1, V2, and Pioneer 10 data, all in the outer heliosphere, while the 1994 O gradients were

calculated from five spacecraft throughout the heliosphere. All of the values agree within the uncertainties. However, the 1-5 MeV/nucleon quasi-local gradients for 1992-1999  $O^+$  are quite different from these figures; with or without the  $10^\circ S$  latitudinal offset, the radial gradient is about 11 %/AU, and the nominal and offset latitudinal gradients are  $-5.3 \pm 1.2$  and  $-2.4 \pm 0.4$  %/degree, respectively.

We saw in the numerical solution to the cosmic ray transport equation (Table 3.5.1 and Figure 3.5.3) that large radial gradients (e.g.,  $\sim 8$  %/AU for 1.3 MeV/nuc  $O^+$ ) in the outer heliosphere are a natural consequence of the processes governing ACR transport in the heliosphere. So the 11 %/AU QLG value is physically reasonable, but why wouldn't the V1-V2-1 AU non-local gradient be sensitive to this large gradient? Part of the answer is related to the adiabatic energy loss process that reduces the gradient of low-energy ACRs in the inner heliosphere as in Figure 3.5.3h. This causes the average inner-to-outer heliospheric radial gradient to be significantly smaller than the local radial gradient in the outer heliosphere. Moreover, the farther the spacecraft are from one another, the easier it is for a large local gradient to be masked (consider the effect of a large  $\Delta r$  in Eq. 3.4.1). Another aspect is the fact that V1 and V2 are significantly separated from the Earth position in both radius and latitude, allowing the simultaneous solution to Eqs. 3.4.4 to share the flux variation between both latitude and radius, further obscuring any large spatial gradients. The overriding reason why the quasi-local gradient is sensitive to the local outer heliospheric gradient is simply that by jettisoning the need for a third spacecraft (at Earth), there are consequently no large  $\Delta r$  or  $\Delta \lambda$  denominators to diminish the impact of the spatial variations near the Voyagers.

For these reasons, we expect that the two gradient methods may differ in the presence of large spatial gradients, spatially dependent gradients, or large spacecraft separations. With the V1-V2-1 AU non-local gradients we have all three of these problems. For the ACR oxygen gradients above  $\sim 10$  MeV/nucleon the agreement is much better (Table 5.2.3), keeping in mind that excellent agreement is not expected since the regions of the heliosphere that are sampled by the quasi-local method and the non-local methods are different, the time periods are not exactly the same, and the energy ranges do not match completely.

Since there are fewer spacecraft with low-energy ACR measurements than are needed to unambiguously determine the spatial gradients, all methods require simplifying assumptions. The primary simplifying assumption for the QLG method is that the ACRs would be well represented by a function of the form  $1 - e^{-r}$  at a stationary position. An analogous simplifying assumption for the V1-V2-P10 (Pioneer 10) three-spacecraft non-local gradients calculated for 10-22 MeV/nucleon He from 1996 (McDonald, Lal, and McGuire, 1998) is that longitudinal symmetry persists from the heliospheric apex, near where V1 and V2 are located, to the opposite side of the Sun, where P10 is located. Although this is not an unreasonable assumption, we do not know very much about the shape of the termination shock (the ACR source), and significant deviations from longitudinal symmetry are possible.

The  $1 - e^{-r}$  assumption used to calculate the quasi-local gradients amounts to assuming near steady-state conditions late in the recovery period. This assumption is supported by a number of observational and theoretical considerations. (1) The  $1 - e^{-r}$  form is prevalent for GCRs and high-energy ACRs throughout the heliosphere,

observations show. (2) When the initial recovery is detectable above the background (i.e., excluding H; see Figure 3.3.1) the  $e$ -folding times are about the same ( $\sim 1$  year) for both the species that evolve as  $1 - e^{-t}$  and those that evolve like  $(1 - e^{-t})e^t$ , suggesting a common initial recovery mechanism. (3) The distinct change to an exponential growth form for the low-energy ACRs after the initial recovery suggests that a second process is at work during the late recovery period. (4) Exponential growth is expected to be the spatial form for both the simple convection/diffusion case (not a poor assumption in the outer heliosphere) and the force-field approximation to the cosmic ray transport equation. (5) The initial recovery period coincides with the period during which the peak energy changes. The solution to the transport equation, at a fixed position, is seen to exhibit a rapid change in the peak energy only while the initial recovery takes place, before the static limit is reached. This suggests that the same behavior in the observed intensity profiles also coincides with the temporally changing phase before a (quasi) steady state is reached. (6) The numerical solution (e.g., Figure 3.5.3b) *automatically* reproduced the rates of change of the data merely by fitting the late (1999) spectral form at one spacecraft, V1, as in panel (a). Notice in panels (b) and (e) that the dashed lines indicate the solution at a fixed position, i.e., the steady state is reached rapidly by the numerical solution and yet the observed rates of increase are well-matched after the initial recovery. (7) The energy spectra in the inner and outer heliosphere are consistent with transport from the outer to the inner heliosphere, as are the high-energy ACR oxygen recovery profiles (i.e., the outer heliosphere recovers earlier). In light of this it would be difficult to explain why the outer heliospheric low-energy ACRs are continuing to increase at a faster rate than in

the inner heliosphere, since, as with the high energy ACRs, outer-to-inner heliospheric transport establishes the expectation that the outer heliospheric particle fluxes should reach a constant level sooner than in the inner heliosphere. This is true for both a constant and time-dependent source. (8) If the source is time dependent, it is not easily explainable by acceleration times, since it would be expected that the higher energy ACRs would take longer to accelerate. (9) The phenomenological model fits the observations well with physically reasonable parameters resulting in a quasi steady state after about 1994. This same model could not fit the observations with a continued time dependence and/or purely positive latitudinal gradients except for a case with an unreasonably large source radius. (10) Since the solar wind speed has been observed to increase with latitude, it would be expected that particles with small mean free paths would be more inhibited at higher latitudes, leading to a negative latitudinal gradient. This would particularly be the case if drift effects were relatively weak—and  $A > 0$  drift phenomena in solar cycle 22 have been observed to be less significant than once was expected. (11) The quasi-local gradient plots are linear during the late recovery, consistent with the quasi-static assumption and the simple constant form for the radial and latitudinal gradients. When the QLG plot is made for an obviously time-dependent period (the initial recovery), a linear distribution of data points is not observed. (12) The model is very simple and without any *ad hoc* or unusual mechanisms; i.e., the model contains near-spherical symmetry (over the observed latitudes), simple diffusion, convection, and adiabatic energy loss as the dominant transport processes, a constant source strength and diffusion coefficient (after the initial recovery), and simple initial and boundary conditions. Nevertheless,

despite this simplicity, most of the phenomena are explainable in terms of these basic processes. For these reasons it appears that the assumption of weak late-recovery time dependence similar to  $1 - e^{-t}$  is justified.

However, with such a complicated system and limited measurements it is not possible to rule out all forms of continued temporal variations after 1994. Additionally, a few observations are consistent with continued temporal variations, such as the continued increase of 1- to 5-MeV/nucleon ACR  $O^+$  at 1 AU, apparent in Figure 3.3.2 (although as suggested in Figure 5.3.1 the low-energy, inner heliospheric ACRs are expected to be the last ACRs to recover according to the numerical model). The difficulties in fitting the ACR  $H^+$  time-intensity profiles have been mentioned in section 3.3.1, nevertheless, there appears to be a significant temporal component in the ACR proton time-intensity profiles (Figure 3.3.1), as the large values for  $\tau$  in Table 3.3.1 indicate. The low rigidity of these ACRs establishes the expectation of a more gradual initial recovery, but perhaps not quite to this degree (cf. Figure 5.3.1).

**Table 5.2.3 Compilation of ACR Intensity Gradient Values**

<i>E</i> (MeV/m)	Time Period	<i>r</i> (AU)	$ \lambda $ (°)	$g_r$ (%/AU)	$g_\lambda$ (%/°)	Reference
Protons						
5 - 11	1992-1999	36 - 76	5 - 33	18 ± 6	-13 ± 5	This work, Table 3.4.3.
5 - 11 <sup>a</sup>	1992-1999	36 - 76	5 - 33	<i>17 ± 5</i>	<i>-5.5 ± 1.9</i>	This work, Table 3.4.3.
24 - 30	1992-1999	36 - 76	5 - 33	16 ± 3	-10 ± 2	This work, Table 3.4.3.
24 - 30 <sup>a</sup>	1992-1999	36 - 76	5 - 33	<i>15 ± 3</i>	<i>-4.6 ± 0.9</i>	This work, Table 3.4.3.
30 - 56	1/1-6/1/1996	49 - 65	3 - 19	3.0 ± 0.2	0.6 ± 0.2	McDonald et al., 1998.
Helium						
3 - 12	1992-1999	36 - 76	5 - 33	13.3 ± 1.6	-7.5 ± 1.6	This work, Table 3.4.3.
3 - 12 <sup>a</sup>	1992-1999	36 - 76	5 - 33	<i>13.0 ± 1.7</i>	<i>-3.3 ± 0.6</i>	This work, Table 3.4.3.
6 - 10	1/1-6/1/1996	49 - 65	3 - 19	3.7 ± 0.3	1.9 ± 0.3	McDonald et al., 1998.
10 - 22	1992 - 1994	36-61	5 - 32	3.92 ± 0.38	0.78 ± 0.18	Stone et al., 1996.
10-20	1993 - 1995	55 - 64	0 - 32	3.0 ± 0.5 <sup>b</sup>	1.5 ± 0.5 <sup>b</sup>	Fujii & McDonald, 1999.
10 - 22	1/1-6/1/1996	49 - 65	3 - 19	3.3 ± 0.3	1.6 ± 0.3	McDonald et al., 1998.
21 - 30	1992-1999	36 - 76	5 - 33	8.1 ± 1.3	-3.9 ± 1.6	This work, Table 3.4.3.
21 - 30 <sup>a</sup>	1992-1999	36 - 76	5 - 33	<i>8.1 ± 1.0</i>	<i>-1.9 ± 0.6</i>	This work, Table 3.4.3.
30 - 57	1993 - 1995	55 - 64	0 - 32	1.7 ± 0.5 <sup>b</sup>	1.5 ± 0.5 <sup>b</sup>	Fujii & McDonald, 1999.
30 - 56	1/1-6/1/1996	49 - 65	3 - 19	1.65 ± 0.25	1.1 ± 0.2	McDonald et al., 1998
Oxygen						
0.6 - 3	1992-1999	36 - 76	5 - 33	11.2 ± 1.1	-5.5 ± 1.2	This work, Table 3.4.3.
0.6 - 3 <sup>a</sup>	1992-1999	36 - 76	5 - 33	<i>11.0 ± 0.5</i>	<i>-2.4 ± 0.5</i>	This work, Table 3.4.3.
1 - 5	1993 - 1996	39 - 65	8 - 33	3.5 ± 0.5 <sup>c</sup>	1.5 ± 2.5 <sup>c</sup>	This work, Table 3.4.2.
1 - 5	1996	48 - 65	15-33	2.6 ± 0.6 <sup>c,d</sup>	2.5 ± 0.6 <sup>c,d</sup>	This work, annual.
1 - 5	1992-1999	36 - 76	5 - 33	10.8 ± 0.9	-5.3 ± 1.2	This work, Table 3.4.3.
1 - 5 <sup>a</sup>	1992-1999	36 - 76	5 - 33	<i>10.5 ± 0.5</i>	<i>-2.4 ± 0.4</i>	This work, Table 3.4.3.
5	1995/170-273	1-63	3 - 76	...	1.8 ± 0.2	Cummings et al., 1997.
5 <sup>a</sup>	1995/170-273	1-63	3 - 76	...	<i>1.0 ± 0.3</i>	Cummings et al., 1997.
5	95/309-96/158	1-64	4 - 47	...	1.4 ± 0.2	Cummings et al., 1997.
5 <sup>a</sup>	95/309-96/158	1-64	4 - 47	...	<i>1.7 ± 0.2</i>	Cummings et al., 1997.
3 - 14	1992-1999	36 - 76	5 - 33	6.8 ± 0.8	-2.6 ± 0.8	This work, Table 3.4.3.
3 - 14 <sup>a</sup>	1992-1999	36 - 76	5 - 33	<i>6.5 ± 0.8</i>	<i>-1.1 ± 0.4</i>	This work, Table 3.4.3.
10	1993/183-365	1 - 58	3 - 41	2.2 ± 0.8	...	Cummings et al., 1995a.
10	1993/183-365	41 - 58	3 - 32	-1.0 ± 1.6	1.9 ± 0.9	Cummings et al., 1995a.
10	1993/183-365	41 - 58	3 - 32	0 <sup>e</sup>	1.3 ± 0.4	Cummings et al., 1995a.
10	1994/209-313	1 - 61	3 - 32	2.6 ± 0.5	2.1 ± 0.6	Cummings et al., 1995b.
10	1995/170-273	1-63	3 - 76	...	2.1 ± 0.3	Cummings et al., 1997.
10 <sup>a</sup>	1995/170-273	1-63	3 - 76	...	<i>1.0 ± 0.3</i>	Cummings et al., 1997.
10	95/309-96/158	1-64	4 - 47	...	1.3 ± 0.2	Cummings et al., 1997.
10 <sup>a</sup>	95/309-96/158	1-64	4 - 47	...	<i>1.7 ± 0.2</i>	Cummings et al., 1997.
8 - 18	1/1-6/1/1996	49 - 65	3 - 19	1.9 ± 0.6	0.2 ± 0.6	McDonald et al., 1998.
7 - 29	1993 - 1996	39 - 65	8 - 33	3.5 ± 2.5 <sup>c</sup>	1.5 ± 2.5 <sup>c</sup>	This work, Table 3.4.2.
7 - 28	1992-1999	36 - 76	5 - 33	0.9 ± 0.9	2.8 ± 0.8	This work, Table 3.4.3.
7 - 28 <sup>a</sup>	1992-1999	36 - 76	5 - 33	<i>1.3 ± 0.8</i>	<i>1.2 ± 0.4</i>	This work, Table 3.4.3.
20	1995/170-273	1-63	3 - 76	...	1.9 ± 0.5	Cummings et al., 1997.
20 <sup>a</sup>	1995/170-273	1-63	3 - 76	...	<i>0.9 ± 0.3</i>	Cummings et al., 1997.
20	95/309-96/158	1-64	4 - 47	...	1.1 ± 0.3	Cummings et al., 1997.
20 <sup>a</sup>	95/309-96/158	1-64	4 - 47	...	<i>1.6 ± 0.3</i>	Cummings et al., 1997.
12 - 39	1992-1999	36 - 76	5 - 33	-0.2 ± 0.5	2.9 ± 0.3	This work, Table 3.4.3.
12 - 39 <sup>a</sup>	1992-1999	36 - 76	5 - 33	<i>0.1 ± 0.4</i>	<i>1.2 ± 0.2</i>	This work, Table 3.4.3.

<sup>a</sup> Latitudinal symmetry offset to 10° S (note *italicized* figures).<sup>d</sup> Calculated from annual averages.<sup>b</sup> Estimated from separate time periods.<sup>e</sup> Zero radial gradient assumed.<sup>c</sup> Non-local gradient; all other gradients from *this work* are quasi-local.

All gradients from referenced works are non-local, and some values are estimated from figures.



## **5.3 – Interpretation and Implications**

### **5.3.1 – Anomalous Cosmic Ray Transport Phenomena**

The consistent picture of anomalous cosmic rays in the heliosphere that was presented in section 1.2.1 emerges from the observations and analysis we have completed. The dominant processes governing the transport of ACRs as they recover beginning in late 1991, after the large March and June solar events, are convection and diffusion and adiabatic energy loss. This is shown in several ways, starting with the 1993-1998 ACR oxygen spectra in the inner heliosphere, at the SAMPEX satellite, and the 1996 anomalous oxygen spectra in the outer heliosphere, at the Voyager probes (Figure 3.2.8). It is seen that the inner heliospheric ACRs are modulated to a greater degree than the outer heliospheric data, with the spectral peak at 1-AU at approximately three times the energies of that in the distant heliosphere. This is what we would expect to see for particles diffusing from the outer to the inner heliosphere; i.e., more modulation in the inner heliosphere due to the longer path. If drift processes were dominant, the ACRs should transport down over the poles and out along the heliospheric current sheet, in which case the path lengths would not be very different at Earth as compared to the positions of V1 and V2. The dominance of convection and diffusion is also supported by the easily-obtained agreement of the observed spectra and time-intensity profiles with the drift-free numerical model solution, both in the inner and outer heliosphere (§3.5). Also the small positive latitudinal gradient we determined (§3.3.4, 3.4.4) for ACR oxygen with energies above ~10 MeV/nucleon, in agreement with other investigators, indicates weak drifts, and the negative latitudinal gradients calculated for lower energy ACRs indicates that drifts are even less

important for this population, at least away from the HCS. Finally the recovery profiles agree with the expectations we have for convective and diffusive transport from the outer to the inner heliosphere, as shown in Figure 5.3.1. for ACR oxygen, and discussed in section 3.2.3. For this arrangement the numerical solution, along with experience with analytically soluble diffusion problems, shows that the ACRs should recover earlier in the outer heliosphere than in the inner heliosphere, as is shown in panel (a) in Figure 5.3.1. (The solution used to produce Figure 5.3.1 corresponds to the solution displayed in Figure 3.5.2.) This is just what is seen for 7-29 MeV/nucleon ACR Oxygen, with the outer heliospheric ACRs recovering between six months and one year earlier than the inner heliosphere (depending on whether one uses  $t_i$  or  $t_i + \tau$  as the measure of this). A one year inner-outer heliospheric offset for 8- to 18-MeV/nucleon  $O^+$  is also noted by McDonald *et al.* (2001).

The ACRs reach a nearly steady state after mid-1994 throughout the heliosphere. This can be seen in the recovery constants  $\tau$ , which cluster around one year for oxygen and helium (Table 3.3.1). Consistency with the relative lack of temporal variations after 1994 (and before the increased modulation begins at 1-AU in 1997) is assumed in using the quasi-local gradient method and the results were self-consistent with this assumption. The phenomenological model also represents the data well for the case when time variations are minimal after 1994 (cf. Figure 3.3.4j) and, perhaps most directly, the solutions to the transport equation match the observations' rapid approach to steady state, while still explaining the rates of increase of post-1994 ACR intensity profiles very well in terms of the spacecraft motion through significant spatial gradients (Figure 3.5.2 and 3.5.3). Additionally the 7-to 29-MeV/nucleon 1-

1 AU oxygen intensities are nearly constant after 1994 (and the high-energy O fluxes at both Voyagers are very constant for at least six years starting in 1994). Although the low-energy oxygen intensity at 1-AU does continue to vary after 1994, this is not surprising since low-energy, inner-heliospheric particles are expected to recover the latest (as the 1 AU and 3 MeV/nucleon curves in panels (a) and (b), respectively, of Figure 5.3.1 show).

Sizeable positive radial gradients up to  $\sim 10\%/AU$  were measured for the lowest-energy  $O^+$  with the three separate methods of Chapter 3. Despite significant differences between the various techniques (see section 5.1.1), we independently determined consistently large radial gradients, preferentially for lower-energy ACRs (Table 3.5.1). The threefold agreement of these methods lends support to their acceptance. The radial gradients were even larger for He and H than for O, although shorter periods of data (H) and lack of 1-AU data (H and He) do not provide as much assurance as do the oxygen results (Table 3.4.1). Nevertheless the rigidity dependence of the gradients is consistent across all the species. These gradient measurements indicate that the large increases in low energy ACR fluxes observed at the Voyager spacecraft are primarily due to the motion of the spacecraft rather than inherent temporal or solar cycle effects. In addition to the rates of increase of ACR flux at the spacecraft being well-described by the numerical model, as mentioned above (Figure 3.5.2 and 3.5.3), the intensity levels at the various energies at Voyager 1 are well-matched with the model, as are the 1-AU data and the V2 data (although here the latitudinal gradients prevent the spherically symmetric model from attaining complete agreement). These aspects of the numerical solution and the consistent radial

gradients determined by the three Chapter 3 methods (one of which *is* the numerical solution of course) provides strong support for the interpretation of the large flux increases in low energy ACRs from 1994 to 1999 being predominantly due to the gradients through which the two probes are moving.

Not only does the numerical solution rely only on convection, diffusion, and adiabatic deceleration to describe the transport of the ACRs, but the model is spherically symmetric. Except for some differences at Voyager 2 (see section 3.5.4 and below) the oxygen data are fit surprisingly well by this model despite particularly simple assumptions. In addition to those mentioned, a further feature of the numerical solution is that the ACR source intensity is held constant throughout the modeled recovery. Furthermore the initial condition is a completely empty heliosphere. Yet all of the general features of the data were reproduced by this model (Figure 3.5.2 and 3.5.3). It should be emphasized that the spherically symmetric geometry we discuss is based on observations at absolute latitudes below  $\sim 33$  degrees; i.e., we do not claim that the ACR source flux is constant at all latitudes, just that the spherically symmetric model is consistent with the observations locally. In fact, it is likely that the global transport processes and source flux are inconsistent with spherical symmetry at high latitudes.

In considering the time dependence of the ACR source Figure 5.3.1 is helpful to distinguish a constant source from a variable source. As discussed in section 3.2.3, the model of Steenberg and Moraal (1996) can be used to test the possibility there is a time dependent source spectrum due to finite acceleration times. With their sophisticated model they show that this time dependence at the shock would result in

the higher-energy ACRs recovering later than the lower-energy ACRs since it takes more time to accelerate particles to higher energies. However, as was discussed above, the higher energy ACRs are universally observed to recover earlier and reach a constant asymptotic value early (strikingly so for Oxygen above 13 MeV/nucleon, e.g., in Figure 3.3.1). Therefore it is unlikely that this form of continued ACR acceleration is taking place, and is much more likely that, after 1994, the source flux is nearly constant.

The latitudinal gradients (Table 3.4.1) provide information about drift effects as positive latitudinal gradients are a fundamental prediction of drift theory during the positive heliomagnetic polarity,  $A > 0$ . Only the high-energy anomalous oxygen exhibited (small) positive latitudinal gradients, just as other authors have seen (e.g., Cummings *et al.*, 1995a). This indicates that these ACRs are affected by large scale curvature and gradient drifts, to some degree. However the low-energy ACRs were determined to have negative latitudinal gradients, indicating that drift effects were not significant. The reduced importance of drifts for low- versus high-energy ACRs is not necessarily inconsistent with the overall drift theory since the drift effects are predicted to be rigidity dependent, but the negative latitudinal gradients for low-energy ACRs do provide evidence that *these* ACRs are not significantly affected by curvature and gradient drifts. In Section 5.2.2 the possibility that the positive latitudinal gradient of the solar wind speed could cause the negative latitudinal intensity gradient for ACRs is discussed. In fact a straightforward comparison of the drift velocity of various ACRs to the solar wind velocity is made in section 5.2.2, and the results indicate good agreement between the size of the  $V_D:V$  ratio and the

corresponding observed latitudinal gradients. That is, the latitude gradients were positive only for ACRs with  $V_D:V$  ratio greater than one, where drifts would be expected to be important (Table 5.2.1). The rigidity  $R_C$  at which the latitudinal gradient reverses is about 2 GV according to the phenomenological model of section 3.3, which is also consistent with the sign of the quasi-local latitudinal gradients (Table 3.4.1) and the comparison of the drift and solar wind speeds. Further discussion of this issue can be found in section 5.3.2.

The quasi-local gradient method was presented (§3.4.2) and applied to the Voyager ACR observations (§3.4.4). It was shown that one can make temporal assumptions (analogous to the usual spatial assumptions required to use the non-local gradient method) to determining spatial gradients. For the ACR data considered here the assumption of near time independence after 1994 is more defensible than the assumption of spatially constant gradients over the distance from Earth to the Voyagers. We know quite a bit about the temporal dependence of anomalous and galactic cosmic rays during solar cycle 22, such as the tendency of observed cosmic ray intensities, under very broad conditions, to approach a constant asymptote after an initial recovery period with a form like  $1 - e^{-t}$ . Conversely the spatial distribution of ACRs is less-well understood owing to the relative absence of observations between the inner and outer heliosphere. Moreover, independent analysis of the Voyager and 1-AU ACR data with other methods (§3.3, §3.5) lead us to the conclusion that a near-steady state after 1994 does appear to explain the observations while the spatial distributions of ACRs over the 1- to ~50-AU range are not consistent with constant radial gradients, as summarized above. The application of the quasi-local gradient

technique is straightforward in its essence, being merely a linear fit to easily determined combinations of the data. Namely, the ordinate is the logarithm of the ratio of the intensities from pairs of observed events (intensity at a given position and time), divided by the radial separation of the two events. The abscissa is the ratio of the latitudinal difference between the two events and the radial difference (Eq. 3.4.6). These quantities can be easily calculated for all possible event-pairs in the data from a particular period and fit with a line, the slope and intercept of which are equal to the latitudinal and radial gradients, respectively (Figures 3.4.1 to 3.4.10). We pointed out that more complicated arrangements involving more parameters are also possible with the general quasi-local gradient method.

The high-frequency behavior of ACRs during the recovery period became somewhat regular at Voyager 1 during 1998 and 1999. Statistically significant variations with a period of approximately 150 days were observed that were in phase for ACR oxygen, helium, and protons. These variations are also apparent in non-LECP ACR measurements, but when 1998 and 1999 150- to 380-MeV/nucleon GCR He data from Voyager 1 (F.B. McDonald, private communication, 2001) were analyzed with the periodogram technique (§4.2.2), no significant periodicity near 150 days was detected. Also no significant, related periodicity was observed at Voyager 2. Since there is a substantial record of similar periodicities in various solar and near-Earth measurements (§4.1), including the near-Earth IMF and solar wind speed, the possibility exists that the ACR periodicity is related to these inner heliospheric periodicities through a mechanism such as periodically propagating compressed regions of a solar wind with elevated IMF strength that modulate the ACRs as the

regions sweep past the spacecraft. However to date no clear ~150-day periodicity has been reported in inner heliospheric measurements at times close to 1998 or 1999 and the weak fields near Voyager 1 and 2 make periodicity measurements difficult, and none have been reported. If the interpretation is correct, however, it would suggest an interesting feature of the heliosphere: that the ACRs in the outer heliosphere respond to subtle regular variation emanating from the inner heliosphere but not initially to the large changes that caused the 1-AU data to decline so noticeably beginning in 1997. Therefore confirmation of a connection between inner and outer 150-day variations would provide another avenue with which to probe the phenomena of ACR transport.



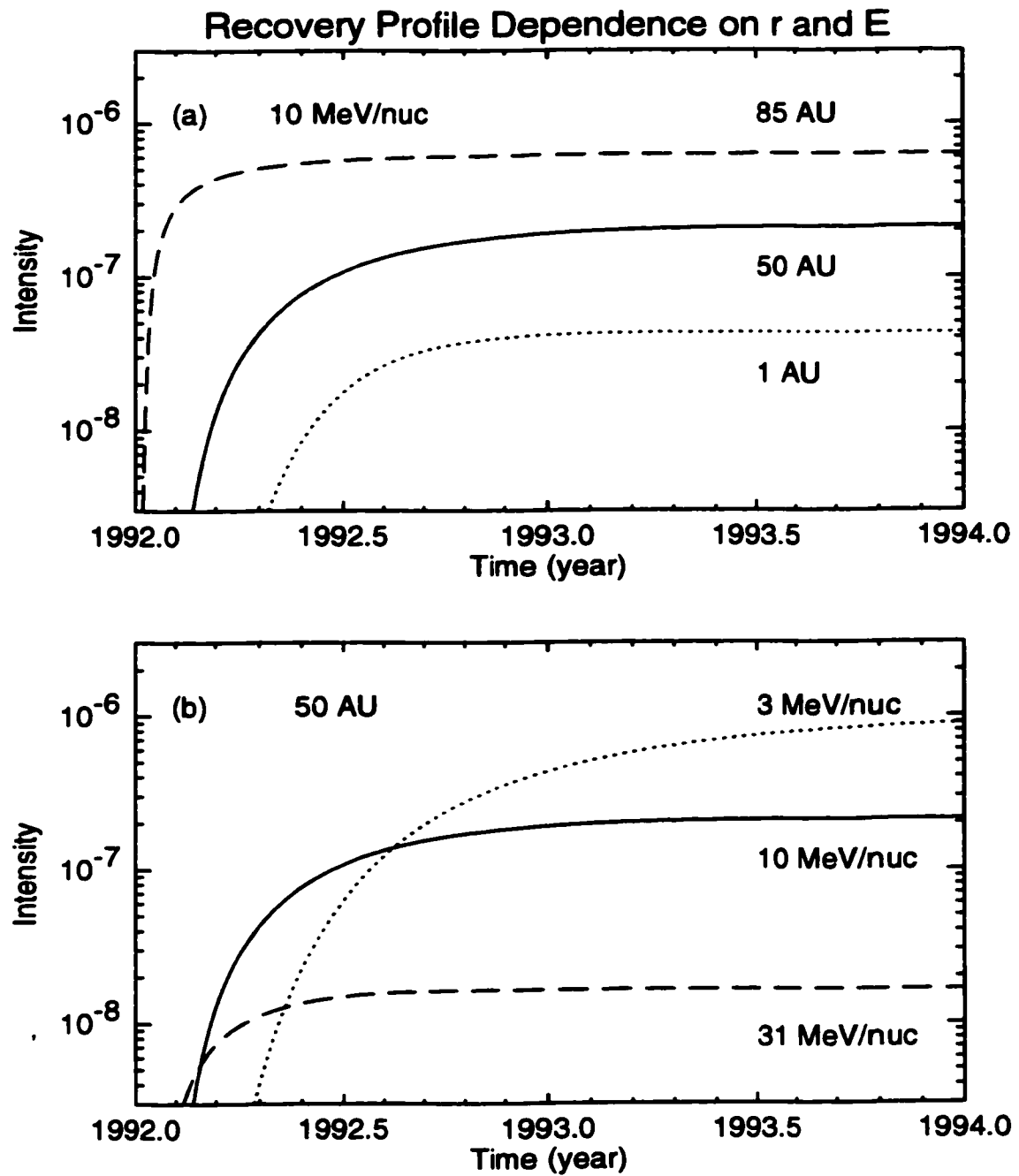


*Figure 5.3.1 The Radial and Energetic Dependence of the ACR Recovery Profile Time profiles from the solution to the Fokker-Planck equation from Figure 3.5.2.*

### 5.3.2 – Global Heliospheric Implications

Here we discuss some implications the results of this work may have for cosmic rays in the heliosphere, beyond those immediately related to the observations. It was pointed out in section 5.2.2 that the lack of significant  $A > 0$  drift effects for low-rigidity ACRs is not tantamount to a direct challenge of drift theory since the theory predicts such a rigidity dependence in the drift velocity (Jokipii, Levy, and Hubbard, 1977). However it is harder to reconcile the fact that the drift/diffusion theory of cosmic ray transport predicts that it is the *initial* energy a particle has before it has lost energy by moving inward through the heliosphere, that largely controls the occurrence of the drift effects (Jokipii and Kopriva, 1979). This means that drift effects are expected to be felt down to lower energies than is suggested by a naive comparison of the predicted drift velocity of an observed ion to the solar wind velocity as was done in Table 5.2.1.

That, nevertheless, this naïve comparison works rather well to organize the latitudinal gradient may be a manifestation of the inhibition of ACR transport over the poles that has been observed (e.g., McKibben, 1998) and was predicted (Jokipii and Kota, 1989; Jokipii *et al.*, 1995) as a modification of the classical drift theory (cf., §1.1.4) due to enhanced polar magnetic turbulence. That is, if ACRs are less likely to enter the heliosphere at the poles, they must be entering closer to the equator, in which case energy loss between the ACR source and the Voyagers is less than what would be expected were the ACRs predominantly gaining access in the polar region and drifting to the equator and out along the heliospheric current sheet. This is due to the equator-to-pole electrostatic potential difference of ~240MV (Jokipii, 2000).

In the equatorial-access case the energy loss of the particles between the source and the observation point would be less than in the polar-access case, therefore the *naïve* comparison (Table 5.2.1) would be more appropriate as the energy loss the ACRs undergo before they are detected is reduced. In other words, if the particles eventually detected as low-energy ACRs at the Voyagers were drifting from the poles to the equator we would expect a large energy loss ( $\sim 240$  MeV/charge) meaning that the particles were initially at energies high enough that the drift effects should be large. That we don't see these drift effects in ACRs with rigidities below 2 GV indicates, self consistently, that the particles are most likely not entering the heliosphere above the poles, but rather, preferentially, near the equator.

This low-rigidity ACR behavior, in addition to being affected by the impeded diffusion and drift over the solar poles may be influenced by the neutral region effect of the heliospheric current sheet described in section 5.2.3. If this effect operates, it would provide easy access of particles with gyroradii greater than half the HCS spacing  $\delta r$  to the middle heliosphere. Since there is no preferred direction of particle motion in the neutral region, it is the site of the source, (at the termination shock for ACRs, or outside the heliosphere for galactic cosmic rays), that would cause a net inward transport of cosmic rays during either solar polarity. More work is needed to determine whether this neutral region effect is important. As it stands, the arguments of section 5.2.3 seem to indicate that the minimum required rigidities of  $\sim 1$ - to 4-GV for the effect to be significant in the outer heliosphere (Table 5.2.2) are too high to influence the low-rigidity ACRs ( $< 2$ GV) that exhibit the negative latitudinal gradients indicating drift-free transport.

Even without this extra effect, the mere ease of access at the equator relative to the impeded access at the poles could help explain the small positive latitudinal gradients of the ACR oxygen above  $\sim 10$  MeV/nucleon and the large negative latitudinal gradients of lower-energy oxygen and ACR H, and He. The high energy oxygen could still drift at a rate diminished with respect to the classical theory causing a small positive latitudinal gradient, while the less energetic particles enter preferentially near the equator, diffusing inward there, against the convection of the scattering centers embedded in the solar wind. The positive latitudinal gradient of the solar wind velocity in turn contributes to making the equatorial region a site where access of ACRs is easier, since the opposing convection of the solar wind is slower there than at higher latitudes (see section 5.2.2). The effects of such equatorially-centered transport of galactic cosmic rays with energies above 2 GV were considered by Van Allen (2000). He compared Climax neutron monitor data from over four solar cycles (1953 to 1999) to sunspot number and found the observations to be consistent with diminished access at the poles. We note that the neutral region effect *is* expected to be important for such GCRs, and therefore this effect, in addition to diminished polar access, may help to provide a detailed explanation of the transport of these particles as well.

#### **5.4 – Conclusions**

We have studied long and short term phenomena associated with the transport of anomalous cosmic rays in the inner and outer heliosphere during the solar cycle 22 recovery phase beginning in late 1991. Our analysis of Voyager 1 and 2  $H^+$ ,  $He^+$ , and  $O^+$  measurements from the LECP experiments, and  $O^+$  data from the LICA instrument

on SAMPEX, has shown that the dominant ACR transport processes are convection, diffusion, and adiabatic cooling that the ACR spatial distributions, on timescales greater than a year, develop into a nearly static state by mid-1994, after an initial recovery phase. A spherically symmetric model of the ACR transport with a constant source at the termination shock represents the data surprisingly well after the initial recovery period. Therefore the large low-energy ACR intensity increase seen at the Voyager probes after 1994 are predominantly due to the spatial gradients through which the spacecraft are moving, rather than purely temporal variations. During this phase of positive heliomagnetic polarity, the gradient and curvature drift effects, away from the heliospheric current sheet, are significant only for ACRs with rigidities above  $\sim 2$  GV. Analysis of periodic phenomena, on timescales shorter than a year, has uncovered an in-phase, statistically significant periodicity in the intensities of all three ACR species at Voyager 1 during 1998 and 1999. This  $\sim 150$ -day periodicity may be related to similar periodicities observed in solar and near-Earth measurements, including solar wind speed, near-Earth interplanetary magnetic field strength, and ground based neutron monitor observations of galactic cosmic ray rates, but not previously seen in outer heliospheric or ACR data.

The interpretation given above is supported primarily by three methods, an intensity gradient method, a numerical model, and a phenomenological fit. We have presented the quasi-local gradient method, with which it is possible to simultaneously determine radial and latitudinal intensity gradients using data from fewer than three spacecraft, as long as at least one is in motion, something not possible with the non-local gradient method. (We have recently learned that a very similar technique has

been used by Paizis *et al.* (1995) to analyze galactic cosmic rays.) Both the non-local and quasi-local gradient techniques are valid under different sets of conditions but were shown to agree when conditions were mutually satisfied. In addition, long-term ACR transport has been analyzed with the two other main methods, a time-dependent numerical solution to the spherically symmetric Fokker-Planck equation appropriate to cosmic ray transport, and a simultaneous phenomenological fit to 14 Voyager 1 and 2 time-intensity profiles composed of ACR measurements of ions with total kinetic energies down to about 10 MeV. These two methods were shown to be in general agreement with the quasi-local gradient results. A selection of these results for ACR  $O^+$  with energies of 1.3-, 6-, and 21-MeV/nucleon are the average ~1994-1999 radial gradients from ~50 to 70 AU of  $+11.2 \pm 1.1$ ,  $+6.8 \pm 0.8$ , and  $-0.2 \pm 0.5$  %/AU, respectively, and the latitudinal gradients from ~10 to 30 degrees of absolute latitude of  $-5.5 \pm 1.2$ ,  $-2.6 \pm 0.8$ , and  $+2.9 \pm 0.3$  %/degree, respectively. When a  $10^\circ$  S offset of the latitude of symmetry was assumed the radial gradients remained essentially unchanged but the magnitudes at the latitudinal gradients were reduced by approximately one half, with no change in sign.

## APPENDICES

### A – Flux Calculations with the LECP Instruments

#### A.1 – Particle Identification

To lend some detail to the subject of particle identification, first a more complete discussion of the rate and PHA data is necessary, after which a schematic particle identification algorithm will be described (see figure A.2). The rate data consist of the counting rates for each of the 36 (non-LEMPA) rate-channels. To give a more precise description of what a rate-channel is, the CH01 rate-channel (see figure A.1) will be discussed in some detail, as an example.

There are several conditions that must be satisfied for a 1-MeV proton to be identified with the CH01 rate-channel. There are a set of discriminators associated with each detector. If the energy deposit in D1 is sufficient to trigger the E1 discriminator, (where E1, the lowest threshold value on D1, labels the discriminator that is set to trigger at the E1 level), but insufficient to trigger the E1A (second highest threshold for D1) discriminator, then two of the logical conditions are met for this ion to be identified as a CH01 particle. The full logic can be represented by the following:

$$E1 \overline{E1A} E2 \overline{E2A} \overline{E3} \overline{L12A} \overline{A1} \overline{A2},$$

where E1, E1A, E2, etc. are various discriminator threshold levels for D1, D2, etc. The L12A symbol refers to a “slant” threshold (described below) resulting from the sum of D1 and D2 pulse heights and A1 and A2 refer to the discriminator thresholds on each half of the anticoincidence cylinder. The above notation is interpreted as follows: For a particle to be identified as CH01, the E1 threshold must be met by the

D1 signal, the E1A threshold must not be met by D1, the E2 threshold must be met by D2, the E2A must not be met by D2, the E3 threshold must not be met by the D3 detector signal, the L12A threshold must not be met by the sum of D1 & D2, and the A1 & A2 thresholds must not be met by the signals from the two halves of the anticoincidence cylinder.

The L12A threshold is associated with the fact that the LECP instrument uses logarithmic amplifiers, making the PHA channel proportional to the logarithm of the detector signal output. This allows a simplified summing procedure to determine diagonal thresholds such as L12A, visible in figure A.1; these slant discriminators are produced by routing the sum of two logarithmic amplifiers through a single discriminator. The justification for doing so arises from the fact that a product  $P = a\Delta E_1\Delta E_2^b$  can be formed, where  $\Delta E_1$  and  $\Delta E_2$  are the energy deposits in the D1

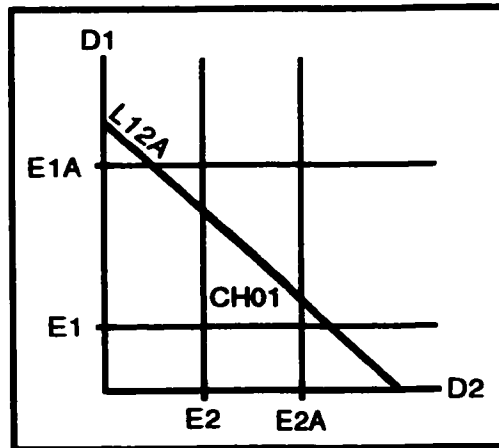


**Figure A.1 LECP Energy Thresholds in D1 vs. D2 PHA Matrix**  
*An illustration of the energy thresholds used by the discriminator circuitry designed to specify rate-channels. For CH01 the energy deposit must be above a minimum value E1 in D1 and must be below a value E1A in D1; must be above a minimum value E2 in D2 and must be below a value E2A in D2; must be below a minimum value E3 in D3; the sum of D1 and D2 must be below a value L12A; and the anticoincidence cylinder must not be triggered. (See text.)*



and D2 detectors, respectively,  $a$  and  $b$  are constants, and  $P$  is a value that uniquely specifies a particle species. The use of logarithmic amplifiers allows a useful redefinition of the energy deposits,  $\varepsilon_1 = \log \Delta E_1$  and  $\varepsilon_2 = \log \Delta E_2$ . The log of the product  $P$  can then be written  $\log P = \log a + \log \Delta E_1 + b \log \Delta E_2$  or more simply  $C = \varepsilon_1 + b\varepsilon_2$ , where the definition,  $C \equiv \log(P/a)$ , is used to simplify the expression.

In this way a value  $P = L12A$ , for example, can be determined that specifies a bound for a particular species via a simple logical sum. These slant discriminators along with the regular threshold discriminators allow the rate-channels to achieve the relatively coarse compositional determination, which allows a simple association between a given rate-channel and a given species over a set energy range. For instance, the CH01 rate-channel is nominally associated with protons in the range of 0.5 to 1.5 MeV.

Before giving a simplified outline of the PHA and particle identification algorithms, it is useful to define four instrumental time intervals. The total accumulation interval (TAI) is the period of time associated with one data record, i.e., all the data recorded in one TAI are stored together in one file record with a header containing data such as the time and date associated with the data. For example in the so called Cruse-5a (CR5a) telemetry mode in which the Voyager spacecraft have been since days 220 and 152 of 1991 (for V1 & V2, respectively), the TAI is 192 s, of which 187.2 s is active time, and the remainder dead time. Within each TAI, the instrument can separately store data from subintervals, called sub accumulation intervals (SAIs). In the CR5a mode, rate data are either stored once or three times per TAI, making the SAI for this mode equal to one third of the TAI, with some rate-

channel accumulations taking place over the sum of three SAIs and others occurring three times per TAI, with each accumulation lasting one SAI. Each SAI is composed of a certain number of basic accumulation intervals (BAIs) of a duration stored in the data record header. Each rate channel has a quality word in the telemetry that indicates the number of BAIs that were active during a given SAI, thus determining the time coverage. The final time interval is the pulse-height analysis interval (PAI), thirty two of which (for CR5a) make up one TAI. During these periods each of the available PHA data points are recorded, to be included in the telemetry stream.

The PHA algorithm is essentially as follows. The first ion (ion A, say) that is identified during any given PAI is analyzed, regardless of its priority, and the data are placed in a temporary buffer. Then, if another particle (ion B) is identified during the same PAI, the priority is checked. Depending on the current state of the rotating priority scheme (based on the priority of the PHA data point telemetered during the previous sub-interval) and the priority levels of ions A and B, the choice is made as to whether the ion B PHA data should replace the ion A PHA data in the buffer. This decision process continues with subsequent ions that are identified (ions C, D, etc.) until the end of the PAI is reached, at which time the PHA data-point is ready to be telemetered.

The particle identification method is illustrated in Figure A.2. The intent of the flow chart is to illustrate the identification method, though it should not be interpreted as a strict interpretation of the logic embodied by the LECP circuitry. For example, in what follows, the transition from one TAI to the next is ignored, as is the instrument's accumulation over each BAI. Only the SAI level of accumulation is illustrated. Also,

the flow chart seems to suggest that the PHA and rate collection is handled by one system. This is done to simplify the presentation of the essentials of the particle identification algorithm.

In the following example, parenthetical numerals refer to the numbered items in Figure A.2 and its caption. Here the example of a 1-MeV proton passing through D1a into D2 is again used to illustrate Figure A.2 and the essentials of the particle identification algorithm: (1) A 1 MeV proton enters the LEPT aperture. (2) It is identified as a CH01 ion, and (3) the rate scaler is incremented. (5) Assuming this is not the first ion in this sub-interval (PAI), (4) the priority is checked. (7) Assuming that priority-3 ions (e.g., CH01) have priority (in the present mode of the rotating priority scheme) and that the priority level associated with the PHA data currently in the buffer is other than priority-3, (6) the PH analyzer analyzes D1, D2, D3, and D4 and (9) stores the data in the buffer. Furthermore, (12) assuming that the present PAI sub-interval is ending, (13) the PHA data are telemetered, including the identification byte containing the CH01 identification and D1a information (i.e., the fact that the ion passed through D1a rather than D1b or D1c). (11) If the present SAI is not completed, then the system returns to the “start” state and awaits another event, (10) otherwise the rate data are telemetered as well.

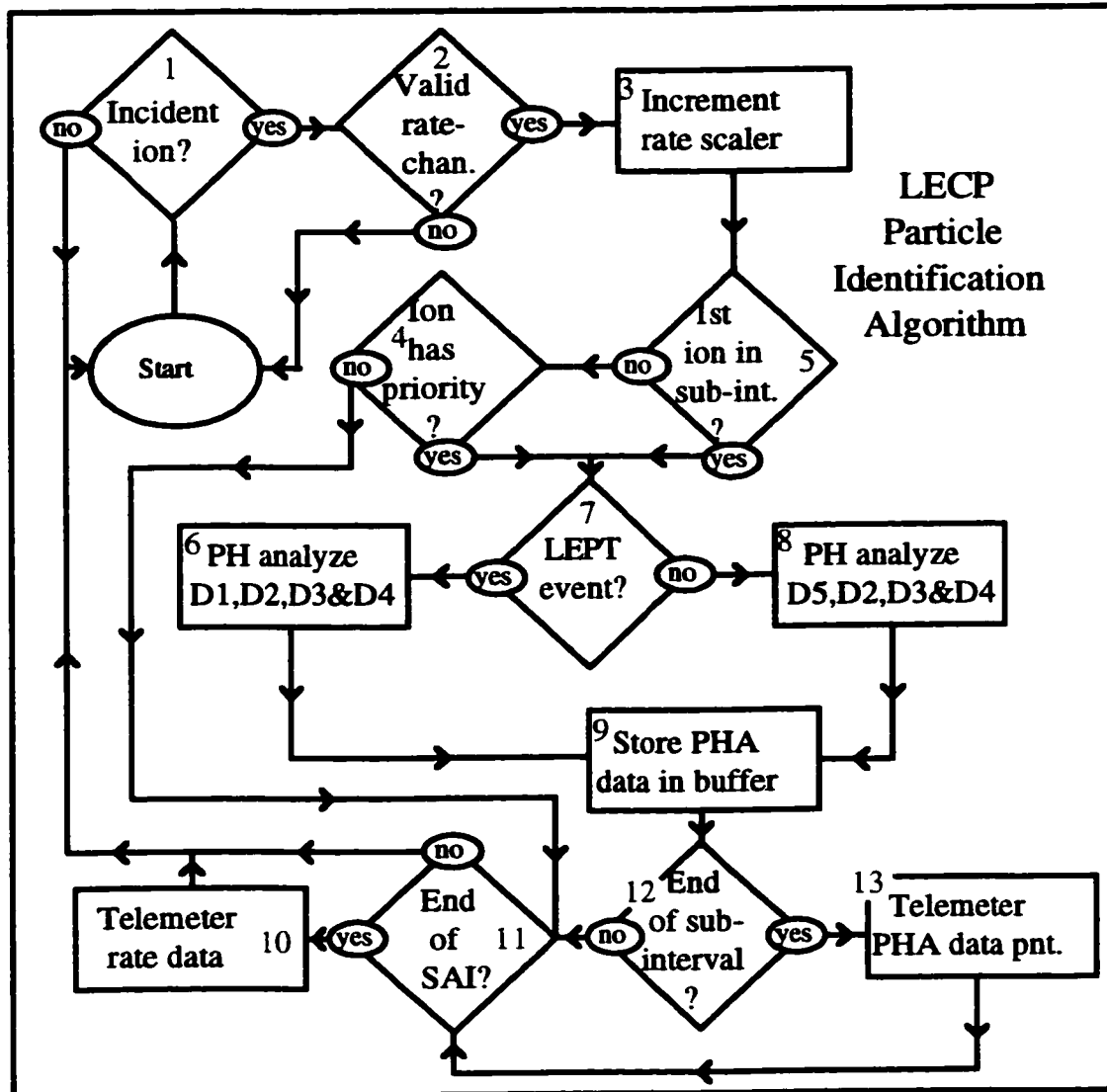


**Figure A.2 Flow Chart of the LECP Particle Identification Algorithm**

(1) Has a potential ion entered the telescope? (2) Does this particle belong to one of the rate-channels? (3) Increment the appropriate rate scaler. (4) Does the present ion have PHA-priority over the PHA data currently in the buffer? (5) Is this ion the first in the PHA sub-interval (PAI)? (6) For LEPT events the D1, D2, D3, and D4 detectors are PH analyzed. (7) Is the present event from the LEPT aperture? (8) For HEPT events the D5, D2, D3, and D4 detectors are PH analyzed. (9) Replace the PHA data in the temporary buffer with the newly analyzed data associated with the present event. (10) Telemeter the rate data and clear the rate scalers to prepare for the next SAI. (Note that, for simplicity, the details concerning BAIs and TAIs are ignored in this figure.) (11) Has the end of the current SAI been reached? The SAI (sub accumulation interval) is associated with the measurement of the rate-data. (12) Has the end of the current PAI been reached. The PAI is associated with the measurement of PHA data. (13) Telemeter the PHA data point. [See note above in (10).]

## A.2 – Flux Calculation

By using both the pulse height data and the counting rates we are able to calculate the differential flux  $\partial J/\partial E$  for several species of ions with energies between roughly 0.3 and 30 MeV/nucleon. The primary tools for making these calculations are the programs we have developed, *VOFLX\_CR5a* and *VOFLX\_87*, which work with LECP data in the CR5a and CR5 telemetry format, respectively. Details of the method used by the programs to calculate the ion flux are discussed by Hill (1998).

The pulse height data from adjacent pairs of detectors in the telescope may be used to construct PHA matrices (Figure A.3), which contain information about the ion's energy deposit  $\Delta E_1$  in the first detector and residual kinetic energy  $\Delta E_2$  deposited in the second (stopping) detector. Various ion species trace out characteristic tracks in the PHA matrix (Figure A.3) therefore, the species can be identified. This identification relies on calculations of charged-particle energy loss in the Si detectors (e.g., Northcliffe and Schilling, 1970) and pre-launch calibration. The rate-scalers count the number of particles per second that are within various rate-channels corresponding to broad regions of the PHA matrix. By dividing the PHA matrix into finer “flux-boxes” that define smaller energy intervals for a specified species, it is possible to calculate the flux over higher-resolution energy ranges. Figure A.3 presents an example of oxygen flux boxes defined for the D5D4 PHA matrix associated with the HEPT aperture.

Each flux box in the PHA matrix (Figure A.3) is designed to identify PHA counts for one species of ion over a defined energy range. The analytical differential

flux  $\partial J/\partial E$  for ions of a single species and energy range is related to the measured differential flux as follows (cf. Appendix C):

$$j \equiv \frac{\partial J}{\partial E} \xrightarrow{\text{measurement}} \frac{\Delta J}{\Delta E} = \frac{1}{G\Delta E} \sum_{i=1}^{N^{\text{box}}} \frac{\sum_t C_{t,i}^{\text{box}} \sum_t C_{t,i}^{\text{rate}}}{\sum_t C_{t,i}^{\text{PHA}} \sum_{t,i} \delta t},$$

where the number of boxcounts  $C^{\text{box}}$  is defined as the number of PHA datapoints having PHA energy-channel values lying within a range defined by the flux box during a given time interval  $\delta t$ ; the number of rate-counts  $C^{\text{rate}}$  is defined as the number of counts determined by the rate-scaler (i.e., for a given rate-channel) associated with a particular flux box during the  $\delta t$  interval; and the number of PHA counts  $C^{\text{PHA}}$  is defined as the number of PHA datapoints having energy-channel values lying within a range defined by the rate-channel during the time interval of interest.  $N^{\text{sum}}$  is the number of flux boxes composing a selected energy range of a given species,  $G$  is the geometry factor (Sullivan, 1971), here  $\Delta E$  is the energy interval (corresponding to the difference between the maximum and the minimum kinetic energy prescribed by the left and right limits of the flux box definition),  $\Delta J$  is a portion of the total flux  $J$ ,  $E$  is the kinetic energy per nucleon, and  $j$  is the differential particle intensity. The time index  $t$  is summed over all of the included total accumulation intervals within the  $\delta t$  interval. A TAI can be excluded from the sum due to various checks made by the analysis software, such as checks for evidence of an error in the data stream or the determination that the spacecraft is in an azimuthal sector that has been excluded from the calculation.

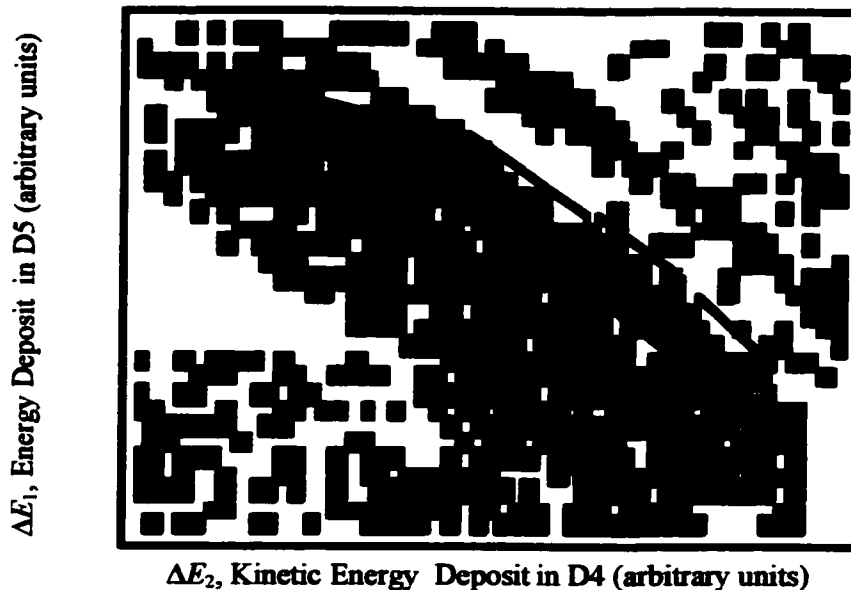


**Figure A.3 Sample PHA Matrix with Flux Boxes**

*A portion of the V1, 1996/1-365, D5 vs. D4 PHA Matrix. The logarithmic color-scale in this two-dimensional histogram represents the number of PHA events during a given time interval with a specified pair of energy deposits  $\Delta E_1$  and  $\Delta E_2$  (the energy deposits in the first and second detectors, respectively), with the color red representing the most and the color black the fewest counts per matrix element. Along with knowledge of the thickness and composition of the detectors, these energy deposit measurements provide a means to calculate the total stopping power -  $dE/dx$  appropriate to a given incident ion with energy  $E$  interacting with a given LECP detector pair. (The differing composition of the layers in each detector actually requires multiple  $dE/dx$  determinations to be made simultaneously.) This information allows us to construct "flux boxes" (drawn in red) that select the ion species with the upper and lower bounds and define a finite, incident kinetic energy interval with the left and right bounds in the PHA matrix. Four such flux boxes are shown for oxygen, while the nitrogen and carbon tracks below oxygen, and the neon track above oxygen are displayed without superimposed flux boxes.*

## B—Notation

### Symbols

$\alpha$	Relativistic Parameter = $(T+2E_0)/(T+E_0)$
$\alpha$	Tilt Angle
$A$	Atomic Mass Number
$A$	Heliomagnetic Polarity Constant
$\beta$	Particle Velocity Relative to the Speed of Light
$B$	Interplanetary Magnetic Field Strength
$C$	Compton-Getting Factor
$\delta r$	HCS <i>Spacing</i> : Half of the HCS Wavelength
$\Delta$	Recovery Coefficient
$E$	Energy per Nucleon
$E_0$	Reference Value for Diffusion Coefficient Energy Dependence
$E_0$	Reference Energy per Nucleon
$E_c$	Cutoff Energy (MeV/nuc)
$E_{\max}$	Maximum Energy per Nucleon Limit in Numerical Model
$E_{\min}$	Minimum Energy per Nucleon Limit in Numerical Model
$E_s$	Reference for Source Spectrum Energy Dependence
$E_0$	Particle Rest Energy = $mc^2$
$f$	Omni-direction Distribution Function
$F$	False Alarm Probability
$g_\lambda$	Latitudinal Intensity Gradient
$g_r$	Radial Intensity Gradient
$\gamma$	Spectral Index
$\gamma$	Energy Dependence of the Diffusion Coefficient
$\gamma_s$	Spectral Power-law Index at the ACR Source
$\eta$	Rigidity Power-law Index
$j$	Differential Intensity or Flux
$j_a$	Time Asymptotic Intensity
$J_{si}$	Source Intensity
$\kappa$	Diffusion Coefficient
$\kappa_0$	Diffusion Coefficient when $E=E_0$
$\lambda$	Heliographic Latitude
$\Lambda$	Scattering Mean Free Path
$n$	Number Density
$\nu$	Frequency



$\nu$	Collision Frequency
$p$	Momentum
$P$	Spectral Power
$q$	Charge = $ze$
$r$	Heliographic radius
$r_{\min}$	Minimum Radius of Model Heliosphere
$r_{\max}$	Maximum Radius of Model Heliosphere $r_{\max} = r_s$
$r_s$	Source Radius
$\rho$	Gyroradius
$R$	Magnetic Rigidity = $pc/ze$
$R_0$	Reference Rigidity
$R_c$	Critical Rigidity of Latitudinal Gradient Sign Reversal
$\sigma_0^2$	Statistical Variance
$s$	Compression Ratio $s = V_U/V_D$
$T$	e-folding Growth Time
$T$	Temperature
$T_c$	Cutoff Energy (MeV)
$\mathcal{T}$	Total Kinetic Energy
$t$	Time
$t_i$	Initial Time
$t_0$	Reference Time
$t_{\max}$	Maximum Time in Numerical Model
$\tau$	e-folding Initial Recovery Time
$u$	Particle Velocity
$U$	Differential Number Density
$U$	Expansion Velocity of Diverging Solar Wind
$V$	Solar Wind Speed
$v$	Particle Velocity
$V_D$	Solar Wind Velocity Downwind of the TS
$V_D$	Drift Velocity Away from the HCS
$V_{Dr}$	Radial Component of the Drift Velocity $V_D$
$V_{ND}$	Neutral Sheet Drift Velocity
$V_U$	Solar Wind Velocity Upwind of the TS
$\Omega$	Angular Rotation Rate of the Sun
$z$	Charge Number
$z$	Normalized Power

## Acronyms

<b>ACE</b>	<b>Advanced Composition Explorer</b>
<b>ACR</b>	<b>Anomalous Cosmic Ray</b>
<b>BC</b>	<b>Boundary Condition</b>
<b>CIR</b>	<b>Corotating Interaction Region</b>
<b>CPT</b>	<b>Charged Particle Telescope</b>
<b>CR</b>	<b>Cosmic Ray</b>
<b>CRS</b>	<b>Cosmic Ray Subsystem</b>
<b>E<math>\beta</math>05</b>	<b>An LECP Counting Rate Sensitive to &gt;70 MeV H</b>
<b>CRTE</b>	<b>Cosmic Ray Transport Equation</b>
<b>FIP</b>	<b>First Ionization Potential</b>
<b>GCR</b>	<b>Galactic Cosmic Ray</b>
<b>HCS</b>	<b>Heliospheric Current Sheet</b>
<b>HEPT</b>	<b>High Energy Particle Telescope</b>
<b>HG</b>	<b>Heliographic</b>
<b>HP</b>	<b>Heliopause</b>
<b>IMF</b>	<b>Interplanetary Magnetic Field</b>
<b>IP</b>	<b>Interplanetary</b>
<b>LECP</b>	<b>Low Energy Charged Particle instrument</b>
<b>LEMPA</b>	<b>Low Energy Magnetospheric Particle Analyzer</b>
<b>LEPT</b>	<b>Low Energy Particle Telescope</b>
<b>LICA</b>	<b>Low-energy Ion Composition Analyzer</b>
<b>LISM</b>	<b>Local Interstellar Medium</b>
<b>PHA</b>	<b>Pulse Height Analysis</b>
<b>PUI</b>	<b>Pick-Up Ion</b>
<b>QL</b>	<b>Quasi-Local</b>
<b>QLG</b>	<b>Quasi-Local Gradient</b>
<b>SAI</b>	<b>Sub Accumulation Interval</b>
<b>SAMPEX</b>	<b>Solar Anomalous Magnetospheric Particle Explorer</b>
<b>SEP</b>	<b>Solar Energetic Particle</b>
<b>TAI</b>	<b>Total Accumulation Interval</b>
<b>TS</b>	<b>Termination Shock</b>
<b>V1</b>	<b>Voyager 1</b>
<b>V2</b>	<b>Voyager 2</b>

## C – A Heuristic Approach to Cosmic Ray Transport

Formal consideration of the problem of cosmic ray transport has been given in the literature (Parker, 1965; Jokipii, 1971; Jones, 1990); however, it is appropriate to discuss the topic from an alternate perspective with the aim of highlighting the physical basis of the cosmic ray transport equation, and of introducing key quantities and notation. Note that in this section the intensity  $j$  is defined with respect to total kinetic energy and that the particle velocity is  $u$ . For the collision frequency the traditional symbol  $\nu$  is used. The omnidirectional distribution function  $f(\mathbf{r}, \mathbf{p}, t)$  can be defined such that the number density  $n(\mathbf{r}, t)$  is obtained from  $n = \int f d^3p = \int d\Omega dp p^2 f = 4\pi \int dp p^2 f$ , where  $p$  is the magnitude of the momentum,  $\mathbf{r}$  is the position vector,  $t$  is the time parameter,  $d\Omega$  is the element of solid angle, and  $dp$  and  $d^3p$  are the momentum and momentum-volume elements. The differential element of total particle number  $dN = f d^3p d^3r$ , where  $d^3r$  is the volume element, can be used to define the measured quantity, differential intensity  $j$ , by  $dN = j dA d\Omega d\mathcal{T} dt$ , with  $dA$  the element of area normal to the particle direction upon detection,  $d\mathcal{T}$  is the element of total kinetic energy defining the interval  $\mathcal{T}$  to  $\mathcal{T} + d\mathcal{T}$  of particle energy, and  $dt$  is the differential time coverage during which the particles are being detected. In this way the differential flux  $j$  is the number of particles per unit area, per unit solid angle, within an energy interval detected per unit time. Now rewriting  $dN$  by considering the volume element described by particles within a given cross-sectional area  $dA$  moving with a velocity  $u$  during an interval  $dt$ , i.e.,  $d^3r = v dt dA$ , we obtain

$dN = p^2 f dp d\Omega v dt dA$ . Noting the  $dp = dT/u$  we equate the two representations of  $dN$ ,  $j dA d\Omega dT dt = p^2 f dT d\Omega dt dA$ , and arrive at the well known relation  $j = p^2 f$ .

With the connection established between  $j$  and the distribution function  $f$ , we may consider the transport problem proper in the following heuristic manner. In the absence of sources, the time rate of change of  $f$  for an element of volume moving at the bulk speed of the fluid of cosmic rays is  $df/dt = 0$ . Allowing a source  $Q$  and assuming a flux of particles according to Fick's law, in which the flux of particles  $\phi$  is proportional to the gradient of the density,  $\phi = -\kappa \nabla f$ , we can employ particle number conservation in this convective frame to obtain,

$$df/dt = Q - \nabla \cdot \phi = Q + \nabla \cdot \kappa \nabla f, \quad (\text{C.1})$$

where here the proportionality  $\kappa$  is the diffusion *tensor*, for generality. (In the convective frame the total and partial time derivative are equal, but this is not shown to avoid the necessity of distinguishing  $\partial f/\partial t$  in each frame.) Transforming to the rest frame by merely noting that the bulk solar wind speed  $V$  is much slower than the particle speed  $v$  for the energetic particles of interest, and ignoring the details (which amount to dropping terms of order  $V/u$ ), we can expand the convective derivative with the Leibniz rule as follows,

$$\frac{df}{dt} = \frac{\partial f}{\partial t} + \sum_{i=1}^3 \frac{\partial f}{\partial x_i} \frac{dx_i}{dt} + \frac{\partial f}{\partial p} \frac{dp}{dt} = \frac{\partial f}{\partial t} + V \cdot \nabla f + \frac{dp}{dt} \frac{\partial f}{\partial p},$$

where  $V$  is the vector solar wind velocity. Combining this with Eq. C.1, (and noting that reference frame labels are not indicated since the transformation is not treated), we arrive at the Fokker-Planck equation,

$$\frac{\partial f}{\partial t} + V \cdot \nabla f + \frac{dp}{dt} \frac{\partial f}{\partial p} = \nabla \cdot \kappa \cdot \nabla f + Q,$$

in the form we desire, save for the force-term on the left hand side, which we consider now. The diverging solar wind results in an acceleration of the energetic particles moving in that medium, i.e., an adiabatic cooling of the cosmic rays as the wind expands or an acceleration as the wind converges.

This can be treated in a most elementary manner by considering a particle in an expanding bubble representing an energetic particle in a volume element of the solar wind medium. If the bubble is expanding at a rate  $dr/dt \equiv U \ll u$ , where  $u$  is the particle speed, and  $r$  is the radial length-scale of the expanding volume, we can consider a particle of mass  $m$  bouncing elastically between two diverging walls, with speeds of  $-U$  and  $U$  for the left and right wall. By formally treating the interactions between the particle and the walls as elastic collisions between a light particle and a massive particle of mass  $M \gg m$ , the momentum change  $dp/dt$  can easily be determined. The bouncing particle's initial speed  $u = u_1$  becomes  $u_2 = -u_1 + 2U$  after the first elastic collision, with the right wall. After the second collision, with the left wall, the particle's speed is  $u_3 = -u_2 - 2U = u_1 - 4U$ . The change in velocity  $\Delta u = u_3 - u_1$  is  $-4U$ . So, during the elapsed period  $\Delta t = 4r/u$  the momentum change becomes  $dp/dt \approx \Delta p/\Delta t = -pU/r$ , or  $dp/dt = -(p/r)dr/dt$ . This implies  $d(pr)/dt = 0$ , which, in using the proportionality to the number density  $r \propto n^{-1/3}$ , becomes  $d(p/n^{1/3})/dt = 0$ . Therefore we obtain  $dp/dt = (p/3)(1/n)dn/dt$ . In the frame of the expanding bubble, we get  $dn/dt = \partial n/\partial t$ , by noting  $V \cdot \nabla n = 0$ , so continuity,  $\partial n/\partial t + \nabla \cdot nV = 0$ , provides the relation  $(1/n)dn/dt = -\nabla \cdot V$ , which says that the density of cosmic rays drops at a rate

proportional to the divergence of the solar wind. With this, the momentum change can be written,

$$\frac{dp}{dt} = -\frac{1}{3}p\nabla \cdot V.$$

The adiabatic deceleration term so evaluated, the complete cosmic ray transport equation is then,

$$\frac{\partial f}{\partial t} = \nabla \cdot \kappa \cdot \nabla f - V \cdot \nabla f + \frac{1}{3}(\nabla \cdot V)p \frac{\partial f}{\partial p} + Q. \quad (C.2)$$

Physically, we see that the first term on the right hand side is due to diffusion of cosmic rays arising from scattering of cosmic rays on magnetic field irregularities in the solar wind. The second term represents the convection process due to the bulk motion of the medium within which the cosmic rays are diffusing, i.e., the solar wind, and the third term comes from the adiabatic acceleration of cosmic rays as the solar wind expands or becomes compressed. The last term is a source term which represents the appearance or disappearance of cosmic rays, due to processes outside of the transport considerations. For example when an ambient interstellar neutral enters the heliosphere and becomes ionized, becoming a pick-up ion, this represents a source of energetic particles.

The diffusion coefficient (e.g., the radial element of the diffusion tensor  $\kappa = \kappa_r$ ) is related to the scattering mean free path  $\Lambda$  and the particle speed  $u$  by the classical expression  $\kappa = u\Lambda/3$ . A few words of justification for this well-known relation are nevertheless useful to complete the connection between directly physical and the more abstract quantities that are the subject of this work. Consider a one-

dimensional random walk consisting of a series of  $N$  steps  $\delta x_i$ , each equal in magnitude to  $\Lambda$  and in either the positive or negative direction. The net displacement is then  $\Delta x = \sum \delta x_i$ , the sum over  $N$  steps. The mean square of this quantity in an ensemble average sense becomes,

$$\langle \Delta x^2 \rangle = \left\langle \sum_{i=1}^N \delta x_i \sum_{j=1}^N \delta x_j \right\rangle = \left\langle \sum_{i=j} \delta x_i \delta x_j \right\rangle + \left\langle \sum_{i \neq j} \delta x_i \delta x_j \right\rangle,$$

where the second to last term is equal to  $N\Lambda^2$  and the last term on average is equal to zero since there are just as likely to be as many positive as negative steps. This leaves  $\langle \Delta x^2 \rangle = N\Lambda^2$ . Scaling the diffusion equation ( $\kappa \sim \partial^2 x / \partial t$ ) indicates that the diffusion coefficient is proportional to the square of the scattering distance per unit time, so  $\kappa \propto \langle \Delta x^2 \rangle / \delta t$ . The distance traveled by a particle in a time  $\delta t$  is  $\delta t = N\Lambda/u$ , so we get  $\kappa \propto u\Lambda$ , which is our result up to a factor of one third arising from the three-dimensional treatment. An alternate approach is given below.

If the ensemble average of the sum of external forces on each particle in a gas is zero, except for the collisional loss of momentum at a rate  $\nu$ , we can write Newton's law as  $m du/dt = -\nu m u$ , for particle mass  $m$  and velocity  $u = dr/dt$ . Taking the inner product of this equation with position  $r$  and explicitly averaging we get  $(d^2/dt^2 + \nu d/dt)\langle r^2 \rangle = 2\langle u^2 \rangle$ , where  $2r \cdot u = dr^2/dt$  and  $2r \cdot du/dt = d^2r^2/dt^2 - 2u^2$  were used, with the approximate solution  $\langle r^2 \rangle = 2\langle u^2 \rangle t / \nu$ , for  $t \gg \nu^{-1}$ . From elementary kinetic theory we have  $m\langle u^2 \rangle / 2 = 3kT/2$ , where  $k$  is Boltzmann's constant and  $T$  is temperature, thus  $\langle r^2 \rangle = (6kT/\nu m)t$ . Fick's law and continuity lead to a diffusion equation for the number density  $\partial n / \partial t = \nabla \cdot \kappa \nabla v$ , the spherically symmetric solution to

which is,  $n(r,t) = N/(4\pi\kappa t)^{3/2} \exp(-r^2/4\kappa t)$ , where here  $N$  is the total number of particles,  $N = \int n 4\pi r^2 dr$ . The mean squared displacement  $\langle r^2 \rangle$  can now be directly evaluated for this distribution of particles  $\langle r^2 \rangle = N^{-1} \int (r^2) n 4\pi r^2 dr = 6\kappa t$ . Since the mean free path is defined as the distance traveled by the particles between collisions,  $\Lambda = u/v$ , we can now write,

$$\kappa = \frac{\langle r^2 \rangle}{6t} = \frac{kT}{\omega m} = \frac{1}{3} \frac{m \langle u^2 \rangle}{\omega m} = \left\langle \frac{1}{3} u \frac{u}{v} \right\rangle = \frac{1}{3} u \Lambda,$$

where the brackets were dropped in the last term to yield the familiar form  $\kappa = u\Lambda/3$ .



## REFERENCES

- Adams, Jr., J.H., M. Garcia-Munoz, N.L. Grigorov, B. Klecker, M.A. Kondratyeva, G.M. Mason, R.E. McGuire, R.A. Mewaldt, M.I. Panasyuk, C.A. Tretyakova, A.J. Tylka, and D.A. Zhuravlev, The Charge State of the Anomalous Component of Cosmic Rays, *Astrophys. J.*, 375, L45-L48, 1991.
- Bai, T., and P.A. Sturrock, The 152-day Periodicity of the Solar Flare Occurrence Rate, *Nature*, 327, 601-604, 1987.
- Bai, T., and E.W. Cliver, A 154 Day Periodicity in the Occurrence Rate of Proton Flares, *Astrophys. J.*, 363, 299-309, 1990.
- Bai, T., and P.A. Sturrock, Evidence for a Fundamental Period of the Sun and its Relation to the 154 Day Complex of Periodicities, *Astrophys. J.*, 409, 476-486, 1993.
- Baker, D.N., G.M. Mason, O. Figueora, G. Colon, J.G. Watzin, and R.M. Aleman, An Overview of the Solar, Anomalous, and Magnetospheric Particle Explorer (SAMPEX) mission, *IEEE Trans. Geosci. Remote Sens.*, 31, 531-541, 1993.
- Barnes, C.W. and J.A. Simpson, Evidence for Interplanetary Acceleration of Nucleons in Corotating Interaction Regions, *Astrophys. J.*, 210, L91-L96, 1976.
- Bertin, P., R. Lallement, R. Ferlet, and A. Vidal-Madjar, Detection of the Local Interstellar Cloud from High-Resolution Spectroscopy of Nearby Stars: Inferences on the Heliospheric Interface, *J. Geophys. Res.*, 98, 15,193-15,197, 1993.
- Bogart, R.S., and T. Bai, Confirmation of a 152 Day Periodicity in the Occurrence of Solar Flares Inferred from Microwave Data, *Astrophys. J.*, 299, L51-L55, 1985.
- Brueckner, G.E., and J.W. Cook, Return of the Hard Solar Flares' 154 Day Periodicity in Solar Cycle 22 and Evidence for a Phase Relationship of this Periodicity Between Cycles 21 and 22, *Astrophys. J.*, 350, L21-L24, 1990.
- Burlaga, L.F., F.B. McDonald, M.L. Goldstein, and A.J. Lazurus, Cosmic Ray Modulation and Turbulent Interaction Regions Near 11 AU, *J. Geophys. Res.*, 90, 12,027-12,039, 1985.
- Burlaga, L.F., and N.F. Ness, Merged Interaction Regions Observed by Voyagers 1 and 2 During 1998, *J. Geophys. Res.*, 105, 5141-5148, 2000.

- Cane, H.V., I.G. Richardson, and T.T. von Roseninge, Interplanetary Magnetic Field Periodicity of ~153 Days, *Geophys. Res. Lett.*, 25, 4437-4440, 1998.
- Cane, H.V., G. Wibberenz, I.G. Richardson, and T.T. von Roseninge, Cosmic Ray Modulation and the Solar Magnetic Field, *Geophys. Res. Lett.*, 26, 565-568, 1999.
- Carbonell, M., and J.L. Ballester, A Short-Term Periodicity Near 155 Day in Sunspot Areas, *Astron. Astrophys.*, 238, 377-381, 1990.
- Chan, J.H., and P.B. Price, Anomalies in the Composition of Interplanetary Heavy Ions with  $0.01 < E < 40$  MeV per amu, *Astrophys. J.*, 190, L39-L41, 1974.
- Chih, P.P., and M.A. Lee, A Perturbation Approach to Cosmic Ray transients in Interplanetary Space, *J. Geophys. Res.*, 91, 2903-2913, 1986.
- Christian, E.R., A.C. Cummings, and E.C. Stone, Evidence for Anomalous Cosmic-Ray Hydrogen, *Astrophys. J.*, 334, L77-L80, 1988.
- Christian, E.R., A.C. Cummings, and E.C. Stone, Observations of Anomalous Cosmic-Ray Hydrogen from the Voyager Spacecraft, *Astrophys. J.*, 446, L105-L108, 1995.
- Christian, E.R., W.R. Binns, J.B. Blake, C.M.S. Cohen, A.C. Cummings, J.R. Dwyer, D.C. Hamilton, M.E. Hill, P.L. Hink, E. Keppler, S.M. Krimigis, R.A. Leske, M.D. Looper, R.G. Marsden, G.M. Mason, J.E. Mazur, R.A. Mewaldt, T.R. Sanderson, E.C. Stone, T.T. von Roseninge, M.E. Wiedenbeck, and N. Yanasak, Observations of the Solar Modulation of Galactic and Anomalous Cosmic Rays During Solar Minimum, *Proc. 26<sup>th</sup> Int. Cosmic Ray Conf.*, 7, 519-522, 1999.
- Cummings, A.C., E.C. Stone, and W.R. Webber, Evidence That the Anomalous Cosmic-Ray Component is Singly Ionized, *Astrophys. J.*, 287, L99-L103, 1984.
- Cummings, A.C., E.C. Stone, and W.R. Webber, Latitudinal and Radial Gradients of Anomalous Cosmic Rays in the Outer Heliosphere, *Geophys. Res. Lett.*, 14, 174-177, 1987.
- Cummings, A.C., R.A. Mewaldt, J.B. Blake, J.R. Cummings, M. Fränz, D. Hovestadt, B. Klecker, G.M. Mason, J.E. Mazur, E.C. Stone, T.T. von Roseninge, and W.R. Webber, Anomalous Cosmic Ray Oxygen Gradients Throughout the Heliosphere, *Geophys. Res. Lett.*, 22, 341-344, 1995a.
- Cummings, A.C., J.B. Blake, J.R. Cummings, M. Fränz, D. Hovestadt, B. Klecker, G.M. Mason, J.E. Mazur, R.A. Mewaldt, E.C. Stone, and W.R. Webber, Radial

and Latitudinal Gradients of Anomalous Cosmic Ray Oxygen Throughout the Heliosphere, *Proc. 24<sup>th</sup> Int. Cosmic Ray Conf.*, 4, 800-803, 1995b.

Cummings, A.C., E.C. Stone, B. Klecker, R.G. Marsden, R.A. Mewaldt, D.V. Reames, K.J. Trattner, T.T. von Rosenvinge, and W.R. Webber, Intensity Gradients of Anomalous Cosmic Ray Oxygen Throughout the Heliosphere, *Proc. 25<sup>th</sup> Int. Cosmic Ray Conf.*, 2, 257-260, 1997.

Cummings, A.C., and E.C. Stone, Anomalous Cosmic Rays and Solar Modulation, *Space Sci. Rev.*, 83, 51-62, 1998.

Dalla, S., and A. Balogh, Recurrence in MeV Proton Fluxes and Anisotropies at 5 AU from the Sun, *Geophys. Res. Lett.*, 27, 153-156, 2000.

Dalla, S., A. Balogh, B. Heber, and C. Lopate, Further Indications of a ~140 Day Recurrence in Energetic Particle Fluxes at 1 and 5 AU from the Sun, *J. Geophys. Res.*, 106, 5721-5730, 2001.

Decker, R.B., S.M. Krimigis, A.G. Ananth, D.C. Hamilton, and M.E. Hill, Small-scale Variations in ACR Intensities at Voyagers 1 and 2 in 1992-1998, *Proc. 26<sup>th</sup> Int. Cosmic Ray Conf.*, 7, 512-515, 1999.

Delache, P., F. Laclare, and H. Sadsaoud, Long Period Oscillations in Solar Diameter Measurements, *Nature*, 317, 416-418, 1985.

Dennis, B.R., Solar Hard X-Ray Bursts, *Sol. Phys.*, 100, 465-490, 1985.

Droge, W., K. Gibbs, J.M. Grunsfeld, P. Meyer, B.J. Newport, P. Evenson and D. Moses, A 153 Day Periodicity in the Occurrence of Solar Flares Producing Energetic Interplanetary Electrons, *Astrophys. J. Suppl. Ser.*, 73, 279-283, 1990.

Drury, L.O'C., An Introduction to the Theory of Diffusive Shock Acceleration of Energetic Particles in Tenuous Plasmas, *Rep. Prog. Phys.*, 46, 973-1027, 1983.

Fan, C.Y., G. Gloeckler, and J.A. Simpson, Proton and Helium Nuclei within Interplanetary Magnetic Regions which Co-Rotate with the Sun, *Proc. Ninth Int. Cosmic Ray Conf.*, 1, 109-111, 1965.

Fichtner, H., H. de Bruijn, and S.R. Sreenivasan, Longitudinal Gradients of the Distribution of Anomalous Cosmic Rays in the Outer Heliosphere, *Geophys. Res. Lett.*, 23, 1705-1708, 1996.

Fisk, L.A., B. Kozlovsky, and R. Ramaty, An Interpretation of the Observed Oxygen and Nitrogen Enhancements in Low-Energy Cosmic Rays, *Astrophys. J.*, 190, L35-L37, 1974.

- Fisk, L.A., The Anomalous Component, its Variation with Latitude and Related Aspects of Modulation, in *The Sun and the Heliosphere in Three Dimensions*, R.G. Marsden, ed., Reidel Publishing, Boston, 401-411, 1986.
- Flügge, S., ed., *Encyclopedia of Physics, XLVI 1, Cosmic Rays I*, Springer-Verlag, Berlin, 1961.
- Forbush, S.E., World-Wide Cosmic-Ray Variations, 1937-1952, *J. Geophys. Res.*, *59*, 525-542, 1954.
- Fujii, Z., and F.B. McDonald, Radial Intensity Gradients of Galactic Cosmic Rays (1972-1995) in the Heliosphere, *J. Geophys. Res.*, *102*, 24201-24208, 1997.
- Fujii, Z. and F.B. McDonald, Study of the Radial and Latitudinal Intensity Gradients of Galactic and Anomalous Cosmic Rays, *Proc. 26<sup>th</sup> Int. Cosmic Ray Conf.*, *7*, 246-249, 1999.
- Gabriel, S., R. Evans, and J. Feynman, Periodicities in the Occurrence Rate of Solar Proton Events, *Sol. Phys.*, *128*, 415-422, 1990.
- Garcia-Munoz, M., G.M. Mason, and J.A. Simpson, A New Test for Solar Modulation Theory: The 1972 May-July Low-Energy Galactic Cosmic Ray Proton and Helium Spectra, *Astrophys. J.*, *182*, L81-L84, 1973.
- Gleeson, L.J., and W.I. Axford, Solar Modulation of Galactic Cosmic Rays, *Astrophys. J.*, *154*, 1011-1026, 1968.
- Gloeckler, G., J. Geiss, H. Balsiger, L.A. Fisk, A.B. Galvin, F.M. Ipavich, K.W. Ogilvie, R. von Steiger, and B. Wilken, Detection of Interstellar Pick-Up hydrogen in the Solar System, *Science*, *261*, 70-73, 1993.
- Hamilton, D.C., M.E. Hill, G. Gloeckler, R.B. Decker, and S.M. Krimigis, Anomalous Cosmic Ray Spectra in the Outer Heliosphere: 1992-1998, *Proc. 26-th Int. Cosmic Ray Conf.*, *7*, 535-538, 1999.
- Heber, B., W. Dröge, H. Kunow, R. Müller-Mellin, G. Wibberenz, P. Ferrando, A. Raviart, and C. Paizis, Spatial Variation of > 106 MeV Proton Fluxes Observed During the Ulysses Rapid Latitude Scan: Ulysses COSPIN/KET Results, *Geophys. Res. Lett.*, *23*, 1513-1516, 1996.
- Heisenberg, W., ed., *Cosmic Radiation*, Dover, New York, 1946.
- Hill, M.E., Methods of Analysis for Voyager LECP Data, *Univ. Maryland, College Park, Department of Physics Paper, PP01-048*, (also [http://space.umd.edu/voyager/Hill\\_UMD\\_MS\\_paper\\_1998](http://space.umd.edu/voyager/Hill_UMD_MS_paper_1998)), 1998.

- Hill, M.E., D.C. Hamilton, and S.M. Krimigis, Periodicity of 151 Days in Outer Heliospheric Anomalous Cosmic Ray Fluxes, *J. Geophys. Res.*, *106*, 8315-8322, 2001.
- Hill, M.E., D.C. Hamilton, J.E. Mazur, and S.M. Krimigis, The 1992 - 2000 Recovery of Anomalous Cosmic Ray Oxygen Throughout the Heliosphere, *Proc. 27-th Int. Cosmic Ray Conf.*, *10*, 4247-4250, 2001.
- Horne, J.H., and S.L. Baliunas, A Prescription for Period Analysis of Unevenly Sampled Time Series, *Astrophys. J.*, *302*, 757-763, 1986.
- Hovestadt, D., O. Voller, G. Gloeckler, and C.Y. Fan, Differential Energy Spectra of Low-Energy (<8.5 MeV per Nucleon) Heavy Cosmic Rays during Solar Quiet Times, *Phys. Rev. Lett.*, *31*, 650-653, 1973.
- Ichimoto, K., J. Kubota, M. Suzuki, I. Tohmura, and H. Kurokawa, Periodic Behaviour of Solar Flare Activity, *Nature*, *316*, 422-424, 1985.
- Jokipii, J.R., Propagation of Cosmic Rays in the Solar Wind, *Rev. Geophys. and Space Phys.*, *9*, 27-87, 1971.
- Jokipii, J.R., E.H. Levy, and W.B. Hubbard, Effects of Particle Drift on Cosmic-Ray Transport, I, General Properties, Application to Solar Modulation, *Astrophys. J.*, *213*, 861-868, 1977.
- Jokipii, J.R., and D.A. Kopriva, Effects of Particle Drift on the Transport of Cosmic Rays, III, Numerical Models of Galactic Cosmic-Ray Modulation, *Astrophys. J.*, *234*, 384-392, 1979.
- Jokipii, J.R., and J. Kota, The Polar Heliospheric Magnetic Field, *Geophys. Res. Lett.*, *16*, 1-4, 1989.
- Jokipii, J.R., The Anomalous Component of Cosmic Rays, in *Physics of the Outer Heliosphere*, S. Grzedzielski and D.E. Page, eds., Pergamon, New York, 169-178, 1990.
- Jokipii, J.R., J. Kota, J. Giacalone, T.S. Horbury, and E.J. Smith, Interpretation and Consequences of Large-Scale magnetic Variations Observed at High Heliographic Latitude, *Geophys. Res. Lett.*, *22*, 3385-3388, 1995.
- Jokipii, J.R., Acceleration, transport and Fractionation of Anomalous Cosmic Rays, in, *Acceleration and Transport of Energetic Particles Observed in the Heliosphere: ACE 2000 Symposium*, ed., R.A. Mewaldt, 2000.
- Jones, F.C., The Generalized Diffusion-Convection Equation, *Astrophys. J.*, *361*, 162-172, 1990.

- Kile, J.N., and E.W. Cliver, A search for the 154 Day Periodicity in the Occurrence Rate of Solar Flares using Ottawa 2.8 GHz Burst Data, 1955-1990, *Astrophys. J.*, 370, 442-448, 1991.
- Klecker, B., M.C. McNab, J.B. Blake, D.C. Hamilton, D. Hovestadt, H. Kastle, M.D. Looper, G.M. Mason, J.E. Mazur, and M. Scholer, Charge State of Anomalous Cosmic-Ray Nitrogen, Oxygen, and Neon: SAMPEX Observations, *Astrophys. J.*, 442, L69-L72, 1995.
- Kreyszig, E., *Advanced Engineering Mathematics*, Wiley, New York, 1993.
- Krimigis, S.M., T.P. Armstrong, W.I. Axford, C.O. Bostrom, C.Y. Fan, G. Gloeckler, and L.J. Lanzerotti, The Low Energy Charged Particle (LECP) Experiment on the Voyager Spacecraft, *Space Sci. Rev.*, 21, 329-354, 1977.
- Krimigis, S.M., R.B. Decker, D.C. Hamilton, and M.E. Hill, Energetic Ions in the Outer Heliosphere, 1992-1997, *Proc. 25th Int. Cosmic Ray Conf.*, 1, 393-396, 1997.
- Krimigis, S.M., R.B. Decker, D.C. Hamilton, and G. Gloeckler, Observations of Pick-Up Ions in the Outer Heliosphere by Voyager 1 and 2, in *Acceleration and Transport of Energetic Particles Observed in the Heliosphere: ACE 2000 Symposium*, R.A. Mewaldt, ed., American Institute of Physics, 333-336, 2000.
- Kudela, K., A.G. Ananth, and D. Venkatesan, The Low-Frequency Spectral Behavior of Cosmic Ray Intensity, *J. Geophys. Res.*, 96, 15,871-15,875, 1991.
- Lean, J.L., and G.E. Brueckner, Intermediate-Term Solar Periodicities: 100-500 Days, *Astrophys. J.*, 337, 568-578, 1989.
- Lean, J., Evolution of the 155 Day Periodicity in Sunspot Areas During Solar Cycles 12 to 21, *Astrophys. J.*, 363, 718-727, 1990.
- Levy, E.H., Theory of the Solar Magnetic Cycle Wave in the Diurnal Variation of Energetic Cosmic Rays: Physical Basis of the Anisotropy, *J. Geophys. Res.*, 81, 2082-2088, 1976.
- Mason, G.M., D.C. Hamilton, P.H. Walpole, K.F. Heuerman, T.L. James, M.H. Lennard, and J.E. Mazur, LEICA: A Low Energy Ion Composition Analyzer for the Study of Solar and Magnetospheric Heavy Ions, *IEEE Trans. Geosci. Remote Sens.*, 31, 549-556, 1993.
- Mazur, J.E., G.M. Mason, J.B. Blake, B. Klecker, R.A. Leske, M.D. Looper, and R.A. Mewaldt, Anomalous Cosmic Ray Argon and Other Rare Elements at 1-4 MeV/nucleon Trapped Within the Earth's Magnetosphere, *J. Geophys. Res.*, 105, 21015-21023, 2000.

- McDonald, F.B., B.J. Teegarden, J.H. Trainor, and W.R. Webber, The Anomalous Abundance of Cosmic-Ray Nitrogen and Oxygen Nuclei at Low Energies, *Astrophys. J.*, 187, L105-L108, 1974.
- McDonald, F.B., N. Lal, and R.E. McGuire, Role of Drifts and Global Merged Interaction Regions in the Long-Term Modulation of Cosmic Rays, *J. Geophys. Res.*, 98, 1243-1256, 1993.
- McDonald, F.B., A. Barnes, L.F. Burlaga, P. Gazis, J. Mihalov, and R.S. Selesnick, Effects of the Intense Solar Activity of March/June 1991 Observed in the Outer Heliosphere, *J. Geophys. Res.*, 99, 14705-14715, 1994.
- McDonald, F.B., A. Lukasiak, and W.R. Webber, Pioneer 10 and Voyager 1 Observations of Anomalous Cosmic-Ray Hydrogen in the Outer Heliosphere, *Astrophys. J.*, 446, L101-L104, 1995.
- McDonald, F.B., P. Ferrando, B. Heber, H. Kunow, R. McGuire, R. Muller-Mellin, C. Paizis, A. Raviart, and G. Wibberenz, A Comparative Study of Cosmic Ray Radial and Latitudinal Gradients in the Inner and Outer Heliosphere, *J. Geophys. Res.*, 102, 4643-4651, 1997.
- McDonald, F.B., N. Lal, and R.E. McGuire, Cosmic Ray Recovery and the Solar Minimum Phase of Solar Cycle 22: An Interim Report, *J. Geophys. Res.*, 103, 373-379, 1998.
- McDonald, F.B., L.F. Burlaga, R.E. McGuire, and N.F. Ness, The onset of Long-Term Cosmic Ray Modulation in Cycle 23 Coupled with a Transient Increase of Anomalous Cosmic Rays in the Distant Heliosphere, *J. Geophys. Res.*, 105, 20,997-21,003, 2000a.
- McDonald, F.B., B. Heikkila, N. Lal, E.C. Stone, The Relative Recovery of Galactic and Anomalous Cosmic Rays in the Distant Heliosphere: Evidence for Modulation in the Heliosheath, *J. Geophys. Res.*, 105, 1-8, 2000b.
- McDonald, F.B., B. Klecker, R.E. McGuire, and D.V. Reames, A Comparative Study of the Cosmic Ray Recovery Process in the Inner and Outer Heliosphere, *Proc. 27th Int. Cosmic Ray Conf.*, 9, 3762-3765, 2001.
- McKibben, R.B., An Experimental Test for the Charge State of the "Anomalous" Helium Component, *Astrophys. J.*, 217, L113-L116, 1977.
- McKibben, R.B., Reanalysis and Confirmation of Positive Latitude Gradients for Anomalous Helium and Galactic Cosmic Rays Measured in 1975-1976 with Pioneer 11, *J. Geophys. Res.*, 94, 17,021-17,033, 1989.

- McKibben, R.B., J.J. Connell, C. Lopate, J.A. Simpson, and M. Zhang, Observations of Galactic Cosmic Rays and the Anomalous Helium During Ulysses Passage from the South to the North Solar Pole, *Astron. Astrophys.*, 316, 547-554, 1996.
- McKibben, R.B., Three-Dimensional Solar Modulation of Cosmic Rays and Anomalous Components in the Inner heliosphere, *Space Science Rev.*, 83, 21-32, 1998.
- Mewaldt, R.A., A.C. Cummings, J.R. Cummings, E.C. Stone, B. Klecker, D. Hovestadt, M. Scholer, G.M. Mason, J.E. Mazur, D.C. Hamilton, T.T. von Roseninge, and J.B. Blake, The Return of the Anomalous Cosmic Rays to 1 AU in 1992, *Geophys. Res. Lett.*, 20, 2263-2266, 1993.
- Mewaldt, R.A., R.S. Selesnick, J.R. Cummings, E.C. Stone, and T.T. von Roseninge, Evidence for Multiply Charged Anomalous Cosmic Rays, *Astrophys. J.*, 466, L43-L46, 1996.
- Möbius, E., D. Hovestadt, B. Klecker, M. Scholer, G. Gloeckler, and F.M. Ipavich, Direct Observation of He<sup>+</sup> Pick-Up Ions of Interstellar Origin in the Solar Wind, *Nature*, 318, 426-429, 1985.
- Moraal, H., and C.D. Steenberg, Basic Properties of Anomalous Cosmic Ray Spectra, *Proc. 26-th Int. Cosmic Ray Conf.*, 7, 543-546, 1999.
- Ness, N.F., and L.F. Burlaga, Spacecraft Studies of the Interplanetary Magnetic Field, *J. Geophys. Res.*, 106, 15803-15817, 2001.
- Northcliffe, L.C., and R.F. Schilling, Range and Stopping-Power Tables for Heavy Ions, *Nucl. Data Tables*, A7, 233-463, 1970.
- Ozguc, A., and T. Atac, Periodic Behavior of Solar Flare Index During Solar Cycles 20 and 21, *Sol. Phys.*, 123, 357-365, 1989.
- Paizis, C., B. Heber, A. Raviart, R. Ducros, P. Ferrando, C. Rastoin, H. Kunow, R. Müller-Mellin, H. Sierks, and W. Wibberenz, Latitudinal Effects of Galactic Cosmic Rays Observed Onboard the Ulysses Spacecraft, *Proc. 24<sup>th</sup> Int. Cosmic Ray Conf.*, 4, 756-759, 1995.
- Parker, E.N., Dynamics of the Interplanetary Gas and Magnetic Fields, *Astrophys. J.*, 128, 664-676, 1958.
- Parker, E.N., The Passage of Energetic Charged Particles through Interplanetary Space, *Planet. Space Sci.*, 13, 9-49, 1965.



- Peletier, D.P., S.A. Gary, and A.F. Hogrefe, Mariner-Jupiter-Saturn Low Energy Charged Particle Experiment, *IEEE Trans. Nucl. Sci.*, NS-24, No.1, 795-800, 1977.
- Pesses, M.E., J.R. Jokipii, and D. Eichler, Cosmic Ray Drift, Shock Wave Acceleration, and the Anomalous Component of Cosmic Rays, *Astrophys. J.*, 246, L85-L88, 1981.
- Potgieter, M.S., and H. Moraal, A Drift Model for the Modulation of Galactic Cosmic Rays, *Astrophys. J.*, 294, 425-440, 1985.
- Potgieter, M.S., J.A. le Roux, and R.A. Burger, Interplanetary Cosmic Ray Radial Gradients with Steady State Modulation Models, *J. Geophys. Res.*, 94, 2323-2332, 1989.
- Potgieter, M.S., Heliospheric Modulation of Cosmic Ray Protons: Role of Enhanced Perpendicular Diffusion During Periods of Minimum Solar Modulation, *J. Geophys. Res.*, 105, 18,295-18,303, 2000.
- Press, W.H., B.P. Flannery, S.A. Teukolsky, and W.T. Vetterling, *Numerical Recipes (FORTRAN)*, Cambridge Univ. Press, New York, 1989.
- Reames, D.V., L.M. Barbier, and T.T. von Rosenvinge, WIND/EPACT Observations of Anomalous Cosmic Rays, *Adv. Space Res.*, 19, 809, 1997.
- Reinecke, J.P.L., and H. Moraal, On the Form of the 1987 Hydrogen Spectrum in the Outer Heliosphere, *Astrophys. J.*, 392, 272-276, 1992.
- Reinecke, J.P.L., and M.S. Potgieter, An Explanation for the Difference in Cosmic Ray Modulation at Low and Neutron Monitor Energies During Consecutive Solar Minimum Periods, *J. Geophys. Res.*, 99, 14761-14767, 1994.
- Ribes, E., P. Merlin, J.-C. Ribes, and R. Barthalot, Absolute Periodicities in the Solar Diameter, Derived from Historical and Modern Data, *Ann. Geophys.*, 7, 321-330, 1989.
- Rieger, E., G.H. Share, D.J. Forrest, G. Kanbach, C. Reppin, and E.L. Chupp, A 154-Day Periodicity in the Occurrence of Hard Solar Flares?, *Nature*, 312, 623-625, 1984.
- Rossi, B.B., *Cosmic Rays*, McGraw-Hill, New York, 1964.
- Russell, C.T., A Brief History of Solar-Terrestrial Physics, in *Introduction to Space Physics*, M.G. Kivelson and C.T. Russell, eds., Cambridge Univ. Press, New York, 1-26, 1995.

- Rygg, T.A and J.A. Earl, Balloon measurements of Cosmic Ray Protons and Helium over Half a Solar Cycle 1965-1969, *J. Geophys. Res.*, 76, 7445-7469, 1971.
- Scargle, J.D., Studies in Astronomical Time Series Analysis, II, Statistical Aspects of Spectral Analysis of Unevenly Spaced Data, *Astrophys. J.*, 263, 835-853, 1982.
- Selesnick, R.S., A.C. Cummings, R.A. Leske, R.A. Mewaldt, E.C. Stone, and J.R. Cummings, Solar Cycle Dependence of the Geomagnetically Trapped Anomalous Cosmic Rays, *Geophys. Res. Lett.*, 27, 2349-2352, 2000.
- Silverman, S.M., The 155-Day Solar Period in the Sixteenth Century and Later, *Nature*, 347, 365-367, 1990.
- Simpson, J.A., M. Zhang, and S. Bame, A Solar Polar North-South Asymmetry for Cosmic-Ray Propagation in the Heliosphere: The Ulysses Pole-to-Pole Rapid Transit, *Astrophys. J.*, 465, L69-L72, 1996.
- Singh, R.K., B. Mitra, N. Durgaprasad, S. Biswas, M.N. Vahia, J.S. Yadav, A. Dutta, and J.N. Goswami, Ionization States of the Anomalous Cosmic Rays, *Astrophys. J.*, 374, 753-765, 1991.
- Skilling, J., Cosmic Rays in the Galaxy: Convection or Diffusion, *Astrophys. J.*, 170, 265-273, 1971.
- Steenberg, C.D., and H. Moraal, An Acceleration/Modulation Model for Anomalous Cosmic Ray Hydrogen in the Heliosphere, *Astrophys. J.*, 463, 776-783, 1996.
- Steenberg, C.D, H. Moraal, and F.B. McDonald, Species Scaling of Modulated Anomalous Cosmic Ray Spectra, *Proc. 25-th Int. Cosmic Ray. Conf.*, 2, 233-236, 1997.
- Steenberg, C.D., Modelling of Anomalous and Galactic Cosmic Ray Modulation in the Outer Heliosphere, *Ph.D. Thesis*, Potchefstroom University for Christian Higher Education, South Africa, 1998.
- Steenberg, C.D and H. Moraal, Form of the Anomalous Cosmic Ray Spectrum at the Solar Wind Termination Shock, *J. Geophys. Res.*, 104, 24879-24884, 1999.
- Stone, E.C., A.C. Cummings, and W.R. Webber, The Distance to the Solar Wind Termination Shock in 1993 and 1994 from Observations of Anomalous Cosmic Rays, *J. Geophys. Res.*, 101, 11017-11025, 1996.
- Stone, E.C., A.C. Cummings, and W.R. Webber, Evolution of the Energy Spectra of Anomalous Cosmic Rays in the Outer Heliosphere, *Proc. 25-th Int. Cosmic Ray Conf.*, 2, 253-256, 1997.

- Stone, E.C., A.C. Cummings, D.C. Hamilton, M.E. Hill, and S.M. Krimigis, Voyager Observations of Anomalous and Galactic Cosmic Rays During 1998, *Proc. 26-th Int. Cosmic Ray Conf.*, 7, 551-554, 1999.
- Stone, E.C., and A.C. Cummings, Estimate of the Location of the Solar Wind Termination Shock, *Proc. 27-th Cosmic Ray Conf.*, 10, 4263-4266, 2001.
- Sullivan, J.D., Geometrical Factor and Directional Response of Single and Multi-Element Particle Telescopes, *Nucl. Instr. Methods*, 95, 5-11, 1971.
- Trattner, K.J., R.G. Marsden, and T.R. Sanderson, The Ulysses North Polar Pass: Latitudinal Gradients of Anomalous Cosmic Ray O, N and Ne, *Geophys. Res. Lett.*, 24, 1719-1722, 1997.
- Valdes-Galicia, J.F., R. Perez-Enriquez, and J.A. Otaola, The Cosmic-Ray 1.68-Year Variation: A Clue to Understanding the Nature of the Solar Cycle?, *Sol. Phys.*, 167, 409-417, 1996.
- Van Allen, J.A., On the Modulation of Galactic Cosmic Ray Intensity During Solar Activity Cycles 19, 20, 21, 22, and Early 23, *Geophys. Res. Lett.*, 27, 2453-2456, 2000.
- Wolff, C.L., The Rotational Spectrum of *g*-Modes in the Sun, *Astrophys. J.*, 264, 667-676, 1983.

